Gamma-ray spectral modulations of astrophysical sources caused by photon-ALPs mixing

Dissertation
zur Erlangung des Doktorgrades
des Department Physik
der Universität Hamburg

vorgelegt von

Jhilik Majumdar
aus Indien

Hamburg
2018

Gutachter der Dissertation:	Prof. Dr. Dieter Horns Prof. Dr. Alessandro Mirizzi
Zusammensetzung der Prüfungskommission:	Prof. Dr. Dieter Horns Prof. Dr. Alessandro Mirizzi Prof. Dr. Caren Hagner Prof. Dr. Günter Sigl Dr. Christian Sander
Vorsitzende der Prüfungskommission:	Prof. Dr. Caren Hagner
Datum der Disputation:	05.07.2018
Vorsitzender Fach-Promotionsausschusses PHYSIK:	Prof. Dr. Wolfgang Hansen
Leiter desDepartments Physik:	Prof. Dr. Michael Potthoff
Dekan der MIN Fakultät:	Prof. Dr. Heinrich Graener

"Only two things are infinite, the universe and human stupidity, and I'm not sure about the former."

Albert Einstein

Abstract

Well-motivated extensions of the standard model of the particle physics predict ultra-light and fundamental pseudo-scalar particles (e.g., axions or axion-like particles: ALPs) to exist. Similarly to the Primakoff-effect for axions, ALPs can mix with photons and consequently be searched for in laboratory experiments and with astrophysical observations. An indication for an anomalous transparency of the Universe has been found for gamma-rays propagating through cosmological distances. A possible explanation of this anomaly could be the mixing of energetic photons with an ultra-light ALPs which is related to a Peccei-Quinn type U(1) symmetry broken at a higher energy scale. In this thesis, we investigated the observational data of orbital gamma-ray telescope and used energy spectra to search for deviations from the expected optical depth and constrain the parameter space of ALPs.

We analyzed the data recorded with the Fermi -LAT from Galactic pulsars selected to have a line of sight crossing spiral arms at a large pitch angle. The large-scale Galactic magnetic field traces the shape of spiral arms, such that a sizable photon-ALP conversion probability is expected for the sources considered. In nine years of Fermi -LAT data, we detect significant spectral features in the selected source-sample consistent with photon-ALPs oscillation with a combined statistical significance of 4.6 σ. From a common fit to all sources, we determine the most-likely parameters for mass m_a and coupling $g_{a\gamma\gamma}$ to be $m_a = (3.6^{+0.5_{\text{stat.}}}_{-0.2_{\text{stat.}}} \pm 0.2_{\text{syst.}})$ neV and $g_{a\gamma\gamma} = (2.3^{+0.3_{\text{stat.}}}_{-0.4_{\text{stat.}}} \pm 0.4_{\text{syst.}}) \times 10^{-10}$ GeV^{-1}. In the error budget, we consider instrumental effects, scaling of the adopted Galactic magnetic field model (20–40 %), and uncertainties on the distance of individual sources. We refined the search method and improved the existing magnetic field models in the Galaxy and in inter-galactic space with the Planck data. We note, however, that we do have limited knowledge about the magnetic field structure, especially for the sources which are located in the inner part of the Galaxy and also that the crucial opening angle of the spiral arms is not well constrained. Besides, with the help of other Galactic magnetic field model, it is interesting to note that our ALP-hypothesis works nicely.

Additionally, a similar study has been conducted for selected bright Galactic plane and non-Galactic plane sources. Some of the sources exhibit spectral irregularities due to

photon-ALPs mixing, however it is nice to see that spectral features for the sources differ with the location as the photons emitted from an astrophysical source traverse through different intensity magnetic field domain. A multi-wavelength spectral energy distribution (SED) for the non-Galactic plane sources have been shown to study the astronomical features of the sources.

Kurzfassung

Gut motivierte Erweiterungen des Standardmodells der Teilchenphysik sagen ultraleichte, fundamentale pseudoskalare Teilchen voraus (z.B. Axionen oder Axion-ähnliche Teilchen: ALPs). Auf der Grundlage des Primakoff-Effekts können Axionen und ALPs in Photonen konvertieren und somit in Labor-Experimenten oder mit Hilfe astro-physikalischer Beobachtungen gesucht werden. Ein Hinweis auf eine anormale Transparenz des Universums für über kosmologische Distanzen propagierende Gamma-Strahlen wurde gefunden. Eine mögliche Erklärung hierfür basiert auf dem Bruch einer Peccei-Quinn U(1) Symmetrie bei höheren Energieskalen. In dieser Arbeit werden Daten des Fermi-LAT gamma-ray Teleskopes ausgewertet, um anhand der gemessenen Energiespektren nach Abweichungen von der erwarteten optischen Tiefe zu suchen, und den Parameterraum der ALPs einzuschrnken.

Fermi-LAT Daten von selektierten galaktischen Pulsaren, deren Sichtlinie die galaktischen Arme mit einem groen Winkel zum galaktischen Zentrum (engl. pitch-angle) kreuzt, wurden analysiert. Das galaktische Magnetfeld folgt der Form der Spiralarme, so dass eine hohe Photon-ALP- Konversionswahrscheinlichkeit für diese Quellen erwartet werden kann. In einem 9 Jahre umfassenden Fermi-LAT Datensatz der selektierten Quellen wurden mit Photon-ALPs Konversion konsistente spektrale Eigenschaften entdeckt. Die kombinierte statistische Signifikanz dieser Analyse beträgt $4.6\,\sigma$. Aus einer Modellanpassung an alle Daten wurden die wahrscheinlichsten Werte für die Masse m_a und die Kopplung $g_{a\gamma\gamma}$ mit $\mathrm{m}_a = (3.6^{+0.5_{\mathrm{stat.}}}_{-0.2_{\mathrm{stat.}}} \pm 0.2_{\mathrm{syst.}})$ neV und $g_a\gamma\gamma = (2.3^{+0.3_{\mathrm{stat.}}}_{-0.4_{\mathrm{stat.}}} \pm 0.4_{\mathrm{syst.}}) \times 10^{-10}$ GeV^{-1} bestimmt. In die systematischen Fehler gehen instrumentale Effekte, die Skalierung des galaktischen Magnetfeldmodells (20-40%) und Unsicherheiten der Distanzen einzelner Quellen ein. Die Methode wurde verbessert, indem existierende galaktische und intergalaktische Magnetfeldmodelle mit Hilfe von Daten des Planck-Satelliten verbessert wurden. Es muss allerdings angemerkt werden, dass die Magetfeldstruktur, insbesondere für Quellen im inneren Bereich der Galaxie, nicht gut bekannt ist. Ausserdem ist der wichtige Öffnungswinkel der Spiralarme nicht gut eingeschränkt. Interessanterweise passt die ALP-Hypothese auch zu den Daten, wenn andere galaktische Magnetfeldmodelle verwendet werden.

Zustzlich wurde eine hnliche Studie mit ausgewählten, hellen Quellen innerhalb und ausserhalb der Galaktischen Ebene durchgeführt. Einige dieser Quellen zeigen auf Photon-ALPs Konversion hindeutende spektrale Eigenschaften. Dabei ist es ermutigend festzustellen, dass die spektralen Abweichungen für unterschiedliche Quellpositionen unterschiedlich stark ausgeprägt sind, da die Photonen einer astrophysikalischen Quelle durch unterschiedliche Magnetfeldstrukturen propagieren.

Contents

Dedicated to my parents ....

Chapter 1

Introduction

The Standard Model (SM) of particle physics has a perfect agreement with the results of collider and the other particle physics experiment, but astrophysical observations show us that the SM only describes 15% of the matter in the universe. Multiple observations at different scales are consistent with the presence of a massive population of non-luminous particles. This type of particle is called *dark matter* (DM) which makes up a significant fraction nearly 80% of matter of the universe. Although DM has a profound impact in the structure formation in the Universe, the nature of it is unknown until today. The search for dark matter is performed with particle collider experiments, ground-based telescopes and satellites with the method of either direct or indirect detection.

1.1 Indication for dark matter

The earliest indication of presence of dark matter came from the velocity dispersions of galaxies within clusters. Zwicky (1933) noticed that the outer members of the Coma cluster were moving far too quickly which hardly could accomplish the gravitational potential of the visible cluster mass. Subsequently, scientists probed the rotation curves of spiral galaxies in galaxy clusters [1, 2] revealing that the nature of the rotation curve must be much more flat due to much larger mass component to be present than the visible one (see figure 1.1).

The rotation curve of a galaxy can be computed with the Newtonian mechanics describes as,

$$\frac{mv^2}{r} = G\frac{mM}{r^2}, \tag{1.1}$$

where, r is the distance from the center of the galaxy, v is the velocity at radius r, M is the mass involved in the center and m is the mass at the point of measurement. From

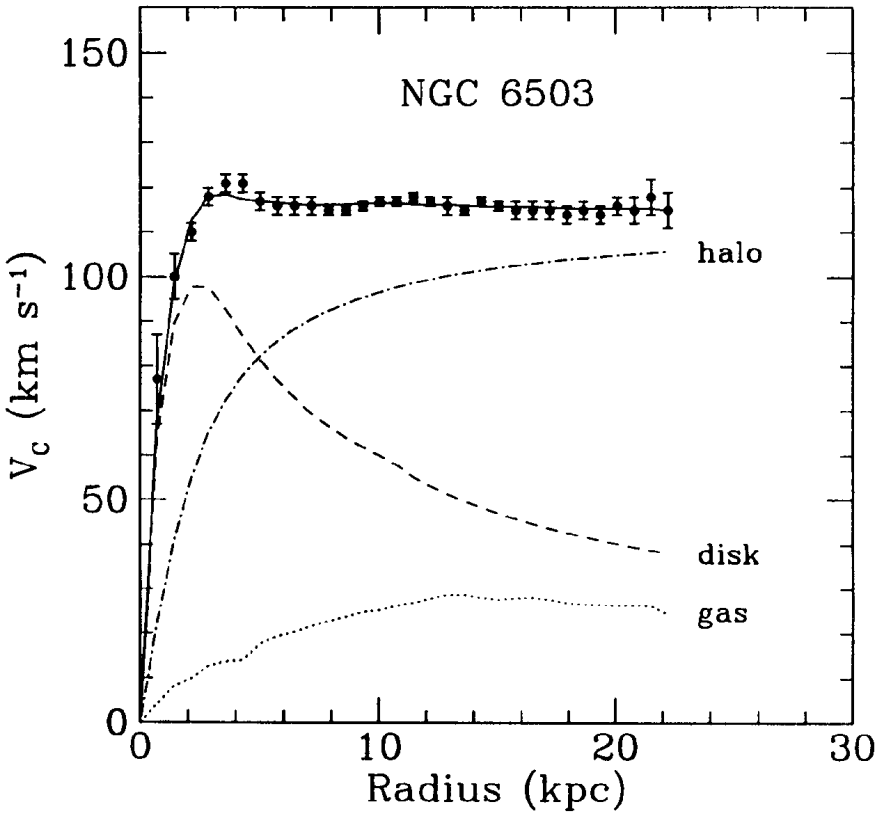

FIGURE 1.1: The observed rotation curve of the spiral NGC 6503 and the solid line would predict rotation velocities as a function from the distance from the center of the galaxy. The dashed and dotted lines are the rotational velocity as theoretically expected from the inherent gas and disc. The fact that the solid is flatter than predicted suggests the presence of a halo of dark matter, extending to large galactic radius (source: [3]).

the eq. 1.1, the velocity at the radius r is written as,

$$v = \sqrt{\frac{GM}{r}} \tag{1.2}$$

Apparently, the core of the galaxy has the majority of the galactic mass. From eq. 1.2, the velocity at larger distance to the core would decrease according to $v \sim r^{1/2}$. On the contrary, the velocity is found to be constant as it crosses the larger distance from the core. This phenomenon indicates the presence of an additional halo of dark matter, far more extended than the observed stellar disk.

From the X-ray intensity distribution, one can also estimate the amount of hot gas present in the cluster (see figure 1.2). The hot-gas region with temperature of $\sim 10^7 - 10^8$ K radiates in X-ray wavelength. From modeling the galaxies, one can estimate the mass in the stellar objects. From the observation, it has been probed that the hot gas is the dominant baryonic mass by a large factor [4, 5]. Observation from the elliptical galaxy

FIGURE 1.2: The Bullet Cluster, in a composite image with optical light from Magellan and Hubble Space Telescope and X-ray light from Chandra X-ray Observatory. The concentration of mass was determined with weak gravitational lensing. In this image, the baryonic matter is shown in pink and the blue part can be well interpreted as DM. (source: X-ray: NASA/CXC/CfA/M.Markevitch et al.; Optical: NASA/STScI; Magellan/U.Arizona/D.Clowe et al.; Lensing Map: NASA/STScI; ESO WFI; Magellan/U.Arizona/D.Clowe et al.).

M87 reveals that the baryonic mass in the Galaxy is comparatively less than that of the hot gas [6].

Dark matter appears neither emitting nor reflecting any form of light. However, it definitely interacts through gravity, and has played the most important role in shaping the Universe at large scales. The most successful technique with which to investigate it has so far been the effect of gravitational lensing.The effects can be classified as strong lensing, weak lensing and micro lensing. The curvature of space-time near any gravitating mass (including dark matter) deflects passing rays of light - observably shifting, distorting and magnifying the images of background galaxies. Distant clusters lensed by closer ones show the evidence of extensive gravitational lensing, far more than can be explained by the observed distribution of luminous matter in the foreground cluster [7, 8].

Observations of the anisotropies of the cosmic microwave background (CMB) [9], the

large scale structure of galaxies strengthen the cosmological evidence of the DM hypothesis. The galactic superstructure reflects the nature of gravitational clustering of matter since the Big Bang to the expansion of the Universe. If dark matter were present during structure formation, it should have influenced the pattern of large-scale structure, which can be derived with N-body simulations. Redshifts from far away galaxies provide the information of the expansion of the universe. The fluctuations of CMB has been observed with large scale surveys as, COBE (the Cosmic Background Explorer [10]); WMAP [11, 12].

1.2 Dark matter candidates

The structure formation of Galaxy refers the DM to be hot or cold [13]. Hot dark matter corresponds to the ultra-relativistic particles, while the cold dark matter makes with slow-moving particles leads to a bottom-up structure formation. A successful dark matter candidate should be electrically neutral and its self-interactions should be small, since dark matter is essentially collisionless. It also should be stable for very long lifetime. Mainly the dark matter particle can be based on the theory of physics beyond standard model (BSM). The possible candidates are described below:

1.2.1 Thermal relics

The most popular dark matter candidates are Weakly Interacting Massive Particles (WIMPs) which interacts with SM fields only via the weak nuclear force, making them non-baryonic and electrically neutral by definition. These are thermally produced in the early Universe with masses at the TeV scale could naturally account for the observational evidences and their high mass ensures that they are sufficiently non-relativistic in order to accomplish structure formation. The density of WIMP (Ω_x) , when they fall out of thermal equilibrium with the hot plasma describes as [14],

$$\Omega_x h^2 \simeq \frac{0.1pb}{\sigma_A \nu} \tag{1.3}$$

where, σ_A is the self-annihilation cross-section. Eq. 1.3 shows that larger self-annihilation cross-sections cause the particle to freeze out later, and so exhibit a lower relic density. In case, the WIMP poses to be self- annihilating, they can produce gamma-rays in course and that could lead to a detection with satellite or ground based gamma-ray telescopes. An indication of a line-like gamma-ray signal has been found in case of Fermi-LAT data for 130 GeV mass range [15], whereas, experimental efforts to detect WIMPs has failed to probe the evidence of supersymmetry [16].

1.2.2 Non-thermal relics

A new light neutral pseudo-scalar boson could be also a probable candidate for the DM. It comes to existence when the U(1) symmetry is spontaneously broken, which produces a massless particle with no spin, known as a Nambu-Goldstone boson. Despite of the smallness of their masses and couplings, for the most part these scalar or pseudo-scalar particles are actually linked to physics at extremely high-energy scales, largely beyond the reach of super-colliders. Another widely-discussed example are the axion-like particles (ALPs), which can occur in a number of SM extensions.

Strong CP problem and the axions Several extensions of the standard model(SM) for particle physics predict the existence of ultra-light pseudo scalar bosons with masses in the sub-eV range [17]. A well-known example of this is the axion, which explains the absence of CP violation in strong interaction [18–20]. The CP violating term which takes care of symmetries in the SM describes as,

$$\mathcal{L} \supset \theta \frac{g^2}{32\pi^2} G^{\mu\nu} \tilde{G}_{\mu\nu}. \tag{1.4}$$

Where, $G^{\mu\nu}$ is the gluon field strength tensor, g is the strong coupling constant and the dual gluon field strength tensor $\tilde{G}_{\mu\nu} = \frac{1}{2}\epsilon_{\mu\nu\alpha\beta}G^{\alpha\beta}$. $\epsilon_{\mu\nu\alpha\beta}$ is the antisymmetric Levi-Civita symbol in four dimensional Minkowski space. the θ term in the eq. 1.4 manages the symmetries in quantum chromodynamics (QCD), but violates time reversal (T) and parity (P), while conserving charge conjugation (C) and thus violates CP. It can be more pronounced introducing the θ term in the neutron electric dipole moment (EDM) describes as, [21, 22],

$$d_n \simeq \frac{e\theta m_q}{m_n^2} \simeq 10^{-16}\theta ecm \tag{1.5}$$

where, m_q is the quark mass and m_n is the neutron mass. It is important to note that, CP violation disappears if either the θ term vanishes or m_q to be zero. However, null measurements of the neutron electric dipole moment constrain the θ term to be:

$$\theta < 10^{-9}. \tag{1.6}$$

Again, the weak interaction can modify the CP violating term as:

$$\bar{\theta} \rightarrow \theta + \arg\det \mathrm{M}. \tag{1.7}$$

where, M is the quark Yukawa matrix. It should be noted that if at least one quark is massless the problem disappears. Indeed, if there is no mass term, we can perform a chiral rotation on the massless quark to compensate all the other contributions. Well,

from lattice QCD, the ratio $\frac{m_u}{m_d} \sim 0.5$ [23] has been profoundly established, the CP problem still remains there.

An inevitable solution to this strong CP problem is to introduce a global chiral U(1) symmetry, which is spontaneously broken (invented by Pecci and Quinn in 1977[ref]). The QCD chiral anomaly causes a non-perturbative explicit breaking of $U(1)_{PQ}$, generating a potential for the axion. The axion is therefore a naturally light pseudo-Goldstone boson. In order to be anomalous, $U(1)_{PQ}$ has to be chiral. At low energies, the Lagrangian for the strong interaction in QCD written as,

$$\mathcal{L} = \theta \frac{g_s^2}{32\pi^2} G^{\mu\nu}\tilde{G}_{\mu\nu} + \frac{1}{2}\partial_\mu a \partial^\mu a + \epsilon \frac{a}{f_a}\frac{g_s^2}{32\pi^2} G^{\mu\nu}\tilde{G}_{\mu\nu}. \tag{1.8}$$

Where, $\frac{a}{f_a}$ is the phase of the scalar field and there is a discrete shift symmetry $a \rightarrow a + 2\pi f_a$ even after explicit breaking, where f_a is known as axion decay constant. In the eq. 1.8, the last term corresponds to the anomaly associated to $\mathrm{U(1)_{PQ}}$ written as,

$$\partial_\mu J^\mu_{PQ} = \epsilon \frac{g_s^2}{32\pi^2} G^{\mu\nu}\tilde{G}_{\mu\nu} \tag{1.9}$$

The coefficient of $G^{\mu\nu}\tilde{G}_{\mu\nu}$ term in the eq. 1.8 becomes,

$$\left(\theta + \epsilon \frac{a}{f_a}\right) \frac{g_s^2}{32\pi^2} G^{\mu\nu}\tilde{G}_{\mu\nu} \tag{1.10}$$

This coefficient is responsible for the effective potential for the axion field and the minimum potential counts at $\bar{a} = -\theta \frac{f_a}{\epsilon}$ and the coefficient turns as for the physical field $(a' = a - \bar{a})$,

$$\epsilon \frac{a'}{f_a}\frac{g_s^2}{32\pi^2} G^{\mu\nu}\tilde{G}_{\mu\nu}, \tag{1.11}$$

which no longer contains θ-term and the Lagrangian (see eq. 1.8) is effectively θ-term free. This is the solution to the strong CP problem is derived by the Vafa-Witten Theorem. In parity-conserving vector-like theories such as QCD, parity conservation is not spontaneously broken [24]. Equivalently, in such theories, dynamical parity violating terms have zero vacuum expectation value.

The additional spontaneously broken Peccei-Quinn symmetry gives rise to a pseudo Nambu-Goldstone boson e.g. axion. The mass term comes for an axion with the mixing between π^0 and η meson,

$$m_a = \frac{\sqrt{z}}{1+z}\frac{f_\pi m_\pi}{f_{PQ}/N}, \tag{1.12}$$

where, z is the ratio of u-quark and d-quark masses (z$\sim$0.5) and N is an integer which denotes the axion color anomaly of the PQ symmetry. Using the values of $f_\pi = 92$ MeV

and $m\pi = 135$ MeV, the axion mass comes as,

$$m_a = 6\text{MeV}\left(\frac{10^9\text{GeV}}{f_a}\right) \tag{1.13}$$

In the presence of an external magnetic field, axions can couple to two photons [25, 26]. The effective Lagrangian of the photon-axion coupling writes as:

$$\mathcal{L} \supset -\frac{1}{4}g_{a\gamma\gamma}F_{\mu\nu}\tilde{F}^{\mu\nu}a = g_{a\gamma\gamma}\vec{E}\cdot\vec{B}a, \tag{1.14}$$

where, a is the axion-like field with mass $m_a, F_{\mu\nu}$ is the electromagnetic field-strength tensor, $\tilde{F}^{\mu\nu} = \frac{1}{2}\varepsilon_{\mu\nu\rho\sigma}F^{\rho\sigma}$ is its dual field, $g_{a\gamma\gamma}$ is the photon-axion coupling constant which ensures the possibility of oscillations between photon and axion states in external transversal magnetic fields [26, 27]. For the axions, $g_{a\gamma\gamma}$ is related to the axion mass (m_a), through the fundamental energy scale (f_a) at which Peccei-Quinn symmetry is broken.

1.3 Axion-like particles

The most relevant axion direct searches try to follow the two-photon coupling. the axion being very weekly coupled for the allowed range of f_a, it is difficult to probe [25]. Therefore, the particles that could couple to two photons even in low energies are Axion like particles (ALPs). ALPs are predicted by several string theory motivated extensions of SM [28–32]. They are not anymore related to the strong CP problem but they could couple to the photons as expressed in Eq 1.1. ALPs mostly share the similar kind of physics to anions. Contrary to axions, mass and coupling constant of ALPs are completely independent to each other.

1.4 Photon-ALPs conversion in the magnetic field

Photon-ALPs mixing occurring in the presence of external magnetic field B can be described by the Lagrangian:

$$\mathcal{L} = \mathcal{L}_\gamma + \mathcal{L}_a + \mathcal{L}_{a\gamma} \tag{1.15}$$

where,$\mathcal{L}_\gamma$ is the Euler-Heisenberg effective Lagrangian for one-loop corrections to classical electrodynamic and $\mathcal{L}_a$ is the Lagrangian for ALPS which contains the kinetic and mass term describes as:

$$\mathcal{L}_a = \frac{1}{2}\partial^\mu a\partial_\mu a - \frac{1}{2}m^2a^2 \tag{1.16}$$

For a monochromatic photon/ALPs beam of energy E propagating along x_3 direction in a cold ionized and homogeneous magnetic medium, it can be shown that the Lagrangian for relativistic ALPs and polarized photons leads to the Schrödinger-like equation of motion:

$$\left(i\frac{d}{dx_3} + E + \mathcal{M}_0\right)\begin{pmatrix} A_1(x_3) \\ A_2(x_3) \\ a(x_3) \end{pmatrix} = 0 \tag{1.17}$$

where $A_1(x_3)$ and $A_2(x_3)$ represent the photon linear polarization amplitude along the x_1 and x_2 axes respectively and $a(x_3)$ denotes the ALPs intensity. the mixing matrix $\mathcal{M}_0$ gets simplified if we restrict $\vec{B}$ to be homogeneous. Let's assume B_T to be the transversal magnetic field. If B_T is chosen to lie along x_2 direction, the mixing matrix can be written as,

$$\mathcal{M}_0 = \begin{pmatrix} \Delta_\perp & 0 & 0 \\ 0 & \Delta_\parallel & \Delta_{a\gamma} \\ 0 & \Delta_{a\gamma} & \Delta_a \end{pmatrix} \tag{1.18}$$

The matrix elements accounts for $\Delta_\parallel = \Delta_{pl} + 7/2\Delta_{QED}$, $\Delta_\perp = \Delta_{pl} + 7/2\Delta_{QED}$, $\Delta_{a\gamma} = g_{a\gamma}B_T/2$ and $\Delta_a = -m_a^2/2E$, where m_a is the ALPs mass. The term $\Delta_{pl} = -\omega_{pl}/(2E)$ accounts for plasma effects where ω_{pl} is the plasma frequency of the medium of the electron density of the medium n_e as $\omega_{pl} \simeq 3.69 \times 10^{-11}\sqrt{n_e/cm^{-3}}eV$. The QED vacuum birefringence effect is included in $\Delta_{QED} \propto B_T^2$. If the photons are lost as a result of the interaction with the extragalactic background light (EBL), the terms $\Delta_{\parallel,\perp}$ are modified to include a complex absorption term $\Delta_{\parallel,\perp} \rightarrow \Delta_{\parallel,\perp} + i(2\lambda_\gamma^{mfp})$, where λ_γ^{mfp} is the mean free path for the photons which undergo through the pair production process. If one neglects, the birefringence effect, it can be shown that the photon ALPs oscillation become maximal and independent of the energy E and ALPs massm_a for energies above the critical energy described by the equation,

$$E_{crit} \equiv E\frac{|\Delta_a - \Delta_{pl}|}{2\Delta_{a\gamma}} \simeq 500GeV\left(\frac{m_a}{neV}\right)^2\left(\frac{B_T}{\mu G}\right)^{-1}\left(\frac{g_{a\gamma\gamma}}{5\times10^{-11}}\right)^{-1} \tag{1.19}$$

where, m_a is here the axion mass, B_T is the critical magnetic field and $g_{a\gamma\gamma}$ is the photon-ALPs coupling in unit of GeV^{-1}. Different high-energy astrophysical phenomena offer a way to test the ALPs hypothesis, through the efficient photon-ALPs mixing in external magnetic fields in the intergalactic medium. The photon-ALPs mixing is efficient at energies larger than the critical photon energy described in the eq. 1.19 [33]. Two possibilities can happen in the basis of critical energy. Firstly, in the high energy limit, where Energy (E) $\gg E_c$, the photon-ALPs conversion probability becomes maximal and energy-independent. In this case, we can expect an attenuation in the photon-flux due to the photons to ALPs conversion in large-scale intergalactic magnetic fields [34, 35].

On the other hand, for the low-energy limit, where E $\ll E_c$, the photon-ALPs mixing is small and we can expect energy dependent photon-ALPs oscillation [36]. If one ignores a possible optical activity the lower part of the mixing matrix $\mathcal{M}_0$ (see eq. 1.18) becomes a 2×2 mixing matrix with the form,

$$\mathcal{M}_0' = \begin{pmatrix} \Delta_{\parallel} & \Delta_{a\gamma} \\ \Delta_{a\gamma} & \Delta_a \end{pmatrix}. \tag{1.20}$$

The matrix is made diagonal by a rotation about an angle,

$$\frac{1}{2}\tan 2\theta = \frac{\Delta_{\mathrm{a}\gamma}}{\Delta_{\parallel} - \Delta_{\mathrm{a}}} \tag{1.21}$$

In analogy to neutrino oscillations, the probability for an axion to convert into a photon after traveling a distance l in a trans- verse magnetic field is,

$$\mathrm{P}_{\mathrm{a}\to\gamma} = \sin^2(2\theta)\sin^2(\frac{1}{2}\Delta_{\mathrm{osc}}\mathrm{l}), \tag{1.22}$$

where $\Delta^2_{osc} = (\Delta_{\parallel} - \Delta_a)^2 + \Delta^2_{a\gamma}$ and the oscillation length $l_{\mathrm{osc}} = 2\pi/\Delta_{osc}$. For large scale magnetic fields, the oscillation length is given as [37],

$$l_{\mathrm{osc}} = 32\ \mathrm{kpc}\sqrt{1 + (E_c/E_\gamma)^2}\left(\frac{B_\perp}{\mu\mathrm{G}}\right)^{-1}\left(\frac{g_{a\gamma\gamma}}{10^{-11}\ \mathrm{GeV}^{-1}}\right)^{-1}, \tag{1.23}$$

which implies that, for typical parameters in the Galaxy, oscillations can be relevant on Galactic scales at GeV energies.

1.4.1 Appearance channel

The phenomenon for the conversion of photons to ALPs and back to photon i.e. photon appearance can follow an attenuation in higher energy for the survival probability of photons. As for observational aspects, very high energy gamma-rays from distant extragalactic sources are attenuated due to the pair production of e^+e^- originated from scattering in the extragalactic background light (EBL) [38]. The opacity of the Universe should depend on the distance to the source. In the last decades, observational searches for distant gamma-ray sources with ground-based gamma-ray Imaging Cherenkov Telescopes have revealed that the universe is more transparent than it was expected [39, 40]. In the first study of anomalous transparency, it was probed that the spectral features at the transition from optically thick to optically thin region deviate by 4.2σ [40] while the systematics cannot describe this effect. This anomalous transparency of the universe can be explained in the realm of photon-ALPs mixing. In the context of appearance channel, during propagation in the intergalactic medium with a magnetic field of

nG, photon-ALPs mixing is consistent with ALPs mass $m_a < \mu$eV and photon-ALPs coupling constant$\sim 10^{-11} GeV^{-1}$ [41–45]. With a large sample of very high energy (VHE) gamma-ray spectra, lower limit on photon-ALPs coupling has been set to be $g_{a\gamma\gamma} \geq 2 \times 10^{-12} GeV^{-1}$ in large scale magnetic fields [46].

The predicted attenuation is visible in the spectra until at very high energy, the back-conversion of ALPs may detect and dominate over the absorption process. Based on the physics of the appearance channel, observational studies from SN 1987A has been able to put constraint in photon-ALPs parameter space [47]. In a core- collapse supernova, ALPs are expected to be produced with Primakoff effect and in the magnetic field of our Galaxy, they can be converted to photons. This mechanism is used to constrain the $g_{a\gamma\gamma}$ from the lack of the gamma-ray signal detected with gamma-Ray Spectrometer(GRS) while SN1987A exploded.

Another search of appearance channel of photons with the help of the Fermi-LAT data from BL Lac type of objects exhibits that the ALPs mass and the coupling range are consistent to the TeV transparency results of ALPs [48]. The appearance channel is way more sensitive as long as the photon-ALPs mixing is concerned. The reconversion of photons depends on the Galactic magnetic field as well as the direction to the source.

1.4.2 Disappearance channel

On the other hand, the reconversion of ALPs to photon opens up a possibility to look into the disappearance channel. The probability to convert the photons to ALPs state in the Galactic magnetic field makes an energy dependent suppression in photon flux that can lead to a strong mixing regime. From equation 1.6, it is obvious that the astrophysical sources with a distance in kpc range, Galactic transversal magnetic field of order μG , photon-ALPs coupling constant in units of $10^{-11} GeV^{-1}$ and ALPs mass in neV requires the resultant critical energy to observe spectral features of the disappearance channel to be in MeV to GeV range. Several observational results e.g. HESS results from BL Lac object PKS 2155-304 [49], Fermi-LAT collaboration results of the gamma-ray spectrum from NGC1275 [50] have looked into the disappearance channel and constrained the parameter space that is sensitive to ALPs.

In this thesis, we also investigate photon-ALPs oscillation features in the disappearance channel. We take Fermi-LAT data for bright gamma-ray astrophysical Galactic plane or non-Galactic plane and we look for significant spectral irregularities that might be induced by photon-ALPs oscillations in the regular Galactic magnetic field. In order to look for photon-ALPs oscillations we need to concentrate in lower energy part of the

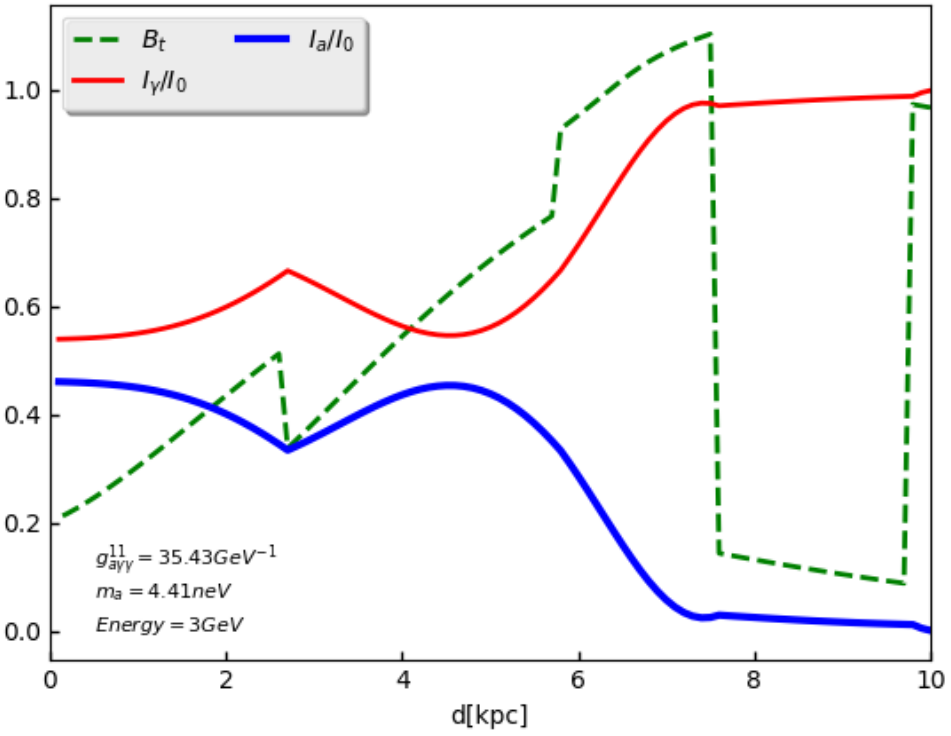

FIGURE 1.3: Change in photon intensity and ALPs intensity with the change of transversal component of Galactic magnetic field. The green line corresponds to the transversal magnetic field, red line describes the relative photon intensity while the blue line gives the relative ALPs intensity. Photon intensity(I_γ) and ALPs intensity I_a) together makes the total intensity (I_0), that is unity. The horizontal axis represent the distance to the source in kpc range. In the figure it is obvious that with the decrease in photon intensity, ALPs intensity increases.

spectra where irregularities can be expected as a result of mixing. Figure 1.3 is an example of photon-ALPs oscillation in the Galactic transversal magnetic field. During the photon propagation, over high transversal magnetic field domain, the photon intensity decreases and axion intensity increases. On the other hand, lower Galactic magnetic field intensity makes ALPs reconverted to photons.

1.5 ALPs detection and current limits on ALPs contour

Due to the photon-ALPs coupling, ALPs can play an important role in astrophysical observations. However, the observations with space based and ground based gamma-ray telescopes as well as experimental searches for ALPs have been able to limit the hints and exclusions in photon-ALPs parameter space (see figure 1.4).

In the context of explaining anomalous transparency of the Universe with photon-ALPs oscillations, one requires an ultra-light ALP which couples to two photons with the coupling constant $g_{a\gamma\gamma} \geq 2 \times 10^{-12} GeV^{-1}$ and $m_a \leq 10^{-7} eV$. The parameter space where photon-ALPs mixing would affect cosmic transparency has been constrained by observational searches from SN 1987A with a bound $g_{a\gamma\gamma} < 5 \times 10^{-12} GeV^{-1}$ and $m_a \leq 10^{-10} eV$ [47]. Observation by the Fermi-LAT collaboration of the gamma-ray spectrum from NGC1275 has set a mass range of $0.5 \leq m_a \leq 5$ neV of non photon-ALPs mixing region [50]. HESS observational results from BL Lac object PKS 2155-304 has also constrained $g_{a\gamma\gamma} < 2.1 \times 10^{-11} GeV^{-1}$ and $15 \leq m_a \leq 60$ neV [49]. Apart from γ-ray observations, X-ray data of NGC 1275 has been able to place constraints on ALPs-photon parameter $g_{a\gamma\gamma} \leq 1.4 - 4 \times 10^{-12} GeV^{-1}$ for $m_a \leq 10^{-12}$ eV [51, 52].

A sizable part of the favored region in axion and ALP parameter space can be explored with the current and next generation of experimental searches based on axion or photon-ALP oscillations in the external magnetic fields. Helioscopes aim to detect solar axions and ALPs produced by their conversion into photons inside of a strong magnet pointing towards the Sun [53, 54]. The CERN Axion Solar Telescope (CAST) experiment sets currently the helioscope limits to be $6.6 \times 10^{-11}\text{GeV}^{-1}$ [55]. The International Axion Observatory (IAXO) is a new generation axion helioscope aiming at a sensitivity to the axion-photon coupling of a few 10^{12}GeV^{-1} [56, 57]. This is of the orders of magnitude beyond the limit currently achieved by CAST. IAXO will follow a toroidal design for the magnet, together with X-ray optics and detectors attached to each of the magnet bores [58].

Again, light shining through wall (LSW) experiments aim both for production and detection of axions and ALPs in the laboratory. The idea behind the experiment is that laser photons is allowed to be sent along a strong magnetic field which makes the photons to convert into axions or ALPs towards a blocking wall. Later on, behind the wall the axions may then reconvert, again in a strong magnetic field, into photons which can reach to the detection level. In the figure 1.2, the light-green region labeled as 'ALPS II' will be explored by second generation ALPS experiment.

The Axion Dark Matter eXperiment (ADMX) collaboration designed an experiment with the goal to reach KSVZ axions saturating our galactic halo, whose local density would be $\rho_a \sim 0.45 GeV/cm^3$. ADMX detects axions by their stimulated conversion into microwave photons in a high Q cavity permeated by a large magnetic field. In the plot 1.2, the parameter space in red color which is sensitive to the ADMX experiment has been labeled as ADMX.

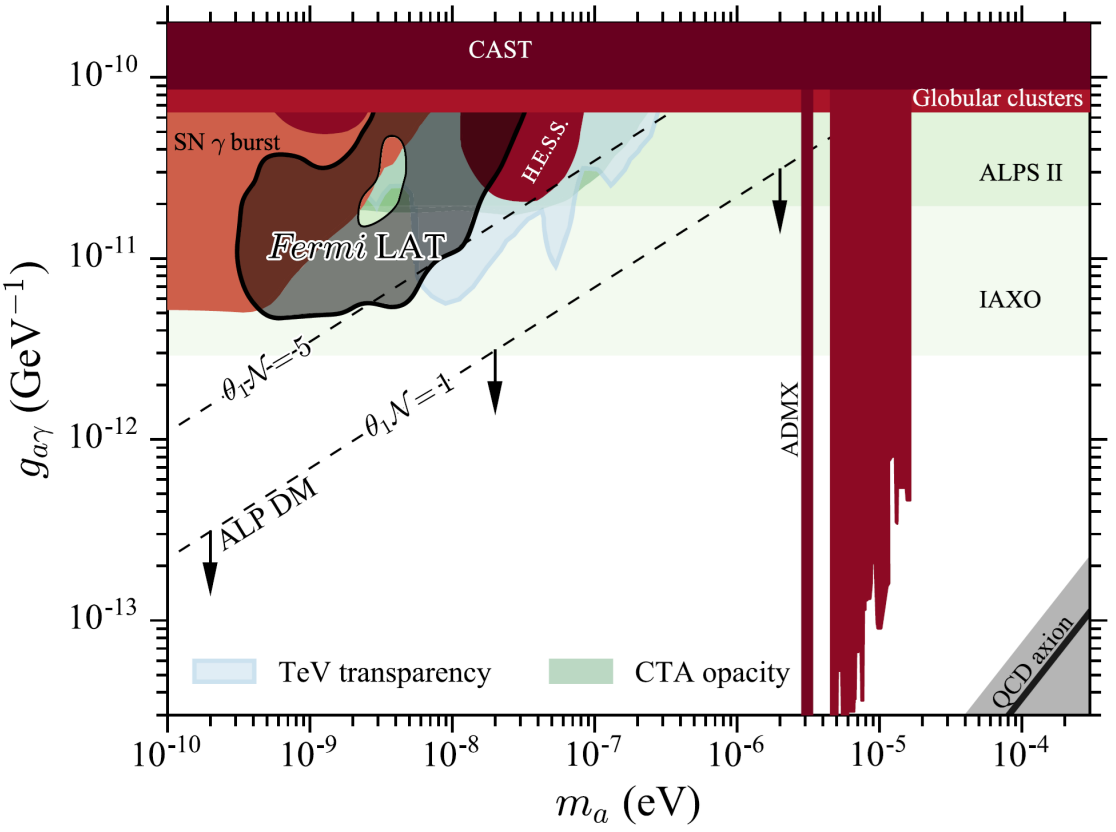

FIGURE 1.4: The current limit on ALP parameters space from the article from Fermi collaboration [50]. The constraints are shown in different shades of red while the hints and the next generation experimental sensitivity areas are shown in different shades of greens. The QCD axion is shown as a gray shaded band and solid black.

1.6 Fermi large area telescope

The Fermi gamma ray space telescope is an imaging, very high energy gamma-ray telescope which studies the gamma-rays astrophysical phenomenon in the energy range of 100 MeV to more than 300 GeV (see figure 1.5). This international and multi-agency space mission consists of a large area telescope (LAT) and a gamma-ray burst monitor (GBM). The Fermi LAT is an imaging gamma-ray telescope which has much larger collection area, angular resolution and wider field of view. With its very large field of view, the LAT covers about 20% of the sky at any given moment. In sky-survey mode, which is the primary observing mode, the LAT will cover the entire sky every three hours. GBM has a field of view several times larger than the LAT and provides spectral coverage of gamma-ray bursts that extends from the lower limit of the LAT down to 10 keV.

1.6.1 Fermi LAT instruments

The LAT instrument consists of a converter tracker, a calorimeter and an anti-coincidence detector [59] (see figure 1.5).

Tracker The Tracker has 16 tracker modules of high-Z material where gamma-rays can create e^+e^- pairs [59]. Each of the modules has 18 tracking planes (x-y tracking planes) and each of the tracking planes consists of two layers of single sided silicon strip detectors. The silicon strip detectors are interleaved between thin planes of tungsten which serve the purpose of converting material.

Calorimeter The LAT calorimeter serves a dual purpose: 1. measuring the energy deposition of incoming particle shower produced from incoming gamma-rays and 2. distinguishing the cosmic background from electromagnetic shower profile [59]. Each calorimeter module consists of 96 thallium-doped CsI crystals with a size of 2.7 cm $\times$ 2.0 cm $\times$ 32.6 cm. The crystals are separated from each other and arranged into 8 layers of 12 crystals. The total vertical depth of the calorimeter is 8.6 radiation length whereas the total instrument has the depth of 10.1 radiation lengths.

Anticoincidence detector (ACD) The Anticoincidence detector allows the photons to enter into the LAT, rejecting the background particles [59]. For serving the purpose of a shield, the ACD needs to have a very high detection efficiency for charged particles and to minimize the "backsplash" effect. The "backsplash" effect is created due to the generation of secondary particles (i.e. 1001000 keV photons) from HE events (typically $\geq$ 1 GeV) as a result of Compton scattering within the ACD. To minimize the false the "backsplash" effect, the anti-coincidence detector is made up of 89 segmented plastic scintillators which is arranged in a 5 $\times$ 5array on the top and 4 $\times$ 4 arrays in every sides.

Data acquisition system (DAQ) The data acquisition system is one of the integral part of the LAT. It can collect data from the other sections of LAT instrument i.e. from the tracker, the calorimeter, and the ACD and implement multi-level event trigger. The DAQ consists of very high level electronics and microprocessor.

1.6.2 Fermi LAT performance

Event reconstruction, analysis and classification Fermi-LAT is located in 565-km altitude with the inclination angle of 25.6° and an orbital period of 96 minutes [59]. With its high instrument properties, LAT is able to reject 99.999% of signals generated from cosmic rays. If several hits are occurring in the tracker, an event is recorded.

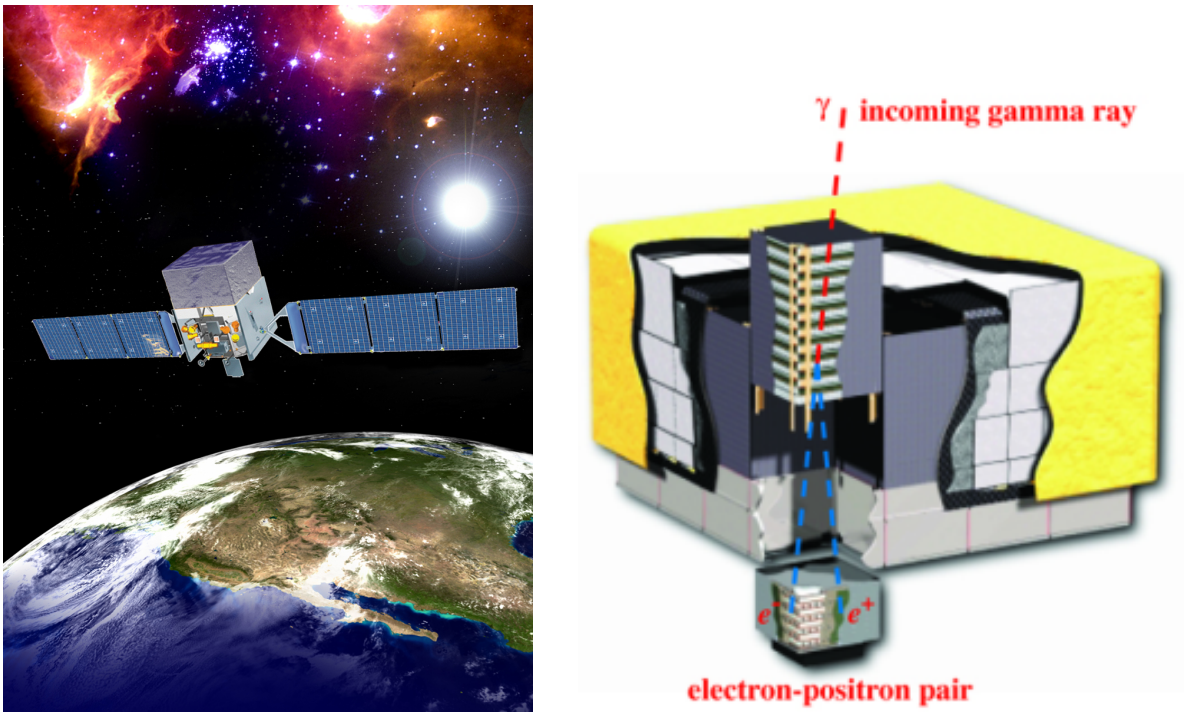

FIGURE 1.5: Left: The Fermi satellite in the sky. Image credit: NASA's Fermi official website. Right: The internal view of the LAT detector. It consists of the tracker, the calorimeter and the anti-coincidence detector [59].

Depending on the information about signals in the individual tracker, pattern based recognition technique and fitting algorithms are used to reconstruct the track [60]. After the track reconstruction, vertex solutions between two tracks are calculated retaining the full covariance matrix of each track. The event filtering is done with different filtering algorithms (e.g. the GAMMA filter, the HIP filter, the DIAGNOSTIC filter. [60]). Apart from this, the calorimeter information is needed to improve the directional accuracy of the reconstructed tracks which probes the direction of the incoming γ-ray. To estimate the energy, three algorithms are used: a parametric correction (PC), a fit to the longitudinal and transverse shower profile (SP) and a maximum likelihood (LH) method which is based on correlations between the total deposited energy in the calorimeter and the number of hits in the track (see [60] section 3.2). The LH method is only valid for the events up to 300 GeV and SP method is used energies beyond 1 GeV. For each event, the output from tracker, calorimeter and ACD is studied and optimized with Monte-Carlo simulations. The event energy is determined with a classification tree (CT) analysis which gives the best estimation of energy (see [60] section 3.3). For background CR rejection, the event has to pass through several filters. The background separated

events are associated with the event classes that range from transient (high statistics but potentially high CR contamination) to ultra clean (high purity but low statistics).

P8 Improvements The full performance was first evaluated based on full Monte-Carlo simulations of the detector response and later updated via on-orbit measurements. For high-level science analysis, the performance can be summarized on the basis of three components : effective area, PSF and energy dispersion.

Effective Area The LAT effective area is essentially a measure of how efficiently γ-rays can be detected with the LAT at a given energy. It is derived with high statistics MC simulations and the simulation data is compared with the flight data to correct the effective area (see [60] section 5). Effective area of the LAT is expressed in terms energy and the direction of the incident gamma-ray in the instrument frame [60]. The MC simulated effective area is modified for ghost events and live time fraction.

Point Spread Function The PSF describes the shape of the image produced by a delta function for the point source on the detector. The LAT uses a King-profile to parametrize the PSF (see [60], section 6.). One can quantify the PSF by the containment radius of the distribution of the incoming γ-rays, which is usually expressed in degrees. In gamma-ray telescopes with solid state detectors, the main cause of the spreading of the PSF is the Coulomb multiple Scattering. In the 95% containment radius for events, PSF varies with energy and amounts to 10° at 100 MeV due to multiple scattering which makes the track reconstruction very difficult at these energies.

Energy Dispersion The energy dispersion measurement for LAT instrument plays a crucial role for searching spectral features. It denotes the spread of reconstructed energy around true energy. The reconstructed energy distribution is not symmetric over true energy, because of the distribution of shower in the calorimeter. The energy resolution is defined as the full-width of the energy window at 68% containment (see [60], section 7.) and it depends on the actual energy and incidence angle of the electromagnetic shower.

1.7 Fermi data analysis with science tools

Data analysis technique with Fermi-LAT science tool, for the astrophysical sources has been discussed in this chapter. We use eight and half years of Fermi-LAT Pass 8 data of the Galactic plane and non-Galactic plane sources. We briefly convey the Fermi-LAT instrumental description and their functionality below as well as the data analysis technique with the science tools. We also comment on the derivation of systematic uncertainty related to the flux calculation in this chapter. Finally, we describe the

spectral modeling and the χ^2 fitting to the derived flux points, so that we can conclude on goodness of fit.

In this section, the method is illustrated for the detection, flux determination and spectral modeling of the Fermi LAT sources. The spectrum results that we show in this thesis are obtained via a binned likelihood analysis performed with the Fermi-LAT Science tools software package version v10r0p5[1]. Data for the astrophysical sources for particular time periods can be obtained from LAT data server[2]. For a shorter period of dataset, it is better to use unbinned analysis, while for binned analysis longer period of dataset is relevant. For the analysis, an event file, a spacecraft data and the current background models are required. Fermi-LAT ScienceTools software contains a list of sciencetools which are used for solving particular purposes. After extracting the data, we use *gtselect* tool to cut on the event class, keeping only the SOURCE class events (event class 128) and event type 3 (front and back conversion type together). After the data selection is made, we need to take the good time intervals (GTI) in which the satellite was working in standard data taking mode and the data quality was good. For this task we use *gtmktime* to select GTIs by filtering on information provided in the spacecraft file. This tool helps to exclude the time periods when some spacecraft event has affected the quality of the data. For creating countsmap of the region of interest we use the gtbin tool with the option *CMAP*. We choose a region of interest of 15 degrees with a pixel size of 0.1 degree/pixel and to create the counts map we use *gtbin* tool.

To take into account the diffused galactic and the extragalactic isotropic diffuse emission scenario we use gll_iem_v06.fits and iso_P8R2_SOURCE_V6_v06.txt[3] models respectively. Nextly, we created a source model XML file. The model file contains our best guess at the locations and spectral forms for the sources within 15° ROI to the targeted point source. The LAT instrument response functions depend on the angle between the direction to a source and the instrument z-axis, which is referred as 'off-axis angle'. The livetimes of the number of counts are calculated as a function of the three dimensional space comprising the sky position and 'off-axis angle'. Using the spacecraft file *gtltcube* tool creates a livetime cube, which is a HealPix table, covering the entire sky. We use *gtexpcube2* tool to generate a set of exposure maps for different energies from a livetime cube. Next,*gtsrcmaps* science tool convolves the components that comprise specified source model with the instrument response for a given observation. It takes each source spectrum in the XML model, multiplies it by the exposure at the source position, and convolves that exposure with the effective PSF. The output with a FITS data structure contains one table extension for each source of the xml model.

[1] https://fermi.gsfc.nasa.gov/ssc/data/analysis/software/
[2] https://fermi.gsfc.nasa.gov/cgi-bin/ssc/LAT/LATDataQuery.cgi
[3] https://fermi.gsfc.nasa.gov/ssc/data/access/lat/BackgroundModels.html

Finally, we run *gtlike* science tool to perform a binned likelihood analysis of the LAT data. The likelihood statistic is the probability of obtaining observational data for a given input model. In our case, the input model is the distribution of gamma-ray sources on the sky, and includes their intensity and spectra. *gtlike* provides as output the TS and the predicted number of counts, and the spectral parameters (Normalization factor, the spectral index, cut off energy etc. depending on the spectral model) for each source reported in the source model file.

1.8 Astrophysical sources of high energy γ-rays

In this thesis, we discussed about gamma-ray spectrum from different types of astrophysical sources such as: pulsars, active galactic nuclei (AGN), blazar etc. With advanced technology, it has been easy to observe these astrophysical sources in the very high energy (VHE) regime. Most of the sources we analyzed are pulsars, which are present in our Galaxy and outside the Galaxy as well. Here we discuss about the sources as following:

1.8.1 Pulsar

Most of the sources we analyzed are pulsars, which are present in our Galaxy and outside the Galaxy as well. The magnetic axis of pulsars is inclined with respect to the rotational axis. Thus, for an observer with a line of sight close to the magnetic axis, the emission appears to be pulsating. Its period is very much stable over time and sometimes to be rapidly rotating which are called millisecond pulsar with a rotational period of 1-10 millisecond .The electromagnetic radiation emitted by pulsars is taken from the rotational energy of the neutron star which can go up to the order of 10^{45} J. The extreme physical conditions of pulsars along with their high pulse stability make them very interesting objects for a wide field of astrophysics.

Two astronomers, Baade & Zwicky, in 1934, proposed that during Supernova explosions small, extremely dense objects could be created in the center of the exploding star. Regarding the identification of pulsars, these are the fast rotating neutron star which are born out of an explosion of massive stars with a mass $\geq 8M_{\odot}$. Created in the collapse of the stars core, neutron stars are the most compact objects next to black holes. As a consequence of the conservation of angular momentum and magnetic flux of the progenitor star, pulsars gain their small rotational periods and huge magnetic fields. From the observations, it has been confirmed that pulsars must be highly magnetized and most of the electromagnetic radiation takes the form of low frequency magnetic

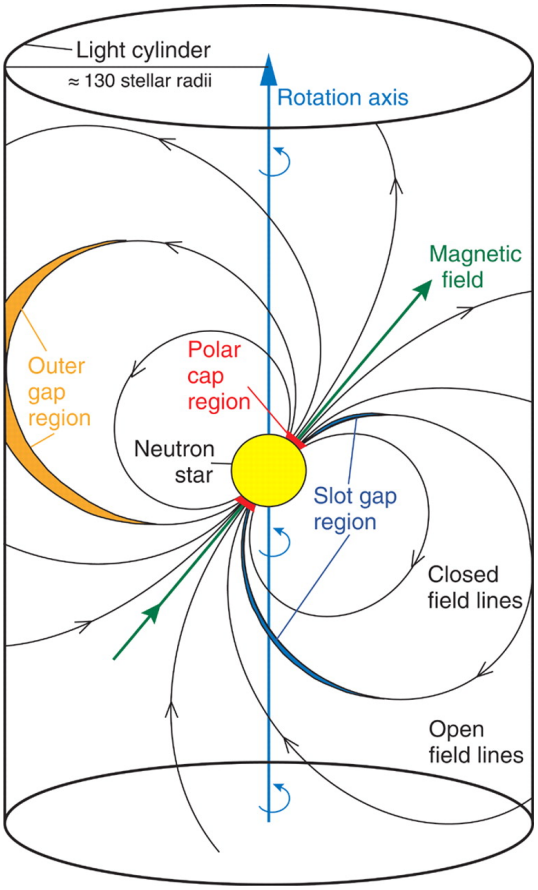

FIGURE 1.6: Electrons are trapped and accelerated along the magnetic field lines of the pulsar and emit electromagnetic radiation via the synchrotron-curvature mechanism. Vacuum gaps or vacuum regions occur at the polar cap and the outer gap region is close to the light cylinder [61].

dipole radiation. The power emitted by a rotating magnetic dipole is given by,

$$\dot{E} = -\frac{B_p^2 R^6 \Omega^4 sin^2\alpha}{6c^3} \tag{1.24}$$

where, $\Omega = 2\pi/P$ is the angular frequency,B_p is the magnetic field strength at a pole on the pulsar surface, α is the angle between rotational and magnetic axes and lastly, R is the pulsar radius. The spin frequency evolution also predicts the evolution of the spin period and the characteristic age (τ) of the pulsar given by,

$$\tau = \frac{P}{(n-1)\dot{P}} \tag{1.25}$$

where, n is the breaking index and at n=3, τ becomes $\frac{P}{2\dot{P}}$.

There are presently about 200 pulsars known. The vast majority are seen only in radio,

but the numbers detected at optical, X-ray and gamma-ray wavelengths are growing. Pulsar population are divided into two categories: normal pulsars (spin periods in the range of 0.1s to 1s) and millisecond pulsars (period at the order of millisecond and oldest pulsar population of ages 10^{10} yrs). The properties of millisecond pulsars and X-ray binaries show that 90% of all millisecond pulsars are in a binary orbit while this is true for only less than 1% of the normal pulsars [62]

Pulsed emission from γ-ray pulsars originates inside the magnetosphere (see figure 1.6), from the radiation of the charged particles near the magnetic poles or from the outer gap. Polar cap model for pulsar emission suggests about particle acceleration and radiation near the pulsar surface at the magnetic poles [63]. In this model, the high energy spectrum is cut-off by magnetic pair production above magnetic field strength dependent energy. Although the electric field parallel to the magnetic field is zero at the surface, the space-charge from the free emission falls below the co-rotation charge along open field lines and this electric field above the magnetic poles accelerate particles which radiate photons via inverse Compton scattering (ICS) process. The emitted photons produce electron-positron pairs in the strong magnetic field and as a result, super-exponential energy cutoff in the emission spectrum is expected at several GeV [64]. In the outer gap model, very high energy spectrum turnover around 10 GeV has been explained. This model assumes that the particle acceleration occurs in the outer magnetosphere [65]. Contrary, to the polar cap model, an ICS peak at some TeV arise due to charges escaping from the light cylinder along open field lines above the null charge surface. In [65, 66], it has shown that the emission can only take place from one pole. In this model, photon-photon pair production can take place in the outer gap along null charge surfaces. The photons in turn are generated by cosmic rays of primary particles or ICS of primary particles with infra-red photons. In the very high energy spectrum, the ICS contribution at 100 GeV energy is a result of comparatively lower magnetic field in the outer gap area than the pulsar surface.

1.8.2 Active galactic nuclei

Galaxies can be classified according to different physical properties, like mass, size, morphology, color, age of the stellar populations, nuclear activity. An active galactic nuclei is the compact region at the center of the galaxy e.g. Seyfert galaxies and quasars. Seyfert galaxies are very luminous active galaxies, and distant and bright sources of electromagnetic radiation, with strong, high-ionization spectral emission lines. Quasars (quasi-stellar objects) are extremely luminous and were first identified as being high redshift sources of electromagnetic energy, including radio waves and visible light, that were point-like, similar to stars. AGN comprises the luminosity of 10^{12} times of solar

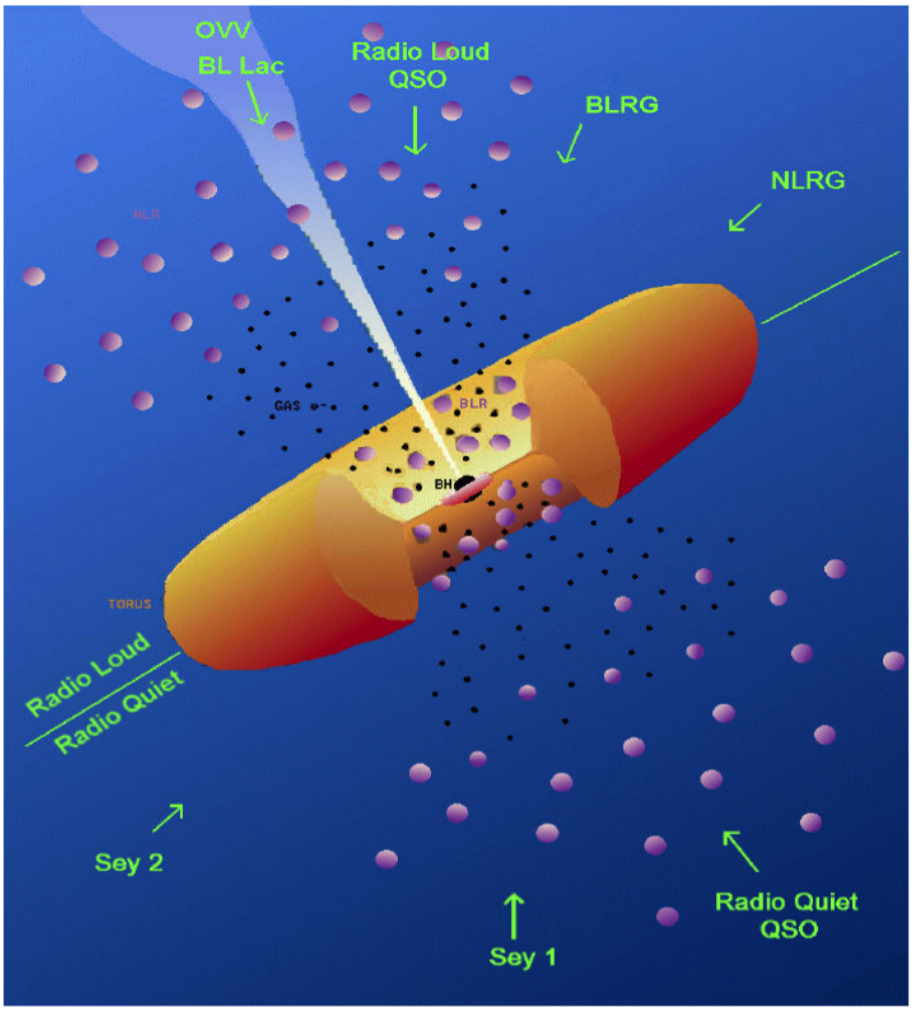

FIGURE 1.7: An unified model of AGN. It consists of a central black hole surrounded by an accretion disk. The arrows denote the viewing angle which define the different categories of AGN. Based on this model, the AGN is classified to be radio-loud source or radio-quiet galaxies. Picture credit: Urry & Padovani [67], 1995.

luminosity. Any spherically symmetric object which is stable must be gravitationally bound against being blown apart should satisfy the Eddington condition,

$$L \leq L_E = 4\pi c G m_H M/\sigma_T = 1.3 \times 10^{38}(M/M_\odot)\text{ergs}^{-1} \tag{1.26}$$

where, G is the gravitational constant, m_H is the proton mass and σ_T is the Thomson cross section. Eq. 1.26 can be written as in terms of solar luminosity,

$$\frac{L}{L_\odot} \leq 3.2 \times 10^4 \frac{M}{M_\odot}. \tag{1.27}$$

So the AGN luminosity is to be around $10^{12}L_\odot$. AGNs are the most energetic source with an accretion disk around a super-massive black hole and jets, originating in the

nuclear region and collimated by a strong magnetic field, propagate in the medium perpendicularly to the galaxy plane (see figure 1.7). According to continuum emission, AGNs can be categorized into radio-quiet and radio-loud objects. The primary observational distinctions between the two types are that The radio-loud objects produce large scale radio jets and lobes, with the kinetic power of the jets being a significant fraction of the total bolo-metric luminosity and on the other hand, the weak radio ejecta of the radio-quiet objects are energetically insignificant. While the radio-loud galaxies prefers to be associated with elliptical galaxies, the radio-quiet are the spiral galaxies [68]. Steep and flat spectrum radio quasars (FSRQs) associated to the radio-loud counterparts. The radio-loud objects which shows strong emission lines dominated by a relatively featureless non-thermal emission are called BL Lac objects. More generically, if these objects have the jet axis is close to the line of sight, they are called as *blazars*.

AGNs produce γ-ray and radio emission, with the strong energetic of the jetted relativistic outflow being responsible for accelerating particles to the high energies needed for γ-ray production [69].

The aim of this work is to perform a detailed study to determine the features of ALPs. The first chapter begins with a short reminder on existing ALPs bounds and how they can play an important role for astrophysical observations. We then quickly move to the derivation of the mixing of photons with axion-like particles. In chapter 2, we discuss the photon-ALPs mixing phenomenon occurring in the Galactic plane. We also give a highlight how the mixing depends on the ALPs parameters. Chapter 3 is contained with the spectrum analysis of Galactic pulsars and modeling of the gamma-ray spectrum with ALPs parameters. Chapter 4 and 5 is providing a detailed study of ALPs imprint on Galactic plane sources and non-Galactic plane sources respectively. Chapter 6 is focusing on the summary of this work and future prospects.

Chapter 2

Modelling of photon-ALPs mixing in Galactic magnetic field

Magnetic fields are the major factors in the interstellar medium (ISM) of spiral, barred and irregular galaxies. It provides enormous pressure that contribute to balance in the ISM against the gravitation. It also supports in star formation as they enable the removal of angular momentum from the protostellar cloud via am-bipolar diffusion [70]. Magnetic field plays an important role in distribution of cosmic rays in the ISM, affecting thermal conduction in galaxy clusters [71]. The magnitude of the Galactic magnetic field is determined from the intensity of radio synchrotron emission arising from cosmic ray electrons in the magnetic field. In case of determining the large scale magnetic field, assumption of the energy equipartition between the energy densities of the total magnetic field and the total cosmic rays are made. Although the large scale structure has not yet been clear, radio synchrotron observations of nearby galaxies reveal that the field orientation are constrained in spiral arms [72]. The equipartition assumption holds nicely with the large scale structures unlike the small scale structures. The small scale random field structures come from the diffused polarized radio emission and the Faraday rotation of the polarized emission from pulsars and background sources [73].

Milky Way's interstellar medium are relevant to ALP-photon conversion because of the large scale magnetic field, the free electron density provided by the warm ionized medium. In this chapter, a brief outlook has been given on Galactic magnetic field. Also a short highlight on the photon-ALPs mixing imprint on the Galactic plane has been illustrated. Additionally, we also calculate the photon-survival probability on the Galactic plane and discuss how the probability depends on the ALPs parameters ($g_{a\gamma\gamma}$, m_a) and photon energy.

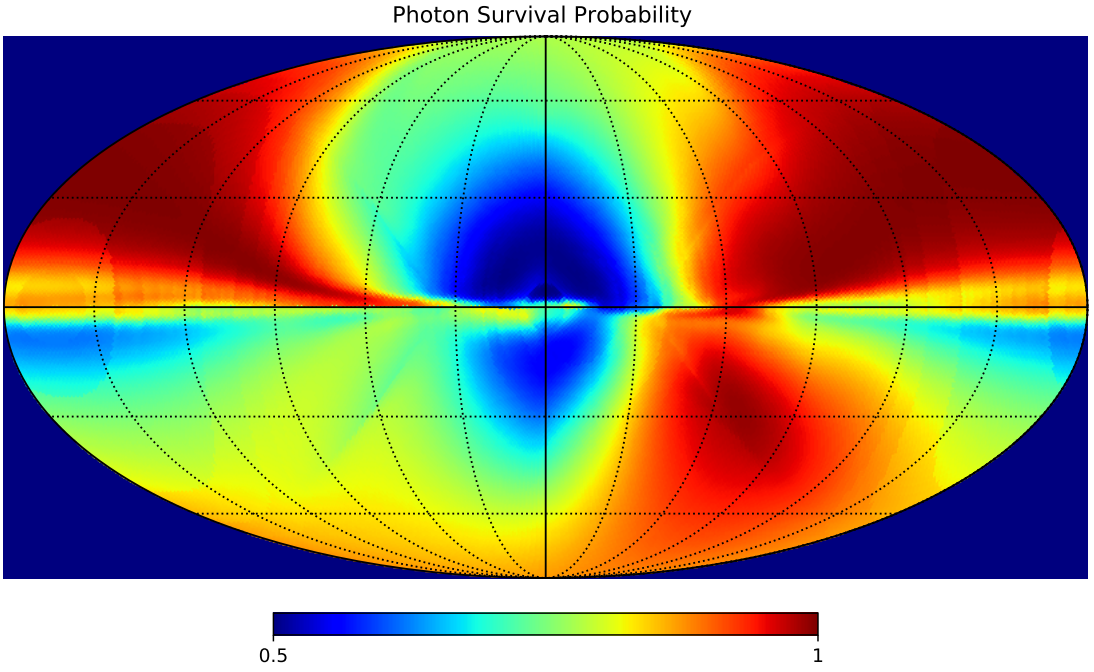

FIGURE 2.1: An all sky map of photon survival probability for photon-ALPs oscillation in the Milky way. The colormap denotes the survival probability at a distance of 15 kpc, photon-ALPs coupling constant of $9\times10^{-11}\text{GeV}^{-1}$ and ALPs mass of 1.5neV.

2.1 Galactic magnetic field

We use the mostly accepted model by Jansson and Farrar [74], based on 40,000 extra-galactic Faraday rotation measures. The properties of the Milky way's interstellar medium are very much relevant for photon-ALPs conversion.

In this model, magnetic field is the sum of most familiar three components : *the large scale regular field*, *small scale the random field* and *the straighted field*.

1. The coherent field :The large scale coherent field includes three components - a disc field, a halo field above and below the disc, and an out of plane component.The coherent field strength varies in the order of few μG. The component of the coherent field has been described in the appendix (see appendix B).

2. The random field : The random field consists of a superposition of the spiral disc and a smooth halo component [75] with a random field direction and modelled with 13 free parameters.

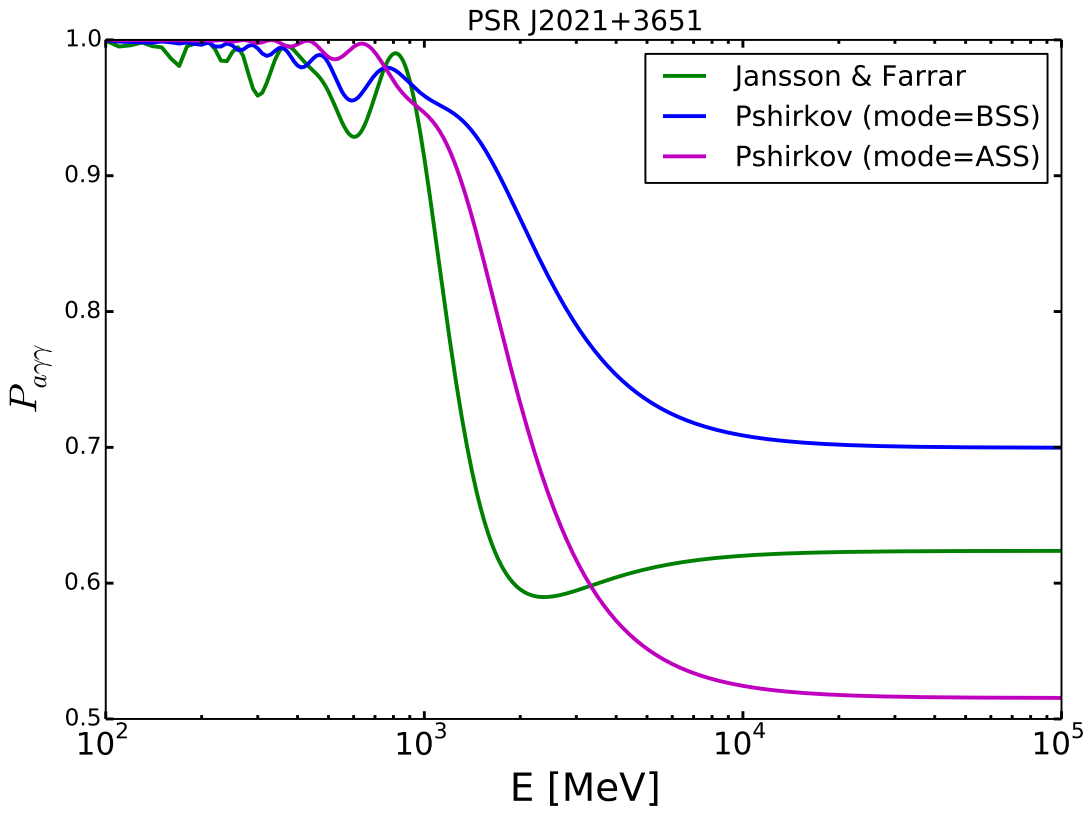

FIGURE 2.2: Photon survival probability as function of the energy for the source PSR J2021+3651 at a distance on 10 kpc, for $g_{a\gamma\gamma}$= 2.3 $\times 10^{-10}$GeV^{-1} and m$_a$= 3.54 neV. The three colored lines correspond to three magnetic field models.

3. The striated field The striated field is an addition to the Jansson and Farrar model which averages the random field to be zero [75]. The physical motivation to add this component is local stretching or compression of random magnetic field component. The striated field has a magnitude 1.25 times of the coherent field with random field directions.

For our analysis, we take into account the large scale coherent magnetic field and ignore the small scale field. To observe the photon-ALPs signature in the energy spectrum derived from the astrophysical sources, large scale field is important. The oscillation length (see eq. 1.23) for photon-ALPs mixing can be measured in kpc range which is equivalent to the coherent magnetic field length.

2.2 Photon propagation through the Galactic magnetic Field

The basic phenomenology for photon-ALPs mixing in the magnetic field has been discussed here. Photon-ALPs mixing scenario with a monochromatic beam has been shown in section 1.4. As in VHE the polarization cannot be measured properly, it is better to assume for an unpolarized beam of light. If an unpolarized photon beam is involved, the polarization density matrix becomes [42]:

$$\rho(x_3) = \begin{pmatrix} A_1(x_3) \\ A_2(x_3) \\ a(x_3) \end{pmatrix} \otimes \Big(A_1(x_3) A_2(x_3) a(x_3) \Big)^* , \tag{2.1}$$

which obeys the Von Neumann-like equation,

$$i\frac{d\rho}{dx_3} = [\rho, \mathcal{M}_0], \tag{2.2}$$

associated with eqn. 1.18. This equation can be solved by [42],

$$\rho(x_3) = \mathcal{T}(x_3, 0)\rho(0)\mathcal{T}^\dagger(x_3, 0). \tag{2.3}$$

The probability of a photon/ALPs beam from a state ρ_1 to a state ρ_2 at a distance x_3 is

$$P_{0,\rho_1\to\rho_2}(x_3) = Tr\left(\rho_2 \mathcal{T}(x_3, 0)\rho_1 \mathcal{T}^\dagger(x_3, 0)\right). \tag{2.4}$$

For general cases, $\vec{B}$ is not aligned towards the z axis but forms an non-vanishing angle ψ with it. Now the mixing matrix $\mathcal{M}_0$ makes the transformation from $\mathcal{M}_0^{(0)}$:

$$\mathcal{M} = V^\dagger(\psi)\mathcal{M}_0 V(\psi), \tag{2.5}$$

Where, the solution of the rotation matrix describes as,

$$V(\psi) = \begin{pmatrix} cos\psi & -sin\psi & 0 \\ sin\psi & cos\psi & 0 \\ 0 & 0 & 1 \end{pmatrix}. \tag{2.6}$$

Now the transfer matrix can be calculated from 2.5,

$$\mathcal{T}(x_3, 0; \psi) = V^\dagger(\psi)\mathcal{T}(x_3, 0)V(\psi), \tag{2.7}$$

with an illustrative way,

$$\mathcal{T}(x_3, 0; \psi) = \sum_{n=1}^{3} e^{i\lambda_n x_3} T_{0,n}(\psi) \tag{2.8}$$

where, $T_{0,n}$ can be derived from the following way,

$$T_{0,1}(0) = \begin{pmatrix} 1 & 0 & 0 \\ 0 & 0 & 0 \\ 0 & 0 & 0 \end{pmatrix} \tag{2.9}$$

$$T_{0,2}(0) = \begin{pmatrix} 0 & 0 & 0 \\ 0 & sin^2\alpha & -sin\alpha cos\alpha \\ 0 & -sin\alpha cos\alpha & cos^2\alpha \end{pmatrix} \tag{2.10}$$

$$T_{0,3}(0) = \begin{pmatrix} 0 & 0 & 0 \\ 0 & cos^2\alpha & sin\alpha cos\alpha \\ 0 & sin\alpha cos\alpha & sin^2\alpha \end{pmatrix}. \tag{2.11}$$

In the above matrices, α denotes the photon-ALPs mixing angle describes as,

$$\alpha = \frac{1}{2} arctg \left(\frac{2\Delta_{a\gamma}}{\Delta_{pl} - \Delta_{aa}} \right) = \frac{1}{2} arctg \left\{ \left(\frac{B}{M} \right) \left(\frac{2E}{m^2 - \omega_{pl}^2} \right) \right\}. \tag{2.12}$$

Where, m is the ALPs mass, ω_{pl} is the plasma frequency, B is the magnetic field. M is a constant with the form of,

$$M = 1.2 \times 10^{10} k \left(\frac{f_a}{10^7 \text{GeV}} \right) \text{GeV}, \tag{2.13}$$

where, k is a model-dependent parameter and f_a stands for the scale at which $U(1)_{PQ}$ symmetry is spontaneously broken.

A photon-ALP system can be described in terms of a three state wave function including two states of photon polarization and one state of ALP. The angle between magnetic field (B) and photon momentum is assumed to be θ. As, only the transversal component of the magnetic field is involved to the coupling between photon and ALPs the effective magnetic field is to be B$\sin\theta$.

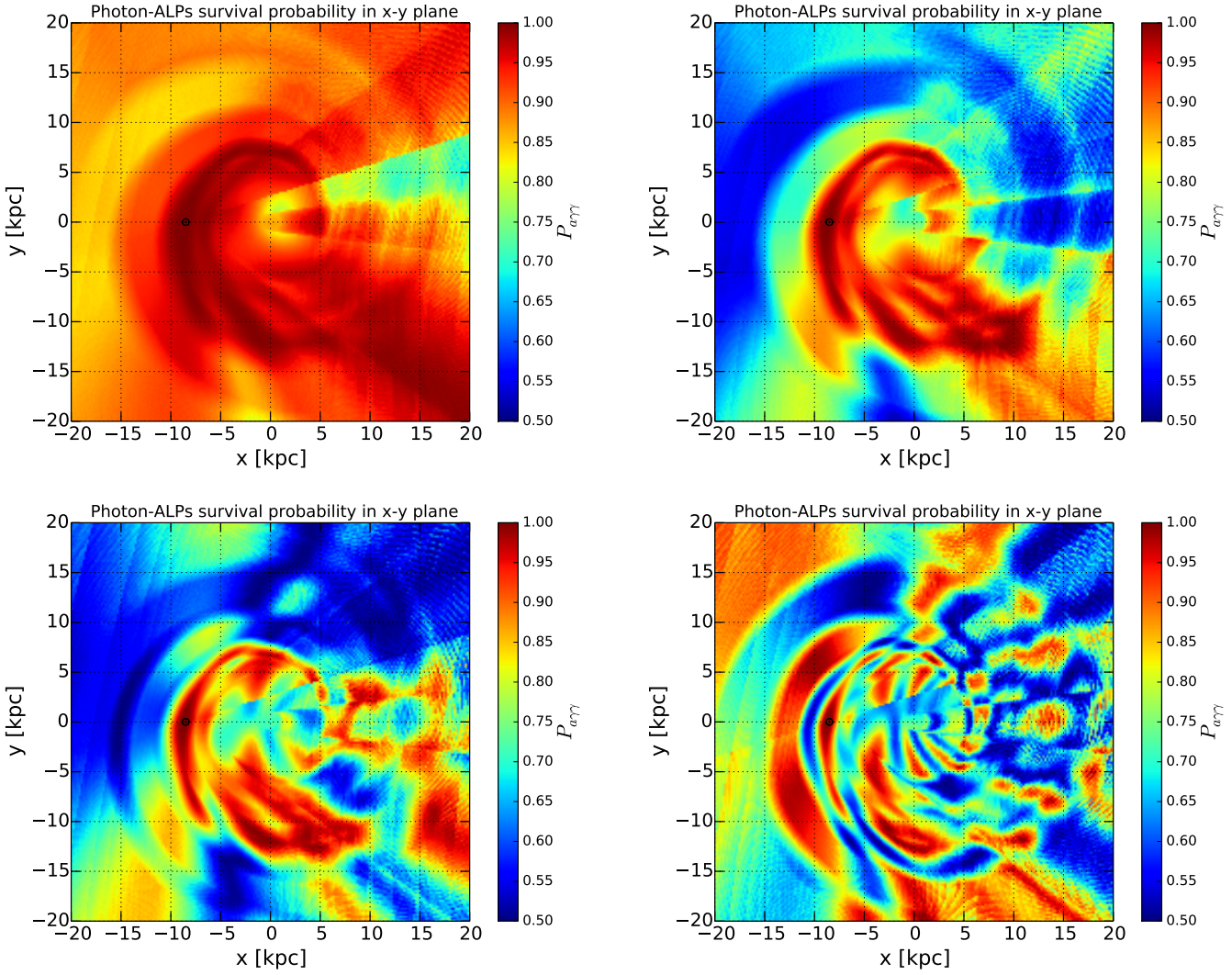

FIGURE 2.3: The photon survival probability in photon-ALP oscillations in the Galactic magnetic field. We project the survival probability in the Galactic plane for a fixed ALPs mass of 3.54 neV and photon energy of 2 GeV. Photon-ALP coupling has been changed as $g_{a\gamma\gamma}$= 7×10^{-11}GeV^{-1}, 15×10^{-11}GeV^{-1}, 23×10^{-11}GeV^{-1}, 40×10^{-11}GeV^{-1} respectively for the figures from upper left panel. The color scale corresponds to the survival probability on the Galactic disk.

The probability for an axion to convert into photon after traveling a distance l in a transversal magnetic field is

$$P_{a\gamma\gamma} = sin^2(2\theta)\, sin^2(\frac{1}{2}\Delta_{osc} l) \tag{2.14}$$

where, $\Delta^2_{osc} = (\Delta_{\parallel} - \Delta_a)^2$ and the oscillation length comes as l= $(2\pi/\Delta_{osc})$.

2.3 Photon survival probability on the Galactic plane.

Photons emitted from the astrophysical sources, while traversing through the large scale Galactic magnetic field, converts to an ALPs state and again reconvert to the photons. The photon survival probability across the Milky way is relevant to multiple effects. The effects can be probed for different photon-ALPs coupling constant, different ALPs mass and photon energy. The photon survival probability is highly depending on the magnetic field model of the Milky way although the local magnetic field properties are quite unknown. We use large scale magnetic field models based on the Faraday rotational measurements. We highlight the mostly accepted the Milky way field model, Jansson and Farrar model (see section 2.1). The coherent field component has been illustrated in the appendix A. An all sky map of photon survival probability for photon-ALPs oscillation in the Galactic magnetic field has been shown in the figure 4.1.

Additionally, conversion probability maps has been highlighted for pulsar J2021+3651 in the figure 2.2 at a known distance of 10 kpc [76]. Bright objects can be detected due to expected suppression in the energy spectrum. It is important to note that, the oscillation can be visible in the lower energy of the photons. This is the reason why in the previous chapter, we emphasize on the spectral modulation in the lower energy part ($<$ cutoff energy) of the spectrum for the astrophysical sources.

We note how the ALPs mass (m_a), photon-ALPs coupling constant ($g_{a\gamma\gamma}$) and photon energy are relevant to the photon survival probability.

Photon-ALPs coupling constant The photon survival probability on the Galactic disk for different photon-ALPs coupling constant ($g_{a\gamma\gamma}$) has been given in figure 2.3. With the increase of $g_{a\gamma\gamma}$, the pattern of the survival probability changes. For lower values of $g_{a\gamma\gamma}$, $P_{a\gamma\gamma}$ makes almost no changes and near to the Sun the conversion probability of ALPs to photon is ~ 1. As the photon-ALPs coupling increases, the photon survival probability makes local pattern in the Galactic plane indicating the large number of photon-ALPs oscillation over large distances.

ALPs mass The photon survival probability on the Galactic disk for different ALPs mass has been shown in the figure 2.4 . With the decrease of ALPs mass value, the survival probability on the Galactic plane follows higher conversion probability from ALPs to photon. In the top left panel of figure 2.4, we can see that the survival probability for lower ALPs mass nicely follow the Galactic spiral arm structure i.e. lower the mass higher the conversion of ALPs to photon. On the contrary, in case of higher ALPs mass

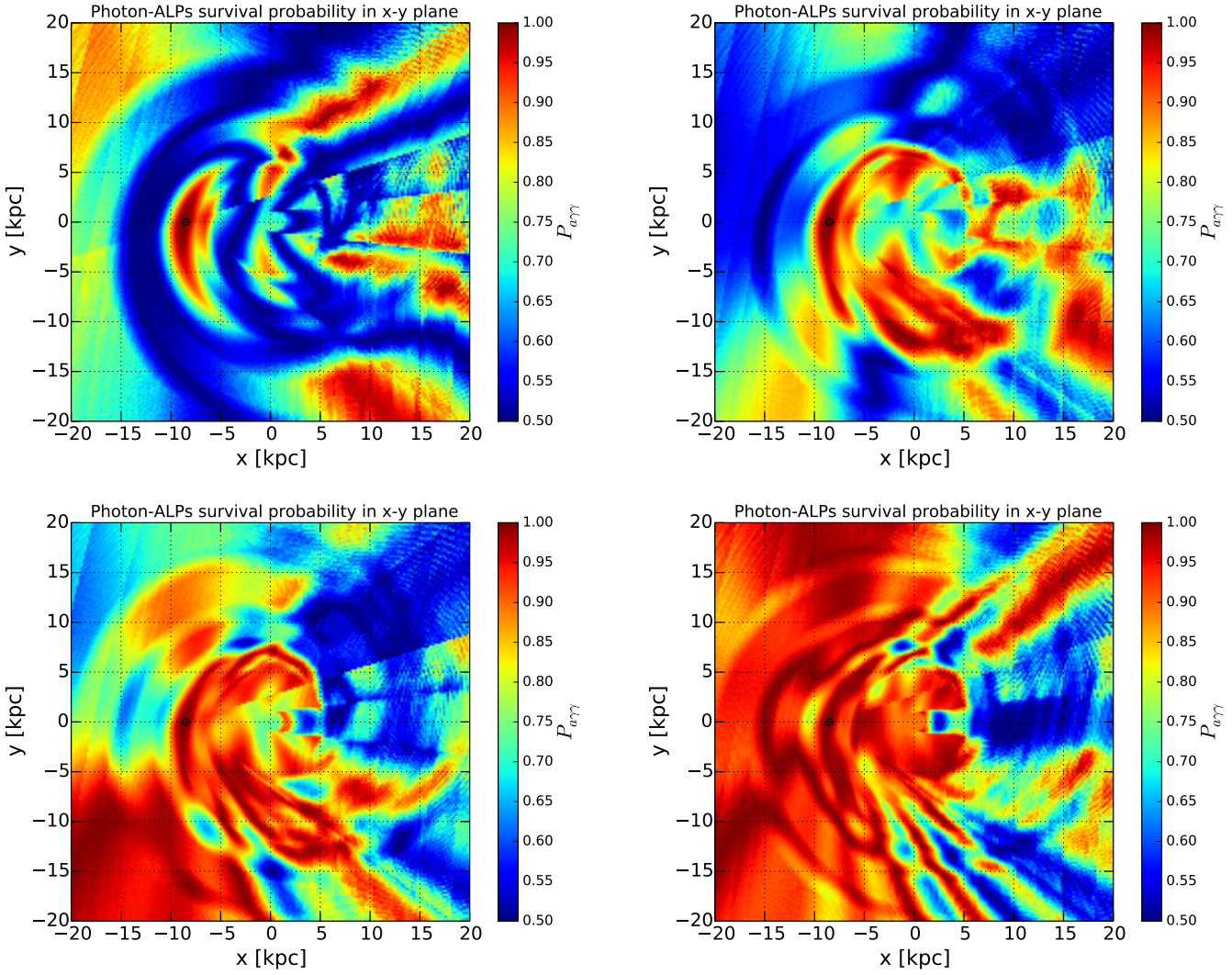

FIGURE 2.4: The projected photon survival probability in photon-ALP oscillations in the x-y plane of the Galactic magnetic field for a fixed photon-ALPs coupling of $23\times10^{-11}\text{GeV}^{-1}$ and photon energy of 2 GeV. The ALPs mass has been changed as m_a= 1.2, 3.54, 4.5, 6 neV respectively for the figures from upper left panel onwards. The color scale corresponds to the survival probability on the Galactic disk.

the photon survival probability makes almost no change (see figure 2.4 at right panel of bottom row).

Photon energy Photon Energy dependence of the survival probability has been overlaid in the figure 2.5. For allowed large scale of the Galactic magnetic field values of order μG, an ALP mass of 3.54 neV and a coupling of $2.3\times10^{-10}\text{GeV}^{-1}$, with the change in photon energy survival probability makes changes. It is important to note that, the photon survival probability does not make any change in the local areas (close to the Sun) as the parameters change.

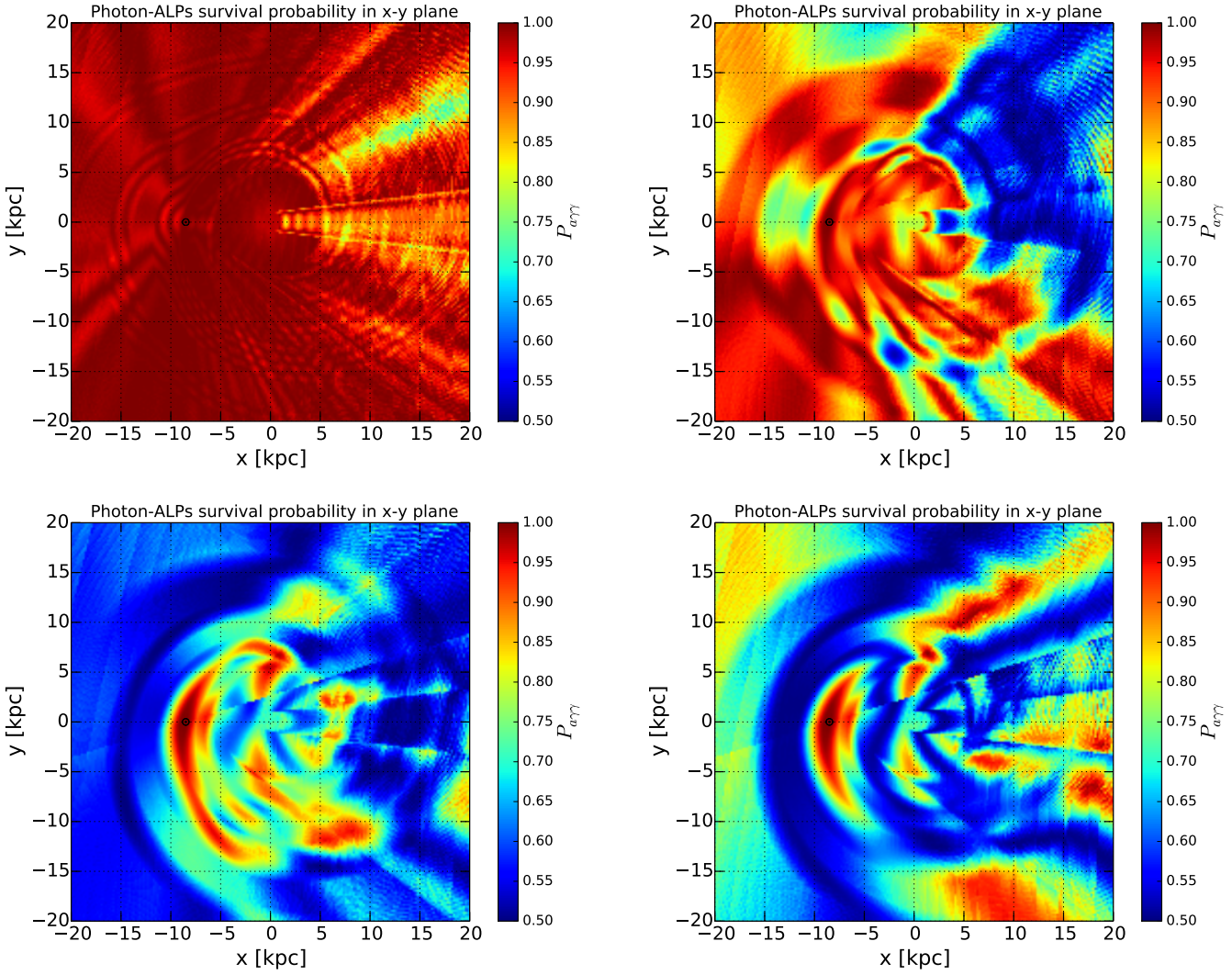

FIGURE 2.5: The projected photon survival probability in photon-ALP oscillations in the x-y plane of the Galactic magnetic field for a fixed photon-ALPs coupling of $23\times10^{-11}\text{GeV}^{-1}$ and ALPs mass of 3.54 neV. The photon energy has been changed as m_a= 0.2, 1, 3, 10 GeV respectively for the figures from upper left panel onwards. The color scale depicts to the survival probability on the Galactic disk.

In astrophysical environments, magnetic fields are usually not homogeneous. In the case of a propagation through a turbulent magnetic field, the beam path can be divided into coherent domains of size of the coherence length of the field. The parameter effects has been studied in the figures 2.3, 2.4 and 2.5 where one can notice some discrete line features on the survival probability map on the Galactic plane. This phenomenon can be justified with the given magnetic field model of our Galaxy (B.1). In the Jansson and Farrar model [74], for the 3kpc $\leq$ Galactocentric radius $\leq$ 5kpc are consistent with a 'molecular ring' with constant magnetic field strength. Starting from 5kpc, the spiral arms has been opened in an angle on 11.5°. The large scale magnetic field has nearly the shape of spiral arms where, the local field aligned tangentially to the spiral arms.

Photons at a line of sight touches the relatively high intensity spiral arms, can make discontinuity in the photon survival probability map.

Chapter 3

ALPs modeling for pulsar sources

In this chapter, spectral modulation due to photon-ALPs mixing in case of pulsars have been described. We discussed about source selection criteria, brief description about each source along with the data analysis technique. We illustrated our spectral modulation results and calculated the significance level.

In this work, for the first time, we investigate photon-ALPs oscillation features in the disappearance channel for the Galactic gamma-ray sources, notably pulsars detected by the *Fermi*-LAT, a pair conversion telescope collecting gamma rays between 20 MeV to more than 500 GeV. To date, more than 160 gamma-ray pulsars have been observed by the LAT [76, 77]. We focus on Galactic gamma-ray pulsars for the following reasons:

- a large number of them has been detected by the LAT, allowing to identify an almost universal observed gamma-ray spectrum;
- many of them are bright enough to permit an accurate determination of the spectrum with a fine energy binning, crucial to look for spectral distortions;
- the variety of distances and positions in the Galaxy allows to study how spectral variations depend on the structure of the Galactic magnetic field and to have control samples for a precise assessment of systematic uncertainties;
- distances of pulsars from Earth are known reasonably well, thanks to radio dispersion measurements [78, 79].

We consider *Fermi*-LAT data from six selected bright gamma-ray pulsars [76] and we look for significant spectral irregularities that might be induced by photon-ALPs oscillations in the regular Galactic magnetic field. The photons emitted by these Galactic sources penetrate the Galactic magnetic field while propagating and might oscillate into ALPs

with a given probability, depending on the magnetic field configuration. To compute the conversion probability of photons into ALPs (and vice versa), we use the Jansson & Farrar Galactic magnetic field model [74, 80], which describes the regular coherent magnetic field component of the Milky Way, updated to take into account the latest Planck measurements [81]. The detailed description of this model is provided in the appendix B. From eq. 1.19, given the μG field strength of the Galactic magnetic field and critical energy in the GeV range, photon-ALPs oscillation would be sensitive to an ALP mass of the order of neV for couplings $g_{a\gamma\gamma} \sim 10^{-11}\,\mathrm{GeV}^{-1}$. For allowed values of $g_{a\gamma\gamma} \sim 10^{-11}\,\mathrm{GeV}^{-1}$ the mixing is non-linear in the spiral arms and in the large-scale field of the inner Galaxy. In order to look for photon-ALPs oscillations, we need to focus on the low-energy spectrum where irregularities can be expected as a result of mixing.

3.1 Pulsar sources selection

The shortest oscillation length (see eq. 1.23) and therefore the strongest effect is expected for sources located at a large distance and along a line of sight with large $B_\perp$. The source population with the best determined distances are pulsars. Pulsars have been observed in the entire Galaxy. We have selected from the *Fermi* pulsar catalog the brightest pulsars with known distances and lines of sight that traverse spiral arms at large pitch angles [82, 83]. To date, about 160 gamma-ray pulsars have been observed with *Fermi*-LAT [76]. After applying the selection criteria (known distance and located at a favorable lines of sight), we have chosen the resulting six brightest gamma-ray pulsars from the second *Fermi*-LAT pulsar catalog (see table 3.1). The positions of the pulsars including uncertainties on their heliocentric distance are marked in figure 3.1. All six pulsars are rotation powered and fairly young. A brief description of each of the pulsars are as follows:

PSR J1420-6048 : PSR J1420-6048 at a distance of (5.7 ± 0.9) kpc (the distance is estimated from dispersion measure of radio-timing data [84]) is a 68 ms pulsar in the Kookaburra nebula which has been extensively studied in X-ray, radio, and infrared [85]. It is extended along the radio structure and has a flat spectrum above 1 TeV. Radio observations at several frequencies of the northern wing with the Australia Telescope Compact Array(ATCA) and a deep XMM-Newton observation studied the morphology of the PWN part[86].

PSR J1648-4611 : PSR J1648-4611 at a distance of (4.9 ± 0.7) kpc (the distance is estimated from the dispersion measure given in [87] and using the electron distribution model [88]) is tentatively associated with a very-high-energy (VHE) gamma-ray source

observed with HESS (HESS J1646-458) [89] in the vicinity of the massive stellar cluster Westerlund 1. Being a suitable source favored with very high energy (VHE) particle acceleration, a hadronic parent population could be accelerated within the stellar cluster of Westerlund 1. Besides of this, two hard X-ray sources, Suzaku J1648−4610 (Src A) and Suzaku J1648−4615 (Src B), were found in the field of view of PSR J1648-4611 [90].

PSR J1702-4128 : The pulsar PSR J1702-4128 at a distance of (4.7 ± 0.6) kpc has been associated with a HESS source J1702-420 at VHE energies. PSR J1702-4128 is energetic enough to account for the observed VHE gamma-ray emission by converting roughly 14% of its spin-down luminosity [91]. The nearby SNR G344.7-0.1 is small and not coincident with the VHE gamma-ray source.

PSR J1718-3825 : PSR J1718-3825 at a distance of (3.6 ± 0.4) kpc has been associated with pulsar wind nebulae at VHE energies [92, 93]. PSR J1718-3825 is a 75 ms pulsar discovered by [94] at radio wavelength. The γ-ray light curve of PSR J1718-3825 is single peaked (full-width-half-maxima is 0.20 in phase) and it lags the radio profile by 0.42 in phase [84].

PSR J2021+3651 : PSR J2021+3651 (distance of 10^{+2}_{-4} kpc from dispersion measure and X-ray absorption [95]) is a 17 kyr pulsar detected in radio, X-rays, and gamma rays (possibly associated with VER J2019+368 [96]). This object resembles the Vela pulsar quite a lot. We note that a recent X-ray absorption study [97] favors a smaller distance of $1.8^{+1.7}_{-1.4}$ kpc. PSR J2021+3651 is located in the Cygnus region where diffuse emission is bright enough to resolve poorly the neighboring sources and the light curve consists of two narrow peaks of similar amplitude separated by 0.468 ± 0.002 in phase[98].

PSR J2240+5832 : The recently Nancay radio telescope discovered the northern-hemisphere pulsar PSR J2240+5832. It is located in an outer spiral arm similar to PSR J2021+3651 at a distance of (7.7 ± 0.7) kpc [99]. It has a rotational period of 140 ms and spin down power $\dot{E} = 2.12 \times 10^{35}$ erg s^{-1}.

These objects are located at low Galactic latitude so that the emitted photons traverse Galactic spiral arms (see figure 3.1). In order to estimate systematic uncertainties on the observed spectrum we use the Vela pulsar as a reference source. This pulsar is sufficiently close to determine a geometrical parallax distance of 294^{+76}_{-50} pc [100]. The Vela pulsar is the brightest non-flaring source in the GeV γ-ray sky. Given Vela's apparent brightness, the gamma-ray spectrum is very well measured and does not show any spectral distortion. To derive the systematic uncertainties, we use a similar technique to the *Fermi*-LAT Pass 7 data analysis in [60], see also section 3.3.

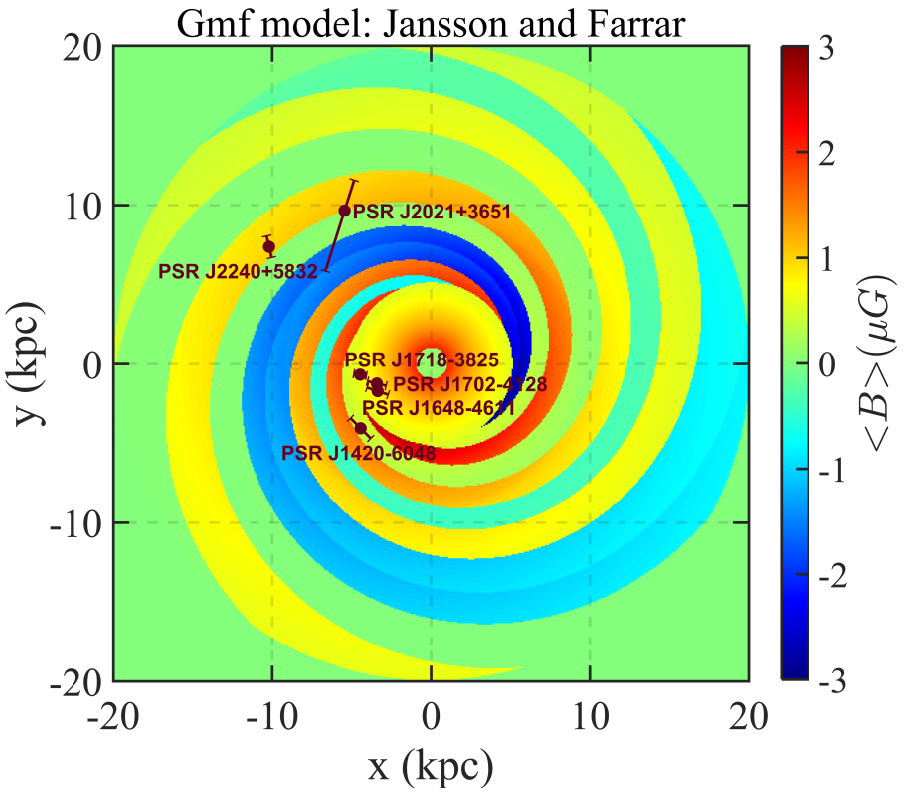

FIGURE 3.1: Source positions in the Galactic plane with the Jansson and Farrar model [74, 80] magnetic field strength indicated by the color scale. Both, PSR J2021+3651 and PSR J2240+5832 are located close to the fifth spiral arm, while PSR J1420-6048, PSR J1648-4611, PSR J1702-4128, and PSR J1717-3825 are in the direction towards the Galactic center. Error bars at the source positions mark the uncertainties on heliocentric distances. The position of the sun (at $x = -8.5$ kpc) is marked as well.

Pulsar name	l_{II} [°]	b_{II} [°]	d [kpc]
J1420-6048	313.54	0.23	5.7 ± 0.9
J1648-4611	339.44	-0.79	4.9 ± 0.7
J1702-4128	344.74	0.12	4.7 ± 0.6
J1718-3825	348.95	0.43	3.6 ± 0.4
J2021+3651	75.22	0.11	10^{+2}_{-4}
J2240+5832	106.57	-0.11	7.3 ± 0.7
J0835-4510(Vela)	263.552	-2.7873	$0.294^{+0.076}_{-0.050}$

TABLE 3.1: Selected gamma-ray pulsars (in order of right ascension) used for the present analysis. The information listed includes Galactic longitude (l_{II}), latitude (b_{II}), as well as heliocentric distance (d) with corresponding errors (see text for further details).

3.2 Data analysis

We use nine years of *Fermi*-LAT Pass 8 data with P8R2 SOURCE V6 IRFs. The *Fermi*-LAT Pass 8 data have an improved angular resolution, a broader energy range, larger effective area, as well as reduced uncertainties on the instrumental response functions [60] compared to previous data releases. For the determination of *Fermi*-LAT source spectra, the `Enrico` scripts to calculate differential energy spectra are used [101]. The width of the logarithmically spaced energy bins has been chosen to be 37% of the median energy resolution. For the analysis, *SOURCE* event class and *FRONT+BACK* event types has been used. Photons with measured zenith angles greater than 90° were excluded to avoid contamination by intense gamma-ray emission from the Earth's limb caused by cosmic rays interacting in the atmosphere. The region of interest (ROI) is centered on the source position and has a radius of 15°. We include all point sources listed in the third *Fermi*-LAT source catalog [77] within 15° from the ROI center. The diffuse background is modeled with the templates for the Galactic and the isotropic extragalactic gamma-ray emission available within the `Fermi Science tools`. We keep the diffuse Galactic emission model as well as the isotropic emission model fixed for the flux determination in the individual energy bins after fitting it over the entire energy range. In the spectral analysis, pulsar spectra are modeled with a PLSubExpCutoff:

$$\frac{dN}{dE} = N_0 \left(\frac{E}{E_0}\right)^{-\Gamma_1} \exp\left[\left(-\frac{E}{E_{\rm cut}}\right)^{\Gamma_2}\right]. \tag{3.1}$$

The free parameters are N_0 (normalization factor at the scale energy E_0), Γ_1 (photon index), and $E_{\rm cut}$ (cutoff energy). For the Vela energy spectrum, the additional parameter Γ_2 is determined from the fit. The spectral parameters of other point sources within 3° from the ROI center are left free to vary, while the parameters for the point sources at larger angular distance are kept fixed.

We investigate the presence of spectral distortions due to photon-ALPs oscillations, by comparing the goodness-of-fit with and without photon-ALPs oscillations. Similarly to a previous study to search for spectral irregularities with *Fermi*-LAT [102], we take into account the energy dispersion matrix D_{kk_p}. We derive the energy dispersion matrix D_{kk_p} via the transformation of the number of counts in true energy of a particular energy bin to the number of counts in that bin of reconstructed energy (see [102] for further details). The modeled spectra are:

$$\left(\frac{dN}{dE}\right)_{\rm w/o\ ALPs} = D_{kk_p} \cdot \left(\frac{dN}{dE}\right)_{\rm intrinsic}, \tag{3.2}$$

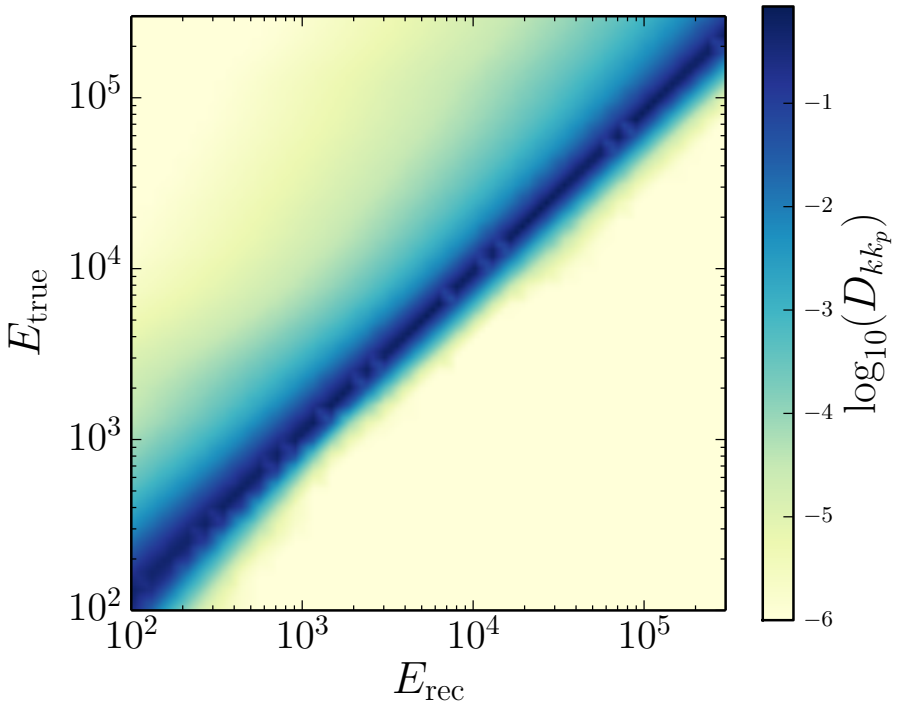

FIGURE 3.2: Energy dispersion matrix, D_{kk_p}, derived for all EDISP event types together. The color bar, i.e., D_{kk_p}, encodes the probability for a shift between reconstructed energy (E_{rec}) and true energy (E_{true}), here in MeV.

and

$$\left(\frac{dN}{dE}\right)_{\text{w ALPs}} = D_{kk_p} \cdot (1 - P_{\gamma\to a}\,(E, g_{a\gamma\gamma}, m_a, d)) \cdot \left(\frac{dN}{dE}\right)_{\text{intrinsic}}, \tag{3.3}$$

where the intrinsic spectrum refers to eq. 3.1. The probability $P_{\gamma\to a}$ is calculated following the approach described in [103] (including the electron density model for the interstellar medium [88] and a recently updated Galactic magnetic field model [74]).

We perform a fit to the differential flux measurements, minimizing the χ^2 function which has been done in previous studies [104, 105] and including the systematic errors estimated from the analysis of the Vela energy spectrum (see section 3.3). We have verified that the log-likelihood as a function of flux normalization in the individual energy bins has indeed a parabolic shape in the figure 3.3 and therefore we conclude that a χ^2-analysis for these bins are appropriate.

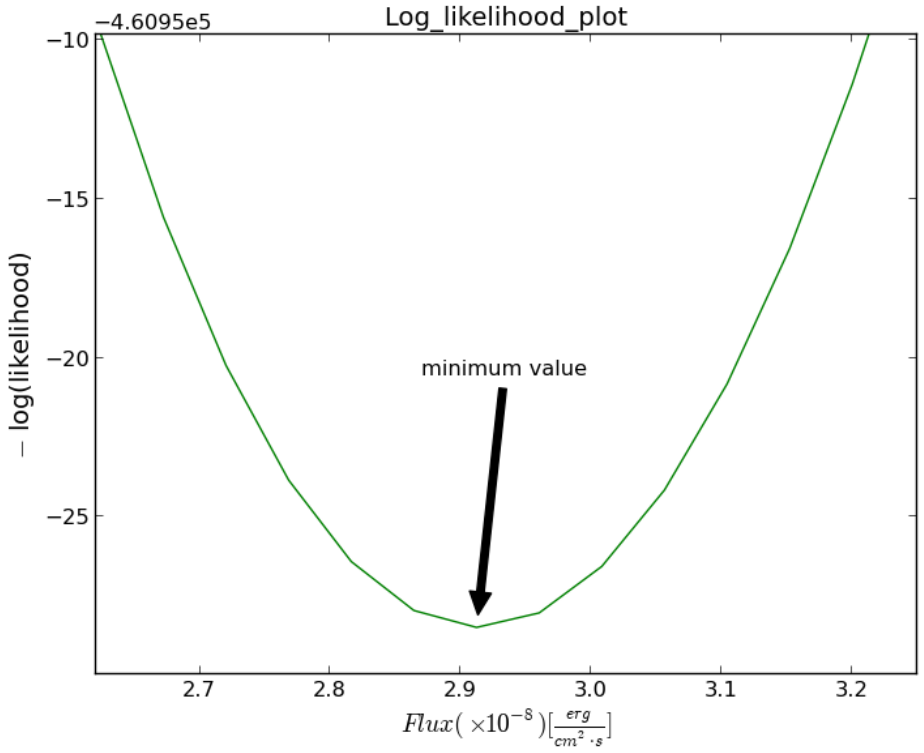

FIGURE 3.3: -log(likelihood) value as a function of photon flux of 6th energy bin for the source PSR J2021+3651. The log-likelihood of this energy bin has a parabolic pattern which is also true for the other energy bins.

3.3 Systematic uncertainties

In the most extensive study of the systematic uncertainties of flux measurements [60] a number of effects contributing to systematic uncertainties are considered, including residual particle background, effective area, energy resolution, point-spread function, and (global) uncertainties on energy scale. First, we discuss the effect of the uncertainties on the analysis carried out here and, secondly, we consider an extensive approach to estimate the effect of uncertainties in a data-driven way.

Known systematics: The effect of particle background has been checked by repeating the analysis with different event classes. Approximately, the uncertainties related to the event classes are derived as 10% at 100 MeV, decreasing to 5% at 560 MeV and increasing to 10% at 10 GeV and above [60]. The uncertainty associated to the point spread (PSF) function estimated by comparing the 68% and 95% PSF containment radii from a set of calibration point sources. During Fermi sky observing mode, the effective area gets smaller for larger photon incidence angle and resultantly, PSF is

Pulsar name	N_0 $[10^{-9}\mathrm{MeV}^{-1}\,\mathrm{cm}^{-2}\,\mathrm{s}^{-1}]$	E_0 [GeV]	Γ_1	E_{cut} [GeV]
J1420-6048	0.0014(2)	5.6	1.79(4)	4.3(4)
J1648-4611	0.0022(1)	2.9	0.98(3)	3.1(2)
J1702-4128	0.15(3)	0.1	0.8(1)	0.8(1)
J1718-3825	0.021(1)	1.2	1.58(4)	2.2(2)
J2021+3651	0.15(1)	0.8	1.59(3)	3.2(3)
J2240+5832	0.0065(1)	1.2	1.5(1)	1.6(4)
J0835-4510 (Vela)	105(2)	0.1	Γ_1 =1.27(1) Γ_2= 0.541(2)	0.654(3)

TABLE 3.2: Fit results for individual pulsars without photon-ALPs mixing. The table contains the best fitted parameters i.e., normalization factor at scale energy (E_0), photon index, cutoff energy of each sources. The combined statistical and systematic (1σ) uncertainties estimated from the fit are listed as well.

dominated at γ-rays at smaller incidence angles e.g. $\cos\theta \in [0.5, 1.0]$ [60]. The Fermi collaboration made an attempt to calculte the uncertainty related to the energy scale calibration from beam data and in-orbit cosmic-ray muon data. The uncertainty is derived as $(+2\%/-5\%)$ in the energy range between 1 GeV–100 GeV and $(+4\%/-10\ \%)$ at below 100 MeV and above 300 GeV [60]. It is difficult to constrain the energy scale at the low and very high ends of the LAT energy range, where the energy resolution increases with a factor of 2.

Data driven method: With the data driven approach, we try to estimate the systematic uncertainties relevant to this analysis. Similar to the analysis carried out in [60], we use the energy spectrum of the Vela pulsar and derive the flux in 9 bins per decade of energy. The resulting energy spectrum is modelled by a function given in eq. 3.1. The parameters are estimated using a χ^2-minimization which allows to evaluate the goodness of fit. After probing the residuals, we add in quadrature to the statistical uncertainties a relative systematic uncertainty on the flux measurement. We increase the relative uncertainty in such a way so that the resulting χ^2 per degrees of freedom becomes ~ 1. The result for the spectrum analysis of the Vela pulsar is illustrated in figure 3.4. This approach provides a maximum relative uncertainty on the flux to be 2.4% with a minimum influence that can lead to the deviation from smooth spectrum. The high energy regime of the spectrum exhibits a relative deviation nearly about 4% from the smooth fit which corresponds to the PowerLaw component in the spectrum measured with H.E.S.S. [106]. This is a similar method for determining the systematic uncertainties, often used in X-ray spectroscopy so that systematic uncertainties on the flux measurement do not affect the goodness of fit [107, 108].

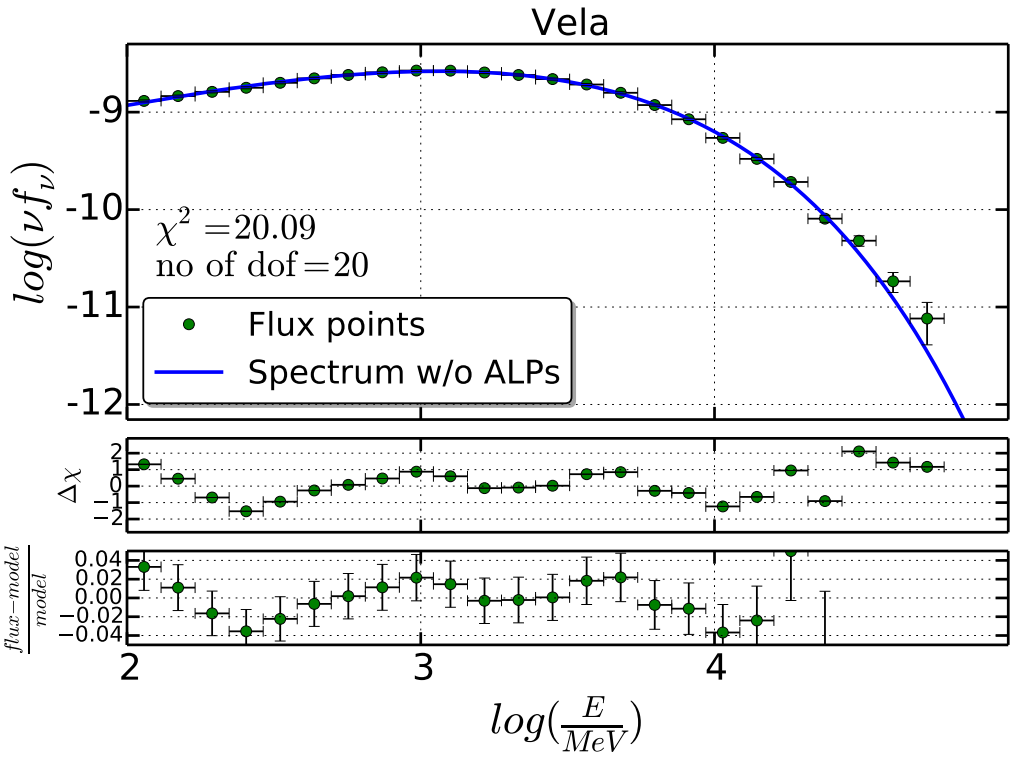

FIGURE 3.4: The phase-averaged energy spectrum of Vela (upper panel), the residuals (middle panel), and relative deviations (lower panel) overlaid with a best-fit model (eqn. 3.1). Assuming a relative systematic uncertainty of the flux of 2.4 % (added in quadrature to the statistical errors), an acceptable fit ($\chi^2(dof) = 20.09(20)$) is achieved.

3.4 Spectral modulation due to photon-ALPs mixing

3.4.1 Energy spectra and fits

The results of the spectral analysis and fitting of PLSubExpCutoff models to the spectral points, i.e., fit without photon-ALPs mixing, are summarized in the table 3.2. There, we list for each pulsar the best-fit normalization factor N_0, the photon index Γ, and the cutoff energy $E_{\rm cut}$. In figure 3.5, the spectral energy distribution for one particular source (PSR J2021+3651) is shown, overlaid with the best-fitting model from eq. 3.1 (blue thin line). Obviously the resulting $\chi^2 = 51.25$ with 14 degrees of freedom for that source is not satisfactory (see table 3.4, second column for the resulting χ^2-values for all the considered pulsars).

We consider as an alternative hypothesis, that the observed energy spectra are modified by photon-ALPs mixing in the intervening Galactic magnetic fields (see eq. 3.3).

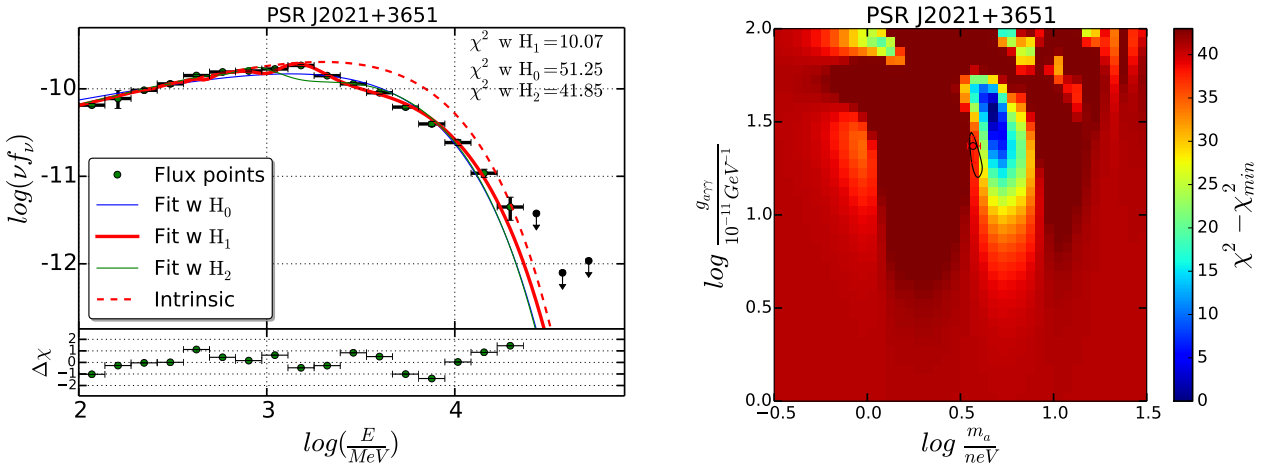

FIGURE 3.5: The spectral energy distribution of PSR J2021+3651 (green points with combined systematic and statistical uncertainties) overlaid with the best-fit models (blue thin: H_0 hypothesis , red thick:H_1 hypothesis, green thin: H_2 hypothesis). In addition, the intrinsic spectrum (as emitted) is shown by the red dashed line to highlight the effect of photon-ALPs mixing. Relative deviations between flux points and fitted spectrum with H_1 hypothesis (lower left panel) has been shown. Right panel: A scan of the plane of mass and coupling, where the color scale indicates the increase of χ^2 with respect to the global minimum and the black region determines the 2σ uncertainty combined contour of the pulsar sources.

Pulsar name	N_0 $[10^{-9}\mathrm{MeV}^{-1}\,\mathrm{cm}^{-2}\,\mathrm{s}^{-1}]$	Γ_1	E_{cut} [GeV]	$g_{a\gamma\gamma}$ $\left[10^{-10}\,\mathrm{GeV}^{-1}\right]$	m_a [neV]
J1420-6048	0.0016(2)	1.74(4)	5.4(6)	1.7(3)	3.6(1)
J1648-4611	0.0028(2)	0.88(3)	3.4(2)	5.3(9)	4.3(1)
J1702-4128	0.13(3)	0.9(1)	1.0(2)	4.4(2)	8.1(5)
J1718-3825	0.024(2)	1.48(4)	2.1(1)	2.4(3)	8.9(2)
J2021+3651	0.18(1)	1.45(3)	3.5(1)	3.5(3)	4.4(1)
J2240+5832	0.005(1)	1.5(1)	2.4(6)	2.1(4)	3.7(3)

TABLE 3.3: Fit results for individual pulsars with photon-ALPs mixing. The table gives the best fitted parameters i.e., normalization factor of each source defined at scale energy (E_0, see table 3.2), spectral index, cutoff energy, photon ALPs coupling constant ($g_{a\gamma\gamma}$), and ALPs mass (m_a) of each source including uncertainties.

Including the effect of spectral modulation from photon-ALPs oscillations improves the goodness of fit consistently for the selected sources (see table 3.3 for the best-fitting values and third column for the resulting χ^2-values). We discuss in the following the most significant source PSR J2021+3651 before including the other sources in a combined analysis (figure 3.5).

The spectra of the analyzed objects are shown together with the best fitting models and the plane of parameters (figure 3.6: PSR J1420-6048 PSR J1648-4611; figure 3.7: PSR J1702-4128, PSR J1718-3825, and PSR J2240+5832).

With the introduction of two additional free parameters ($g_{a\gamma\gamma}$ and m_a) we can re-fit the spectrum of PSR J2021+3651 and achieve with $\Delta\chi^2 = 41.2$. Upon closer inspection of the energy spectrum (figure 3.5 left panel), the improvement is a result of the apparent deviation of a smooth PowerLaw at an energy of about 2 GeV and a flux dropping off at higher energies modifying an exponential cutoff. Both features are well-described by the characteristic modulation of the photon-ALPs oscillation. We note that the shape of the modulation is directly linked to the strength of the transversal magnetic field and extension of the spiral arms traversed by the line of sight.

The effects of mixing are illustrated in figure 1.3, where the intensity of an unpolarized photon beam at energy 3 GeV and distance 10 kpc in the direction of PSR J2021+3651 is followed through the magnetic field of the intervening interstellar medium. For the favored coupling and mass, the photon intensity is reduced to roughly 60% of the initial value. The oscillation length is similar to the distance leading to a noticeable increase as well as a decrease of photon intensity along the line of sight.

When scanning the parameters of mass and coupling (figure 3.5 right panel), there are quite narrow minima in the plane of χ^2 which are aligned along the direction of larger coupling. Turning back to figure 1.3, this repetitive pattern is the result of multiple oscillations for larger values of the coupling along the line of sight. For decreasing coupling, the case of no-mixing is recovered. The local minima are adjacent to local maxima which lead to a tight constraint on the mass parameter.

Similar improvement to the goodness of fit ($\Delta\chi^2$) can be seen for the other five objects considered. The resulting best-fit parameters (including the re-fit spectral parameters) are listed in table 3.3. The favored mass range is similar among the objects to be around 3 neV with a coupling between 1.7 and 5.3 (in units of 10^{-10} GeV^{-1}). The improvement in χ^2, the resulting degrees of freedom for the individual spectra are listed in table 3.4.

The observed energy spectra and best-fit models for the other objects are shown in the appendix (figures 3.6 and 3.7). While for all spectra similar improvements are seen, there is an indication that the modulation in the spectra are very similar for objects which are

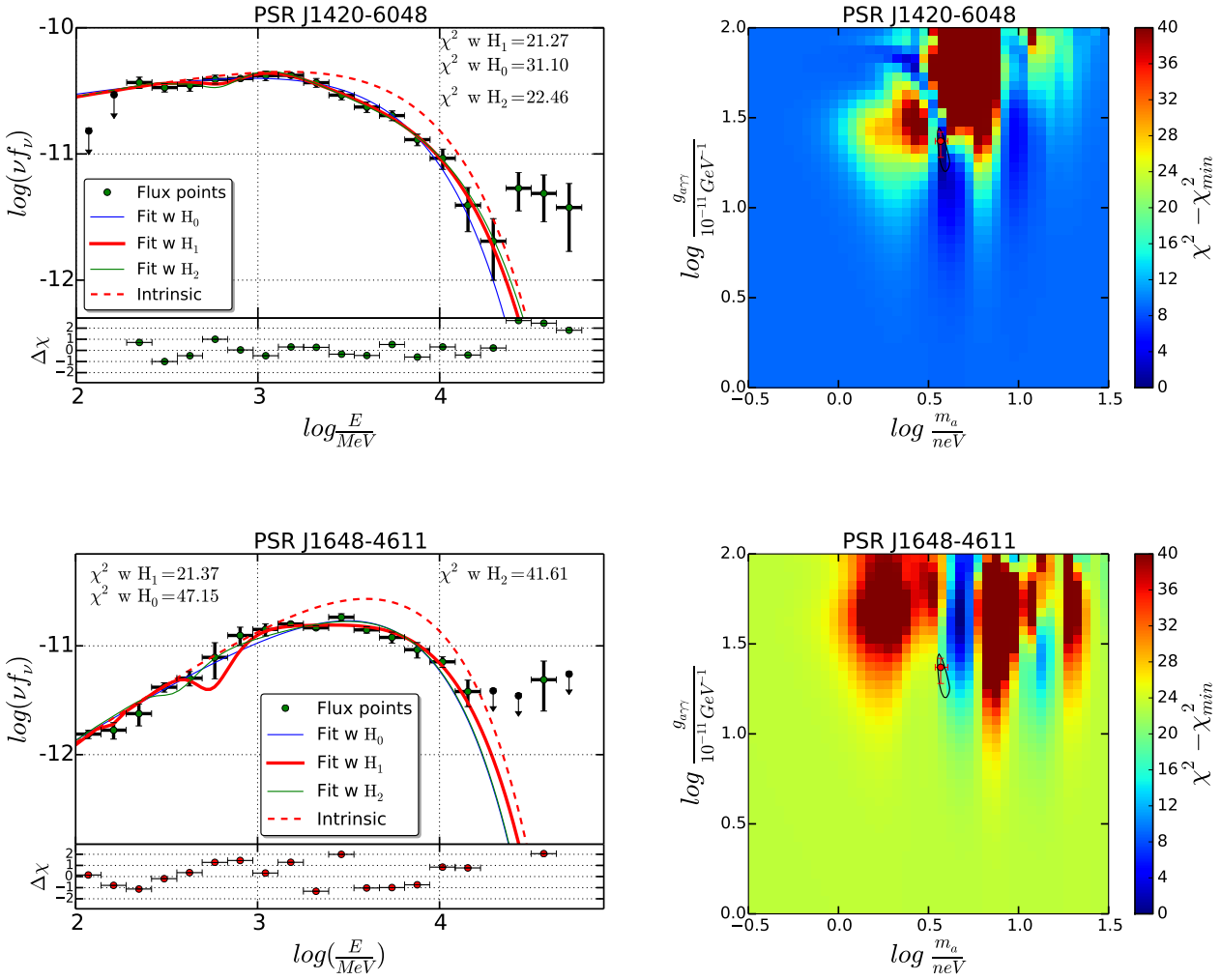

FIGURE 3.6: Upper panel: Spectrum and best-fit contour plot of PSR J1420-6048. Lower panel: Spectrum and best-fit contour plot of PSR J1648-4611. In the left column, the green points correspond to the energy flux points derived using Fermi-LAT binned analysis, blue line refers to the best fit model to the flux points H_0 hypothesis, whereas the red thick line and the green thin line follow the best fit model to the flux points with H_1 hypothesis and H_2 hypothesis respectively. $\triangle\chi$ values has been plotted in the bottom panel of each spectrum plot. In the right column, the best fit contour has been illustrated in the$(g_{a\gamma\gamma}, m_a)$ plane where, the lower values in the colorbar gives the best fit mixing region and the and the black region stands for the 2σ uncertainty combined contour.

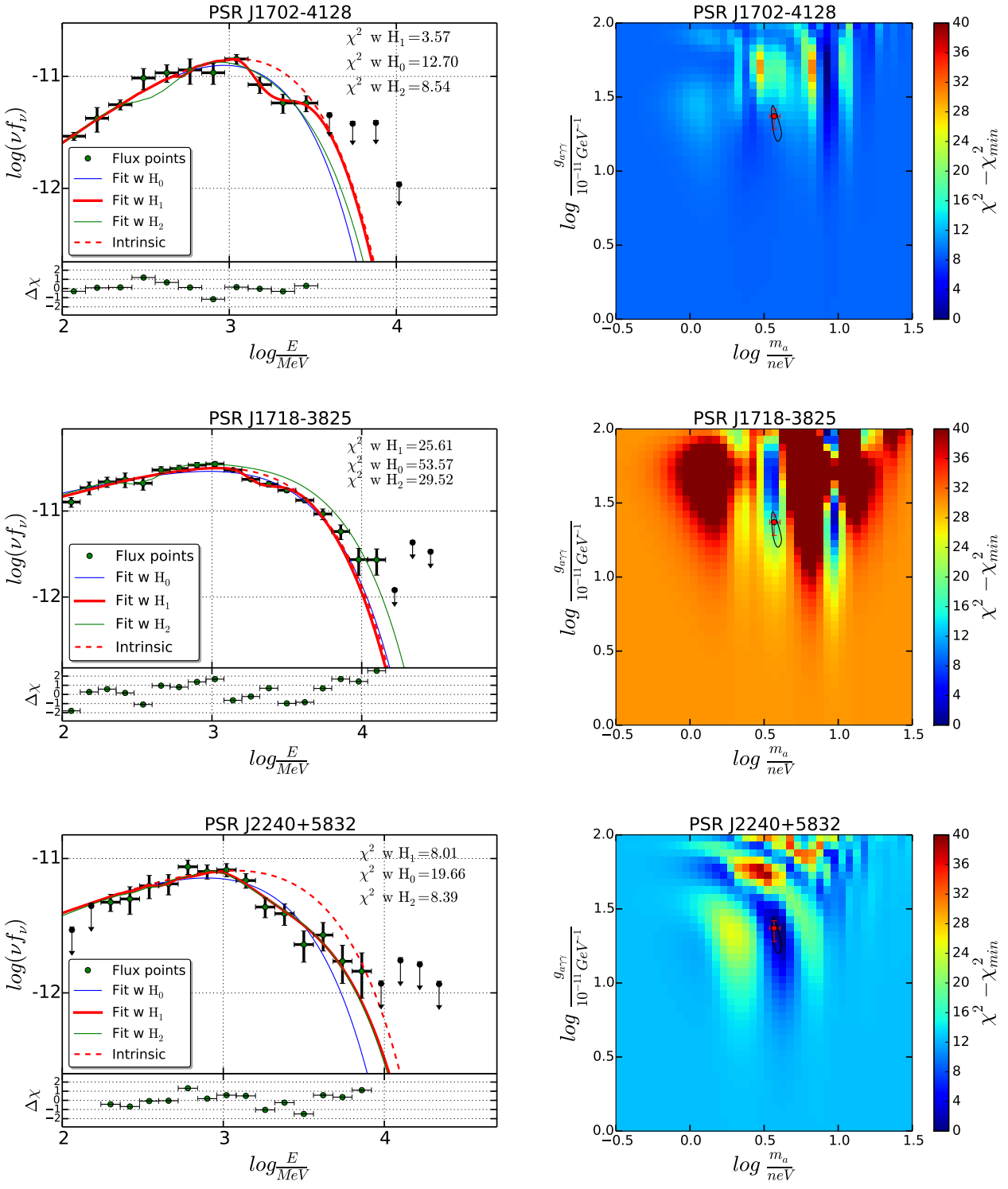

FIGURE 3.7: Same as figure 3.6 with different pulsar sources.

Pulsar name	$\chi^2(dof)$ H_0	$\chi^2(dof)$ H_1	Significance (H_1/H_0)	$\chi^2(dof)$ H_2
J1420-6048	31.10(15)	21.27(13)	1.38 σ	22.46(15)
J1648-4611	47.15(14)	21.37(12)	2.38 σ	41.61(14)
J1702-4128	12.70(8)	3.57(6)	2.01 σ	8.54(8)
J1718-3825	53.57(15)	25.61(13)	2.40 σ	29.52(15)
J2021+3651	51.25(14)	10.07(12)	3.86 σ	41.85(14)
J2240+5832	19.66(11)	8.01(9)	2.11 σ	8.39(11)
Combined	215.42(77)	89.9(65)	5.52 σ	152.37(75)

TABLE 3.4: A comparison of the χ^2 values obtained for the three hypotheses: H_0: no ALPs oscillation, H_1: ALPs oscillation with values of coupling and mass left free for individual sources, H_2: ALPs oscillation for a global estimate of coupling and mass. The significance is calculated using the excess variance technique (see section 3.4.2 for further details.

aligned in the same region of the Galaxy (e.g. PSR J2021+3651 and PSR J2240+5832, similarly the pair PSR J1702-4128 and PSR J1718-3825) (see section 3.7 for a discussion of this observation).

3.4.2 Significance level

In order to compute the significance level in table 3.4, we use the excess variance technique which is based upon the F-test for the two hypotheses: H_0, i.e. no-ALPs, see eq. 3.2 and H_1, i.e. photon-ALPs mixing included, see eq. 3.3. Assuming a sample size n, k and m parameters for hypotheses H_0 and H_1 respectively, we construct the following quantity:

$$f := \frac{(\chi^2_{\mathrm{H_0}} - \chi^2_{\mathrm{H_1}})/(m-k)}{\chi^2_{\mathrm{H_1}}/(n-m)} \sim F_{m-k,n-m}. \tag{3.4}$$

The quantity is distributed as the F-distribution with $m-k$ degrees of freedom for the summed squares in the nominator and $n-m$ degrees of freedom in the denominator. The significance of the result has been estimated to be 5.52σ for the combined sample (H_1). We list the corresponding values for the other pulsars as well as for the combined data in table 3.4. We also consider the hypothesis H_2, where we carry out a χ^2-minimization of all spectra with a common value of $g_{a\gamma\gamma}$ and m_a. For this case, the overall fit deteriorates and the resulting χ^2 value is shown in table 3.4, the significance for this hypothesis is 4.6σ using eq. 3.4 (see also discussion in section 3.7).

3.4.3 Combined fit and parameter estimate

After we have established that the ALPs-hypothesis provides a significantly better description of the data, we continue and estimate the best-fitting ALPs-related parameters

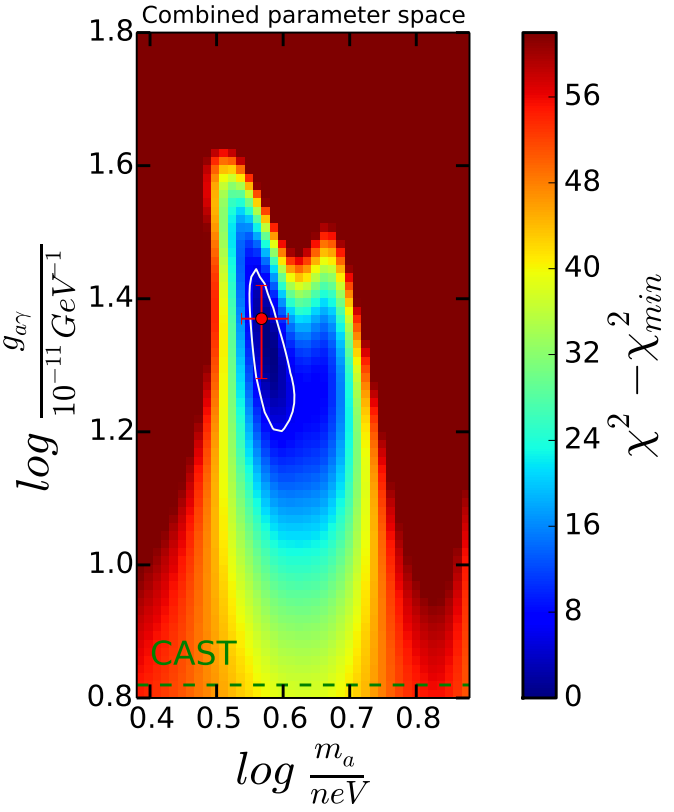

FIGURE 3.8: Significance map of combined χ^2 analysis for the pulsars. The white marked region in the $(g_{a\gamma\gamma}, m_a)$ plane indicates the photon-ALPs mixing contour with 95% confidence level. The red point with the uncertainty refers the minimum position in the ALPs parameter space and projected uncertainties with 68% confidence level. Green horizontal line represents the upper limit on the photon-ALPs coupling strength $g_{a\gamma\gamma}$ of the CERN Axion Solar Telescope (CAST) [109].

(mass and coupling) by summing the individual $\Delta\chi^2$ planes of the six source spectra. The result is shown in figure 3.8. We find for the best estimate of the coupling $g_{a\gamma\gamma} = (2.3^{+0.3}_{-0.4}) \times 10^{-10}\text{GeV}^{-1}$ and ALPs mass $m_a = (3.6^{+0.5}_{-0.2})$ neV. The $2\,\sigma$-uncertainty contour is marked by the white line in the same figure.

3.5 Mixing contour dependence on distance and magnetic field

We estimate the systematic uncertainties related to the magnetic field strength and the uncertainties of the distance. Firstly, for the pulsar J2021+3651 we have seen the mixing parameters highly depend on the Jansson & Farrar magnetic field spiral arms. As it's very close to the fifth spiral arms, the photon-ALPs coupling constant and ALPs mass changes a lot with the change in the intensity of this spiral arm, whereas it does not effect so much with the intensity change in other arms. We modify the magnetic

field within the quoted uncertainties of the respective model, in order to understand the effect of its variation on our mixing contours. With an increase of 20% of the magnetic field along the line of sight, the coupling constant is reduced by 20% changing from $3.5 \times 10^{-10}\,\mathrm{GeV}^{-1}$ to $2.8 \times 10^{-10}\,\mathrm{GeV}^{-1}$ (see figure 3.9). Similarly, 40% enhancement in the magnetic field intensity brings the coupling constant even lower. In both cases, χ^2 decreases slightly which implies that the overall fit favors an increased Galactic magnetic field.

For PSR J2021+3651, the effect of the distance uncertainty is most pronounced. Given the rather large uncertainty on the distance, the object is located either in front of or even behind the fifth spiral arm. Reducing the distance by 4 kpc, we obtain a change $\approx 2.4 \times 10^{-10}\,\mathrm{GeV}^{-1}$, corresponding to around 70% enhancement in $g_{a\gamma\gamma}$, while the ALPs mass increases by 0.86 neV. When increasing the distance by 2 kpc, instead, $g_{a\gamma\gamma}$ changes by 24%, i.e., $g_{a\gamma\gamma} \sim 2.7 \times 10^{-10}\,\mathrm{GeV}^{-1}$ and the mass varies around 1 neV. The corresponding spectral fits associated with this analysis are shown in figure 3.10 in the appendix. In order to estimate the uncertainties related to the estimate of the global parameters for mass and coupling, we increase the magnetic field by 20 % for all sources and increase the distance within the uncertainties. The resulting best-fit values are used to estimate the systematic uncertainties to be for mass $m_a = (3.6^{+0.5_{\mathrm{stat.}}}_{-0.2_{\mathrm{stat.}}} \pm 0.2_{\mathrm{syst.}})$ neV and $g_{a\gamma\gamma} = (2.3^{+0.3_{\mathrm{stat.}}}_{-0.4_{\mathrm{stat.}}} \pm 0.4_{\mathrm{syst.}}) \times 10^{-10}\ \mathrm{GeV}^{-1}$.

Again, in the individual pulsar contour plots, we see some pattern follows. Pulsars J2021+3651 and J2240+5831 follow almost same contour pattern while the others make approximately line countour pattern. This behaviour can be interpreted in terms of pulsar position. In the figure 3.1, we see the pulsars J2021+3651 and J2240+5831 sit on the other side of the Galactic center almost in a same distance to us. Hence, the photons emitted by these two sources have to traverse through the same spiral arms making similar types of photon-ALPs phenomenology. The rest of the four sources are located near to the Galactic center and the transversal Galactic magnetic field intensity along the line of site is not so high for them. As a result, they end up with creating narrow and similar type of contour.

3.6 Spectral modulation for Pshirkov magnetic field

For the magnetic field we assume large scale galactic magnetic field models based on Faraday rotation measurements. In the framework of ALPs/photon oscillation, the resulting parameters strongly depend upon the chosen magnetic field model. For our analysis, we use mostly accepted Jansson and Farrar model (see appendix B), where the central part of the Galaxy does not contain adequate information. The Galactic spiral

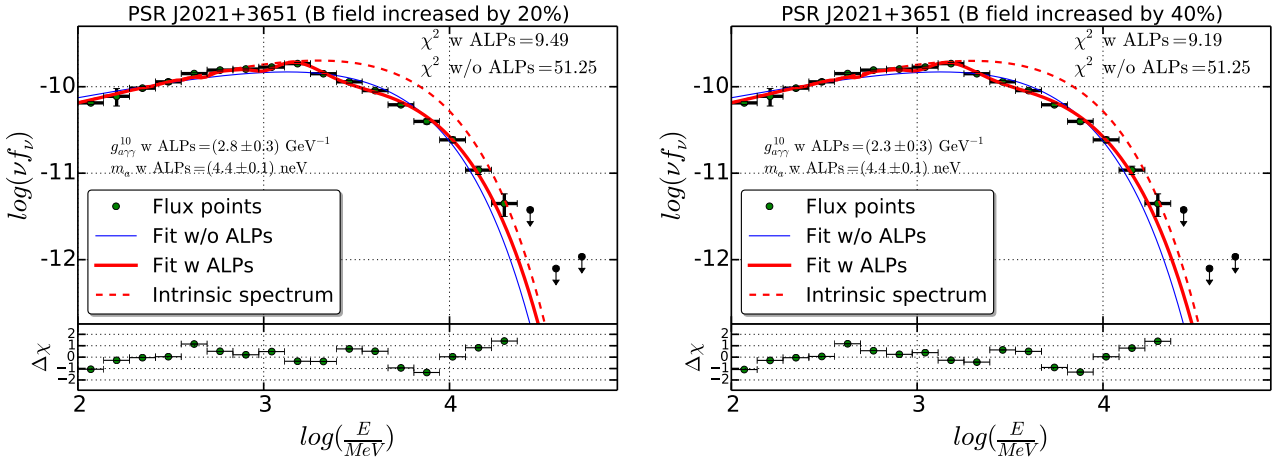

FIGURE 3.9: Variation of $g_{a\gamma\gamma}$ and m_a with the change in Galactic magnetic field intensity. Left panel: The ALPs parameters are derived if we increase the magnetic field intensity by 20%. Right Panel: the fitting corresponds to the magnetic field intensity increased by 40% which reduces the $g_{a\gamma\gamma}$ by 33.8% whereas m_a remains the same. (note, $g_{a\gamma\gamma}^{10}$ is given in units of 10^{-10} GeV^{-1})

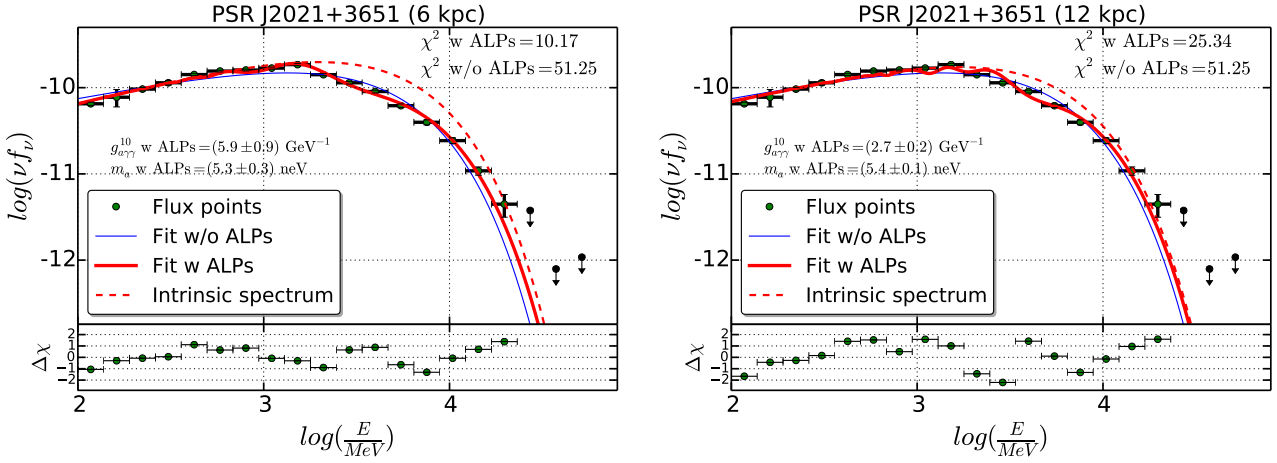

FIGURE 3.10: Pulsar spectra with the variation in the dintance to the source. In the left: pulsar spectrum are derived for a distance of 6 kpc while, in the right panel: the spectrum corresponds to the distance of 12 kpc respectively. (note, $g_{a\gamma\gamma}^{10}$ is given in units of 10^{-10} GeV^{-1})

TABLE 3.5: The variation of ALPs parameters calculated assuming diffrent Bfield and different distance for the global analysis.

Global analysis	$g_{a\gamma\gamma}$ (in $\times 10^{-10}\mathrm{GeV}^{-1}$)	m_a (in neV)
Bfield increased by 20%	2.1(4)	3.7(3)
Bfield decreased by 20%	2.6(2)	3.4(3)
Distance increased by 1kpc	2.3(4)	3.7(3)
Distance reduced by 1kpc	2.6(3)	3.6(3)
Distance increased by 1kpc and Bfield 20% increased	1.9(3)	3.7(3)
Distance reduced by 1kpc and Bfield 20% de creased	2.7(4)	3.6(3)

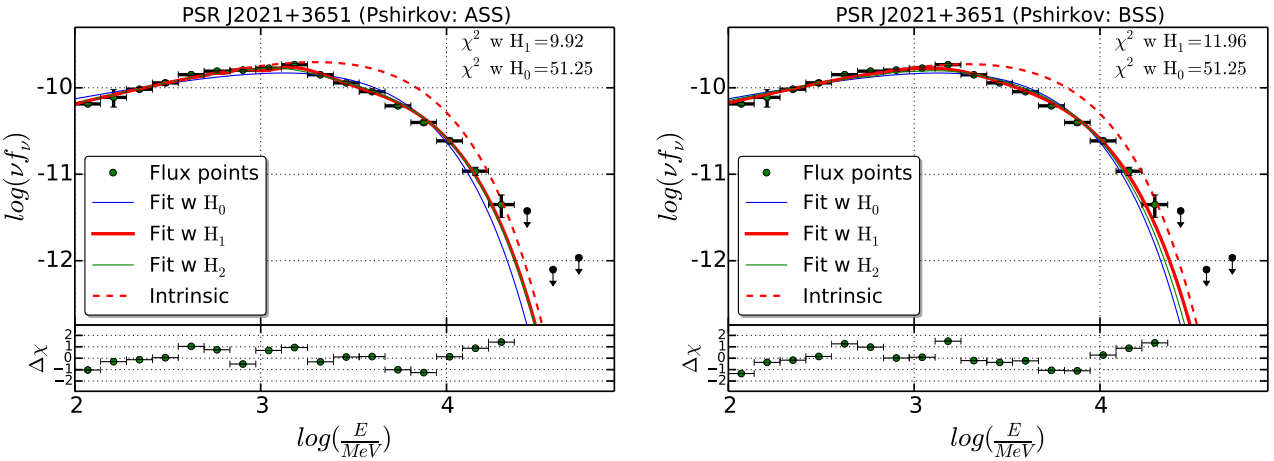

FIGURE 3.11: Spectral fit for the pulsar J2021+3651 taking into account the Galactic magnetic field model of Pshirkov.

arms structure is also not continious exhibiting more discrete pattern. To verify our analysis, we again try to follow the our analysis with different Galactic magnetic field model i.e. Pshirkov model [110]. We find a sufficient improvement in the gamma-ray spectral fit in accordance with the ALPs parameters over null hypothesis. With both the two version of the Pshirkov model (axisymmetric, or ASS model and bisymmetric, or BSS model), the χ^2 per dof gets imporved presenting an acceptable fit. Regarding H_1 hypothesis, we conclude the ALPs parameters to be $g_{a\gamma\gamma} = (6.2 \pm 0.2) \times 10^{-10}\mathrm{GeV}^{-1}$ and $m_a = (4.3 \pm 0.2)$neV (for Pshirkov ASS model); $g_{a\gamma\gamma} = (1.6 \pm 0.1) \times 10^{-10}\mathrm{GeV}^{-1}$ and $m_a = (3.8 \pm 0.2)$neV (for Pshirkov BSS model). The results for PSR J2021+3651 has been illustrated in the figure 3.11.

3.7 Comparison of resultant mixing contour with existing ALPs hints and constraints

We study for the first time modulations in the gamma-ray spectra of bright Galactic pulsars induced by photon-ALPs mixing in the Galactic magnetic field. With the *Fermi*-LAT dataset of nine years from six different pulsar candidates selected according to their location in the Galaxy and brightness, we investigate the presence of the spectral irregularities. We find an indication (at the 4.6σ-level, H_2) for the presence of spectral irregularities, absent in the nearby bright Vela pulsar. While the spectral variations are as large as $20\,\% - 40\,\%$, the maximum systematic relative flux uncertainties found for the Vela spectrum is 2.4 %.
In the combined analysis, we estimate $g_{a\gamma\gamma} = (2.3^{+0.3_{\text{stat.}}}_{-0.4_{\text{stat.}}} \pm 0.4_{\text{syst.}}) \times 10^{-10}$ GeV^{-1} and $m_a = (3.6^{+0.5_{\text{stat.}}}_{-0.2_{\text{stat.}}} \pm 0.2_{\text{syst.}})$ neV. We note, that the combined data-set is not well-described by a fixed value of photon-ALPs coupling and mass (table 3.4, marked as H_2). The differences of the mass, coupling for individual lines of sight (table 3.3) are similar but not consistent within the statistical uncertainties. Mass and coupling should be unified for all lines of sight. However, we do have limited knowledge about the magnetic field structure, especially for the sources which are located in the inner part of the Galaxy (see figure 3.1) - we also note that the crucial opening angle of the spiral arms is not well constrained. The magnetic field models are derived on the basis of Faraday-rotation measures which are sensitive only to the longitudinal magnetic field which is not of relevance for photon-ALPS coupling. Additionally, in the inner Galaxy the structure of spiral arms is not well resolved and unknown magnetic field components could be present. We note that the good fit of the model with slightly varying values of mass and coupling does indeed produce an acceptable fit (hypothesis H_1 marked in table 3.4).

The favored 2σ contour derived from this analysis is compared with the other existing results in figure 3.12. The best-fit parameters are well consistent with the lower-limit analysis related to the TeV transparency [103] as well as the a similar analysis marked CIBER [112]. There is no obvious conflict with the constraints derived from searches for irregularities in gamma-ray spectra from PKS 2155 (HESS [113]) and NGC1275 (*Fermi*-LAT [102]). At a first glance, the non-observation of a prompt gamma-ray signal from SN1987 [114] and the limit from the CAST helioscope [109] are in tension with the signal observed here. It is however important to note that the interstellar environment where the conversion takes place could provide possible explanation to this phenomenon.

We also note that the signal is well within reach of the upcoming ALPS-II light shining through wall experiment [115]. The International Axion Observatory (IAXO) [116], the

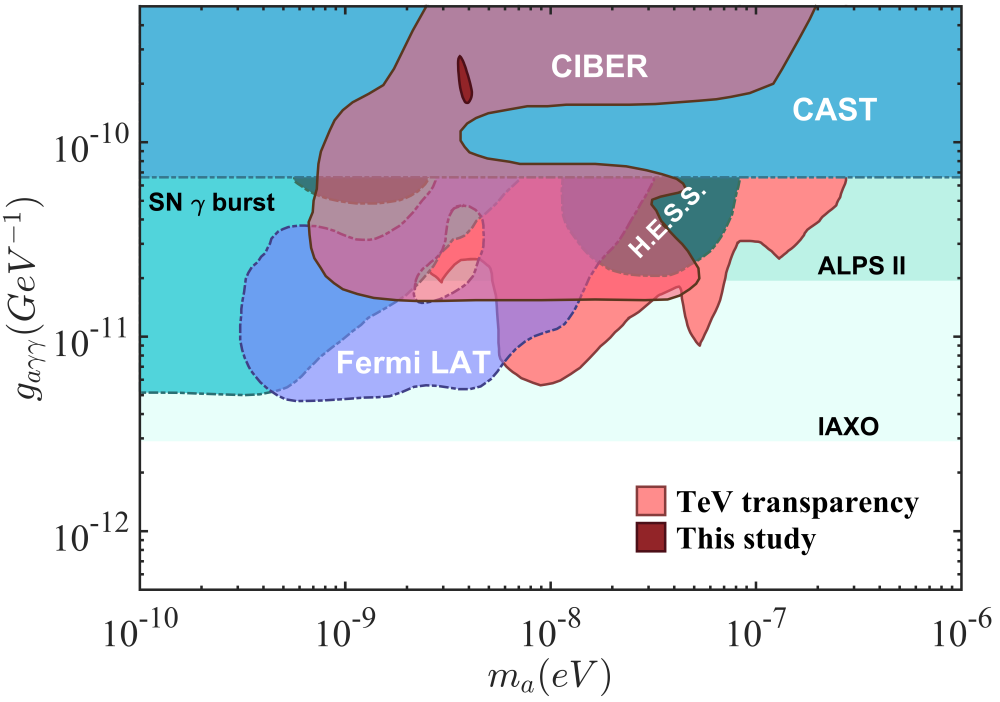

FIGURE 3.12: Limits on ALPs parameter space in the $(m_a, g_{a\gamma\gamma})$ plane [111]. The parameter space surrounded by solid lines present the hints from ALPs. The horizontal light sky blue bands are shown as the sensitivity of ALPS-II and IAXO experiments. The regions enclosed by dotted lines and different shades in blue represent the constraints on ALPs contour given by different observations and experiments. The brown-shaded contour represents the parameters estimated from pulsar spectra as found by the present analysis.

next generation axion helioscope experiment also coincides with the sensitivity region, what we achieved.

On the other hand, we have seen that the Galactic magnetic field has not been well constrained i.e. the uncertainties related to the Galactic magnetic field spiral arms varies in kpc range. Our analysis is very much magnetic field model dependent. It will be possible to reduce the uncertainties of the magnetic field with full sky polarization survey, enabling a more precise determination of the magnetic field.

Since the objects observed are pulsars, there may be a source intrinsic effect (even though the Vela pulsar does not show any modulations). In a recent study of the extended Galactic supernova remnant IC433, a similar type of analysis was carried out with consistent results [117] which strengthens the case for an explanation which is not related to the source or its emission process.

At present, we have not been able to identify a known propagation effect which could lead to a similar type of spectral modulation. The analysis presented here can be easily extended to the other sources in our galaxy. In the next chapters, we made an attempt to extend the analysis for the other Galactic plane sources (e.g. pulsars as well as other astrophysical sources) along with the non-galactic plane sources.

Chapter 4

ALPs phenomenology on the Galactic plane sources

Several surveys of the Galactic sources have been performed with gamma-ray telescopes at MeV to TeV energies. The Fermi large area telescope has been able to detect different classes of astrophysical sources like, pulsars, supernova remnants, molecular cloud etc. In this chapter we report on the observation and the energy spectrum of the few bright Galactic plane objects. We also discuss about the energy dependent suppression of each source due to photon-ALPs mixing.

4.1 Source selection

We have selected the brightest 40 sources from the Fermi 3FGL catalog [77] in the region of Galactic latitude b [-10°$< b <$ 10°]. The selected sources have been shown in the fig.4.1. To observe the photon-ALPs mixing implications, the Galactic plane bright sources play an important role as the mixing can occur in the comparatively high magnetic field region (mostly the Galactic spiral arms) of the Galactic disk. The type of the sources have been determined from the SIMBAD source catalog and the distance are unknown in case of most of the sources. We list all the sources in the table 4.1, 4.2 and 4.3 according to their parametrization models.

4.2 Data Analysis

For the analysis, the nine years of Fermi-LAT data have been used for a energy range of 100 MeV to 300 GeV. We have followed the same technique for data analysis as described

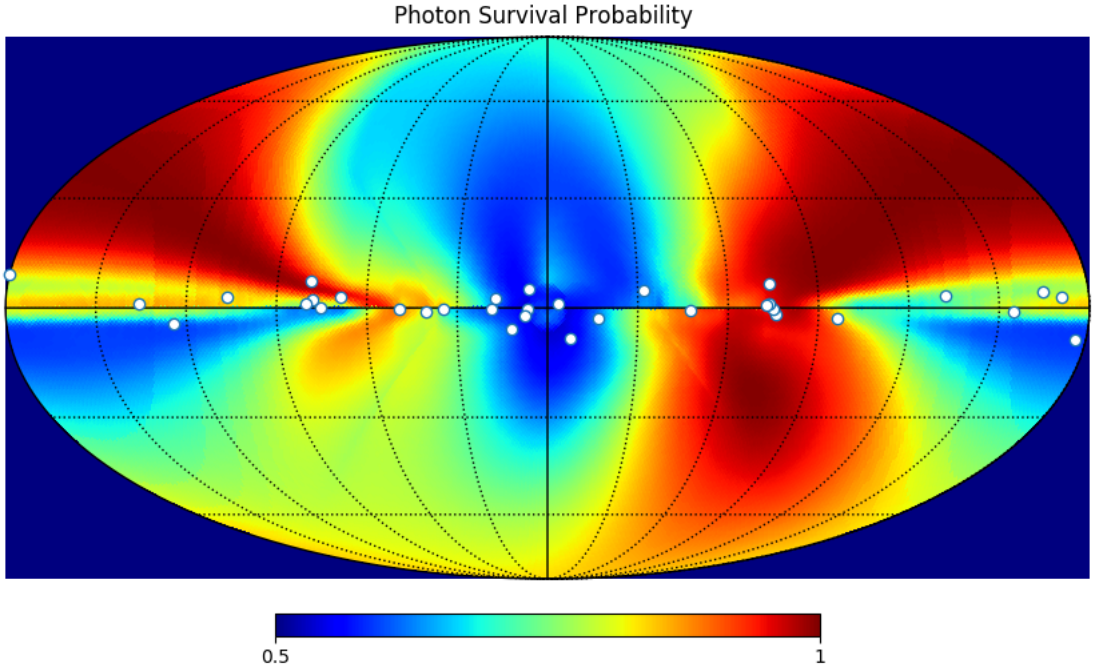

FIGURE 4.1: An all sky map of photon survival probability for photon-ALPs oscillation in the Milky way. The colormap denotes the survival probability at a distance of 15 kpc, photon-ALPs coupling constant of $1.5\times10^{-10}\text{GeV}^{-1}$ and ALPs mass of 1.5 neV. The small white circles are the Galactic plane sources listed in table 4.1, 4.2 and 4.3.

Source name	l_{II} [°]	b_{II} [°]	source type
J0633.7+0632	205.09	-0.92	pulsar
J0633.9+1746	195.13	4.27	pulsar
J1057.9-5227	285.98	6.64	pulsar
J1413.4-6205	312.37	-0.72	pulsar
J1709.7-4429	343.09	-2.68	pulsar
J1732.5-3130	356.31	1.01	pulsar
J1741.9-2054	6.41	4.89	pulsar
J1809.8-2332	7.38	-2.00	pulsar
J1813.4-1246	17.24	2.44	pulsar
J1826.1-1256	18.55	-0.38	pulsar
J1907.9+0602	40.18	-0.90	pulsar
J1952.9+3253	68.78	2.82	pulsar
J2021.5+4026	78.23	2.08	pulsar
J2032.2+4126	80.21	1.01	Be-star
J2229.0+6114	106.65	2.95	pulsar

TABLE 4.1: Selected number of very bright Galactic plane sources. The energy spectra of these sources have been modelled with a PLExpCutoff parametrization. The table contains the Galactic longitude (l), Galactic latitude (b) and the source types.

Source name	l_{II} [°]	b_{II} [°]	source type
J0102.8+5825	124.42	-4.41	Quasar
J0240.5+6113	135.67	1.08	High Mass X-ray Binary
J0730.2-1141	227.76	3.13	Quasar
J1801.3-2326e	6.52	-0.25	SuperNova Remnant
J1802.6-3940	352.44	-8.42	Blazar
J1833.6-2103	12.16	-5.70	Quasar
J1855.9+0121e	34.65	-0.38	SuperNova Remnant
J1923.2+1408e	49.116	-0.46	SuperNova Remnant

TABLE 4.2: Selected number of very bright Galactic plane sources. The energy spectra of these sources have been modelled with a LogParabola parametrization. The table contains the Galactic longitude (l), Galactic latitude (b) and the source types.

Source name	l_{II} [°]	b_{II} [°]	source type
J2001.1+4352	23.98	-23.14	BL Lac type object
J2201.7+5047	97.64	-3.54	Gamma-ray source

TABLE 4.3: Selected number of very bright Galactic plane sources. The energy spectra of these sources have been modelled with a normal PowerLaw parametrization. The table contains the Galactic longitude (l), Galactic latitude (b) and the source types.

in the section 3.2 except the parametrization of the sources. According to the modelling of source spectrum, we categorize the sources into three types:

- Few sources are modelled with PLExpCutoff describes as,

$$\frac{dN}{dE} = N_0 \left(\frac{E}{E_0}\right)^{-\Gamma_1} \exp\left(-\frac{E}{E_{\text{cut}}}\right) \tag{4.1}$$

  Mostly, the sources are modelled according to eq. 4.1 are pulsars.

- Few of sources are modelled with LogParabola describes as,

$$\frac{dN}{dE} = N_0 \left(\frac{E}{E_0}\right)^{(\alpha+\beta log(E/E_0))} . \tag{4.2}$$

  This parametrization is typically used for modeling blazar spectra.

- Rest of the sources are modelled with simple PowerLaw written as,

$$\frac{dN}{dE} = N_0 \left(\frac{E}{E_0}\right)^{\Gamma} . \tag{4.3}$$

Where, N_0 is the normalization factor and E_0 is the scale energy. We also perform a fit to the spectral data point to determine the best fit ALPs parameters.

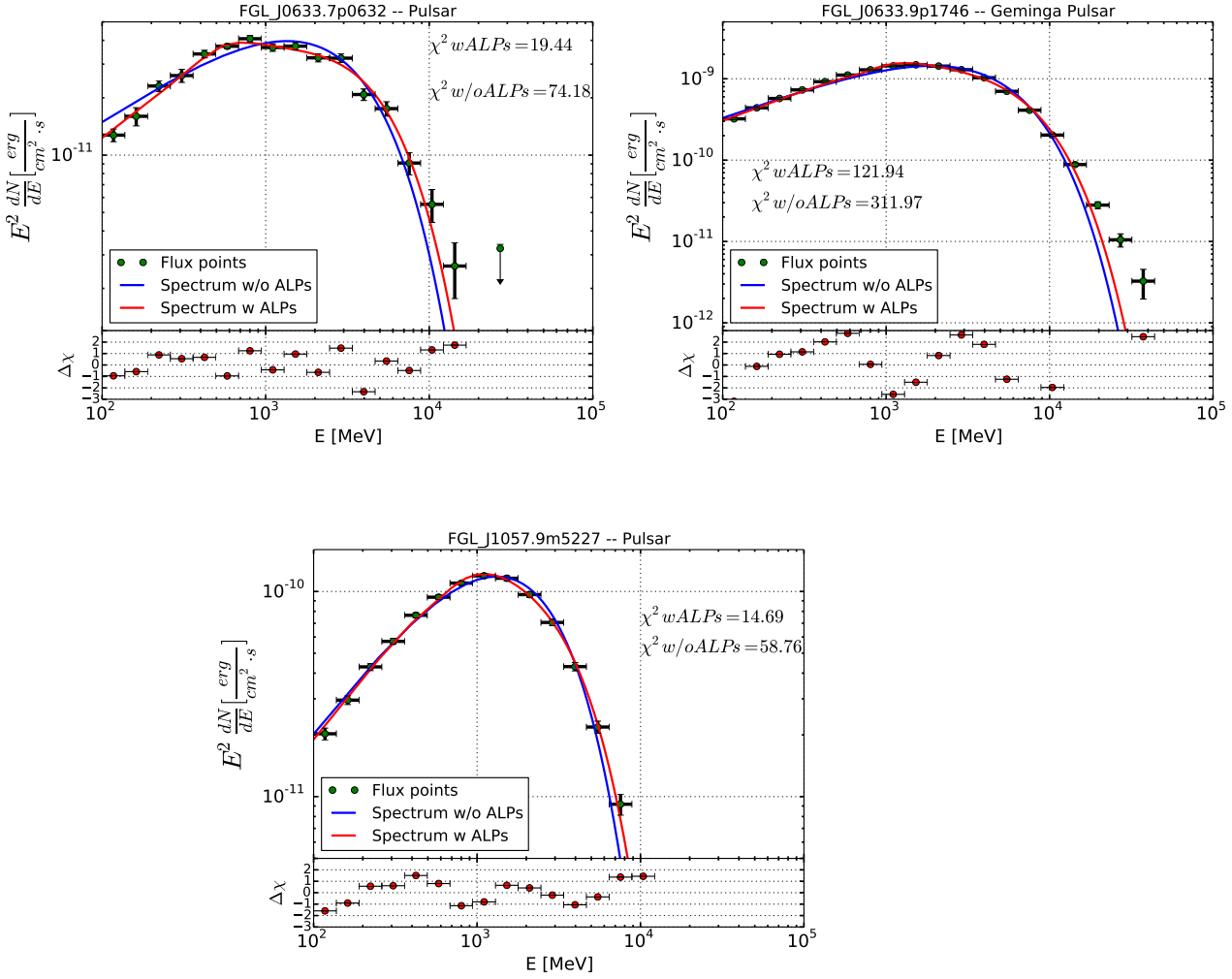

FIGURE 4.2: Energy spectrum for Pulsar sources. Green points correspond to the flux points from each energy bins. Blue line denotes the fitted spectrum without ALPs parameters and the red line is the best fit spectrum including $g_{a\gamma\gamma}$ and m_a.

4.3 Individual Source spectrum

According to the parametrization modelling, a brief overview has been given for each source in the following sections 4.3.1, 4.3.2 and 4.3.3. The choice of parametrization for the spectra is strongly related to the observational point of view.

4.3.1 Sources with PLExpCutoff modelling

We have chosen the parametrization in the similar way that has been illustrated in the Fermi 3FGL article [77] [1]. Almost all the sources that has been parameterized with

[1] https : //fermi.gsfc.nasa.gov/ssc/data/access/lat/4yr_catalog/3FGL_Table4_full.pdf

PLExpCutoff model are pulsars. We provide a brief description for most of the sources which fall in this category as follows:

J0633.7+0632 This is a radio-quiet Fermi pulsar with a period (P) = 297 ms and a characteristic age of 59 kyr [118]. Chandra observations revealed that the pulsar is associated with the pulsar wind nebula (PWN) [119]. In a detailed study with the Chandra observation, the distance to the pulsar is constrained in a range of 1–4 kpc from the spectral fits [120]. Later on, the results from XMM-Newton observations for this pulsar confirm a non-thermal PowerLaw and a thermal component to be presented in this PWN composite and the distance to be constrained to be 0.7–2.2 kpc [121]. The gamma-ray spectrum has been shown in the figure 4.2.

J0633.9+1746 This is the well known Geminga pulsar, a very strong gamma-ray source from the constellation Gemini [122]. It was later detected in X-ray [123] and optical wavelengths [124]. The deepest X-ray investigation of the Geminga pulsar has revealed a PWN associated to it [125]. The PWN composite shows a rapid variation of half light-year long tail as an extension of the jet at a rate of 20% of light speed. A smooth gamma-ray spectra has been shown in the figure 4.2.

J1057.9-5227 This gamma- ray pulsar, has been found in a blind search with Fermi-LAT six years data, located very close to the Galactic plane. With a characteristic age of 535 kyr, this pulsar appears to be a radio-loud pulsar [126] (see the gamma-ray spectrum in the figure 4.2).

J1413.4-6205 PSR J1413.4-6205 is located at a distance of 1.4 kpc with a characteristic age of 63 kyr [126] appears to be a radio-quiet pulsar. This very energetic pulsar has clearly a counterpart associated to an EGRET source named EGR J1414-624 [127].

J1709.7-4429 It is a strong gamma-ray point source appears to be a MeV-GeV counterpart of a TeV PWN TeV J1708-443 detected with the AGILE [128]. This pulsar has an age of 17 kyr and it seems to be a radio-loud pulsar confirmed from the observation [126].

J1732.5-3130 This gamma- ray pulsar also has been found in a blind search with Fermi-LAT six years data appears to be a radio-quiet pulsar with a characteristic age of 111 kyr [126]. The gamma-ray spectrum is shown in the figure 4.3.

J1741.9-2054 PSR J1741.9-2054, located at very close to the Galactic center (within $15^\circ \times 15^\circ$ region about the direction of the GC 15 ROI) [129], appears to be a radio-loud pulsar [126]. This is a very old pulsar with the age of 386 kyr.

J1809.8-2332 Similar to PSR J1741.9-2054, J1809.8-2332 is also located within 15° ROI to the Galactic center [129]. Apart from gamma-ray observation, this source appears to be one of the brightest X-ray source. Chandra images of this region reveal a point X-ray

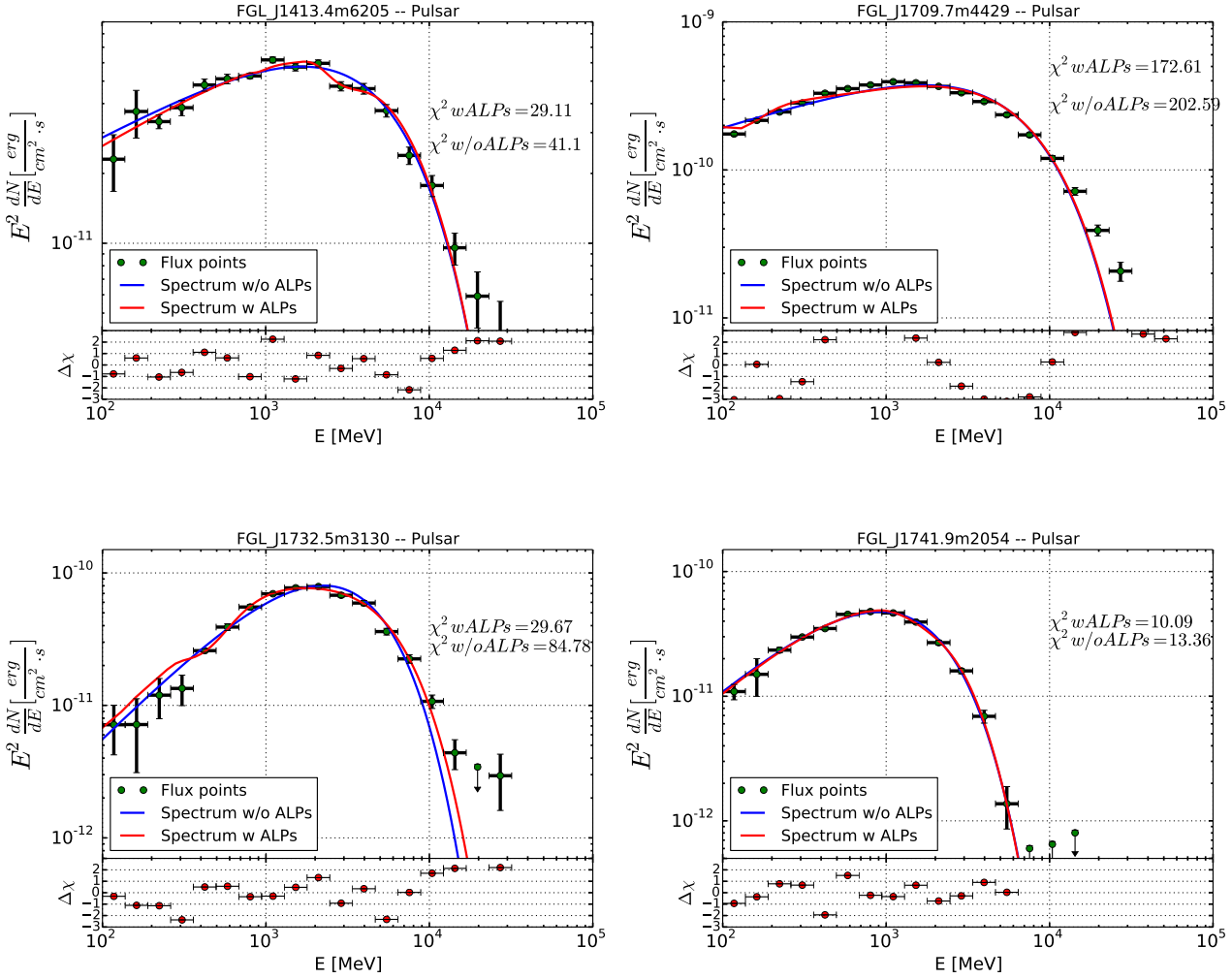

FIGURE 4.3: Similar to the figure 4.2 with different pulsar sources.

source connected to a non-thermal X-ray/radio nebula [130]. The X-ray point source is very much associated to the pulsar wind nebula [131] (see the HE part of the gamma-ray spectrum in the figure 4.4). This pulsar has a characteristic age of 68 kyr.

J1813.4-1246 This pulsar, with the highest spin-down luminosity, has been one of the first 16 blind search pulsars discovered with the LAT. The bright X-ray source, Swift J181323.4-124600, was noted as the counterpart to this pulsar [119]. Distance of this pulsar is still unknown. In particular, the average observed radio-loud pulsar is younger than the radio-quiet one and is located at smaller Galactic latitude. From the observational point of view, this pulsar seems to be a radio-quiet one [132].

J1826.1-1256 The pulsar PSR J1826-1334 (previously known as PSR B182313) was detected in the radio regime within the Jodrell Bank observatory 1400 MHz survey. It has

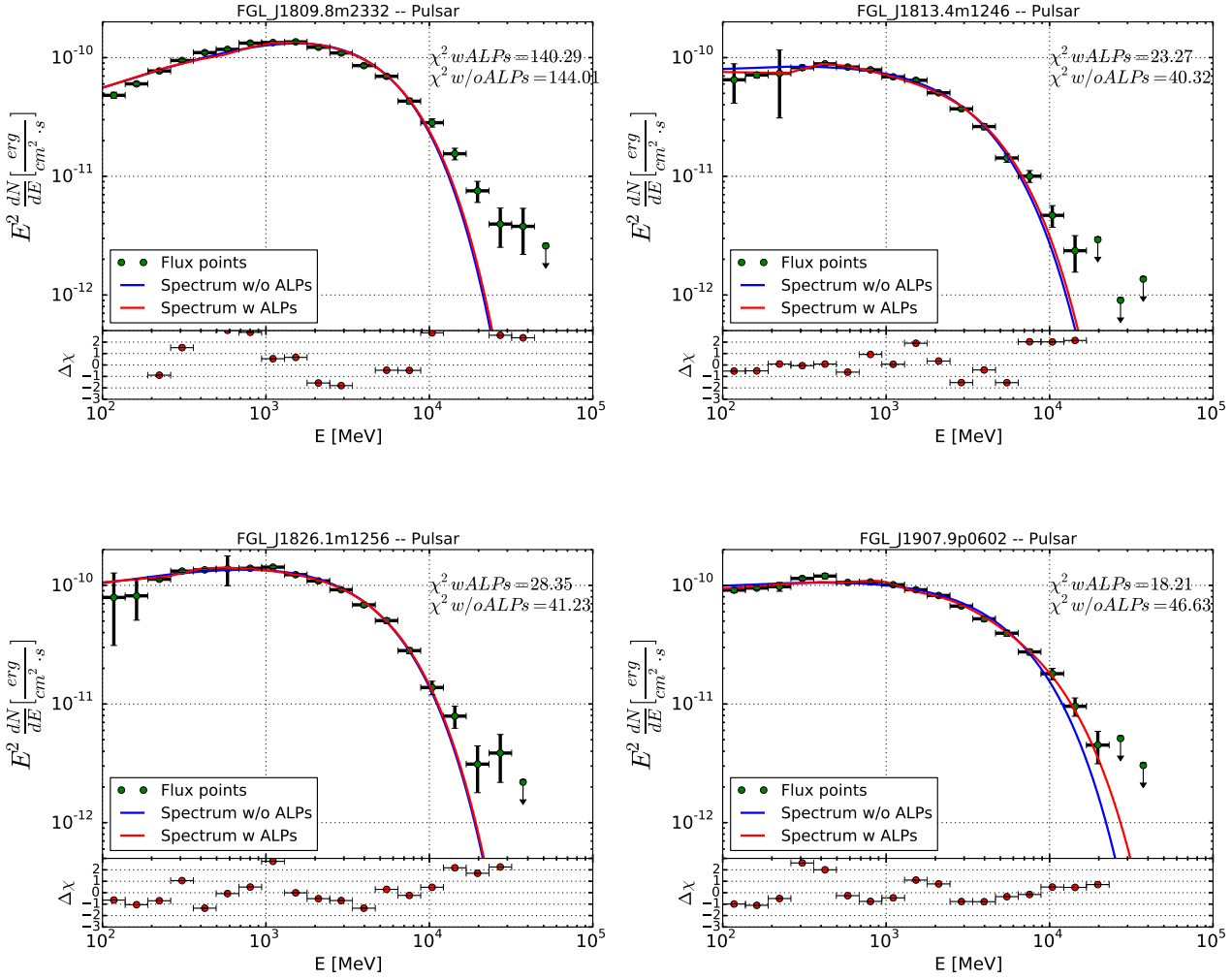

FIGURE 4.4: Similar to the figure 4.2 with different pulsar sources.

the characteristic age of 21.4 kyr and the current spin-down luminosity of $2.8 \times 10^{36} \text{ergs}^{-1}$. The distance to the pulsar was estimated based on the dispersion of the radio pulses to be 4.12 kpc. Measurements with VLA revealed a shell or a pulsar wind nebula in the vicinity of PSR J1826-1334 [133] (also see the HE part of the gamma-ray spectrum in the figure 4.4). There is a HESS source associated to the pulsar named as HESS J1825-137 [133] has been observed with the H.E.S.S. Galactic plane survey in 2004 [134].

J1907.9+0602 The TeV source MGRO J1908+06 is a steady powerful TeV pulsar wind nebula of PSR J1907+0602 with an integrated luminosity over 1 TeV 1.8 times the luminosity of the Crab Nebula [135]. This pulsar is pulsating with a period of 106.6 ms. The dispersion measurement with radio pulsations with the Arecibo telescope at 1.5 GHz reveals the distance to the pulsar is to be 3.2 ± 0.6 kpc [136] . The implied distance to the pulsar is compatible with that of the supernova remnant G40.50.5 associated to

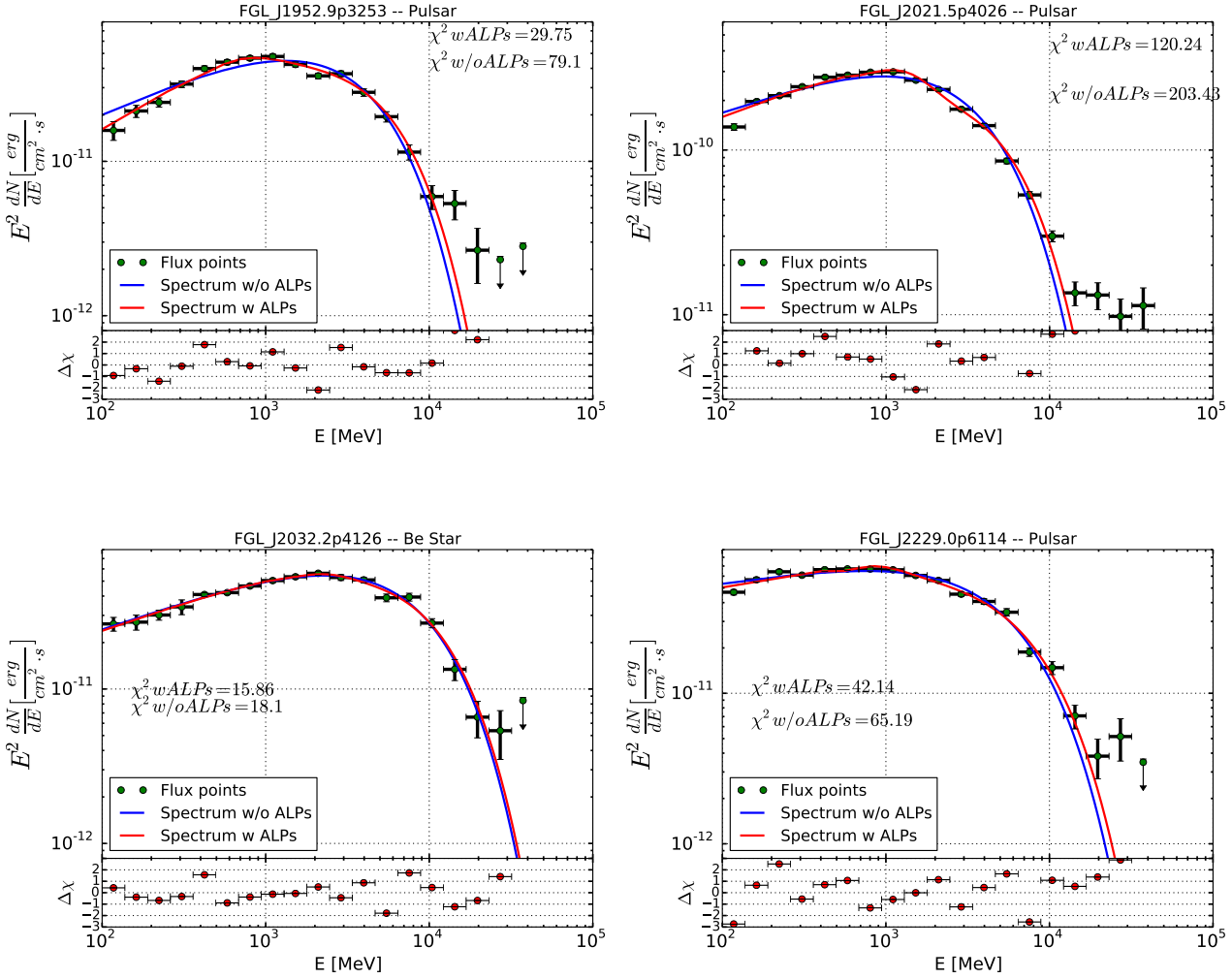

FIGURE 4.5: Similar to the figure 4.2 with different pulsar sources.

pulsar, located on the far side of the TeV nebula from PSR J1907+0602 while the S74 molecular cloud located on the nearer side.

J1952.9+3253 PSR J1952.9+3253, located very close to the Galactic plane with a characteristic age of 107 kyr has been appeared to be a radio-loud pulsar [126].

J2021.5+4026 PSR J2021+4026, previously identified as an X-ray source with XMM-Newton (2XMM J202131.0+402645), is located in the Gamma Cygni region appearing to be a Geminga-like pulsar [137]. Its spin frequency is 3.8 Hz and the characteristic age is about 77 kyr making it to be a young energetic pulsar. Although the radio and the optical searches of this pulsar became unsuccessful to find any counterparts, a deep X-ray observation with Chandra and XMM-Newton found an association with X-ray

source S20 [138]. J2021+4026 is seen within the radio shell of the supernova remnant (SNR) G78.2+2.1 [139] (see the gamma-ray spectrum in the figure 4.5).

J2032.2+4126 PSR J2032+4127 is a radio-loud gamma-ray pulsar which is orbiting around a high-mass Be type star LS2883. It's orbital period is very long, nearly 25 to 50 years [140]. This composite is similar to a gamma-ray binary system. A rapid increase in the X-ray flux has been observed with the Swift data in this system. This enhancement in the high-energy emission could be a result of an interaction between the pulsar wind and the Be-star disk. The electrons-positrons in the pulsar wind are accelerated with the shock producing non-thermal emissions from radio wavelength to TeV gamma-ray range. In a detailed way, the synchrotron radiation and the inverse-Compton scattering (ICS) process produces radio/X-ray emission and TeV gamma-ray emission for the composite [140]. The Fermi-LAT gamma-ray spectrum is depicted in the figure 4.5.

J2229.0+6114 More than a decade ago, this pulsar has been observed in radio and X-ray with ROSAT and ASCA observations at a period of 51.6 ms and had also been found associated with the EGRET Source 3EG J2227+6122 [141]. This pulsar is quite comparable to the Vela pulsar according to the characteristic age (10 kyr) and energetic ($2.2 \times 10^{37} \mathrm{ergs}^{-1}$). J2229.0+6114 is associated to the Boomerang arc-shaped PWN G106.65+2.96 [142]. The Fermi-LAT gamma-ray spectrum is overlaid in the figure 4.5.

4.3.2 Sources with LogParabola modelling

The sources, parameterized with the LogParabola model are highlighted below. LogParabola is typically used for modeling blazar spectra. A source list containing their location and source type has been shown in the table 4.2. Brief outlook on each source is given below.

J0102.8+5825 J0102.8+5825 is an active galactic nuclei (AGN) detected by Fermi-LAT at a redshift of z = 0.644 [143, 144]. From the observation, it has been confirmed that it has a steady flux. The energy spectrum of this source is shown in figure 4.6.

J0240.5+6113 J0240.5+6113, also known as LSI +61°303 is a high-mass x-ray binary source located at a distance of 2kpc [145]. This source is associated with the TeV source named as TeV J0240+612 [128]. The gamma-ray energy spectrum of it has an interesting tail that would combine nicely with the MAGIC/VERITAS data at higher energies. J0240.5+6113 has a rotational period of 27 days.

J0730.2-1141 3FGL J0730.2-1141 is a flat spectrum radio quasar (FSRQ) with a redshift z =1.591 and a low duty cycle variability [146]. This source is a counterpart of

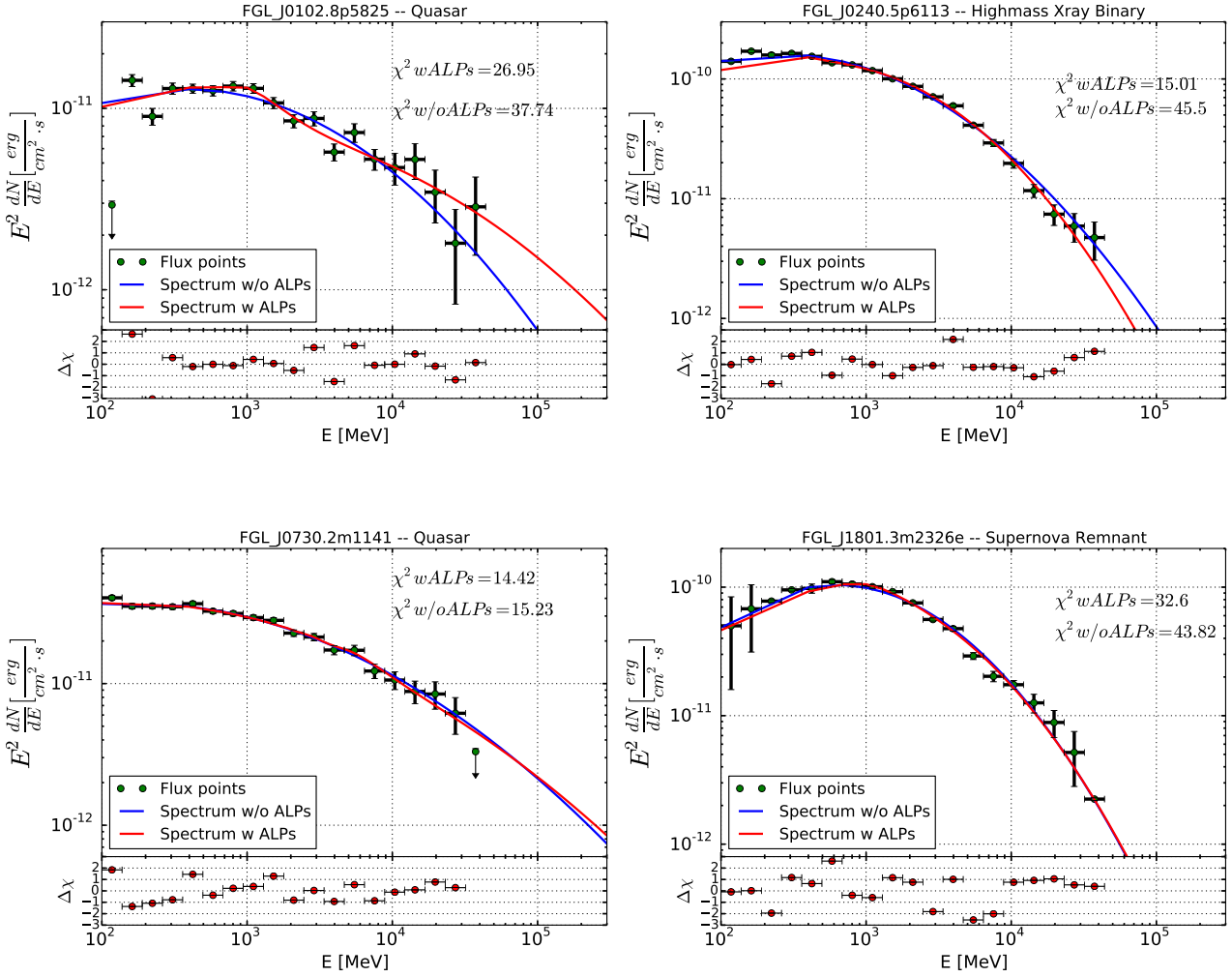

FIGURE 4.6: Energy spectrum for Galactic plane sources with LogParabola parametrization. Green points corresponds to the flux points from each energy bins. Blue line denotes the fitted spectrum without ALPs parameters and the red line is the best fit spectrum including $g_{a\gamma\gamma}$andm_a.

PKS 0727-11 and has also been studied in the third catalog of AGN detected by the Fermi-LAT [147].

J1801.3-2326e J1801.3-2326e is associated with the extended source W28 which has a disk like spatial form with an extension of 0.39 degree [148]. J1801.3-2326e dominates the emission in the northeast corner of W28 [149]. This source is also a MeV-GeV counterpart of the TeV source TeVJ1801-233 [128] which is also known as HESS J1801-233 [150]. In the vicinity of this composite, a pulsar named PSR J1801-23 is located at a distance of 13.5 kpc [150]. In the gamma-ray energy spectrum, it seems to be a result of π^0-bump. Although, we modelled this source with LogParabola method, a broken PowerLaw modelling could be apt for it (see figure 4.6).

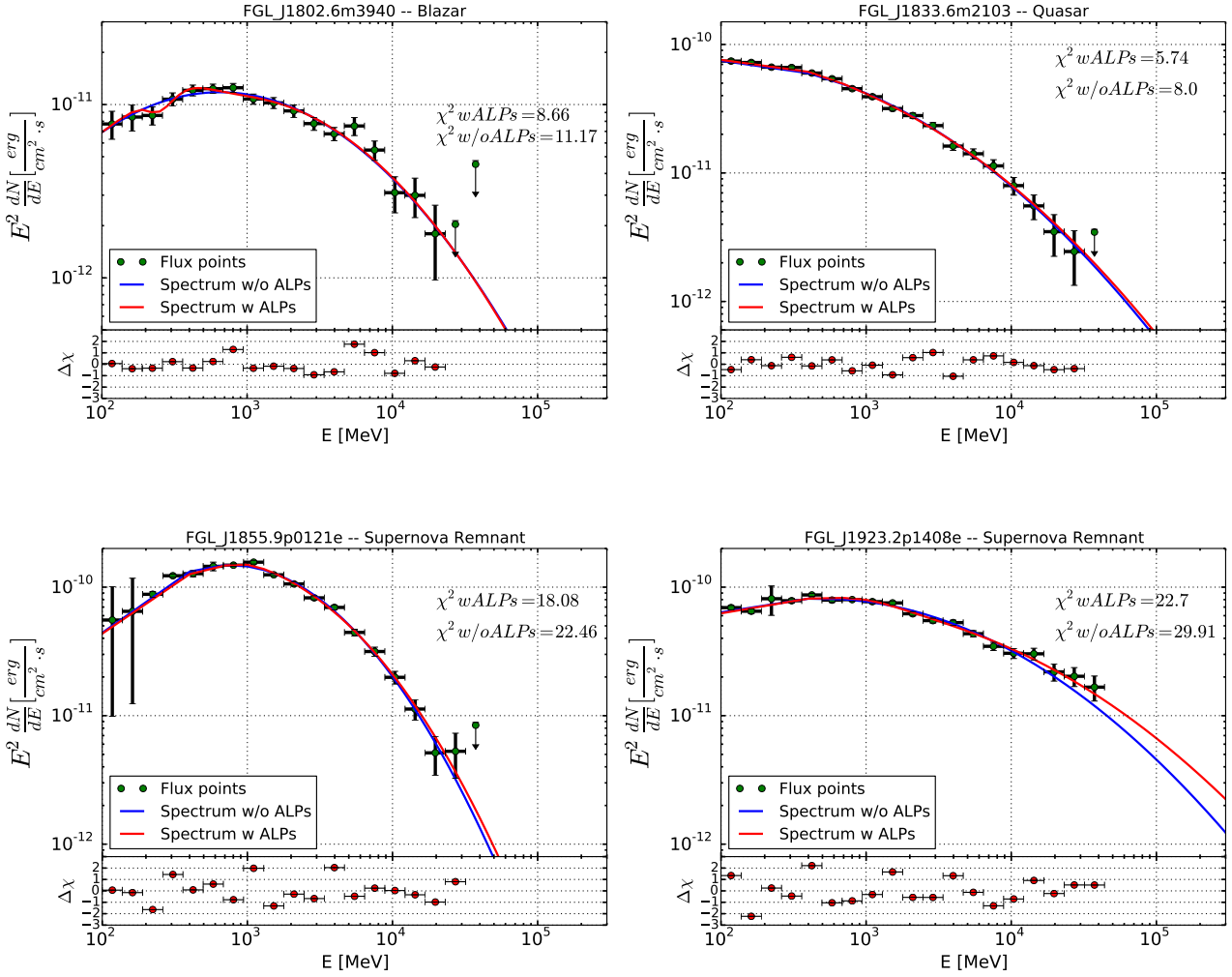

FIGURE 4.7: Similar to the figure 4.6 with different astrophysical sources.

J1802.6-3940 J1802.6-3940 is a blazar, with a redshift z=1.319 has been studied in the third catalog of AGN detected by the Fermi-LAT [147]. It is interesting to make a broad band SED which will constrain the Inverse Compton (IC) peak just below 1 GeV (see the gamma-ray spectrum of this source in the figure 4.7).

J1833.6-2103 J1833.6-2103, a counterpart associated with PKS 1830-21, has been observed with the Australia Telescope Compact Array 20GHz radio survey [151]. It has short flares nearly a month long.

J1855.9+0121e J1801.3-2326e is associated with the extended source SNR G34.6-0.5 (W44) [152]. It has a spatial form of 2D Ring and is one of the first supernova remnant with a detected π^0-bump (see figure 4.7).

J1923.2+1408e 3FGL J1923.2+1408e is associated with the extended source SNR G049.1-00.1 which is formerly known as W51C with an extension of 0.29 degrees [153]. The W51 cloud complex in is one of the most probable area for high-mass star formation at a distance of 5 kpc [154]. In the gamma-ray energy spectrum of this source, one can observe a clear break at the energy on about 290±20 MeV which is a result of π^0-bump [153] (see figure 4.7).

4.3.3 Sources with PowerLaw modelling

J2001.1+4352 J2001.1+4352, a BL lac type object was found to be variable both in the X-ray as well as the optical band. The redshift of this source is still unknown. It has a counterpart named as MG4 J200112+4352 which mostly show a bright flat spectrum in radio [155]. One strong flare has been observed confirmed in one bin in 30d light curve. The broadband characterization of this blazar with MAGIC data revealed that at least some of the radio, optical and gamma-ray emission is produced by the same population of particles accumulated in a single region [156]. The redshift of this source has been estimated z=0.18 ± 0.04 from MAGIC observation. The SED of this source confirms it to be a high frequency peaked blazar (HBL) type object (see figure 4.9).

J2201.7+5047 J2201.7+5047, located at the vicinity of AGL J2241+4454 [157], has a strong variability confirmed by the blazar catalog *BZCAT*.

4.4 Discussion

Some of the Galactic bright pulsar candidates i.e. J0633.7+0632, J1057.9-5227, J1413.4-6205, J1732.5-3130, J1907.9+0602, J1952.9+3253, J2021.5+4026 show a clear spectral modulation due to photon-ALPs mixing in the Galactic magnetic filed. The best fit ALPs parameters have been quoted in the table 4.4, 4.5 and 4.6. To fit the high energy tail of the Vela and Geminga, it is better to fit them with PLSubExpCutoff model (see section. 3.2). From the pulsar spectrum it is important to note that the χ^2 value substantially improved if we introduce the ALPs parameters to the χ^2 fit of the spectral points. The sources which are modelled with the LogParabola parametrization, comparatively show less improvement in the fit with ALPs parameters than the pulsars do, except the sources like, J0102.8+5825, J0240.5+6113, J1801.3-2326e and J1923.2+1408e.

We tried to fit a model of PowerLaw + LogParabola to the SED of the blazar J2001+4352 (see figure 4.9). The strong spectral feature we notice in the SED of this source is that it has a double peaked structure which makes J2001.1+4352 fall into the category of

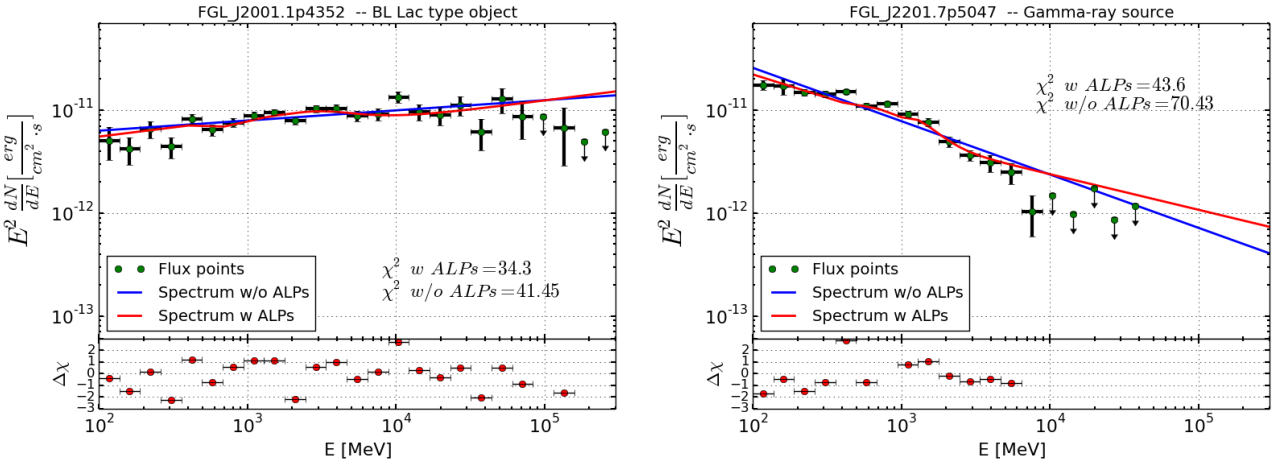

FIGURE 4.8: Energy spectrum for Galactic plane blazar and other gamma-ray sources with PowerLaw parametrization. Green points corresponds to the flux points from each energy bins. Blue line denotes the fitted spectrum without ALPs parameters and the red line is the best fit spectrum including $g_{a\gamma\gamma}$ and m_a.

Pulsar name	N_0 $[10^{-9}\mathrm{MeV}^{-1}\,\mathrm{cm}^{-2}\,\mathrm{s}^{-1}]$	E_0 [GeV]	Γ_1	E_{cut} [GeV]	$g_{a\gamma\gamma}$ $[10^{-10}\,\mathrm{GeV}^{-1}]$	m_a [neV]
J0633.7+0632	0.033(1)	1.1	0.76(3)	5.4(6)	2.5(1)	3.1(1)
J0633.9+1746	108(3)	0.1	0.81(2)	2.92(6)	2.4(1)	4.8(3)
J1057.9-5227	0.27(1)	0.7	1.09(3)	1.4(1)	5.7(9)	4.1(2)
J1413.4-6205	0.0224(3)	1.3	0.37(1)	4.42(1)	3.5(3)	3.2(1)
J1709.7-4429	25.9(4)	0.1	0.35(1)	4.8(1)	0.9(3)	3.6(1)
J1732.5-3130	0.0201(6)	1.6	1.18(4)	2.1(1)	2.2(2)	3.9(1)
J1741.9-2054	0.158(7)	0.6	1.08(4)	0.87(4)	1.2(3)	3.4(2)
J1809.8-2332	0.091(2)	1.0	0.48(1)	3.3(1)	1.0(3)	4.3(3)
J1813.4-1246	0.234(4)	0.7	0.11(1)	2.5(1)	3.5(9)	5(1)
J1826.1-1256	0.114(2)	1.0	0.25(1)	3.3(1)	1.3(3)	4.1(1)
J1907.9+0602	0.237(1)	0.7	1.3(1)	5.7(4)	4.4(5)	6.0(2)
J1952.9+3253	0.0954(5)	0.7	0.68(4)	2.9(2)	6.8(8)	3.4(2)
J2021.5+4026	0.57(1)	0.6	0.42(1)	2.83(9)	5.7(4)	6.5(2)
J2032.2+4126	0.0137(2)	1.5	0.38(2)	6.3(4)	2.4(8)	8(1)
J2229.0+6114	0.119(3)	0.7	0.22(1)	4.9(3)	2.0(2)	4.4(2)

TABLE 4.4: Fit results for individual pulsars with photon-ALPs mixing. The table gives the best fitted parameters i.e., normalization factor of each source defined at the scale energy (E_0), spectral index, cutoff energy, photon ALPs coupling constant ($g_{a\gamma\gamma}$), and ALPs mass (m_a) of each source including uncertainties.

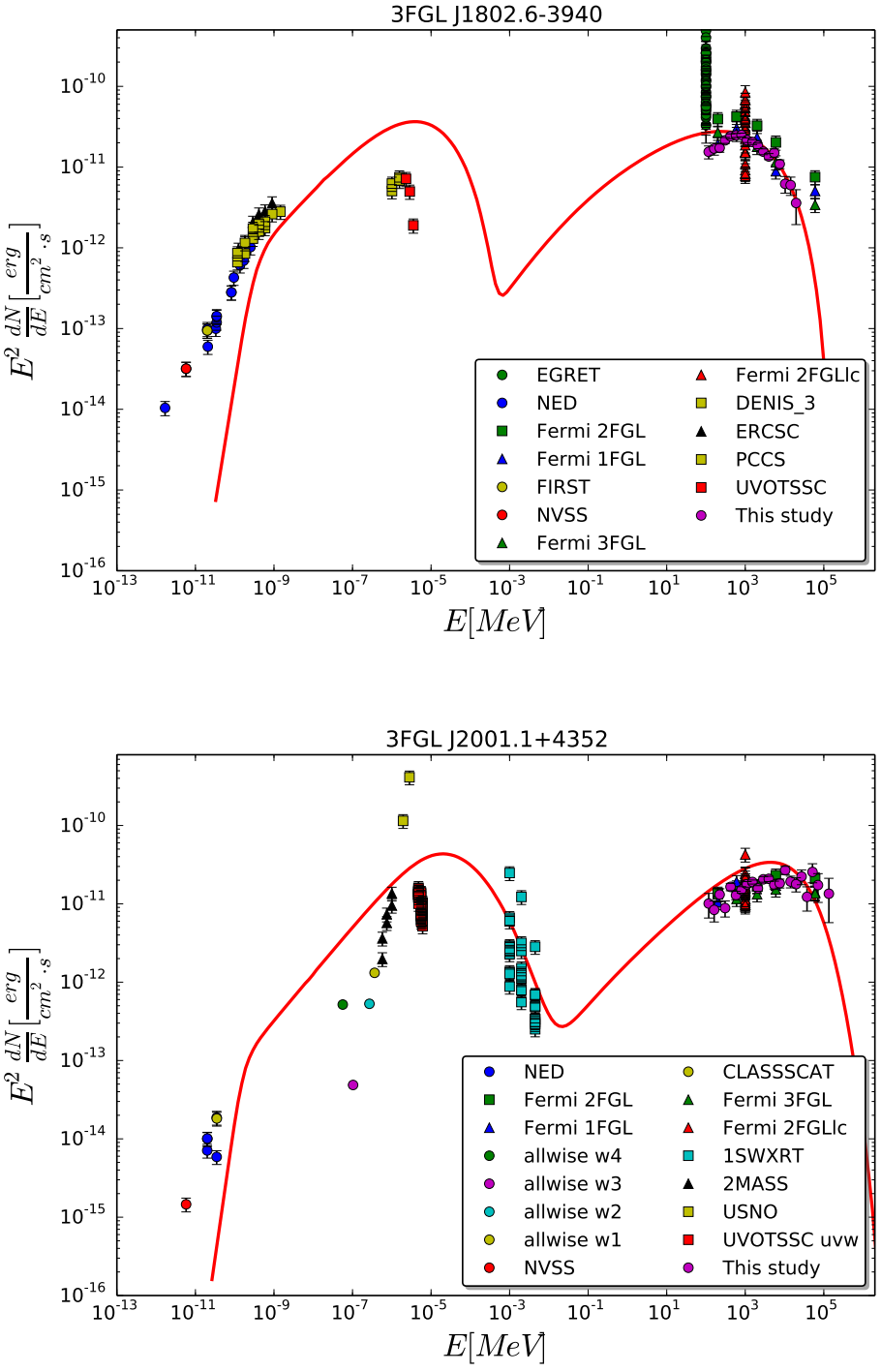

FIGURE 4.9: Spectral energy distribution of the sources J1802-3940 and J2001+4352. The different color spectral points refers to the multi-wavelength observation for the source. The red line corresponds to a model that fits to the data points. The magenta points in the SED corresponds to the present analysis of 3FGL data with 25 energy bins.

Pulsar name	N_0 $[10^{-9}\mathrm{MeV}^{-1}\,\mathrm{cm}^{-2}\,\mathrm{s}^{-1}]$	E_0 [GeV]	α	β	$g_{a\gamma\gamma}$ $\left[10^{-10}\,\mathrm{GeV}^{-1}\right]$	m_a [neV]
J0102.8+5825	0.64(6)	0.1	0.24(8)	0.06(2)	2.0(8)	4.3(2)
J0240.5+6113	7(2)	0.1	0.75(2)	0.21(1)	3(1)	1.8(2)
J0730.2-1141	2.2(8)	0.1	0.8(2)	0.069(8)	5.1(8)	3.25(8)
J1801.3-2326e	2.8(9)	0.1	0.89(2)	0.23(1)	1.6(2)	4.0(1)
J1802.6-3940	0.43(5)	0.1	0.6(1)	0.16(2)	2.1(7)	3.1(1)
J1833.6-2103	4(1)	0.1	0.13(1)	0.09(1)	1.1(3)	2.6(2)
J1855.9+0121e	2.7(2)	0.1	1.21(4)	0.28(1)	1.8(4)	3.5(2)
J1923.2+1408e	3.9(1)	0.1	0.31(3)	0.087(8)	2.1(4)	4.1(4)

TABLE 4.5: Fit results for individual Galactic plane sources with photon-ALPs mixing. These sources are modelled with LogParabola parametrization. The table gives the best fitted parameters i.e., normalization factor of each source defined at scale energy (E_0), α, β, photon ALPs coupling constant ($g_{a\gamma\gamma}$), and ALPs mass (m_a) of each source including uncertainties.

Pulsar name	N_0 $[10^{-9}\mathrm{MeV}^{-1}\,\mathrm{cm}^{-2}\,\mathrm{s}^{-1}]$	E_0 [GeV]	Γ	$g_{a\gamma\gamma}$ $\left[10^{-10}\,\mathrm{GeV}^{-1}\right]$	m_a [neV]
J2001.1+4352	0.51(2)	0.1	0.18(8)	4.4(8)	3.7(2)
J2201.7+5047	0.68(2)	0.1	0.34(2)	4.2(1)	3.1(2)

TABLE 4.6: Fit results for individual Galactic plane sources with photon-ALPs mixing. These sources are modelled with PowerLaw parametrization. The table gives the best fitted parameters i.e., normalization factor of each source defined at scale energy (E_0), index, photon ALPs coupling constant ($g_{a\gamma\gamma}$), and ALPs mass (m_a) of each source including uncertainties.

a Blazar. The SED contains the wide range of spectral points i.e. from radio-optical to X-ray and GeV gamma-rays. It is clear that the x-ray spectrum is steep and the synchrotron is very close to the optical or UV energy. Maximum inverse Compton emission comes from the GeV domain. From the observation of SED, [158] confirms that a single population of high-energy electrons in the relativistic jet originate by the synchrotron process resulting from the radio to the soft X-ray band. Soft-target photons could be present either in the jet or in the surrounding material which might be a result of inverse Compton scattering process at the higher frequencies [158].

Chapter 5

ALPs phenomenology on the non-Galactic plane sources

Gamma rays cannot penetrate the Earth's atmosphere to the ground. For the direct detection of them, we have to go to space, where the space telescope surveys of the entire sky at high energies. Normally, gamma rays originate from the most extreme places in the universe i.e. from the large-scale population of cosmic rays interacting with the interstellar medium, and also from the high energy sources such as supernova remnants, pulsars, and their nebulae, massive stars etc. The high-energy environments in the universe that make gamma rays, are needed to be explored to learn the evolution of galaxies. NASA's Fermi Gamma-ray telescope studies the most powerful sources of radiation in the universe i.e. gamma-rays.

In the previous chapters, we studied the ALPs phenomenology for the astrophysical sources that are located to the Galactic plane e.g. mostly in the region of Galactic latitude b $\in$ [-10°, 10°]. Now, we attempt to find the nature of the sources that are located outside the Galactic plane with the help of gamma-ray mission conducted with the Fermi-LAT.

5.1 Source selection

We take nine years of Fermi-LAT data for 100 most bright sources which are located in the Galactic latitude b $<$ [-10°] & b $>$ [10°]. The sources are shown in the figure 5.1. It would be interesting to see how the spectral irregularity change due to photon-ALPs mixing in the Galactic plane. Residing outside of the Galactic plane (at higher latitude), photons from these sources does not have much possibility to penetrate through the

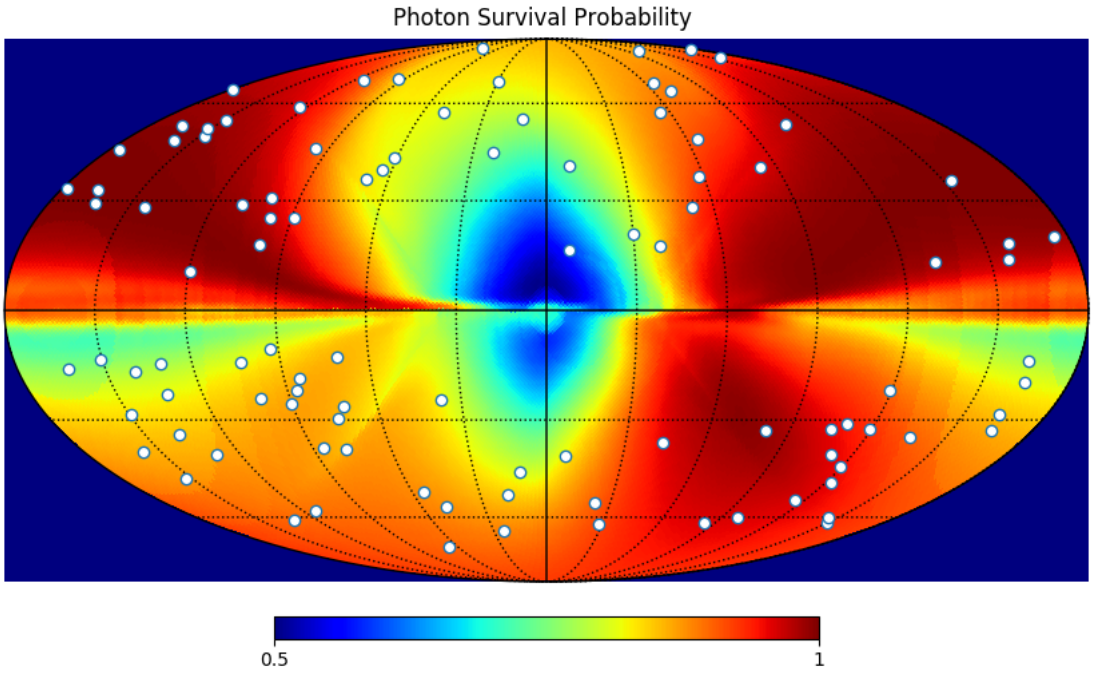

FIGURE 5.1: An all sky map of photon survival probability for photon-ALPs oscillation in the Milky way. The colormap denotes the survival probability at a distance of 15 kpc, photon-ALPs coupling constant of 9×10^{-11}GeV^{-1} and ALPs mass of 1.5 neV. The small circles denote the position of non-Galactic sources located at a b < [-10°] & b > [10°].

Galactic spiral arms. We list all the sources in the table 5.1, 5.2 and 5.4, where the Galactic longitude, latitude and the types of the sources have been mentioned. In the section 5.3, we briefly describe each source.

5.2 Data Analysis

For the analysis, the nine years of Fermi-LAT data have been used at the energy range of 100 MeV to 300 GeV for all the sources. We have followed the same technique for data analysis as described in the section 3.2 and for the parametrization we perform the same as described in section 4.2 i.e. three categories has been determined like :

- sources modelled with PLExpCutoff parametrization (see eq. 4.1),
- sources modelled with LogParabola function (see eq. 4.2),
- sources modelled with PowerLaw parameterization (see eq. 4.3).

Source name	l_{II} [°]	b_{II} [°]	source type
J0007.0+7302	119.66	10.46	pulsar
J0030.4+0451	113.14	-57.60	pulsar
J0357.9+3206	162.75	-15.98	pulsar
J0614.1-3329	240.49	-21.83	pulsar
J1231.2-1411	295.53	48.38	pulsar
J1311.8-3430	307.69	28.18	pulsar
J1836.2+5925	88.88	24.99	pulsar
J2055.8+2539	70.69	-12.52	pulsar
J2124.7-3358	10.93	-45.44	pulsar
J2214.6+3000	86.85	-21.66	pulsar
J2229.7-0833	55.23	-51.71	pulsar
J2241.6-5237	337.44	-54.91	pulsar
J2302.7+4443	103.39	-13.98	pulsar

TABLE 5.1: Selected number of very bright Galactic plane sources. The energy spectrum of these sources has been modelled with a PLExpCutoff parametrization. The table contains the Galactic longitude (l), Galactic latitude (b) and the source types.

5.3 Source details

5.3.1 Non-galactic plane pulsars

The sources modelled with PowerLaw exponential cutoff parametrization are non-Galactic pulsars. Most of the pulsars are associated with a binary millisecond pulsar and have been observed in X-ray to optical wavelengths. Brief description of each pulsar has been described as follows:

PSR J0007+7302 PSR J0007+7302 is a 14 kyr gamma-ray pulsar coincident with RX J0007.0+7302, a plerion-like X-ray source at the center of the CTA 1 supernova remnant [159]. It has been observed in optical wavelengths measuring the distance near about 1.4 ±0.3 kpc.

PSR J0030+0451 PSR J0030+0451 is a nearby (300 ± 90 pc) isolated millisecond pulsar with a very small period ($\dot{P} \leq 30ms$). PSR J0030+0451 was discovered by two independent radio surveys, the Arecibo Drift Scan Search [160] and the Bologna sub millisecond pulsar survey . Its spin-down age is 7.6×10^9 yrs [161].

J0357+3205 PSR J0357+3205, discovered by LAT has also been observed in X-ray and optical wavelengths. The source is located off the Galactic plane, at a latitude of -16°. The timing signature of this pulsar has been detected with a blind search, revealing the period (P) of 0.444 s. The energetic studies show a diffused feature associated with the pulsar [162].

Source name	l_{II} [°]	b_{II} [°]	source type
J0108.7+0134	131.86	-60.99	Quasar
J0112.1+2245	129.14	-39.86	BL Lac - type object
J0137.0+4752	130.79	-14.29	Quasar
J0144.6+2705	137.28	-34.29	BL Lac - type object
J0210.7-5101	276.11	-61.76	BL Lac - type object
J0211.2+1051	152.59	-47.36	BL Lac - type object
J0222.6+4301	140.15	-16.76	BL Lac - type object
J0237.9+2848	149.47	-28.52	Quasar
J0238.6+1636	156.77	-39.10	BL Lac - type object
J0245.9-4651	261.83	-60.10	Quasar
J0252.8-2218	209.72	-62.09	Quasar
J0319.8+4130	150.58	-13.25	Seyfert 2 Galaxy
J0334.3-4008	244.77	-54.05	BL Lac - type object
J0403.9-3604	237.73	-48.46	Quasar
J0423.2-0119	195.28	-33.12	Quasar
J0428.6-3756	240.70	-43.61	BL Lac - type object
J0522.9-3628	240.62	-32.71	BL Lac - type object
J0526.6-6825e	278.84	-32.85	LMC – Galaxy
J0532.0-4827	255.02	-32.80	BL Lac - type object
J0532.7+0732	196.85	-13.72	Quasar
J0538.8-4405	250.08	-31.09	BL Lac - type object
J0719.3+3307	185.03	19.85	Quasar
J0721.9+7120	143.98	28.02	BL Lac - type object
J0725.2+1425	203.63	13.91	BL Lac - type object
J0742.6+5444	163.04	29.08	Quasar
J0808.2-0751	229.04	13.17	Quasar
J0818.2+4223	178.20	33.40	BL Lac - type object
J0854.8+2006	206.80	35.81	BL Lac - type object
J0920.9+4442	175.69	44.80	Quasar
J0957.6+5523	158.59	47.92	Quasar
J1033.8+6051	147.77	49.10	Seyfert 1 Galaxy
J1037.5+5711	151.80	51.76	BL Lac - type object
J1058.5+0133	251.51	52.77	BL Lac - type object
J1127.0-1857	276.72	39.58	Quasar
J1159.5+2914	199.45	78.37	Quasar
J1224.9+2122	255.05	81.66	Quasar
J1229.1+0202	289.97	64.35	BL Lac - type object
J1239.5+0443	295.22	67.41	Quasar
J1246.7-2547	301.61	37.06	Quasar
J1256.1-0547	305.09	57.06	Quasar
J1310.6+3222	85.62	83.30	BL Lac - type object
J1312.7+4828	113.36	68.25	Quasar
J1345.6+4453	95.09	69.19	Quasar
J1427.0+2347	29.49	68.20	BL Lac - type object
J1427.9-4206	321.45	17.26	Quasar
J1457.4-3539	329.88	20.53	BL Lac - type object

TABLE 5.2: Selected number of very bright Galactic plane sources. The energy spectrum of these sources has been modelled with a LogParabola parametrization. The table contains the Galactic longitude (l), Galactic latitude (b) and the source types.

Source name	l_{II} [°]	b_{II} [°]	source type
J1504.4+1029	11.38	54.58	Quasar
J1512.8-0906	351.28	40.13	Quasar
J1522.1+3144	50.16	57.02	Quasar
J1542.9+6129	95.38	45.39	BL Lac - type object
J1555.7+1111	11.19	21.91	BL Lac - type object
J1625.7-2527	352.14	16.32	Quasar
J1635.2+3809	61.11	42.34	Quasar
J1709.6+4318	68.39	36.22	Quasar
J1849.2+6705	97.49	25.04	Seyfert 1 Galaxy
J2025.6-0736	36.89	-24.39	BL Lac - type object
J2056.2-4714	352.58	-40.38	Quasar
J2143.5+1744	72.11	-26.08	Seyfert 1 Galaxy
J2147.3-7536	315.79	-36.53	Quasar
J2157.5+3126	84.75	-18.24	Quasar
J2158.8-3013	17.72	-52.24	BL Lac - type object
J2202.7+4217	92.59	-10.44	BL Lac - type object
J2203.4+1725	75.67	-29.63	BL Lac - type object
J2232.5+1143	77.41	-38.58	Quasar
J2236.3+2829	90.10	-25.63	BL Lac - type object
J2236.5-1432	47.89	-56.20	BL Lac - type object
J2258.0-2759	24.35	-64.91	Seyfert 1 Galaxy
J2311.0+3425	100.41	-24.02	Quasar
J2329.3-4955	332.00	-62.31	Quasar
J2345.2-1554	65.69	-70.98	BL Lac - type object

TABLE 5.3: Continued to table 5.2.

PSR J0614-3329 PSR J0614-3329 is a millisecond pulsar with a spin period of 3.148670 ms, spin-down age of 2.8 Gyr and orbital period of 53.585 days [163].

PSR J1231-1411 PSR J1231-1411 is 3.68 millisecond radio pulsar (MSP) which is also discovered with the Fermi-LAT. It has a spin-down age of 2.6 Gyr [163]. The Neutron Star Interior Composition Explorer (NICER) discovered the pulsation from this MSP in its first few months data release[164].

PSR J1311-3430 PSR J1311-3430 is a 2.5-millisecond pulsar, located at $\sim$ 1.4 kpc away from Sun, with a large radial-velocity amplitude of 609.5$\pm$7.5 km s^{-1} [165] to be a *black-widow* binary pulsar system. In this interpretation of MSP, the strong brightness variation occurred due to the strong heating in one side of companion star with pulsar's intense electromagnetic radiation. The pulsar is in a circular orbit with an orbital period of only 93 minutes which is the shortest of any spin-powered pulsar binary ever found [166].

PSR J1836+5925 : PSR J1836+5925 is a 173 ms pulsar with a characteristic age of 1.8 million years, a spin-down luminosity of 1.1×10^{34} erg s^{-1}, locating 25° off to the

Source name	l_{II} [°]	b_{II} [°]	source type
J0136.5+3905	132.41	-22.94	BL Lac type object
J0303.4-2407	214.63	-60.16	BL Lac type object
J0442.6-0017	197.20	-28.46	Quasar
J0449.4-4350	248.80	-39.91	BL Lac type object
J0457.0-2324	223.70	-34.89	Quasar
J0509.4+0541	195.40	-19.62	BL Lac type object
J0738.1+1741	201.85	18.07	BL Lac type object
J0809.8+5218	166.25	32.91	BL Lac type object
J1015.0+4925	165.53	52.71	BL Lac type object
J1058.6+5627	149.60	54.43	BL Lac type object
J1104.4+3812	179.82	65.035	BL Lac type object
J1217.8+3007	188.87	82.05	BL Lac type object
J1248.2+5820	123.73	58.77	BL Lac type object
J1653.9+3945	63.59	38.85	BL Lac type object
J1748.6+7005	100.52	30.70	BL Lac type object
J1800.5+7827	110.03	29.07	BL Lac type object
J2000.0+6509	98.01	17.66	BL Lac type object

TABLE 5.4: Selected number of very bright Galactic plane sources. The energy spectrum of these sources has been modelled with a normal PowerLaw parametrization. The table contains the Galactic longitude (l), Galactic latitude (b) and the source types.

Galactic plane [167]. Contrary to the regular gamma-ray pulsar feature, this pulsar has a a large off-peak emission component in the spectrum. The XMM-Newton survey observed a X-ray counterpart which makes this source similar to Geminga pulsar.

PSR J2055+2539 : PSR J2055+2539, a 1.24 Myr pulsar (located nearly 1.8 kpc away from Sun [168]), was discovered in gamma-rays in a blind frequency search using 11 months of data of the Fermi-LAT [169]. This is a radio-quiet gamma-ray pulsar which has a non-thermal X-ray counterpart detected with XMM-Newton observation [170].

PSR J2124-3358: PSR J2124-3358 is an isolated 4.9 ms pulsar observed with ASCA X-ray astronomy mission. It is located at 410 pc away from us [171]. Its X-ray pulsation was detected with ROSAT HRI in the 0.1 - 2.4 keV band [171]. The pulsar wind nebula (PWN) associated with this pulsar shows an asymmetric Hα/UV/X-ray bow-shock which is confirmed with AAT/KOALA (the Kilofibre Optical AAT Lenslet Array) observation.

PSR J2214+3000: PSR J2214+3000 is a bright short period binary millisecond pulsar. Radio observation of this pulsar confirms a rotational period of 3.1 ms, a binary orbital period of 9.8 hrs, and a binary mass function f= $8.7\times10^{-7}M\odot$ [172].

PSR J2302+4443: PSR J2302+4443 is a radio-loud gamma-ray millisecond pulsar with a rotational period of 5.192 ms in a binary system with low-eccentricity orbits

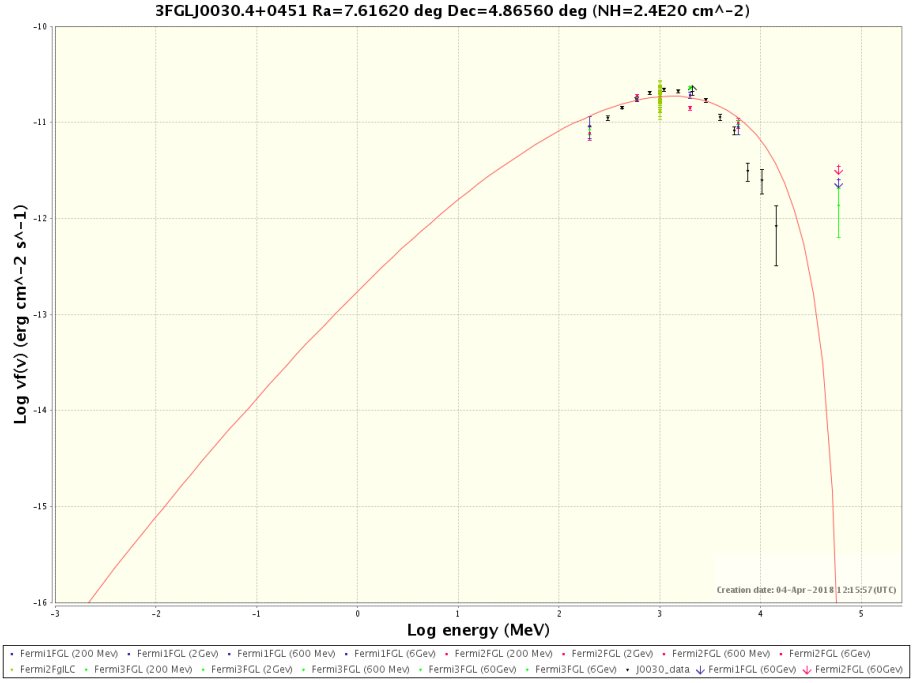

FIGURE 5.2: Spectral energy distribution for the pulsar PSR J0030.4+0451. The high energy SED has been made with the tool SED builder v3.2 [174]. The black data points corresponds to our analysis. Our analysed data points have been compared with Fermi 1FGL, 2FGL and 3FGL spectral points.

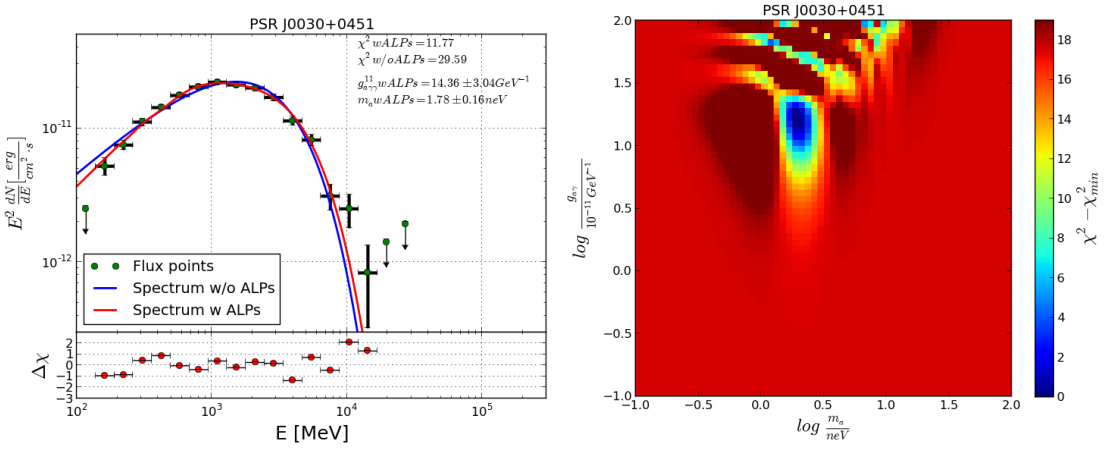

FIGURE 5.3: Left panel: Best-fit model of the spectrum of PSR J0030+0451 3651. Right panel: The χ^2 scan as function of photon-ALPs coupling and ALPs mass.

and orbital periods of 125.9 days [173]. The gamma-ray emission from this pulsar is originated at high altitude in the magnetosphere. X-ray observations show the presence of a X-ray source at the position of the pulsar resulting consistent thermal emission.

5.3.2 Sources with LogParabola modelling

Non-Galactic plane sources modelled with LogParabola have been discussed here. Most of these sources are Quasars or BL Lac type objects. Brief description on each source has been highlighted below. The Fermi-LAT energy spectrum for each source has been shown in the appendix D.

J0108.7+0134 J0108.7+0134, also known as 4C +01.02 has a redshift of z = 2.099. This quasar has been listed in Wilkinson Microwave Anisotropy Probe (WMAP) five years catalog [175].

J0112.1+2245 J0112.1+2245, at a redshift of z= 0.265, is a BL Lac -type object [176].

J0137.0+4752 J0137.0+475, at a redshift of z= 0.859, is a quasar [176].

J0144.6+2705 J0144.6+2705, a BL Lac -type object, has low- synchrotron peak (LSP) in SED.

J0210.7-5101 J0210.7-5101, blazars of uncertain type, has a redshift z= 1.003. This kind of BL Lac type object could have significant contamination from the host galaxy [177].

J0211.2+1051 3FGL J0211.2+1051, also known as MG1 J021114+1051, has a redshift z= 0.20. It showed high and variable polarization during January-February, 2011, on the time-scales of hours [178]. Based on the optical observation, this source has been considered to be a low-energy peaked BL lac object (LBLs).

J0222.6+4301 3FGL J0222.6+4301 is a GeV counterpart of the TeV source TeVJ0222+430. From the SED of the source, it has been confirmed to be an intermediate synchrotron peaked blazar (IBL) [128, 143].

J0237.9+2848 J0237.9+2848 is a Quasar with a redshift of z = 1.206 [143].

J0245.9-4651 J0245.9-4651 also known as PKS 0244-470 located at a redshift of z= 1.385 [143].

J0252.8-2218 J0252.8-2218 is a quasar located at a redshift of z=1.419 [143].

J0319.8+4130 3FGL J0319.8+4130, also known as 3C 84 is an active galactic nuclei at the center of Perceus cluster. It is the radio counterpart of the giant galaxy NGC 1275 which is located at a redshift of z= 0.0176. In the central 10 parsec scale regions of the galaxy, there is a pair of symmetric lobes which could be a result of two galaxies colliding with an evidence of free-free absorption [179–181]. A study with the Korean

VLBI network (KVN) showed the evidence of γ-rays in the downstream jet emission as well as in the nearby region where the jet originates [182].

J0334.3-4008 3FGL J0334.3-4008 is a BL Lac - type object with an unknown distance.

J0403.9-3604 J0403.9-3604, also known as PKS 0402-362 is a quasar at z $\sim$ 1.417. The nuclei is $\sim$ 3 mag more luminous than its host galaxy [183]. The optical spectrum of this source reveals a weak absorption system identified to be MgII 2800 $\mathring{A}$ associated with the companion galaxy.

J0423.2-0119 J0423.2-0119, also known as PKS 0420-01 [176] is a very bright gamma-ray quasar. Gamma-ray flare has been detected with the LAT which peaked in late January 2010. This could be a result of forward-moving transverse shocks during the radio flare [184].

J0428.6-3756 J0428.6-3756 (PKS 0426-380) is a distant flat spectrum radio quasar (FSRQ) with a redshift of z=1.1. PKS 0426-380 has broad lines visible in the low emission state and a large gamma-ray luminosity of 10^{48}ergs^{-1} [185].

J0522.9-3628 J0522.9-3628, also known as PKS 0521-36, exhibits to the the characteristics of BL lac type object as well as Seyfert galaxy. The nucleus has a broad band spectrum ranging from X-rays to the radio wavelength. The galaxy shows somewhat to be elliptical with a filament detected in Hα at the direction of east and south-east of the nucleus. Besides there, an optical jet like feature is also visible for this source [186].

J0526.6-6825e J0526.6-6825e is associated with the Large Magellanic Cloud (LMC) at a distance of 50 kpc. The massive star forming region in the LMC, *30 Doradus* is the main source of bright gamma-ray emission [187]. The gamma-ray observation found also a fainter emission region from the north part of the Galaxy. Although, the spectrum of the LMC emission components is well described by power laws, for global fitting we use the LogParabola parametrization which can follow the flux points nicely in the logarithmically spaced energy bins with a energy range of 100 MeV to 20 GeV (see figure D.3). Detailed gamma-ray study on LMC revealed that the gamma-ray emission does not only originate from the point sources but it comes from cosmic-ray interactions with the interstellar medium and radiation field which are diffused in nature [187].

J0532.7+0732 J0532.7+0732 is located at the redshift z=1.254.

J0538.8-4405 J0538.8-4405 formerly known as PKS 0537-441 is a blazar with a redshift z=0.896.

J0719.3+3307 J0719.3+3307 is a quasar located at a redshift of z = 0.779. It has an opening angle of the jet of 22° and a position angle of parsec scale jet of 76° [188].

J0721.9+7120 J0721.9+7120 has a TeV counterpart named as TeV J0721+713 observed with AGILE with also 3FGL power-law index of 2.04 [128]. This source is a blazar of 'LBL' with redshift z= 0.31.

J0725.2+1425 J0725.2+1425 is a blazar with a redshift of 1.038 [146].

J0742.6+5444 J0742.6+5444 is a FSRQ with a redshift z= 0.72 [189].

J0818.2+4223 J0818.2+4223 is a quasar with the redshift of z=1.837.

J0854.8+2006 J0854.8+2006 is also known as OJ 287 is a binary black hole system with a redshift z = 0.306 [190]. This source has shown strong variability in near-infrared to even x-ray and gamma-ray energies. This source seems to be related to a binary system of super-massive black hole (SMBH) indicating the galaxy to be gas-rich in high redshifts [145]. The optical bump in the SED of this source can be accounting for the accretion-disk emission associated to the primary black-hole of mass $\sim 1.8 \times 10^{10} M_{\odot}$ and the little bump in the optical-UV corresponds to the line emission [191].

J0920.9+4442 J0920.9+4442, also known as S4 0917+624, is a quasar located at a very high redshift z = 2.189. Intra-day variability observations and the VLBI structure analysis of quasar S4 0917+624 confirmed a disappearance of strong IDV after the year 2000 which could be a result of changes in the interstellar medium [192].

J1033.8+6051 J1033.8+6051 (known as S4 1030+61) is a FSRQ with a redshift z = 1.4009 and it has a LSP SED [193]. The jet of the source S4 1030+61 accounts for a superluminal velocity of (6.4±0.4)c [194]. It shows very strong variability in radio and gamma-ray wavelength with a stable, straight jet which might be a result of injection of relativistic particles.

J1037.5+5711 J1037.5+5711, also known as GB6 J1037+5711 is located at the redshift z= 0.175 [195].

J1058.5+0133 J1058.5+0133 is a blazar showing only a single broad emission line [196]. The broadband spectral distribution provides high confidence for the identification of Mg II (at equivalent width =2.2 $\mathring{A}$)

J1127.0-1857 J1127.0-1857 belongs to the FSRQ class located at a distant redshift z=1.048 [197]. The source spectrum has a peak at an energy $\leq$ 100 MeV. The light curve shows a gradual increase of flux at the period of the Fermi-LAT observations [198].

J1159.5+2914 J1159.5+2914, also known as Ton 599 has a redshift z=0.7247. This source has been detected in VHE gamma-rays with MAGIC telescope estimating the flux to be about 0.3 Crab units above 100 GeV [199].

J1224.9+2122 J1224.9+2122 (4C +21.35) located at the redshift z = 0.435 is a peculiar quasar [200]. In early 2010, a very strong GeV outburst composed of several major flares have been observed with the Fermi-LAT. During the flaring activity, VHE emission from 4C +21.35 was detected with the MAGIC telescopes [201].

J1229.1+0202 J1229.1+0202 (known as 3C 273) is a well-known quasar located at a redshift z = 0.158. It has a large scale jet which appears to be extended up to a few tens of kpc from the core [202]. The gamma-ray emission region are located at a distance of 1.2±0.9 pc from the jet [203]. This source showed a prominent flaring activity at GeV energies during a period between July 2009 and April 2010 confirmed with Fermi-LAT observations.

J1239.5+0443 J1239.5+0443 is a gamma-ray source of the Virgo region detected with low significance by EGRET [204] and later with the Fermi-LAT [205]. This source is associated with a FSRQ GB6 J1239+0443 with a redshift z=1.762. A gamma-ray study of this source revealed that the spectrum, with an extension of up to 15 GeV, has no relevant sign of absorption from the broad line region [206].

J1246.7-2547 J1246.7-2547 (associated to PKS 1244-255) is the soft spectra FSRQ which is located at the redshift z=0.633 [207]. This source would be hardly visible with the CTA as the high energy flux is dropping down above 10GeV (see figure D.7)

J1256.1-0547 J1256.1-0547 is associated with 3C 279 with a redshift z=0.536 [176]. Being highly variable this source belongs to be one of the well-known FSRQs. The multi-wavelength SED is characterized by a double peaked structure with a first bump at infrared energies which could be associated to synchrotron emission of relativistic electrons. The high energy peak is at few GeV observed with the Fermi-LAT. In June 2015, the Fermi-LAT observed a giant outburst from the 3C 279 with a peak >100 MeV [208] for two minutes binned timescales.

J1312.7+4828 J1312.7+4828, located at a redshift z= 0.638, is a bright active galactic nucleus. The SED of this source shows a typical blazar like two-peaked structure and gamma-ray-loud narrow-line Seyfert 1 galaxies [209]. In November, 2009 it exhibited a gamma-ray flare with a daily flux of $\sim 10^{-6}$ph cm^{-2}s^{-1} at energies > 100 GeV. During gamma-ray flares, the high-energy emission resulting of inverse Compton process dominates by more than an order of magnitude over the low-energy emission caused by synchrotron process [210].

J1345.6+4453 J1345.6+4453 is a FSRQ located at very distant redshift z = 2.53 [211].

J1427.0+2347 J1427.0+2347 (also known as PKS 1424+240) is a nice HBL candidate with an approximate redshift z=0.604. This source has been observed in VHE gamma-rays with MAGIC and VERITAS [212]. In a recent study, it has been probed that a two zone synchrotron-self-Compton (SSC) model as well as a hadronic model can satisfactorily reproduce the gamma-ray emission scenario from this source [213]. The MAGIC spectrum is corrected for the absorption due to the extragalactic background light and shows a flat spectral nature with no turn down up to 400 GeV [214].

J1512.8-0906 J1512.8-0906 is one of the FSRQs that have been detected at VHE. This is a luminous blazar located at the redshift of z= 0.361. In the broadband SED of this source, a peak in the infrared frequencies is accounted for the synchrotron emission of the inner jet. The UV band in the SED is created by the accretion disk and the X-ray continuum is dominated by the IC emission of the low-energy jet electrons [215]. Multi-wavelength observation of this source by MAGIC collaboration probed the first time a significant VHE gamma-ray variability from J1512.8-0906 [216].

J1625.7-2527 J1625.7-2527 is a FSRQ with redshift z= 0.79 [211].

J1709.6+4318 J1709.6+4318 is a FSRQ with redshift z= 1.03 [211].

J1849.2+6705 J1849.2+6705 is a seyfert galaxy with the redshift z= 0.657 [211].

J2025.6-0736 J2025.6-0736 (also known as PKS 2023-07), is a FSRQ with the redshift z=1.388 [217]. This has been observed the Fermi-LAT as one of the most powerful blazar with an average γ-ray luminosity 10^{48}ergs^{-1} [218].

J2056.2-4714 J2056.2-4714 (also known as PKS 2052-47) is a flat-spectrum radio quasar with a redshift of 1.489 [145].

J2143.5+1744 J2143.5+1744 is a FSRQ with the redshift z = 0.211 [211].

J2147.3-7536 J2147.3-7536, located at a redshift of z =1.139, is a quasar [146]. In July 2009, the flat-spectrum radio quasar PKS 205247 experienced an optical flare, which was followed by a γ-ray flare in August.

J2158.8-3013 J2158.8-3013, is also known as PKS 2155-304, located at a redshift of z= 0.116 [177]. This is a high-frequency-peaked BL Lac object which has been observed in multi-wavelengths. In an optical study based on five years of observation of this source (2009-2014), it has seen a significant variability at all wavelengths, with several prominent flares at the optical and gamma-ray intensity [219]. With the HESS study for this source, it has been found the light curve shows log-normal behavior which could indicate aperiodic variability in the blazars [220].

J2202.7+4217 J2202.7+4217, a BL Lac - type object, has been observed with Fermi-LAT as well as VERITAS [221].

J2203.4+1725 J2203.4+1725, a BL Lac - type object is located at a redshift of z =1.08 [222].

J2232.5+1143 J2232.5+1143 is classified as a object at a redshift of 1.037 [223].

J2236.3+2829 J2236.3+2829 is a LBL type blazar at a redshift of z =0.795 [176].

J2236.5-1432 J2236.5-1432, associated with PKS 2233-148 is a radio-loud BL-Lac type object. In a study of micro-variability of radio-loud quasar showed that there is not such evidence of variability for this source [224].

J2258.0-2759 J2258.0-2759, also known as PKS 2255-282, is a flat spectrum radio-quasar with a redshift of z =0.926 [225]. A multi-wavelength study has been conducted on this source revealing that the broadband SED extends from low radio frequencies to the γ-ray energies [226]. An observation of gamma-ray flare from this source has been found with an evidence of weak gamma-ray variability and a hard power-law index of 1.7± 0.3, above 100 GeV [227].

J2311.0+3425 J2311.0+3425 is a flat spectrum radio-quasar with a redshift of z=1.817. A correlated variability between the radio and gamma-ray activity has been found for this source with a statistical significance of 2.25 σ [189].

J2329.3-4955 J2329.3-4955 is also known as PKS 2326-477, is a quasar with a compact unresolved core structure [228].

J2345.2-1554 J2345.2-1554 is a BL Lac - type object with a redshift of z = 0.621 [143].

5.3.3 Sources with PowerLaw parametrization

J0136.5+3905 J0136.5+3905 is a blazar studied in Fermi-LAT 2FHL catalog [143].

J0303.4-2407 J0303.4-2407, alternatively known as PKS 0301-243, is high-synchrotron-peaked BL Lac object with a redshift of z$\sim$ 0.266. It has been detected at high energies with Fermi-LAT (100 MeV $<$ 100 GeV) as well as at very high energies (E $>$ 100 GeV)with HESS [229, 230]. The multi-wavelength observation reveals strong variability (see figure E.1). A leptonic synchrotron self-Compton model nicely fits to the multi-wavelength data and makes the jet to be particle dominated [229].

J0442.6-0017 J0442.6-0017, with a redshift z= 0.844, is a flat spectrum radio Quasar (see figure E.2).

J0449.4-4350 J0449.4-4350 (known as PKS 0447-439) is one of the brightest extragalactic sources observed in multi-wavelength energies. The optical spectrum of J0449.4-4350 is strongly dominated by non-thermal emission from the jet and observations with ATCA in the radio band reveals it to be an extended, lobe-dominated source [231] (see figure E.3). In 2009-2010 this source has been observed in VHE band with HESS telescope with a photon index of 3.89±0.37(stat)±0.22 (sys) [232].

J0457.0-2324 J0457.0-2324, also known as PKS 0454-234 [143], at z = 1.003 is the soft spectra FSRQ. However, this is bright at the HE gamma ray regime 0.1 GeV and 300 GeV during 4 years. From a study four years Fermi-LAT data of this source, it has been seen that PKS 0454-234 could be detected by the CTA when the target object in the bright period [233] (see figure E.4) .

J0738.1+1741 J0738.1+1741, also known as PKS 0735+17 [143] is a BL Lac object at z$\sim$ 0.424. Observations show that PKS 0735+178 has a flat radio spectrum and radio bursts, violently optical variations confirmed by ten-year optical monitoring of PKS 0735+178 [234]. Although the fluxes in the radio and in the optical are variable (see figure E.6), there is only marginal correlation of variations between them [235].

J0809.8+5218 J0809.8+5218 (known as 1ES 0806+524) is a high-frequency-peaked BL-Lac object, at a redshift z=0.138. This blazar candidate was suggested as VHE gamma-ray source based on the presence of both high-energy electrons and sufficient seed photons [236]. In 2008, this has been detected with VERITAS at a significance of 6.3 σ and at a level of 1.8% of the Crab Nebula flux above 300 GeV [237]. The differential flux spectrum between 300-700 GeV can be fitted with a soft PowerLaw which is comparable to our Fermi data analysis for this source [238] (see figure E.7).

J1015.0+4925 J1015.0+4925 also known as 1H 1013+498 is at a redshift of z =0.212 [143].

J1058.6+5627 J1058.6+5627 is a BL Lac type object [143] (see the high energy SED in the figure E.9).

J1104.4+3812 J1104.4+3812, associated with Mkn 421 is a BL Lac [143] type object. It has a redshift of z=0.031, the broad-band spectral energy distribution is dominated by non-thermal emission that is believed to be produced in a relativistic jet pointing towards the observer. VHE gamma-ray observation with HESS reveals significant variations of the spectral shape detected with a spectral hardening with the increase in flux [239]. X-ray studies indicate smaller variability that seen in VHE (see figure E.10).

J1217.8+3007 J1217.8+3007, also known as B2 1215+30, is a BL Lac-type blazar. It was first detected in VHE with the MAGIC telescope followed by VERITAS. The TeV flux of this source $\sim$ 2.4 times than the Crab nebula flux, confirmed with the long term

VERITAS data. There is some uncertainty in the distance to this source, with values of z= 0.13 [240]. Based on the location of its synchrotron peak, J1217.8+3007 has been either classified as an intermediate or high-frequency peaked BL Lac (see figure E.11). Multi-wavelength studies with Fermi-LAT and swift reveals the correlated gamma-ray HE flux [241].

J1248.2+5820 J1248.2+5820, a Palomar-Green BL-Lac object, located in the Northern hemisphere with an unknown redshift [242].

J1653.9+3945 J1653.9+3945, also known as Mkr 501, is a gamma-ray blazar with a redshift of z= 0.034. The average spectral energy distribution of Mkr 501 is well described by the standard one-zone synchrotron self-Compton model [243] (see figure E.13). This model explains that the electrons are accelerated to extra-relativistic energy as a result of particle acceleration, while the non-thermal photons are produced via synchrotron and inverse Comtpon scattering. A TeV γ-ray flare of Markarian 501 observed with MAGIC telescope on July 9, 2005 [243]. The gamma-ray spectrum can be well-modelled with a single PowerLaw function [244].

J1748.6+7005 J1748.6+7005 is a BL-Lac object with a redshift of z= 0.77 [143].

J1800.5+7827 J1800.5+7827 is a BL-Lac object with a redshift of z= 0.68 [143].

5.4 Discussion

We presented brief discussion on each sources in the section 5.3. In case of pulsar sources we have noticed the apparent suppression in energy spectrum as a result photon-ALPs mixing in the galactic magnetic field. The spectral feature in disappearance channel generally depends on the distance to the source and transversal magnetic field along the line of sight. The modulated spectrum has been illustrated in the appendix C. Analyzing the data of PSR J0030+0451, the photon-ALPs coupling constant and the ALPs mass we get respectively $14.36 \times 10^{-11}\text{GeV}^{-1}$ and 1.78 neV (see figure 5.3). The photon-ALPs mixing phenomenon makes a notable improvement in the χ^2 value of the fitted spectrum reducing χ^2 value by 17 from non-ALPs mixing to ALPs mixing case. We can say the fit results with ALPs parameters is a good fit as the χ^2 per dof is $\sim$ 1 for all the pulsar spectrum. In the fits for each sources, we also include systematic uncertainties as derived from the Vela pulsar analysis. The right panel of the figure 5.3 depicts the blue stripes that corresponds to the photon-ALPs oscillation in traversal magnetic field. The significance of our result for PSR J0030+0451 has been estimated by F-test 2.39σ. We make a combined parameter space for all the 12 pulsar candidates (see figure 5.4) and derive the best parameter space for photon-ALPs coupling constant

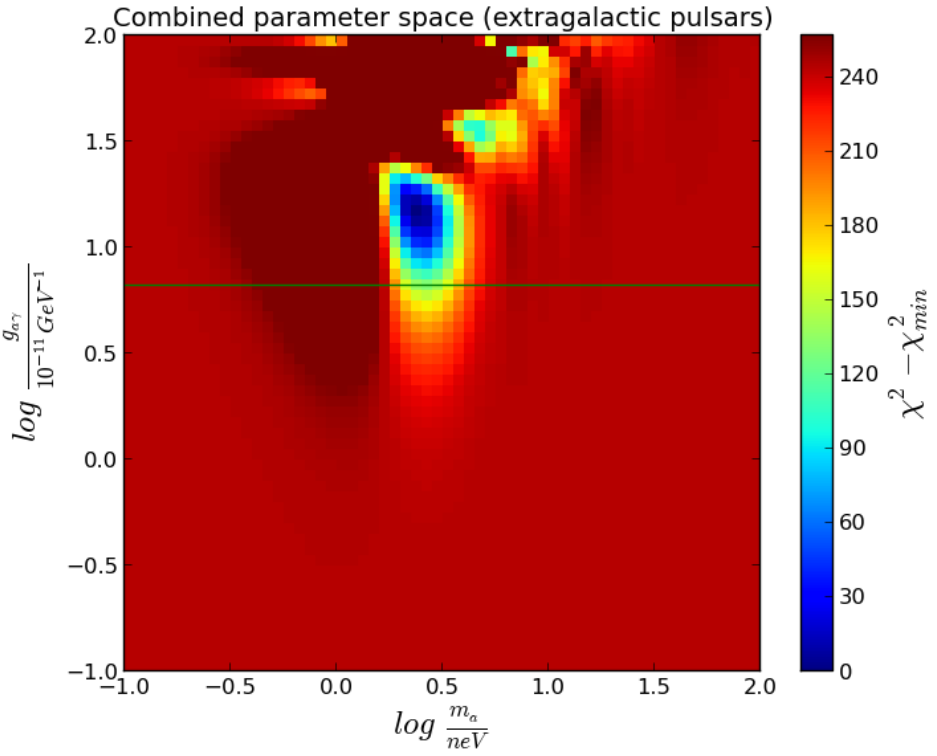

FIGURE 5.4: Combined $\Delta\chi^2$ scan as function of photon-ALPs coupling and ALPs mass for the extragalactic pulsar sources. The colorbar represents the minimum $\Delta\chi^2$ location in the $(g_{a\gamma\gamma}, m_a)$ plane. The green line corresponds to the CAST limit on photon-ALPs coupling constant.

and ALPs mass. Photon-ALPs coupling constant ($g_{a\gamma\gamma}$) we get $14.12 \times 10^{-11}\text{GeV}^{-1}$ and ALPs mass (m_a) we calculate 2.23 neV.

We summarize the non-Galactic plane blazar spectra in the appendix E, where we have shown the broad band SED of few well-known quasars and blazars. A nicely binned HE gamma-ray flux points has been given for each figures to compare our Fermi-LAT data points to the other HE or VHE observational points. Notably, our spectral points nicely match to the Fermi 1FGL, 2FGL and 3FGL data points. In case of Mkn 421, our HE spectral points makes nice co-ordination to the HESS and VERITAS data points (see figure E.10). Same thing follows for the source Mkr 501 (see figure E.13).

Besides, we try to give an imprint on ALPs phenomenology for non-Galactic plane sources with LogParabola parametrization. The individual spectra and the best fitted ALPs parameter values are quoted in the appendix D.

For all the non-Galactic plane sources, we computed the log p value taking into account the χ^2 value and the corresponding degrees of freedom in case of each source. An all-sky map of photon-survival probability at the energy of 1 GeV and sources at a distance of

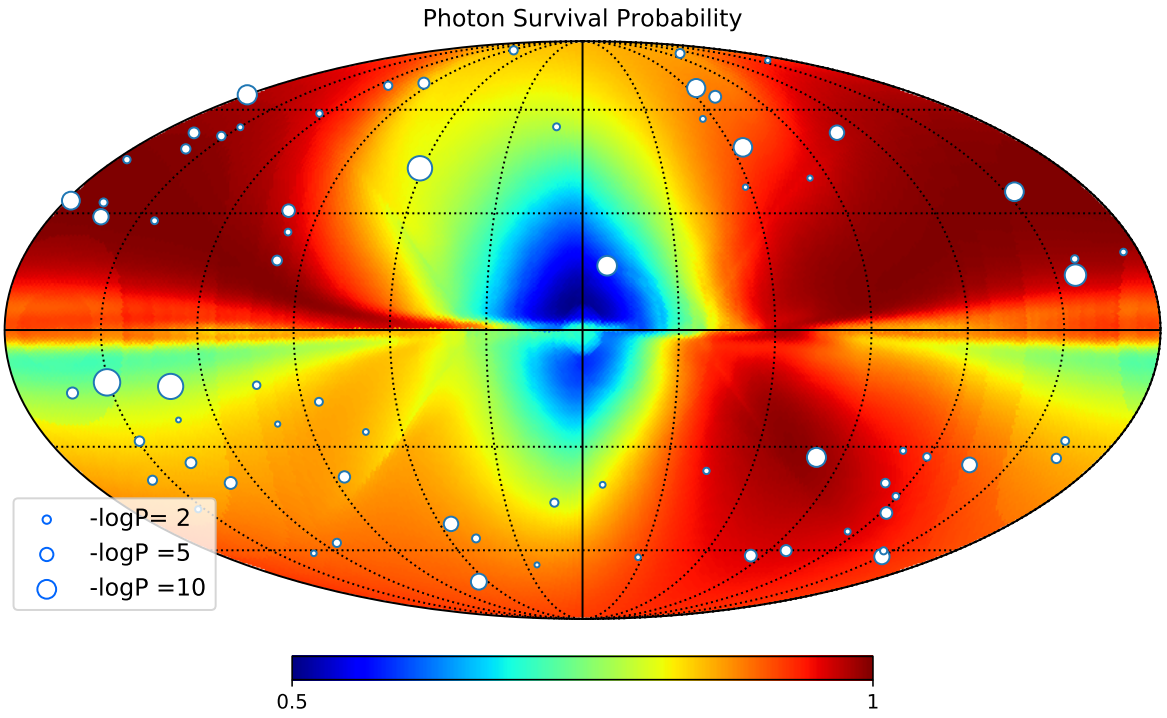

FIGURE 5.5: All-sky map for photon survival probability at a Galactic distance of 15 kpc. The photon-ALPs coupling constant, $g_{a\gamma\gamma}$ is to be $9\times10^{-11}\mathrm{GeV}^{-1}$ and the ALPs mass ($\mathrm{m_a}$) is 1.5 neV. The color scale denotes the photon survival probability ranging from 0.5 to 1. The different size circles represent the p-value related to the photon-ALPs conversion in the Galactic magnetic field. The three different size circle denotes the three different -logp value.

15 kpc has shown. We project the p-values of each source in the figure 5.5. A small p-value indicates strong evidence of ALPs against the null hypothesis e.g. no ALPs case and a larger p-value corresponds to a weak indication of photon-ALPs mixing in the energy spectra.

Chapter 6

Summary and conclusion

In this thesis, the spectral modulation of Galactic and non-Galactic plane sources due to photon-ALPs mixing in the Galactic magnetic field has been studied explicitly. ALPs can oscillate into photons and vice versa in the presence of an external magnetic field. This oscillation of photon and ALPs could have detectable implications for astronomical observations, i.e. a characteristic energy dependent attenuation in Gamma ray spectra for the astrophysical sources. Here we have visited the opportunity to search photon-ALPs coupling in the disappearance channel with the help of the gamma-ray telescope Fermi-LAT. We use nine years of Fermi Pass 8 data for a selection of Galactic and non-Galactic plane Gamma-ray source candidates and study the modulation in the spectra in accordance with photon-ALPs mixing and estimate best fit values of the parameters i.e. photon-ALPs coupling constant ($g_{a\gamma\gamma}$) and ALPs mass (m_a). We find consistent evidence of photon-ALPs mixing for six selected gamma-ray pulsars located in the Galactic plane along a line of sight to the Earth. The hints of spectral modulation as a result of photon-ALPs mixing has been investigated at a combined significance level of 4.6 σ. It is important to note that if we combine all the individual spectrum where every source gets its best fit ALPs parameters, we conclude the combined significance to be 5.2 σ (see table 3.4). Although the fit to the spectral data points with the universal value of ALPs parameters ($g_{a\gamma\gamma} = (2.3^{+0.3_{\rm stat.}}_{-0.4_{\rm stat.}} \pm 0.4_{\rm syst.}) \times 10^{-10}$ GeV^{-1} and $m_a = (3.6^{+0.5_{\rm stat.}}_{-0.2_{\rm stat.}} \pm 0.2_{\rm syst.})$ neV) are not so much acceptable, it is possible that the uncertainty on the Galactic magnetic field model are responsible for the poor fit.

We try to derive the global value of the ALPs parameters from our analysis. Apart from the Galactic magnetic field dependence, it makes the variation with the location of the source. We gave an imprint on the variation of ALPs parameters with the variation of distance in the section. 3.5. Although the best-fit parameters are by a factor of ~ 3 larger than the current best limit on solar ALPs generation obtained with the CAST

helioscope [109] (see figure 3.12), the known modifications of the photon-ALP mixing in the high density solar environment could provide a tenable explanation for the apparent tension between the helioscope bound and the indication for photon-ALPs mixing. The environment in the dilute interstellar medium which has been assumed for the analysis, is much more different from the environment inside a star. In the former case plasma effects and environmental parameters are significant and several suppression mechanisms can take place. In this case, the bounds from CAST might be relaxed according to the solar physics model, as already advocated to reconcile the CAST bounds with the PVLAS experiment results [245]. Although this is an interesting scenario, a detailed calculation should be performed to test its viability in light of the present results.

However, our combined parameter space (see figure 3.12) is well within the accessible range of the next generation ALPs experiments i.e. ALPS II [115] and the future helioscope IAXO [116]. It would be also possible to improve the ALPs contour with future Galactic magnetic field models which could be based on the full-sky polarization survey.

We extend our analysis for the other Galactic and non-Galactic plane astrophysical sources. In general, for Galactic pulsars we have seen a significant improvement to the fit and it holds the same for the other sources as well. This holds the same for the non-Galactic sources. If we introduce the ALPs parameters to the spectral fit, non-Galactic pulsars show significant improvement in χ^2. The combined parameter space for the pulsars provide the the best fit value of ALPs parameters to be ($g_{a\gamma\gamma} = 1.4\times10^{-10}$ GeV^{-1} and $m_a = 1.8$ neV) (see appendix. C). In the appendix E we present the very bright extragalactic the blazar spectrum along with the multi-wavelength SED. Notably, our finely binned spectral points for the high energy blazars are quite consistent with the Fermi 1FGL [246], 2FGL [205] and 3FGL [77] spectral points.

While the photon-ALPs mixing in the Galactic magnetic field exhibit a suppression in energy spectra, the reconversion of ALPs to photons from the sources located at large distance can follow the appearance channel in the optically thick part of energy spectra. In future, it would be nice to analyze the VHE HESS or MAGIC data to combine with the new Fermi-LAT data (Fermi FL8Y)[1] to probe the GeV-TeV counterpart of the gamma-ray sources. In the framework of photon-ALPs conversion in the magnetic field, gamma-ray observations of the sources with very high redshift revealed that the energy spectra is less affected by the absorption than predicted. This could be a result of photon appearance in VHE regime. This phenomenon can be explored with the data of future experiments like Cherenkov telescope array (CTA).

[1] https://fermi.gsfc.nasa.gov/ssc/data/access/lat/fl8y/

Appendix A

Enrico Documentation

To run the Fermi science tools together Enrico documentation [101] has been introduced by D.A. SANCHEZ et al. in 2013[1]. Enrico python package uses all the science tools to analyze Fermi-LAT data. To generate Xml model file, Fits files there are a few simplified command lines. The command-line tools work with a configuration file that needs to be generated by the following command lines:

```
$ enrico_config J2021+3651.conf
Please provide the following required options [default] :
Output directory [~/myanalysis] :
Target Name : PSR_J2021+3651
Right Ascension: 305.2722
Declination: 36.8492
redshift, no effect if null [0] : 0.0
ebl model to used
0=Kneiske, 1=Primack05, 2=Kneiske_HighUV, 3=Stecker05,
 4=Franceschini, 5=Finke, 6=Gilmore : 4
Options are : PowerLaw, PowerLaw2, LogParabola, PLExpCutoff
Spectral Model [PowerLaw] : PLExpCutoff
ROI Size [15] : 15
FT2 file [~/myanalysis/spacecraft.fits] : ~/myanalysis/L150907051842355675 7C68_SC00.fits
FT1 list of files [~/myanalysis/events.lis] : ~/myanalysis/data.list
tag [LAT_Analysis] : LAT_Analysis
Start time [239557418] : 239557417
End time [334165418] : 539769770
Emin [100] : 100
Emax [300000] : 300000
IRFs [CALDB] :
evclass [128] :
evtype [3] :
Corresponding IRFs    =       ('P8R2_SOURCE_V6', ['BACK', 'FRONT'])
Is this ok? [y] : y
Corresponding zmax =  95
```

[1] http://enrico.readthedocs.io/en/latest/

The corresponding xml file can be made with running *enrico-xml* command line as follows:

```
 enrico_xml J2021+3651.conf
use the default location of the catalog
use the default catalog
Use the catalog :  /CATALOG_PATH/gll_psc_v06.fit
[Message]: Adding extended source Cygnus Loop, Catalogue name is 3FGL J2051.0+3040e
[Message]: Summary of the XML model generation
Add  58  sources in the ROI of  12.0 ( 10.0 + 2 ) degrees
9  sources have free parameters inside  3.0  degrees
1  source(s) is (are) extended
Iso model file  /nfs/astrop/d6/majumdar/myanalysis/myanalysis1
/enrico/Data/diffuse/iso_P8R2_SOURCE_V6_v06.txt
Galactic model file  /nfs/astrop/d6/majumdar
/myanalysis/myanalysis1/enrico/Data/diffuse/gll_iem_v06.fits
[Message]: write the Xml file in ~/myanalysis/PSR_J2021+3651_PLExpCutoff_model.xml
```

For running Global fit all the science tool has been merged in one tool which can be called with the following command line:

```
enrico_sed J2021+3651.conf
```

This will make all the steps of Fermi binned analysis (*gtselect*, *gtmktime*, *gtltcube*, *gtsrcmaps* etc...), produce all the required fits files and fit the data *gtlike*. A *.results* file will be produced and where all the results will be stored. The result file contains all the parametersaccording to the spectral model of the target source i.e prefactor, index , cut off energy etc. with the corresponding errors (actual errors and parabolic errors). For binned analysis, we can get the number of bins from 0 (default) to 25 in the configuration file. At the end of overall fit, Enrico runs *NumEnergyBins* analysis by dividing the energy range making another directory for binned analysis. Each bin results files have been stored there including all the parameter values and the corresponding errors. Additionally, we run the Enrico analysis of several job on cluster of CPUs with the help of a shell script.

Appendix B

Galactic magnetic field model

Magnetic field in the interstellar medium is spiral in large scale structure and mostly irregular. The origin of the large scale magnetic field in the Universe is still a mystery to us. The only available constrains of large scale magnetic field are the Faraday rotation measures (RM), polarized synchrotron radiation and also the polarized dust emission from spinning elliptical dust grains [74]. For our analysis to compute the conversion probability of photons into axion-like particles (ALPs) and vice versa we have taken into consideration one of the most accepted and comprehensive GMF model: Jansson & Farrar model (2012) [74]. In this model, seven years RM data and synchrotron emission data of Wilkinson Microwave Anisotropy Probe (WMAP7) have been used. This model of large scale regular field consists of three components: the disk component, the halo component and the out of plane component.

B.0.0.1 The disk component

The disk component follows the structure of the NE2001 thermal electron density model [247]. The disk field is confined to the x-y plane. For the distance for the Galactocentric radius $<$ 3kpc, the magnetic field strength is set to zero while for the 3kpc $\leq$ Galactocentric radius $\leq$ 5kpc are consistent with a 'molecular ring' with constant magnetic field strength. Starting from 5kpc to 20kpc, the magnetic field is modelled with eight logarithmic spiral regions,with the opening angle i = 11.5° [74]. The separations between the spiral arms follow the equation describes as,

$$r = r_{-x} exp\,(\phi tan(90^\circ - i)) \tag{B.1}$$

where, r_{-x} = 5.1, 6.3, 7.1, 8.3, 9.8, 11.4, 12.7, 15.5 kpc, which are the radii where the spiral arms cross the negative x-axis. The magnetic field strength of each of the spiral

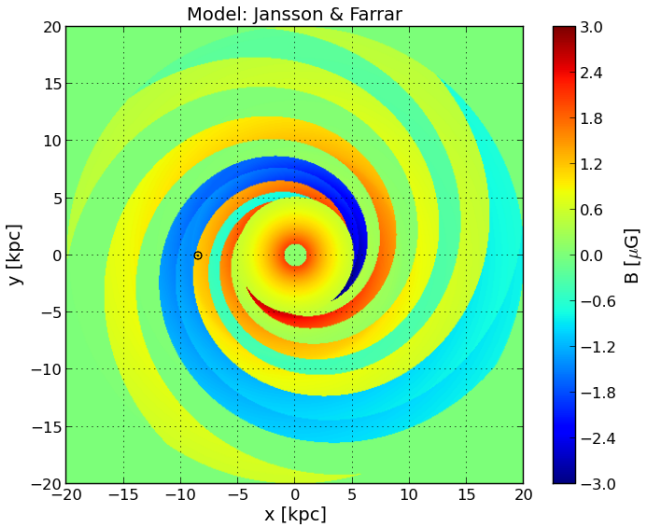

FIGURE B.1: Galactic disk model of the Galactic magnetic Field (Jansson &Farrar model) which is constrained to x-y plane with the galactic radius between 3 kpc and 20 kpc. The central "molecular ring" is stretched from Galactocentric radius 3 kpc to 5 kpc. Between the radius from 5 kpc to 20 kpc there are eight logarithmic spiral arms with an opening angle of 11.5°. The vertical colorbar represents the magnetic field intensity of the disk in the order of μG.

arms has been given in the corresponding article by Jansson and Farrar [74]. The disk field is extended symmetrically with respect to the mid-plane.

B.0.0.2 The halo field component

The halo component is completely toroidal with different field strengths (B_n, B_s) and radial extensions (r_n, r_s) north and south of the Galactic plane:

$$B_{\phi}^{halo}(r,z) = e^{-|z|/z_0} L(z, h_{disk}, w_{disk}) \times \begin{cases} B_n(1 - L(r, r_n, w_h)), & \text{if } z > 0 \\ B_s(1 - L(r, r_s, w_h)), & \text{if } z < 0 \end{cases} \tag{B.2}$$

This halo field has an exponential scale height with the unique field amplitudes in the north and south, B_n to be 1.4 μG and B_s to be -1.1 μG, respectively [74].

B.0.0.3 The out of the plane component

: The out of the plane component, also known as X-field, is to be asymmetric and poloidal. This adds the field strength from outside the galactic plane with a radial and z component. It has four free parameters like: constant elevation angle Θ_x^0 with respect to the mid plane, B_x, Galactocentric radius r_X^c and r_X [74].

For this thesis, the python scripts for the Galactic magnetic field model e.g. Jansson and Farrar model, are used from the article [44] [1].

The components of Jansson & Farrar large scale magnetic field has been updated with the polarized synchrotron and dust emission data measured with Planck satellite [81]. The field strength in the 2nd, 4th and 5th spiral arms have been changed by reducing inner Galaxy dust polarization, replacing synchrotron polarization and increasing high latitude polarization respectively, as mentioned in the Planck literature.

[1] https://github.com/me-manu/gmf

Appendix C

Fitted spectra for non-Galactic pulsar sources

This appendix summarizes the spectral fits to the high energy gamma-ray spectra which are used in Chapter 5 to calculate the combined photon-ALPs contour for non-Galactic sources. We have chosen eleven pulsar candidates which are modelled with power law with exponential cut off parametrization. A brief description for each individual sources has been listed in the section 5.3.1. The figure shows that the bright pulsar spectrum for different sources for the energy range from 100 MeV to 300 GeV. All the green points in each plot stands for the spectral points with the error bars while the red line stands for a spectral fit with the ALPs parameters e.g. $g_{a\gamma\gamma}$ and m_a. Besides, the blue line corresponds to the spectral fit without ALPs parameters. Notably, for all the pulsar spectra, we get a reasonable significance for the fit including the ALPs parameters. The ALPs parameter scan for individual sources has been also portrayed just next to the spectrum of each pulsar.

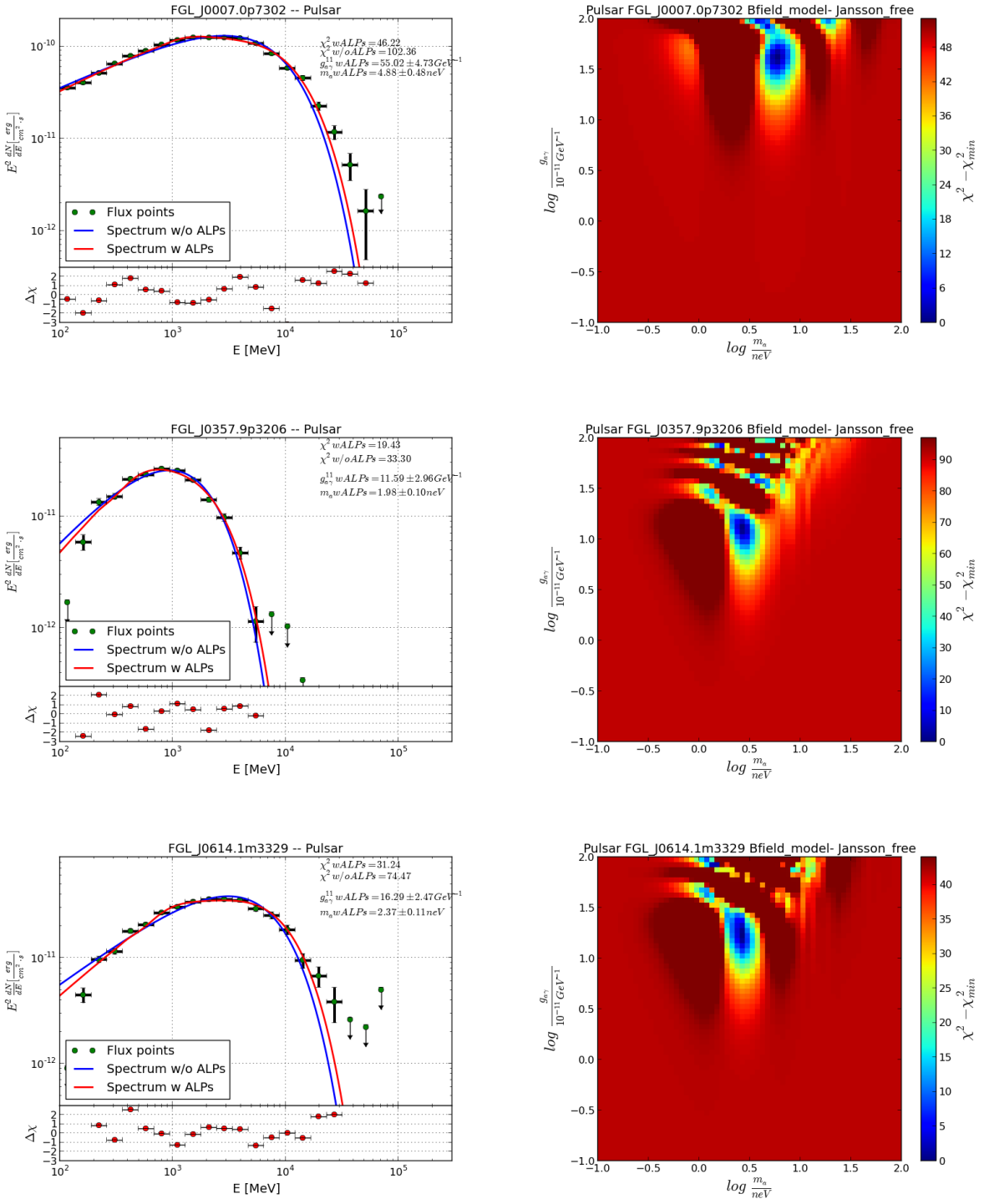

FIGURE C.1: Left panel: Best fit model of the pulsar spectrum (blue line: without ALPs parameters; red line: with ALPs parameters). The relative deviations between the flux points and the spectrum modelled with ALPs parameters have shown in the lower panel of each source. Right panel: A scan of spectrum as a function of ALPs parameters i.e. $g_{a\gamma\gamma}$ and m_a.

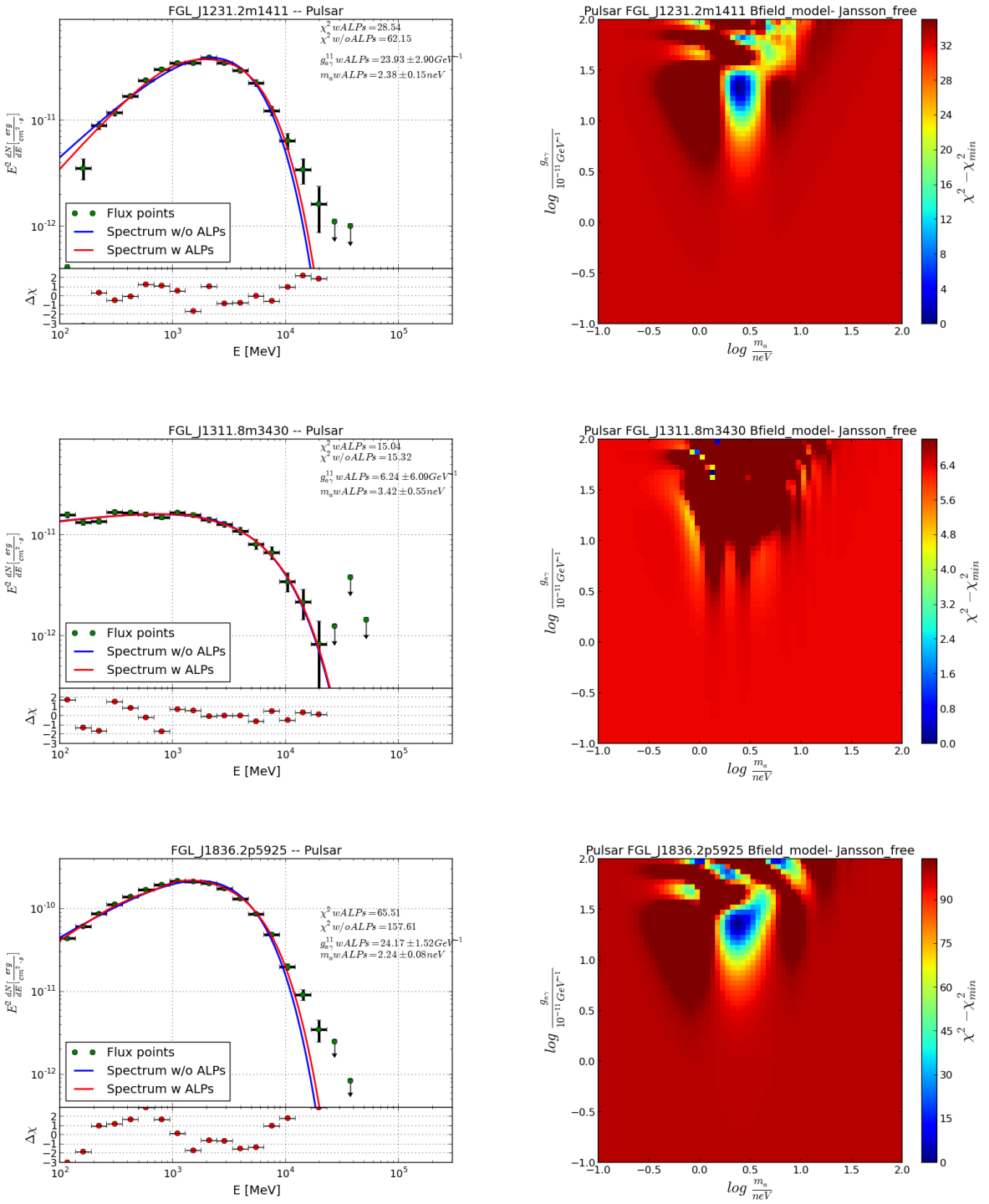

FIGURE C.2: Similar to the figure C.1 with different pulsar sources.

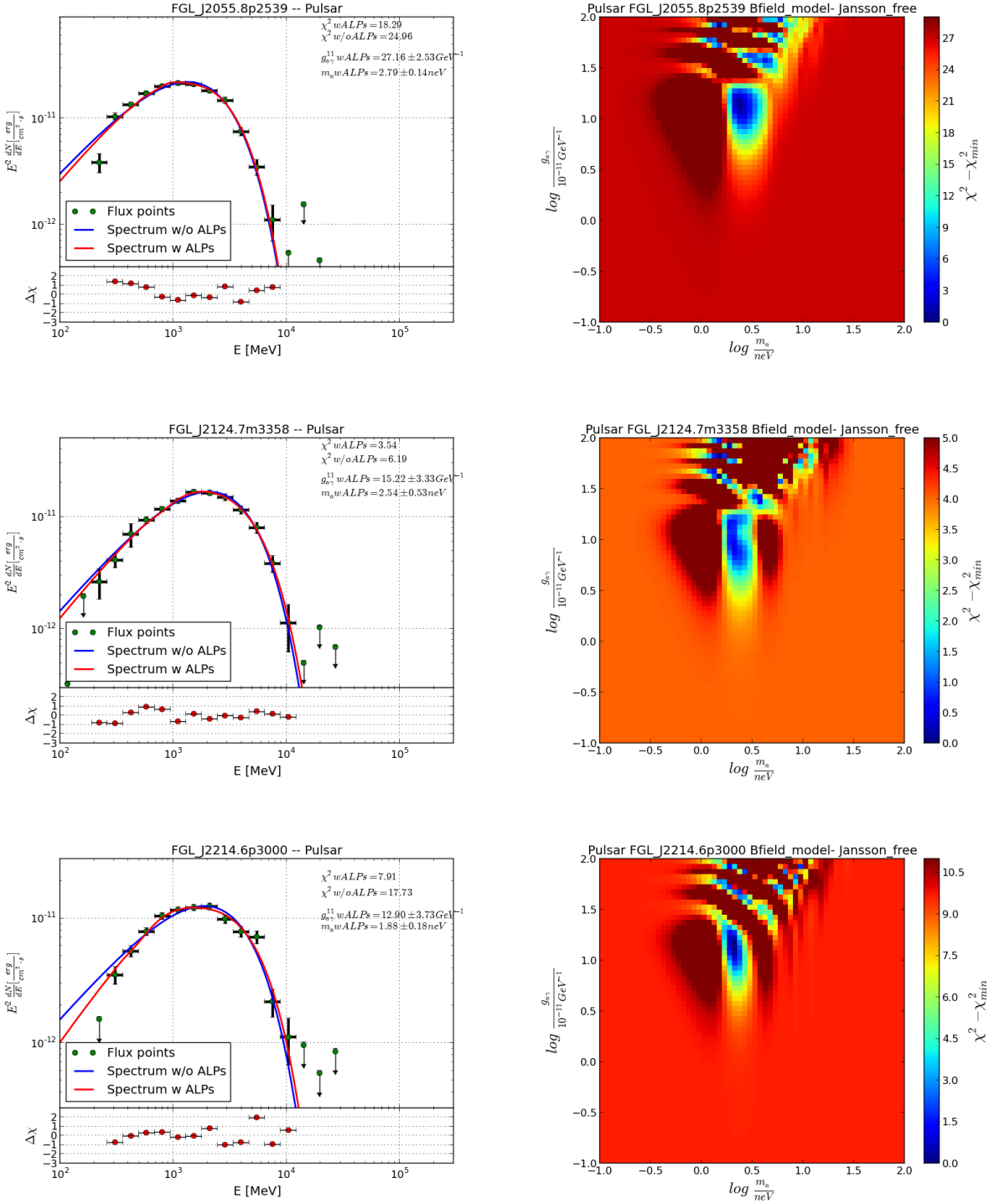

FIGURE C.3: Similar to the figure C.1 with different pulsar sources.

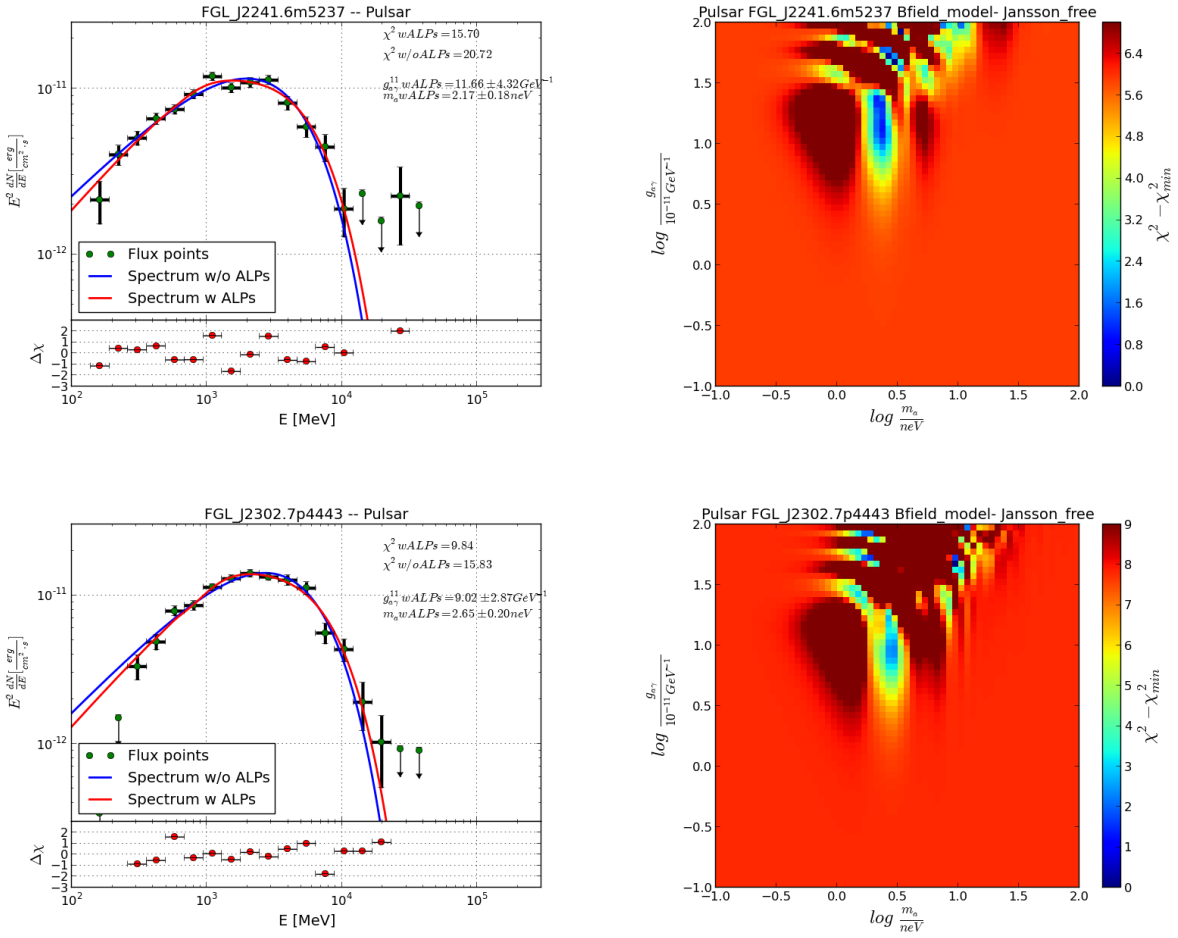

FIGURE C.4: Similar to the figure C.1 with different pulsar sources.

Appendix D

Non-Galactic plane sources spectra with LogParabola parametrization.

The bright non-Galactic plane source spectrum has been shown here. The most bright Fermi-LAT sources has been taken as candidates. These sources are modelled with a LogParabola parametrization. The source details are described in the table 5.2 and brief highlights on each source are mentioned in the section 5.3.2. Each figure contains green spectral points of the particular source from each energy bin including the errors. The spectral points are fitted to with a model with ALPs parameters e.g. photon-ALPs coupling constant ($g_{a\gamma\gamma}$) and the ALPs mass (m_a). The best fit $g_{a\gamma\gamma}$ and m_a values for each source are quoted in the corresponding figure.

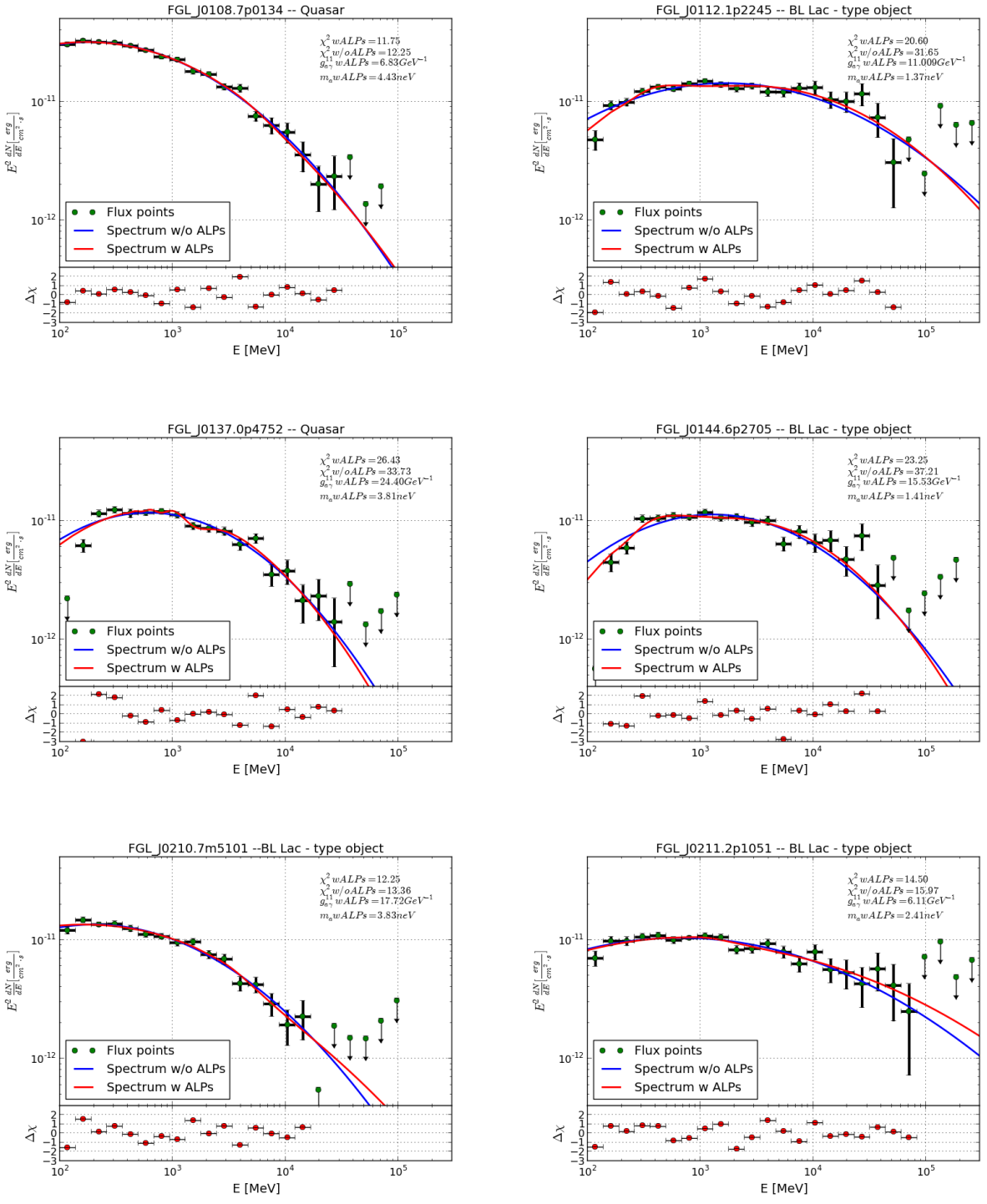

FIGURE D.1: Best fit model of the non-Galactic plane sources spectra (blue line: without ALPs parameters; red line: with ALPs parameters). The green points represent the flux in the each energy bin with the corresponding statistical errors. The relative deviations between the flux points and the spectrum modelled with ALPs parameters have shown in the lower panel of each figure.

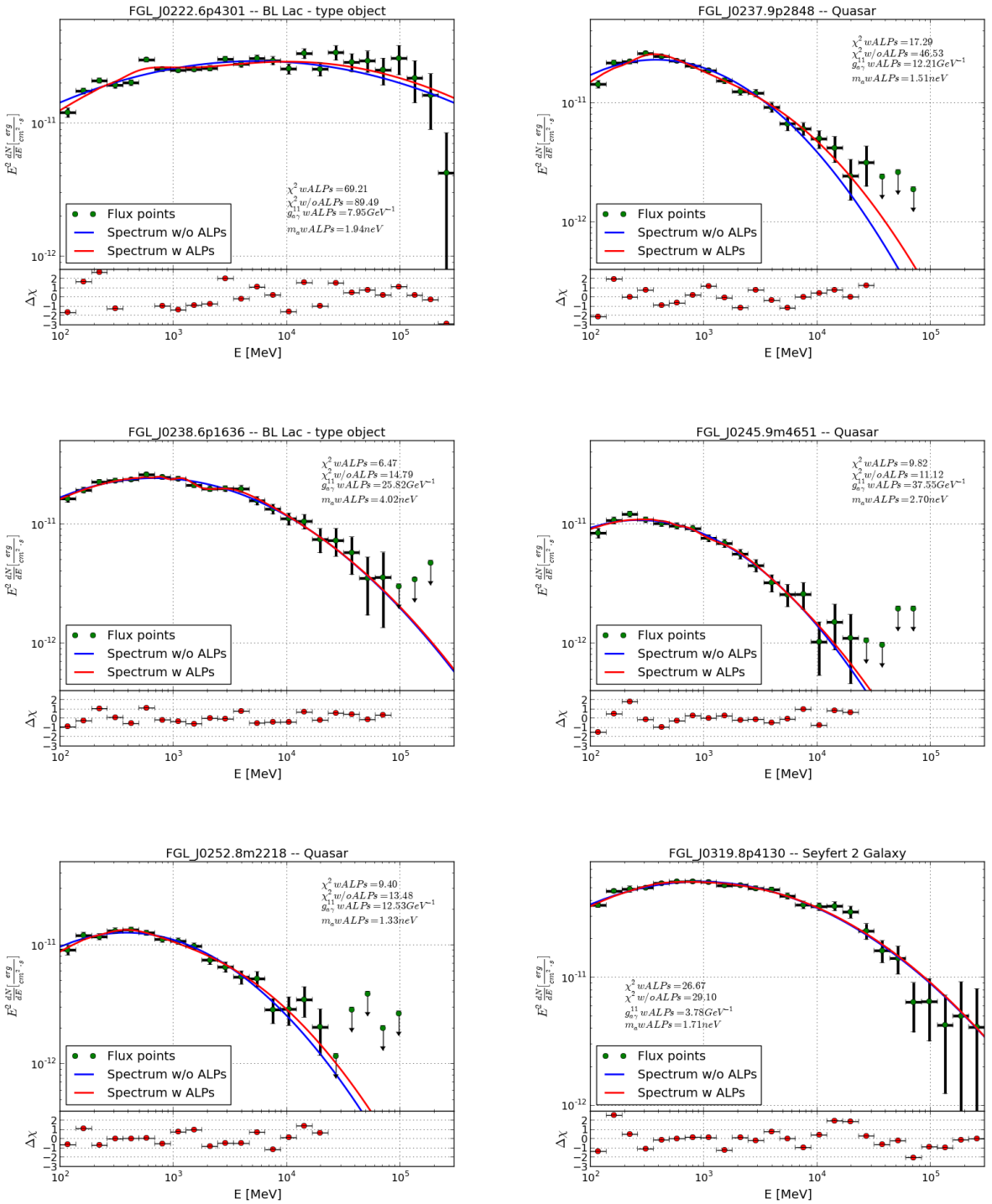

FIGURE D.2: Similar to the figure D.1 with different non-Galactic plane sources.

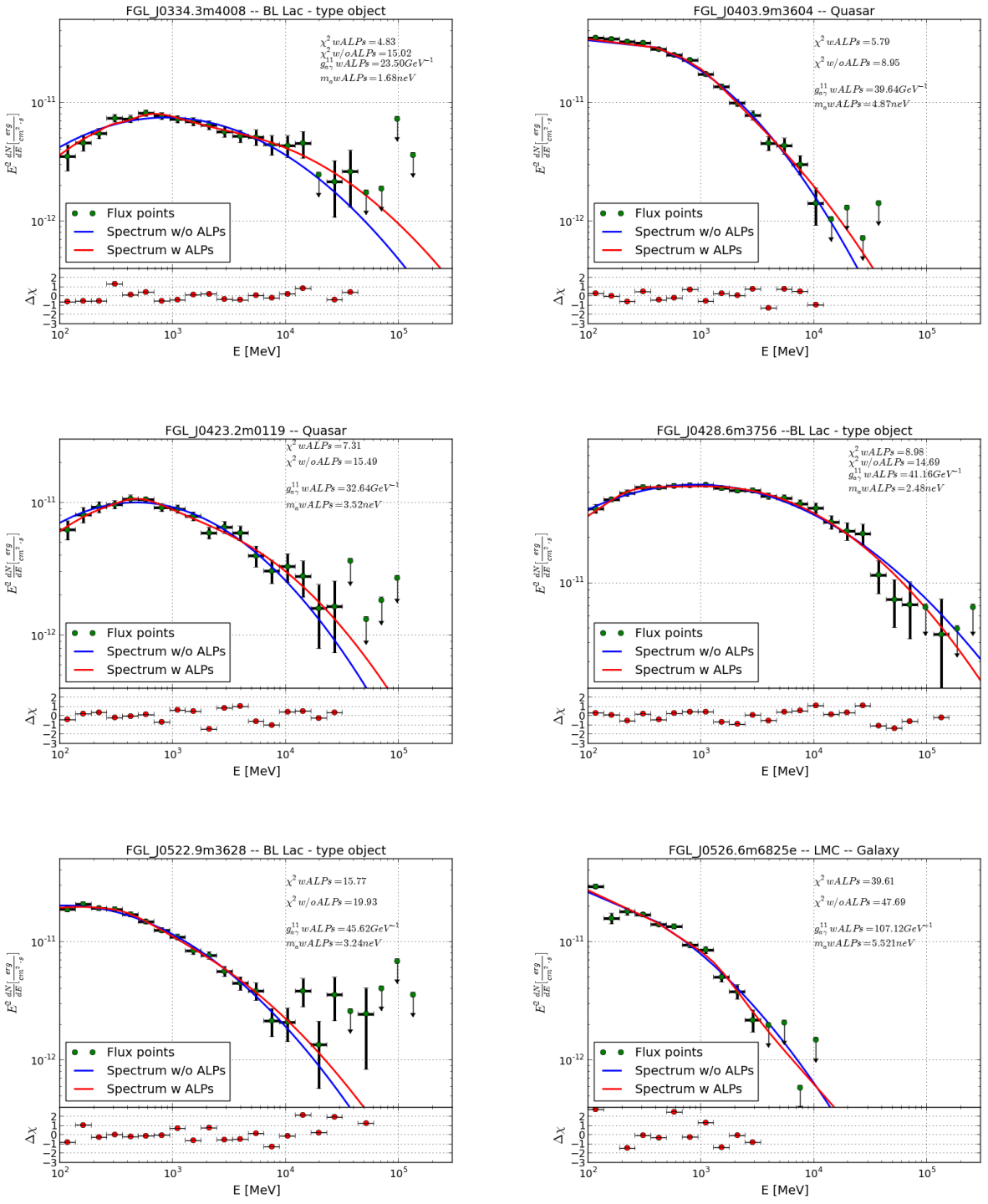

FIGURE D.3: Similar to the figure D.1 with different non-Galactic plane sources.

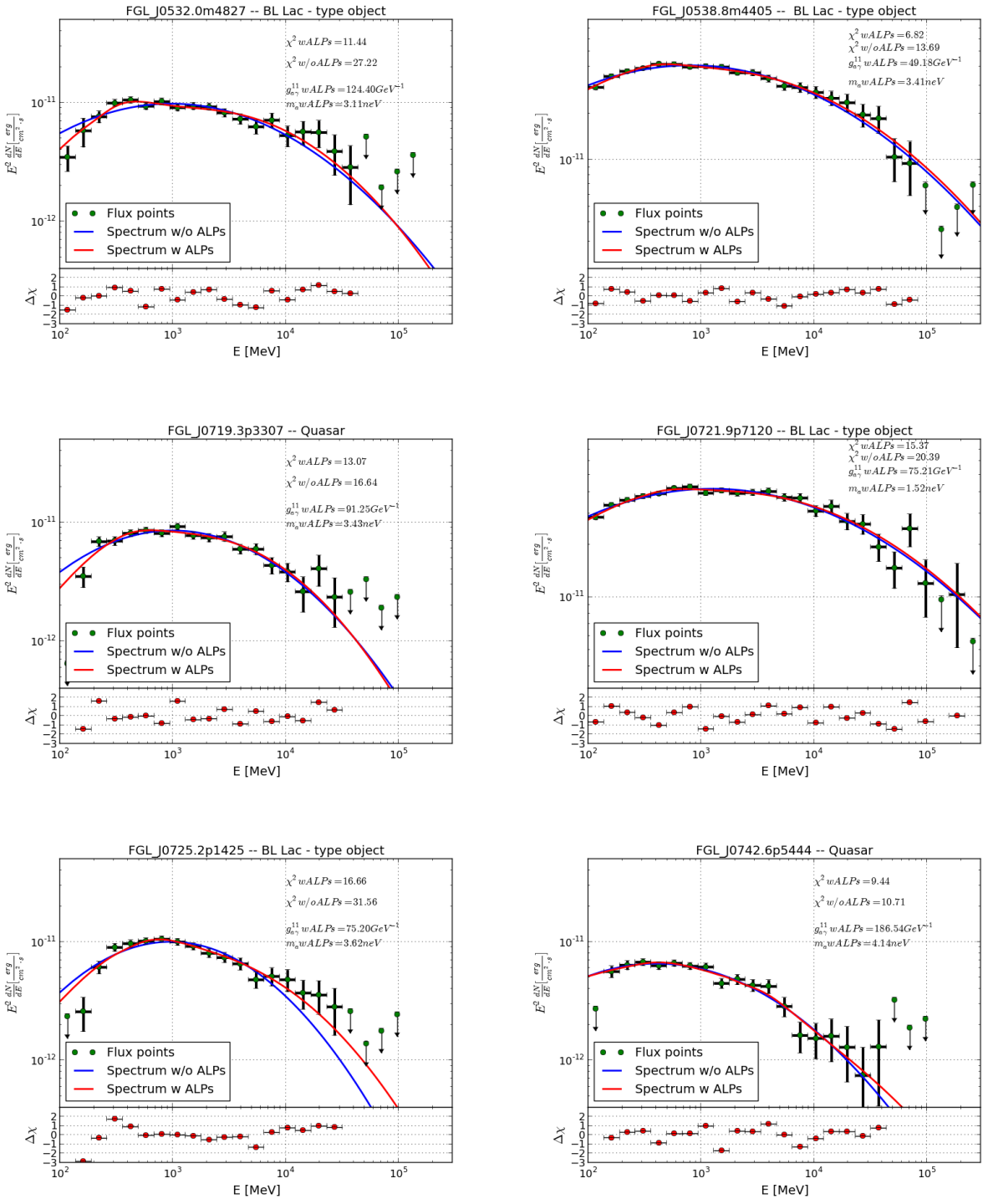

FIGURE D.4: Similar to the figure D.1 with different non-Galactic plane sources.

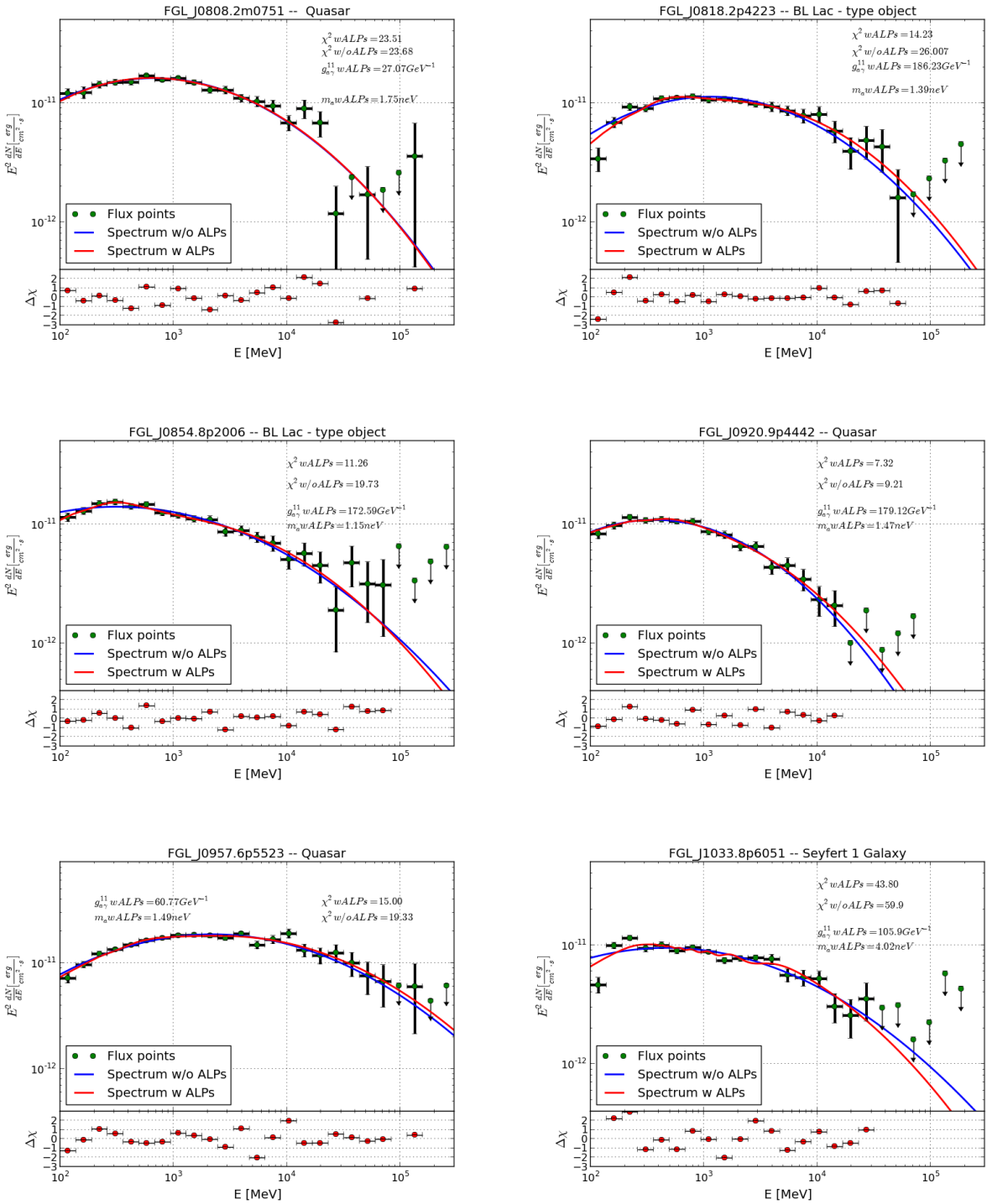

FIGURE D.5: Similar to the figure D.1 with different non-Galactic plane sources.

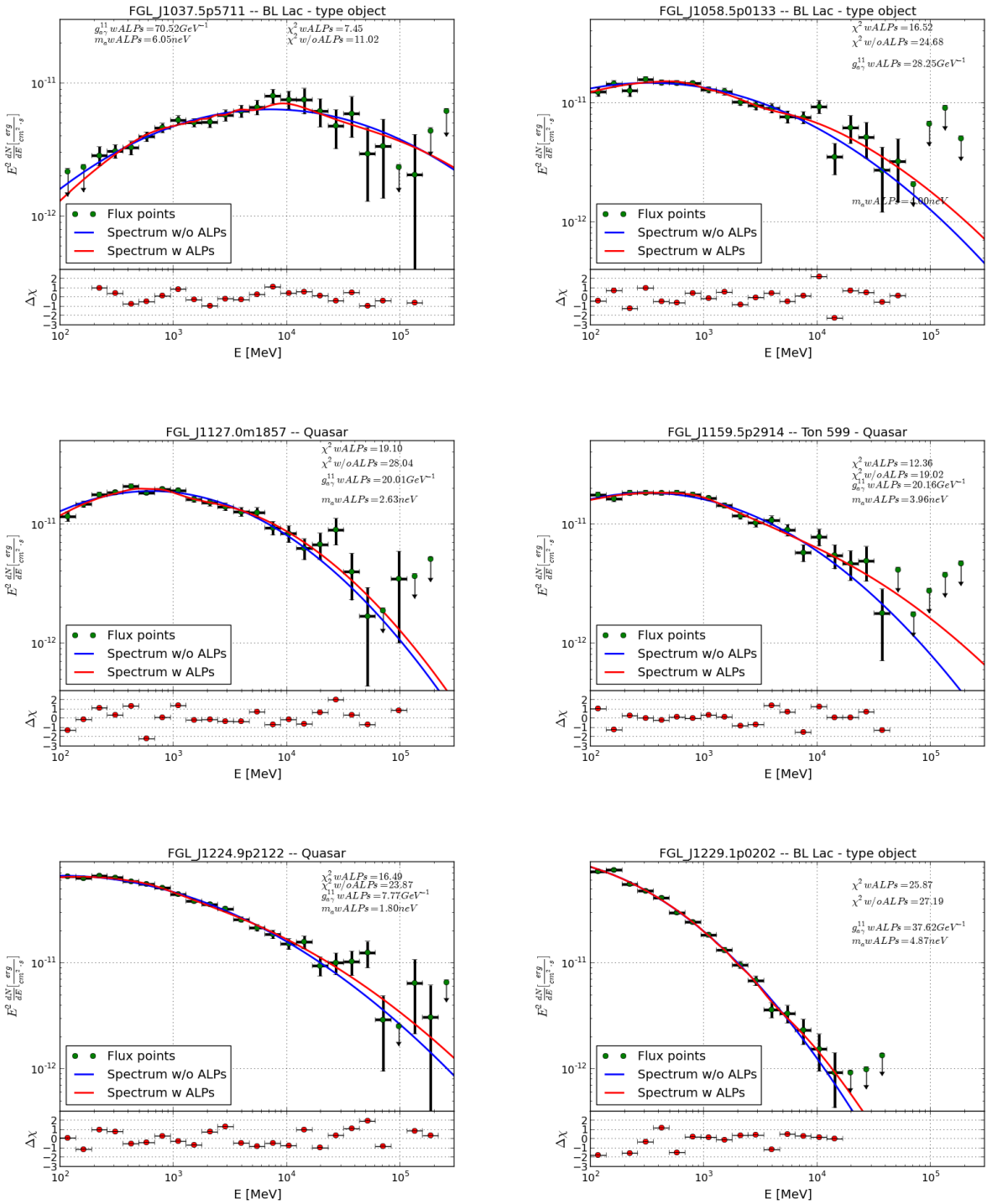

FIGURE D.6: Similar to the figure D.1 with different non-Galactic plane sources.

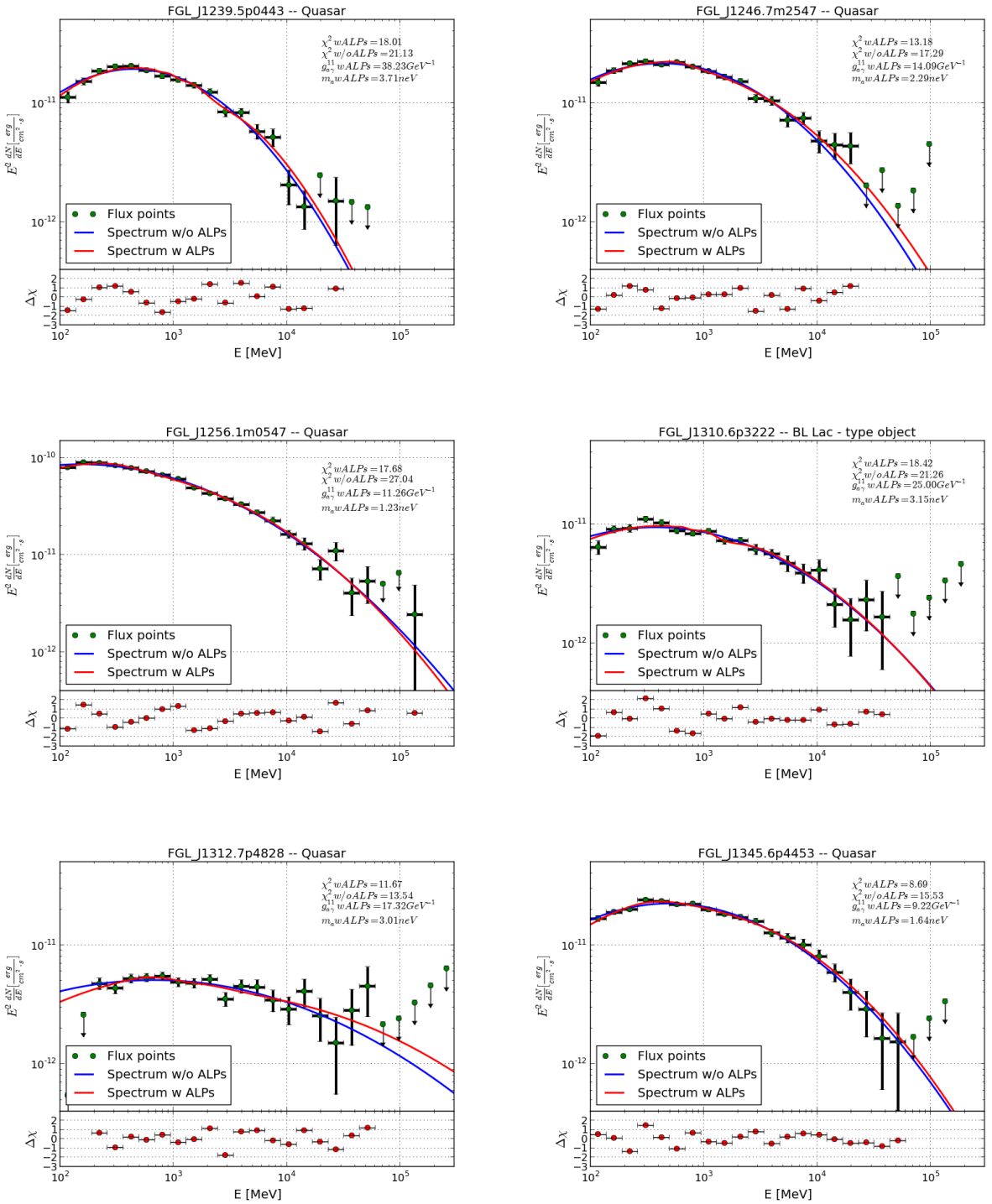

FIGURE D.7: Similar to the figure D.1 with different non-Galactic plane sources.

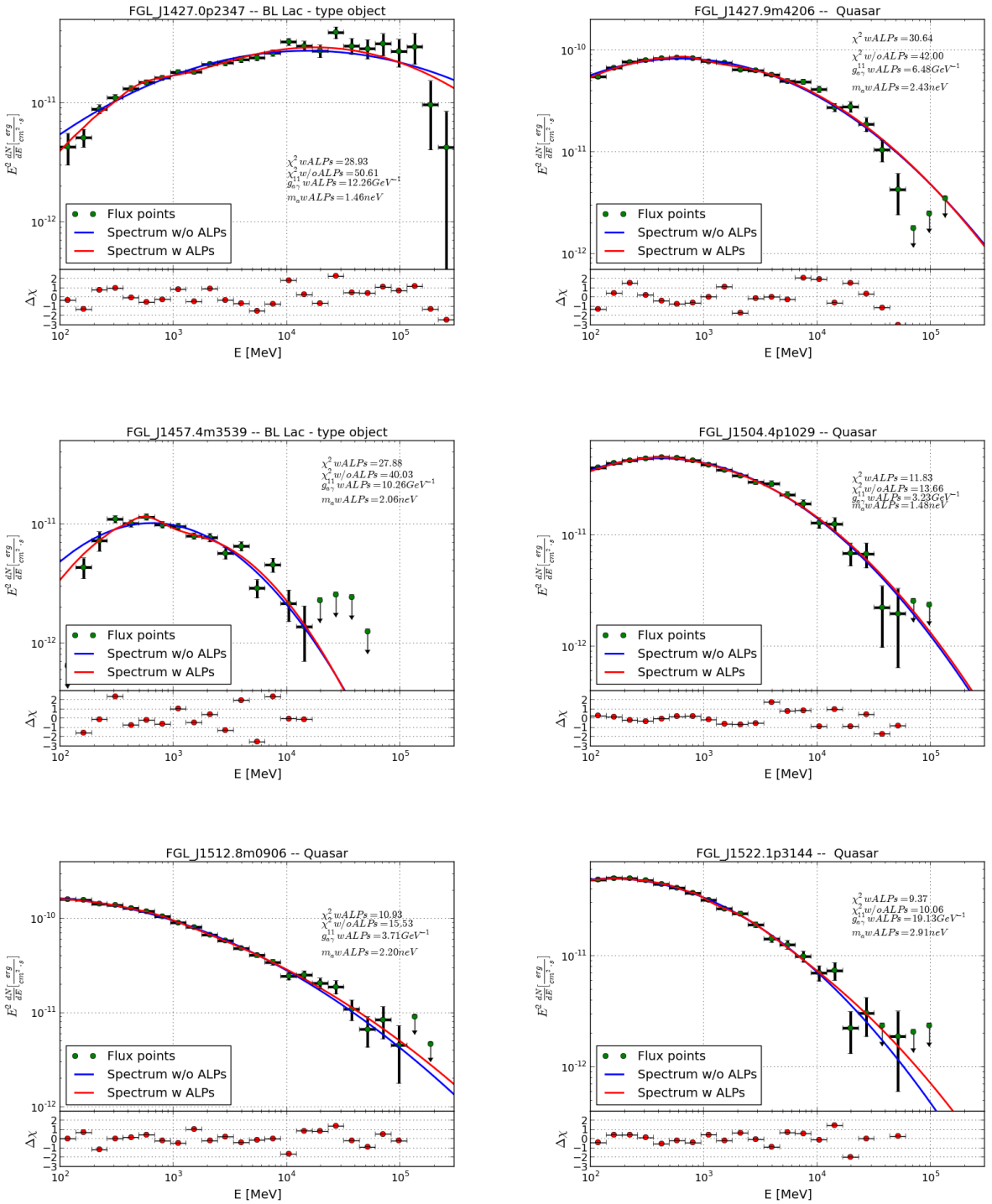

FIGURE D.8: Similar to the figure D.1 with different non-Galactic plane sources.

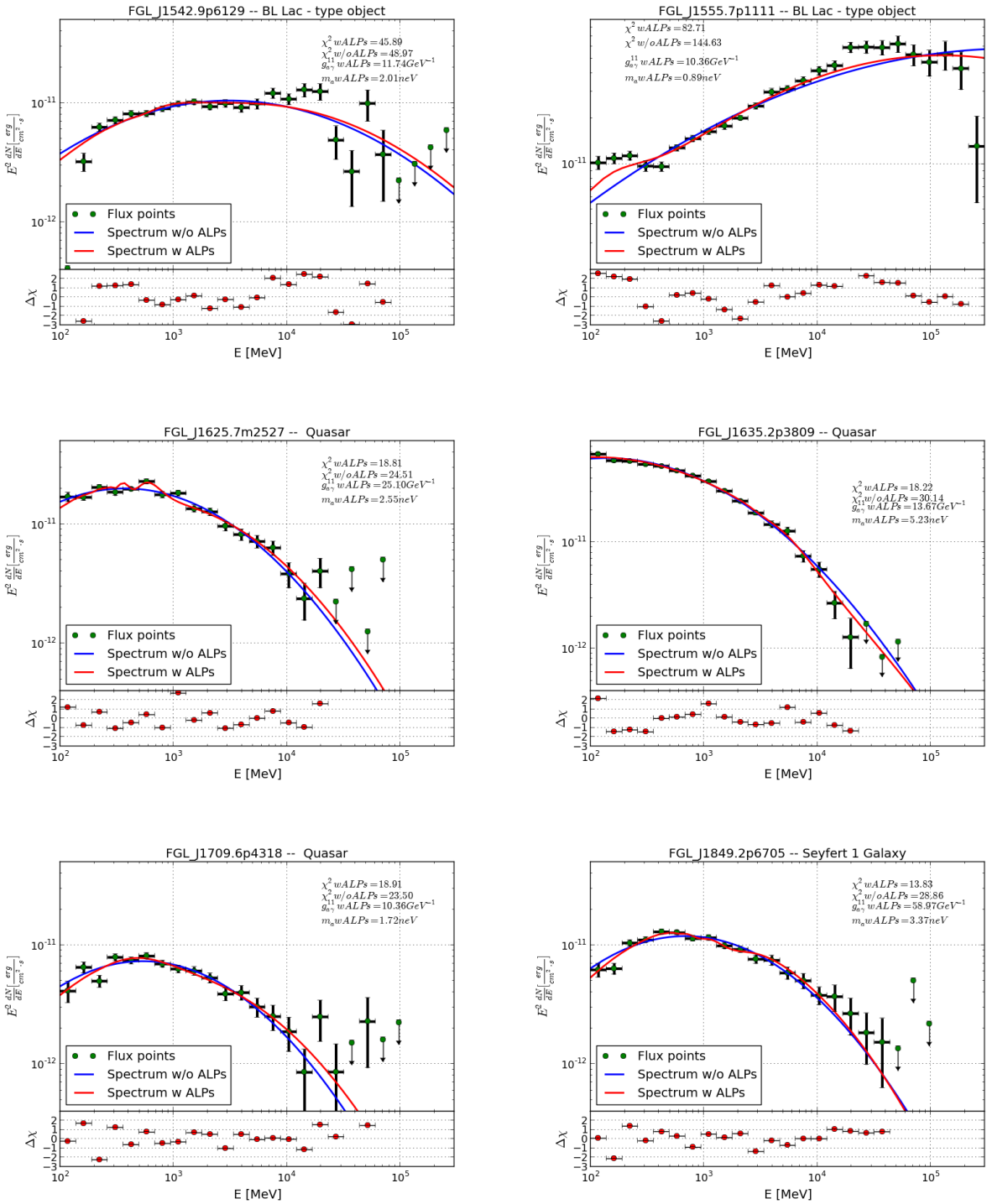

FIGURE D.9: Similar to the figure D.1 with different non-Galactic plane sources.

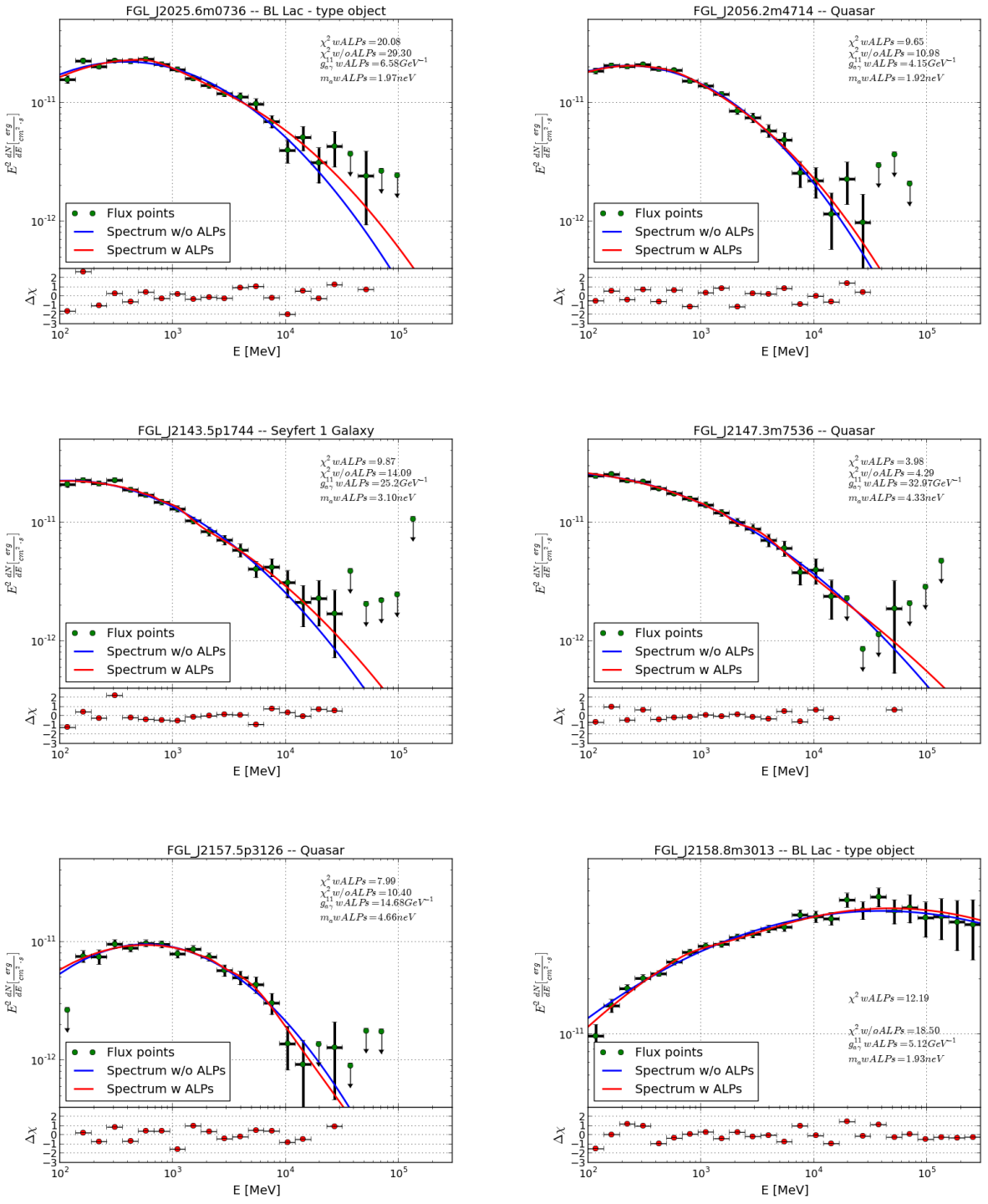

FIGURE D.10: Similar to the figure D.1 with different non-Galactic plane sources.

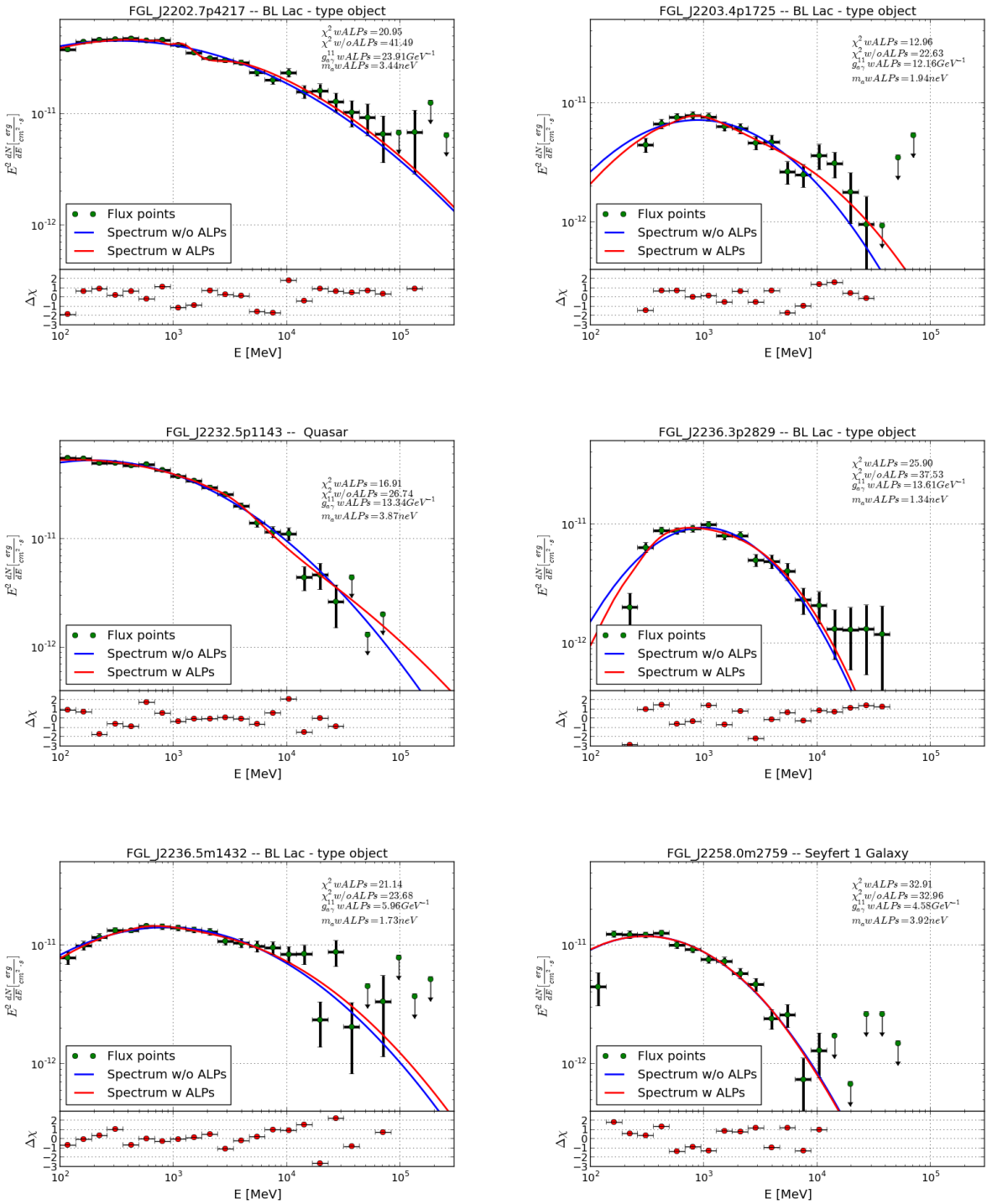

FIGURE D.11: Similar to the figure D.1 with different non-Galactic plane sources.

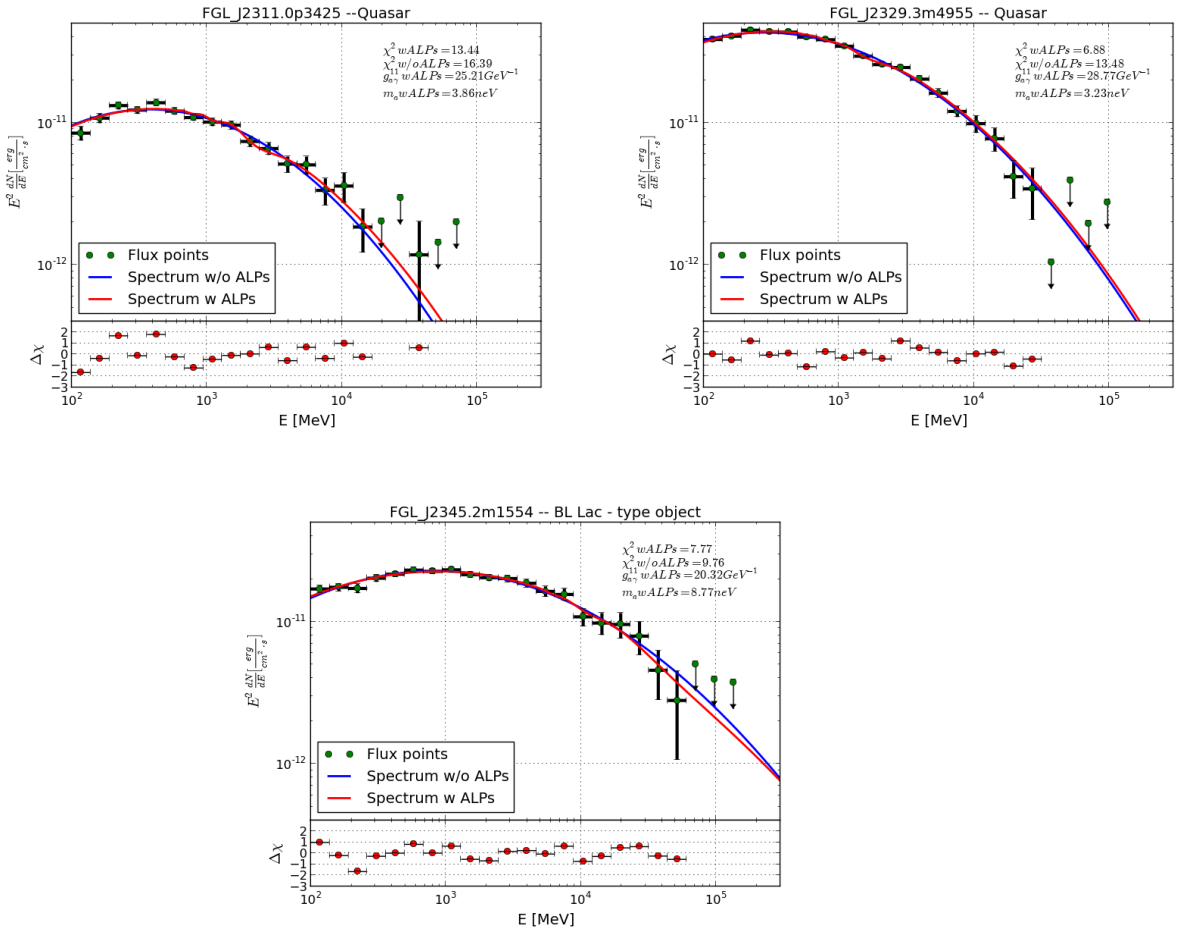

FIGURE D.12: Similar to the figure D.1 with different non-Galactic plane sources.

Appendix E

Broadband SED for blazars

The broadband SED for the very bright non-Galactic plane sources which are modelled with PowerLaw parametrization have been shown here. The source details are described in the table 5.2 & 5.3 and brief highlights on each source are mentioned in the section 5.3.2. We present the flux points of our analysis in magenta colored circles in each figure comparing our result with the other observational points.

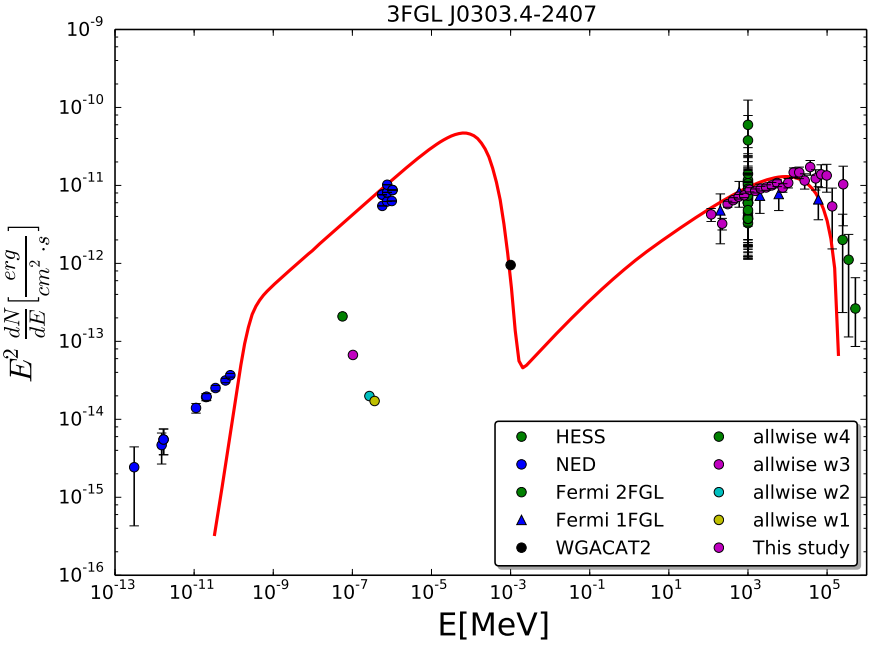

FIGURE E.1: Spectral energy distribution of the source 3FGL J0303-2407. The different color spectral points refers to the multi-wavelength observation for the source. The red line corresponds to a model that fits to the data points. The magenta points in the SED corresponds to the present analysis of 3FGL data with 25 energy bins.

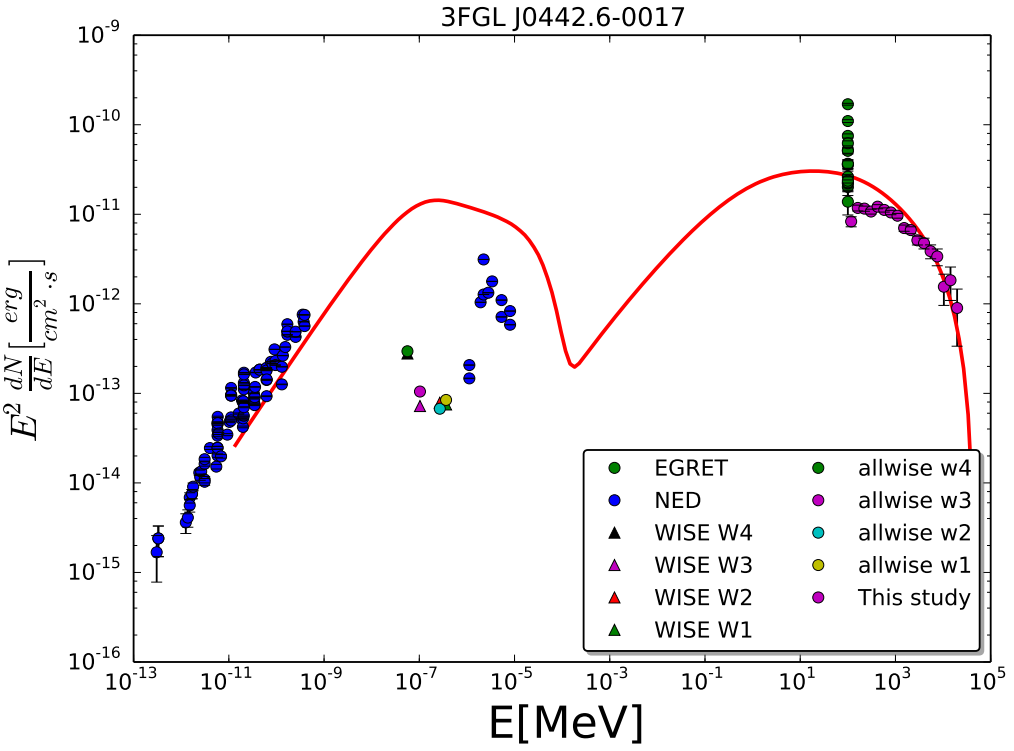

FIGURE E.2: Similar to the figure E.1 for the source 3FGL J0442-0017.

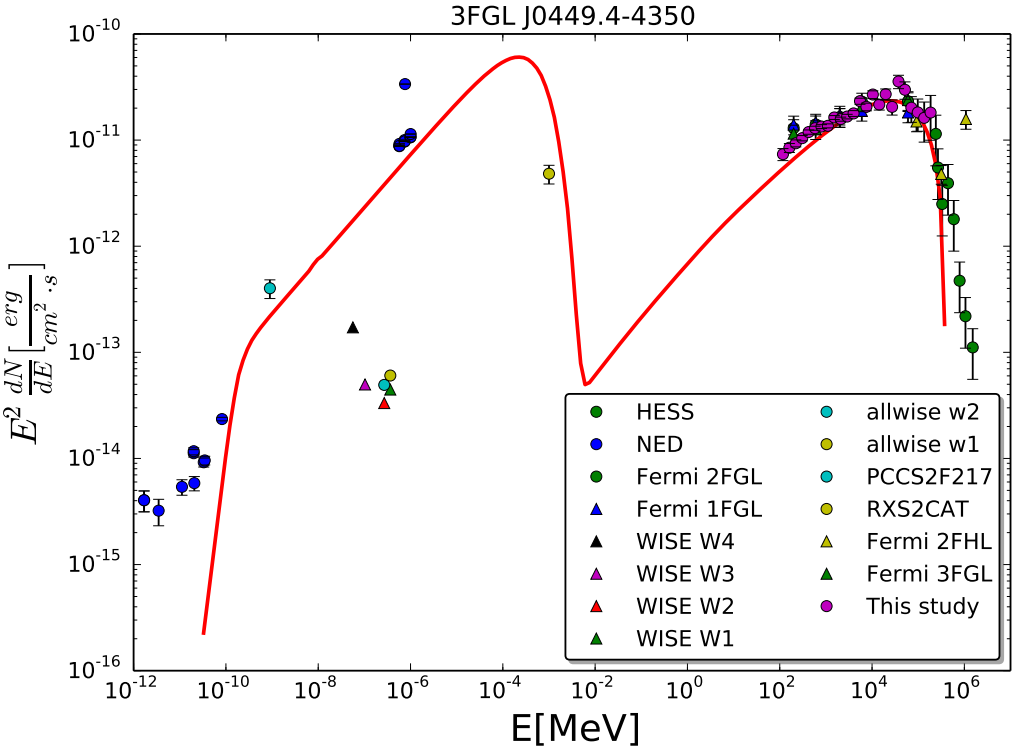

FIGURE E.3: Similar to the figure E.1 for the source 3FGL J0449-4350.

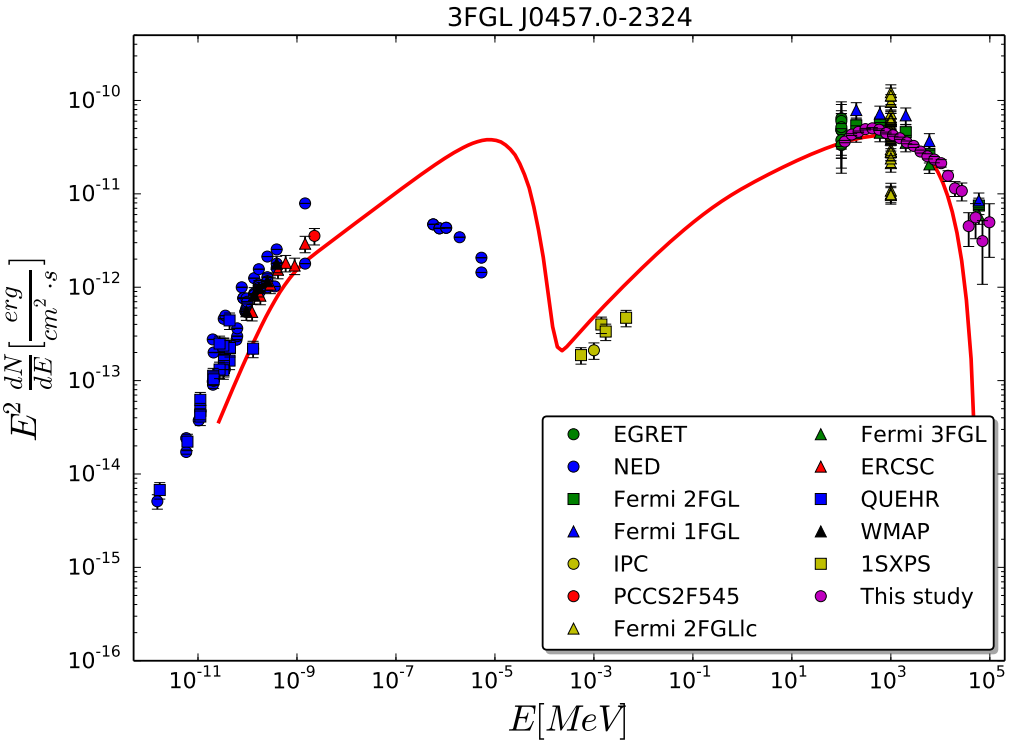

FIGURE E.4: Similar to the figure E.1 for the source 3FGL J0457-2324.

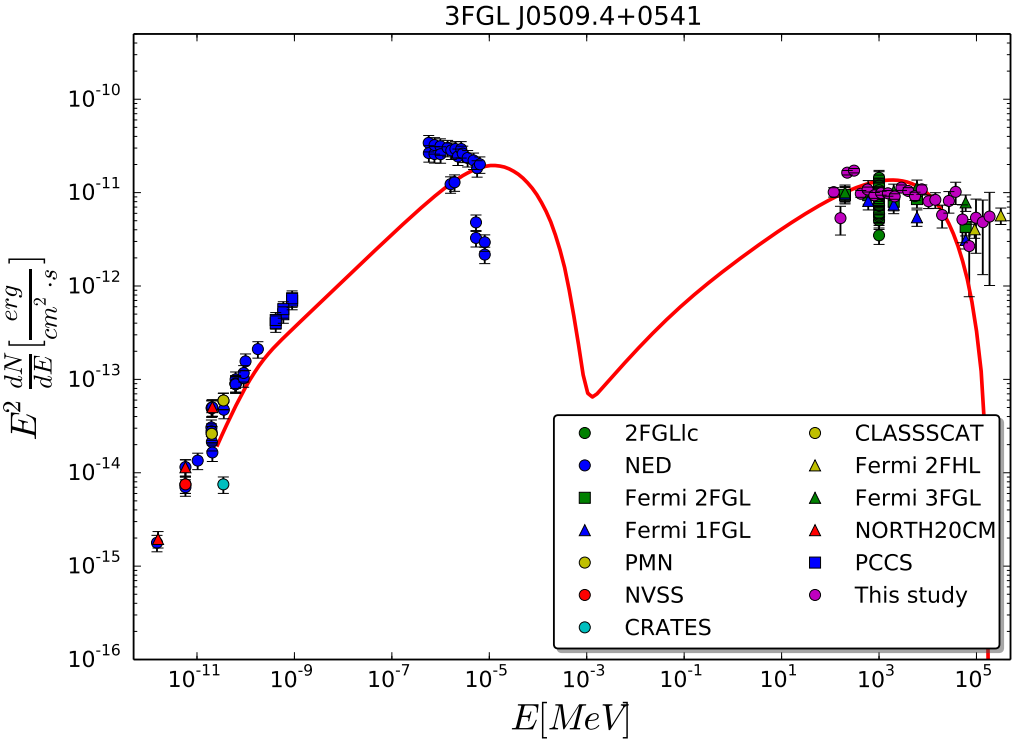

FIGURE E.5: Similar to the figure E.1 for the source 3FGL J0509+0541.

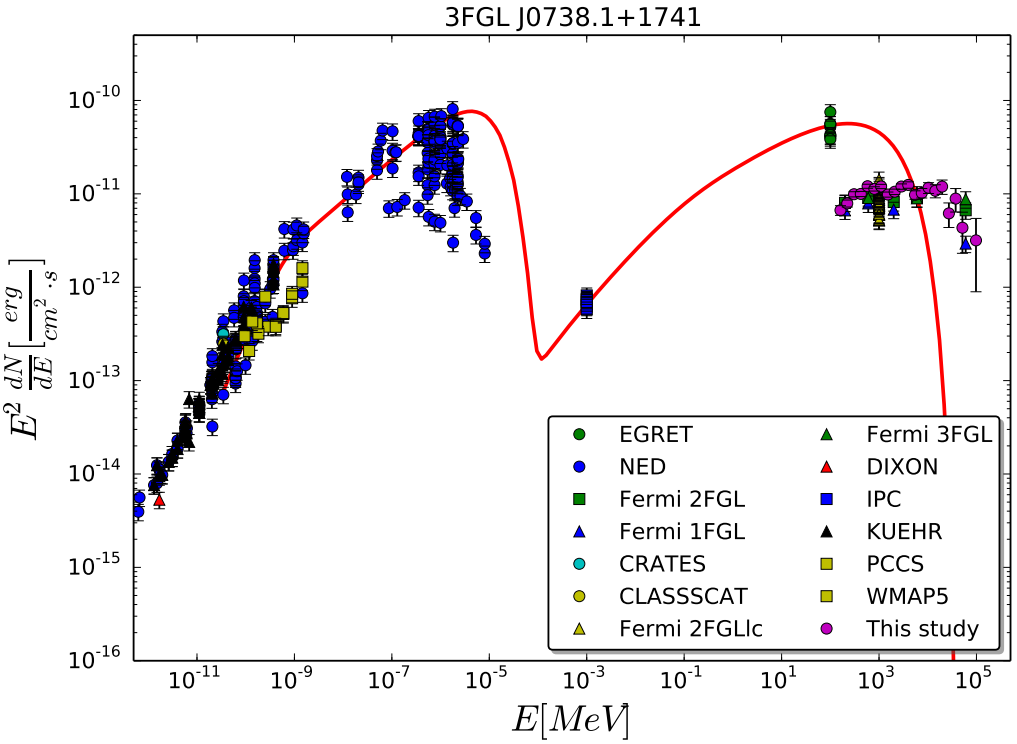

FIGURE E.6: Similar to the figure E.1 for the source 3FGL J0738+1741.

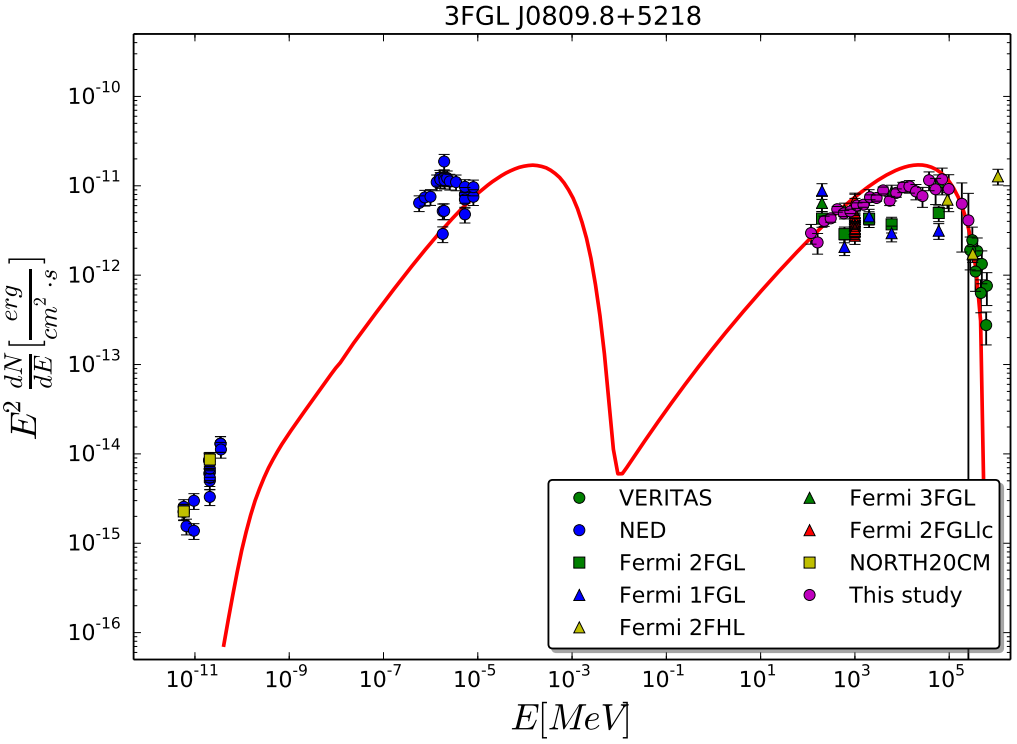

FIGURE E.7: Similar to the figure E.1 for the source 3FGL J0809+5218.

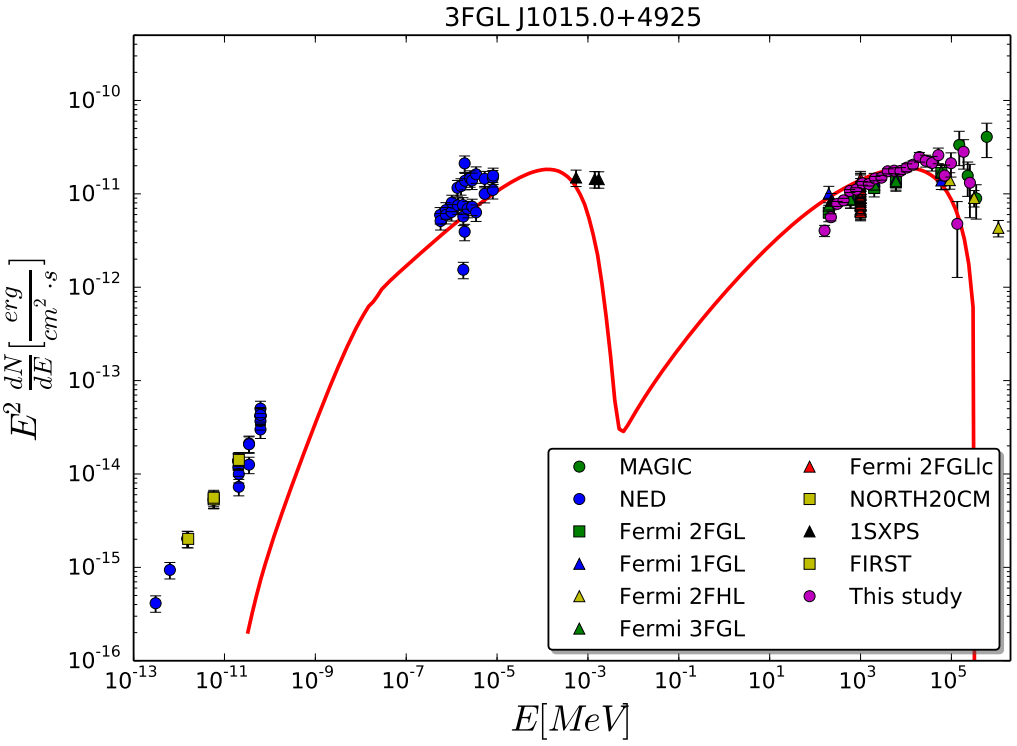

FIGURE E.8: Similar to the figure E.1 for the source 3FGL J1015+4925.

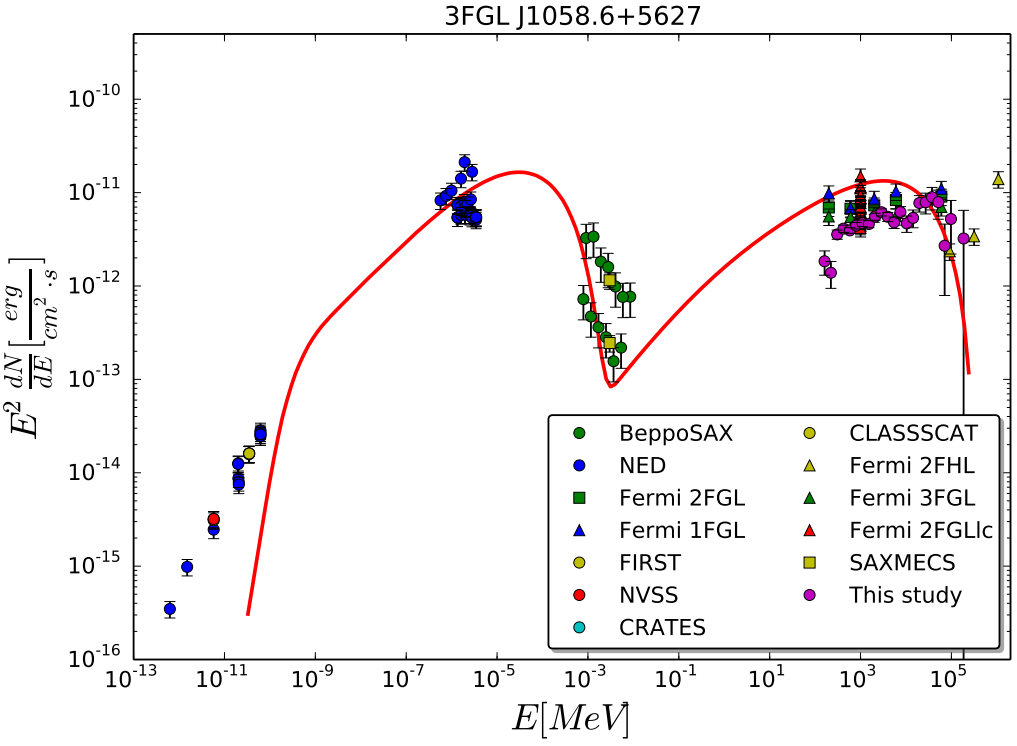

FIGURE E.9: Similar to the figure E.1 for the source 3FGL J1058+5627.

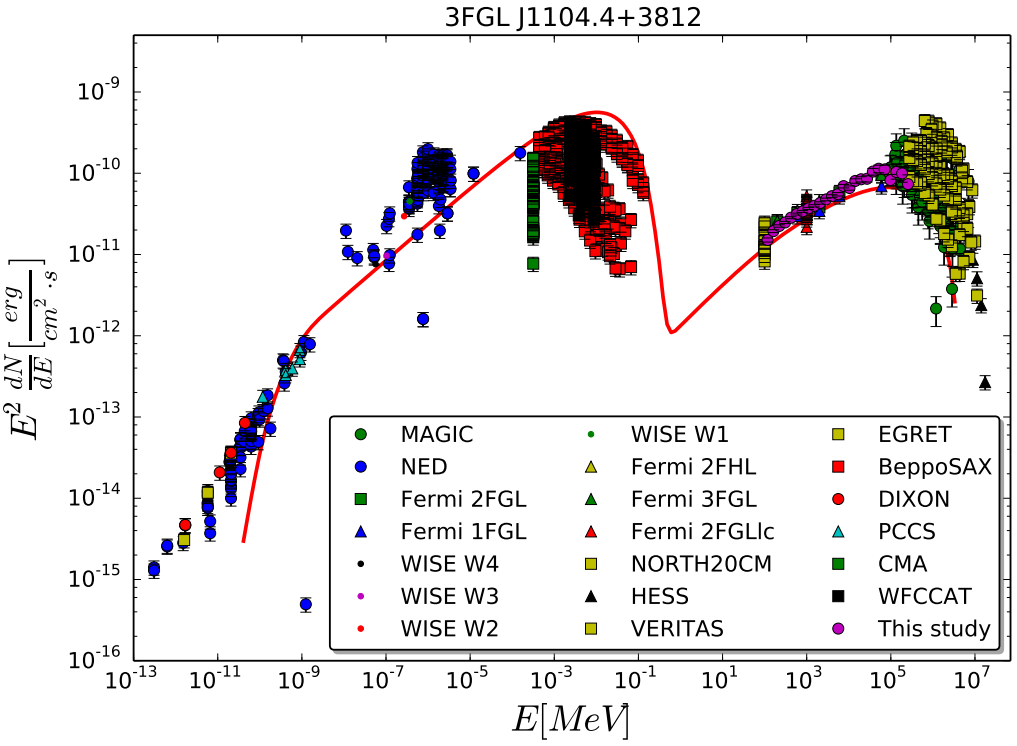

FIGURE E.10: Similar to the figure E.1 for the source 3FGL J1104+3812.

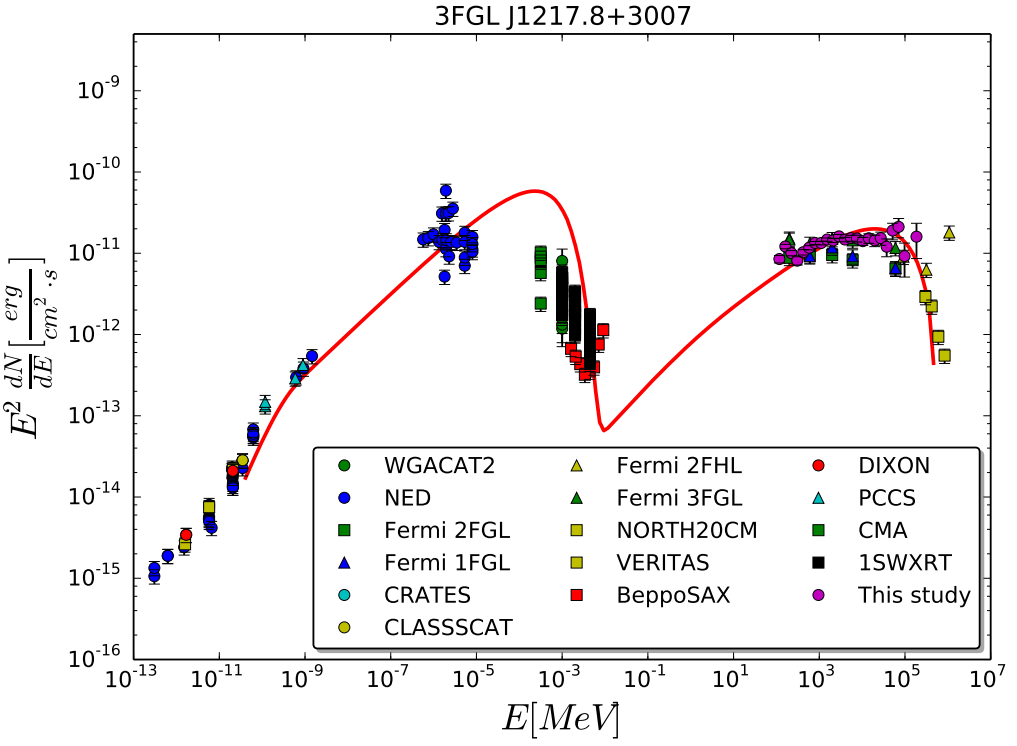

FIGURE E.11: Similar to the figure E.1 for the source 3FGL J1217+3007.

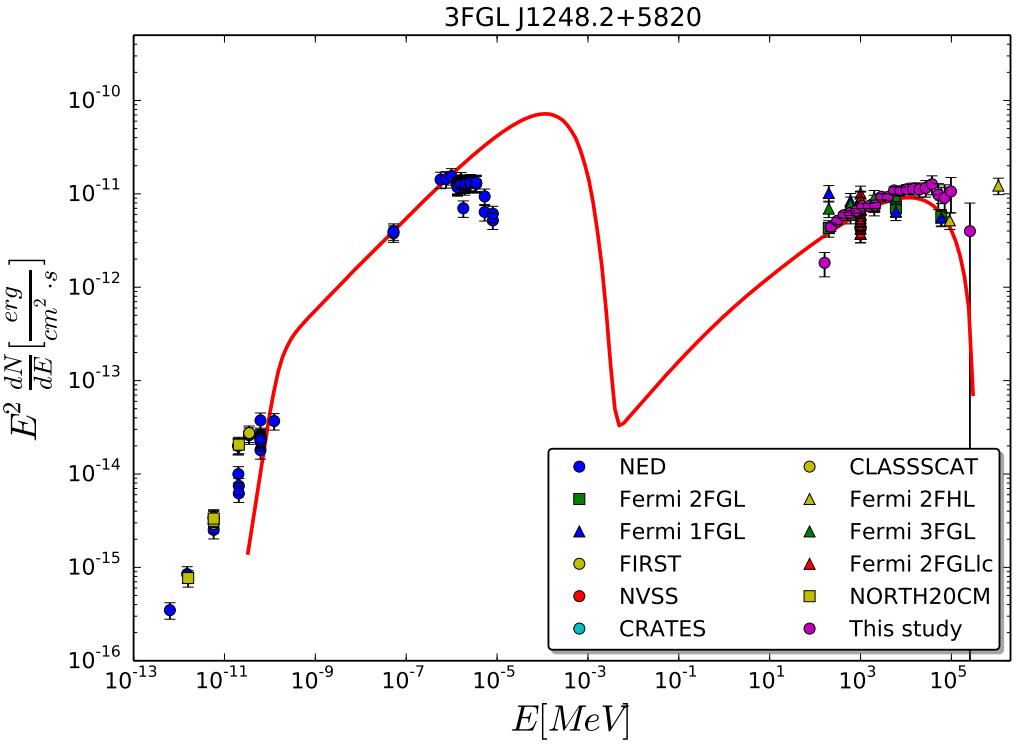

FIGURE E.12: Similar to the figure E.1 for the source 3FGL J1248+5820.

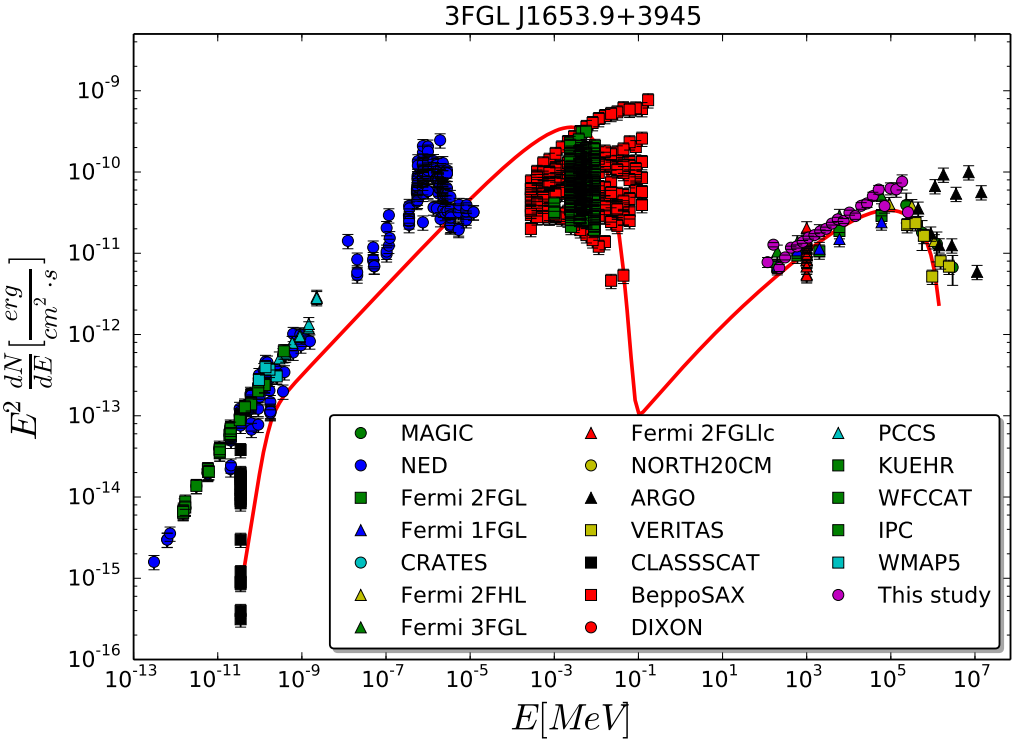

FIGURE E.13: Similar to the figure E.1 for the source 3FGL J1653+3945.

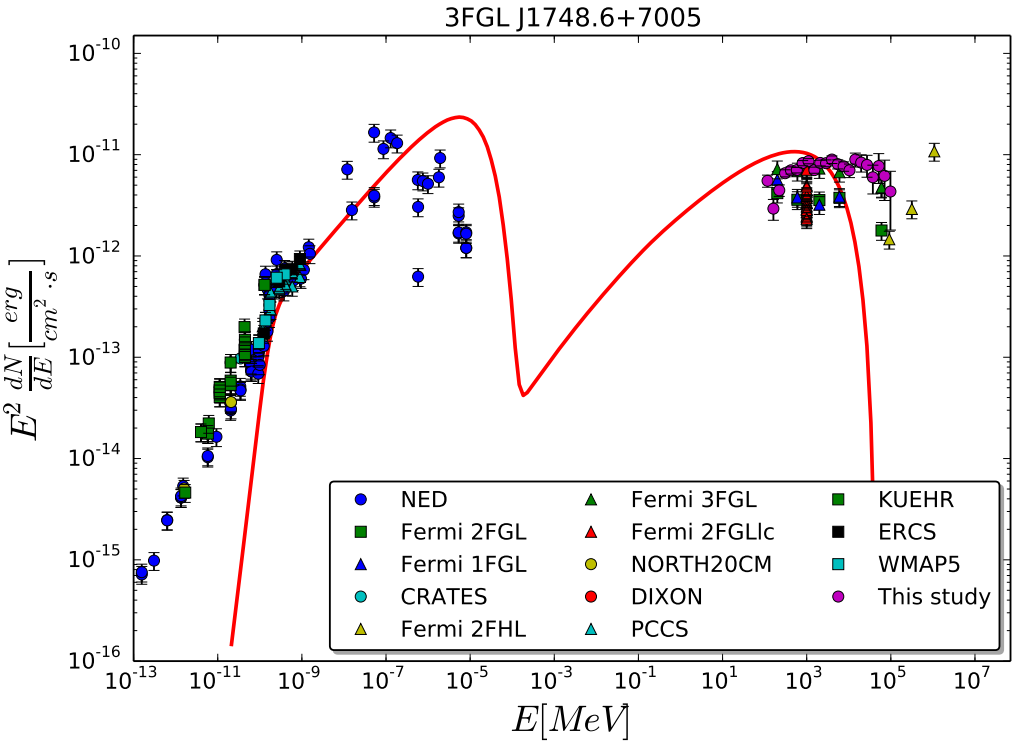

FIGURE E.14: Similar to the figure E.1 for the source 3FGL J1748+7005.

Appendix F

Acronyms

SM	Standard model
BSM	Beyond standard model
DM	Dark matter
CDM	Cold dark matter
ALPs	Axion like particles
SMBH	Supermassive black hole
BL Lac	BL Lacertae
FSRQ	Flat spectrum radio quasar
LBL	Low-frequency peaked BL Lacs
HBL	High-frequency peaked BL Lacs
LSP	Low synchrotron peaked
ISP	Intermediate synchrotron peaked
HSP	High synchrotron peaked
LAT	Large area telescope
PSF	Point spread function
HESS	High Energy Stereoscopic System
SED	Spectral energy distribution
GMF	Galactic magnetic field
HE	High energy
VHE	Very high energy
TS	Test statistics
ALPS	Any Light Particle Search
SSC	Synchrotron-self-Compton
ICS	Inverse Compton scattering
SDSS	Sloan Digital Sky Survey
EBL	Extragalactic background light
LSW	Light shining through wall

List of Figures

List of Tables

Bibliography

[1] Y. Sofue and V. Rubin, "Rotation Curves of Spiral Galaxies," *Annual Review of Astronomy and Astrophysics*, vol. 39, pp. 137–174, 2001.

[2] A. B. Newman, T. Treu, R. S. Ellis, and D. J. Sand, "The Density Profiles of Massive, Relaxed Galaxy Clusters. II. Separating Luminous and Dark Matter in Cluster Cores," *The Astrophysical Journal*, vol. 765, p. 25, Mar. 2013.

[3] M. Kamionkowski, "WIMP and Axion Dark Matter," in *High Energy Physics and Cosmology, 1997 Summer School* (E. Gava, A. Masiero, K. S. Narain, S. Randjbar-Daemi, G. Senjanovic, A. Smirnov, and Q. Shafi, eds.), p. 394, 1998.

[4] H. Gursky, "The x-ray emission from rich clusters of galaxies," *Publications of the Astronomical Society of the Pacific*, vol. 85, no. 507, p. 493, 1973.

[5] E. Kellogg, S. Murray, R. Giacconi, T. Tananbaum, and H. Gursky, "Clusters of Galaxies with a Wide Range of X-Ray Luminosities," *Astrophysical Journal*, vol. 185, p. L13, Oct. 1973.

[6] D. Fabricant, M. Lecar, and P. Gorenstein, "X-ray measurements of the mass of M87," *Astrophysical Journal*, vol. 241, pp. 552–560, Oct. 1980.

[7] J. A. Tyson, G. P. Kochanski, and I. P. Dell'Antonio, "Detailed Mass Map of CL 0024+1654 from Strong Lensing," *The Astrophysical Journal*, vol. 498, pp. L107–L110, May 1998.

[8] R. Massey, T. Kitching, and J. Richard, "The dark matter of gravitational lensing," *Reports on Progress in Physics*, vol. 73, p. 086901, Aug. 2010.

[9] W. Hu and S. Dodelson, "Cosmic Microwave Background Anisotropies," *Annual Review of Astronomy and Astrophysics*, vol. 40, pp. 171–216, 2002.

[10] D. J. Fixsen, E. S. Cheng, J. M. Gales, J. C. Mather, R. A. Shafer, and E. L. Wright, "The Cosmic Microwave Background Spectrum from the Full COBE FIRAS Data Set," *The Astrophysical Journal*, vol. 473, p. 576, Dec. 1996.

[11] C. L. Bennett, M. Halpern, G. Hinshaw, N. Jarosik, A. Kogut, M. Limon, S. S. Meyer, L. Page, D. N. Spergel, G. S. Tucker, E. Wollack, E. L. Wright, C. Barnes, M. R. Greason, R. S. Hill, E. Komatsu, M. R. Nolta, N. Odegard, H. V. Peiris, L. Verde, and J. L. Weiland, "First-Year Wilkinson Microwave Anisotropy Probe (WMAP) Observations: Preliminary Maps and Basic Results," *The Astrophysical Journal Supplement Series*, vol. 148, pp. 1–27, Sept. 2003.

[12] M. R. Nolta, E. L. Wright, L. Page, C. L. Bennett, M. Halpern, G. Hinshaw, N. Jarosik, A. Kogut, M. Limon, S. S. Meyer, D. N. Spergel, G. S. Tucker, and E. Wollack, "First Year Wilkinson Microwave Anisotropy Probe Observations: Dark Energy Induced Correlation with Radio Sources," *The Astrophysical Journal*, vol. 608, pp. 10–15, June 2004.

[13] G. R. Blumenthal, S. M. Faber, J. R. Primack, and M. J. Rees, "Formation of Galaxies and Large Scale Structure with Cold Dark Matter," *Nature*, vol. 311, pp. 517–525, 1984.

[14] E. W. Kolb and M. S. Turner, "The Early Universe," *Front. Phys.*, vol. 69, pp. 1–547, 1990.

[15] T. Bringmann and C. Weniger, "Gamma Ray Signals from Dark Matter: Concepts, Status and Prospects," *Phys. Dark Univ.*, vol. 1, pp. 194–217, 2012.

[16] N. Craig, "The State of Supersymmetry after Run I of the LHC," *ArXiv e-prints*, Sept. 2013.

[17] J. Jaeckel and A. Ringwald, "The low-energy frontier of particle physics," *Annual Review of Nuclear and Particle*, vol. 60:405-437, November.

[18] R. D. Peccei and H. R. Quinn, "CP conservation in the presence of pseudoparticles," *Physical Review Letters*, vol. 38, pp. 1440–1443, June 1977.

[19] S. Weinberg, "A new light boson?," *Physical Review Letters*, vol. 40, pp. 223–226, Jan. 1978.

[20] F. Wilczek, "Problem of strong P and T invariance in the presence of instantons," *Physical Review Letters*, vol. 40, pp. 279–282, Jan. 1978.

[21] R. J. Crewther, P. Di Vecchia, G. Veneziano, and E. Witten, "Chiral Estimate of the Electric Dipole Moment of the Neutron in Quantum Chromodynamics," *Phys. Lett.*, vol. 88B, p. 123, 1979. [Erratum: Phys. Lett.91B,487(1980)].

[22] J. M. Pendlebury *et al.*, "Revised experimental upper limit on the electric dipole moment of the neutron," *Phys. Rev.*, vol. D92, no. 9, p. 092003, 2015.

[23] C. Patrignani *et al.*, "Review of Particle Physics," *Chin. Phys.*, vol. C40, no. 10, p. 100001, 2016.

[24] C. Vafa and E. Witten, "Parity Conservation in QCD," *Phys. Rev. Lett.*, vol. 53, p. 535, 1984.

[25] P. Sikivie, "Experimental tests of the 'invisible' axion," *Physical Review Letters*, vol. 51, pp. 1415–1417, Oct. 1983.

[26] G. Raffelt and L. Stodolsky, "Mixing of the photon with low-mass particles," *Phys Rev D.*, vol. 37, pp. 1237–1249, Mar. 1988.

[27] A. A. Anselm, "Experimental test for arion⇌photon oscillations in a homogeneous constant magnetic field," *Phys Rev D.*, vol. 37, pp. 2001–2004, Apr. 1988.

[28] A. A. Anselm and N. G. Uraltsev, "A second massless axion?," *Physics Letters B*, vol. 114, pp. 39–41, July 1982.

[29] E. Massó and R. Toldrà, "Light spinless particle coupled to photons," *Physical Review D.*, vol. 52, pp. 1755–1763, Aug. 1995.

[30] N. Turok, "Almost-Goldstone Bosons from Extra-Dimensional Gauge Theories," *Physical Review Letters*, vol. 76, pp. 1015–1018, Feb. 1996.

[31] K. R. Dienes, E. Dudas, and T. Gherghetta, "Invisible axions and large-radius compactifications," *Phys Rev D.*, vol. 62, p. 105023, Nov. 2000.

[32] C. Corianò and N. Irges, "Windows over a new low energy axion," *Physics Letters B*, vol. 651, pp. 298–305, Aug. 2007.

[33] A. De Angelis, M. Roncadelli, and O. Mansutti, "Evidence for a new light spin-zero boson from cosmological gamma-ray propagation?," *Phys. Rev.*, vol. D76, p. 121301, 2007.

[34] A. de Angelis, O. Mansutti, and M. Roncadelli, "Axion-like particles, cosmic magnetic fields and gamma-ray astrophysics," *Physics Letters B*, vol. 659, pp. 847–855, Feb. 2008.

[35] D. Hooper and P. D. Serpico, "Detecting Axionlike Particles with Gamma Ray Telescopes," *Physical Review Letters*, vol. 99, p. 231102, Dec. 2007.

[36] M. Simet, D. Hooper, and P. D. Serpico, "Milky Way as a kiloparsec-scale axionscope," *Phys Rev D.*, vol. 77, p. 063001, Mar. 2008.

[37] A. Mirizzi and D. Montanino, "Stochastic conversions of TeV photons into axion-like particles in extragalactic magnetic fields," *JCAP*, vol. 0912, p. 004, 2009.

[38] W. Essey and A. Kusenko, "A new interpretation of the gamma-ray observations of distant active galactic nuclei," *Astroparticle Physics*, vol. 33, pp. 81–85, Mar. 2010.

[39] A. de Angelis, O. Mansutti, M. Persic, and M. Roncadelli, "Photon propagation and the very high energy γ-ray spectra of blazars: how transparent is the Universe?," *Monthly Notices of the Royal Astronomical Society*, vol. 394, pp. L21–L25, Mar. 2009.

[40] D. Horns and M. Meyer, "Indications for a pair-production anomaly from the propagation of VHE gamma-rays," *JCAP - IOPscience*, vol. 2, p. 033, Feb. 2012.

[41] A. de Angelis, M. Roncadelli, and O. Mansutti, "Evidence for a new light spin-zero boson from cosmological gamma-ray propagation?," *Phys Rev D.*, vol. 76, p. 121301, Dec. 2007.

[42] A. de Angelis, G. Galanti, and M. Roncadelli, "Relevance of axionlike particles for very-high-energy astrophysics," *Phys Rev D.*, vol. 84, p. 105030, Nov. 2011.

[43] D. Horns, L. Maccione, M. Meyer, A. Mirizzi, D. Montanino, and M. Roncadelli, "Hardening of TeV gamma spectrum of active galactic nuclei in galaxy clusters by conversions of photons into axionlike particles," *Phys Rev D.*, vol. 86, p. 075024, Oct. 2012.

[44] M. Meyer and D. Horns, "Impact of oscillations of photons into axion-like particles on the very-high energy gamma-ray spectrum of the blazar PKS1424+240," p. 7, Oct. 2013.

[45] S. Troitsky, "Towards discrimination between galactic and intergalactic axion-photon mixing," *Phys Rev D.*, vol. 93, p. 045014, Feb. 2016.

[46] M. Meyer, D. Horns, and M. Raue, "First lower limits on the photon-axion-like particle coupling from very high energy gamma-ray observations," *Phys Rev D.*, vol. 87, p. 035027, Feb. 2013.

[47] A. Payez, C. Evoli, T. Fischer, M. Giannotti, A. Mirizzi, and A. Ringwald, "Revisiting the SN1987A gamma-ray limit on ultralight axion-like particles," *JCAP - IOPscience*, vol. 2, p. 006, Feb. 2015.

[48] D. Horns and M. Meyer, "Pair-production opacity at high and very-high gamma-ray energies," *ArXiv e-prints*, Sept. 2013.

[49] A. Abramowski, F. Acero, F. Aharonian, F. Ait Benkhali, A. G. Akhperjanian, E. Angüner, G. Anton, S. Balenderan, A. Balzer, A. Barnacka, and et al., "Constraints on axionlike particles with H.E.S.S. from the irregularity of the PKS 2155-304 energy spectrum," *Phys Rev D.*, vol. 88, p. 102003, Nov. 2013.

[50] M. Ajello, A. Albert, B. Anderson, and B. et al. Fermi-LAT Collaboration, "Search for Spectral Irregularities due to Photon-Axionlike-Particle Oscillations with the Fermi Large Area Telescope," *Physical Review Letters*, vol. 116, p. 161101, Apr. 2016.

[51] M. Berg, J. P. Conlon, F. Day, N. Jennings, S. Krippendorf, A. J. Powell, and M. Rummel, "Constraints on Axion-like Particles from X-Ray Observations of NGC1275," *The Astrophysical Journal*, vol. 847, p. 101, Oct. 2017.

[52] L. Chen and J. P. Conlon, "Constraints on Massive Axion-Like Particles from X-ray Observations of NGC1275," *ArXiv e-prints*, Dec. 2017.

[53] K. Barth, A. Belov, B. Beltran, H. Bräuninger, and J. M. e. a. Carmona, "CAST constraints on the axion-electron coupling," *JCAP*, vol. 5, p. 010, May 2013.

[54] E. Ferrer-Ribas, M. Arik, S. Aune, K. Barth, A. Belov, S. Borghi, H. Bräuninger, G. Cantatore, and J. M. e. a. Carmona, "Results and perspectives of the solar axion search with the CAST experiment," *ArXiv e-prints*, Sept. 2012.

[55] V. Anastassopoulos, S. Aune, K. Barth, A. Belov, and H. e. a. Bräuninger, "New CAST limit on the axion-photon interaction," *Nature Physics*, vol. 13, pp. 584–590, June 2017.

[56] J. K. Vogel, E. Armengaud, F. T. Avignone, M. Betz, P. Brax, and P. e. a. Brun, "The Next Generation of Axion Helioscopes: The International Axion Observatory (IAXO)," *Physics Procedia*, vol. 61, pp. 193–200, 2015.

[57] I. G. Irastorza, F. T. Avignone, G. Cantatore, J. M. Carmona, S. Caspi, S. A. Cetin, and F. E. e. a. Christensen, "Future axion searches with the International Axion Observatory (IAXO)," in *Journal of Physics Conference Series*, vol. 460 of *Journal of Physics Conference Series*, p. 012002, Oct. 2013.

[58] E. Armengaud, F. T. Avignone, M. Betz, P. Brax, and P. e. a. Brun, "Conceptual design of the International Axion Observatory (IAXO)," *Journal of Instrumentation*, vol. 9, p. T05002, May 2014.

[59] W. B. Atwood, A. A. Abdo, M. Ackermann, W. Althouse, B. Anderson, M. Axelsson, L. Baldini, J. Ballet, D. L. Band, G. Barbiellini, and et al., "The Large

Area Telescope on the Fermi Gamma-Ray Space Telescope Mission," *Astrophysical Journal*, vol. 697, pp. 1071–1102, June 2009.

[60] M. Ackermann and M. e. a. Ajello, "The Fermi Large Area Telescope on Orbit: Event Classification, Instrument Response Functions, and Calibration," *The Astrophysical Journal Supplement*, vol. 203, p. 4, Nov. 2012.

[61] E. Aliu, H. Anderhub, and L. A. e. a. Antonelli, "Observation of Pulsed γ-Rays Above 25 GeV from the Crab Pulsar with MAGIC," *Science*, vol. 322, p. 1221, Nov. 2008.

[62] M. Kramer, "Millisecond Pulsarsas Tools of Fundamental Physics," in *Astrophysics, Clocks and Fundamental Constants* (S. G. Karshenboim and E. Peik, eds.), vol. 648 of *Lecture Notes in Physics, Berlin Springer Verlag*, pp. 33–54, 2004.

[63] J. K. Daugherty and A. K. Harding, "Electromagnetic cascades in pulsars," *Astrophysical Journal*, vol. 252, pp. 337–347, Jan. 1982.

[64] V. V. Usov and D. B. Melrose, "Pulsars with Strong Magnetic Fields - Polar Gaps Bound Pair Creation and Nonthermal Luminosities," *Australian Journal of Physics*, vol. 48, p. 571, 1995.

[65] K. Hirotani and S. Shibata, "One-dimensional electric field structure of an outer gap accelerator - II. gamma-ray production resulting from inverse Compton scattering," *Monthly Notices of the Royal Astronomical Society*, vol. 308, pp. 67–76, Sept. 1999.

[66] R. W. Romani and I.-A. Yadigaroglu, "Gamma-ray pulsars: Emission zones and viewing geometries," *Astrophysical Journal*, vol. 438, pp. 314–321, Jan. 1995.

[67] C. M. Urry and P. Padovani, "Unified Schemes for Radio-Loud Active Galactic Nuclei," *Publications of the Astronomical Society of the Pacific*, vol. 107, p. 803, Sept. 1995.

[68] A. S. Wilson and E. J. M. Colbert, "The difference between radio-loud and radio-quiet active galaxies," *Astrophysical Journal*, vol. 438, pp. 62–71, Jan. 1995.

[69] J. H. Beall and W. Bednarek, "On the hadronic beam model for gamma-ray production in blazars," *The Astrophysical Journal*, vol. 510, no. 1, p. 188, 1999.

[70] F. Heitsch, E. G. Zweibel, A. D. Slyz, and J. E. G. Devriendt, "Turbulent Ambipolar Diffusion: Numerical Studies in Two Dimensions," *The Astrophysical Journal*, vol. 603, pp. 165–179, Mar. 2004.

[71] M. A. de Avillez and D. Breitschwerdt, "Global dynamical evolution of the ISM in star forming galaxies. I. High resolution 3D simulations: Effect of the magnetic field," *A&A*, vol. 436, pp. 585–600, June 2005.

[72] R. Beck, "Galactic and Extragalactic Magnetic Fields," vol. 1085, pp. 83–96, Dec. 2008.

[73] X. H. Sun, J. L. Han, W. Reich, P. Reich, W. B. Shi, R. Wielebinski, and E. Fürst, "Erratum: A Sino-German λ6 cm polarization survey of the Galactic plane. I. Survey strategy and results for the first survey region," *A&A*, vol. 469, pp. 1003–1004, July 2007.

[74] R. Jansson and G. R. Farrar, "A New Model of the Galactic Magnetic Field," *APJ - IOPscience*, vol. 757, p. 14, Sept. 2012.

[75] G. R. Farrar, "The Galactic magnetic field and ultrahigh-energy cosmic ray deflections," *Comptes Rendus Physique*, vol. 15, pp. 339–348, Apr. 2014.

[76] A. A. Abdo, M. Ajello, A. Allafort, L. Baldini, J. Ballet, G. Barbiellini, M. G. Baring, D. Bastieri, A. Belfiore, R. Bellazzini, and et al., "The Second Fermi Large Area Telescope Catalog of Gamma-Ray Pulsars," *The Astrophysical Journal Supplement*, vol. 208, p. 17, Oct. 2013.

[77] F. Acero, M. Ackermann, M. Ajello, A. Albert, W. B. Atwood, M. Axelsson, and F. et al., "Fermi Large Area Telescope Third Source Catalog," *The Astrophysical Journal Supplement*, vol. 218, p. 23, June 2015.

[78] R. N. Manchester, A. G. Lyne, F. Camilo, J. F. Bell, V. M. Kaspi, N. D'Amico, N. P. F. McKay, F. Crawford, I. H. Stairs, A. Possenti, M. Kramer, and D. C. Sheppard, "The Parkes multi-beam pulsar survey - I. Observing and data analysis systems, discovery and timing of 100 pulsars," *Monthly Notices of the Royal Astronomical Society*, vol. 328, pp. 17–35, Nov. 2001.

[79] D. J. Morris, G. Hobbs, A. G. Lyne, I. H. Stairs, F. Camilo, R. N. Manchester, A. Possenti, J. F. Bell, V. M. Kaspi, N. D. Amico, N. P. F. McKay, F. Crawford, and M. Kramer, "The Parkes Multibeam Pulsar Survey - II. Discovery and timing of 120 pulsars," *Monthly Notices of the Royal Astronomical Society*, vol. 335, pp. 275–290, Sept. 2002.

[80] R. Jansson and G. R. Farrar, "The Galactic Magnetic Field," *The Astrophysical Journal Letters*, vol. 761, p. L11, Dec. 2012.

[81] Planck Collaboration, R. Adam, and P. A. R. e. a. Ade, "Planck intermediate results. XLII. Large-scale Galactic magnetic fields," *AAP*, vol. 596, p. A103, Dec. 2016.

[82] J. Majumdar, F. Calore, and D. Horns, "Modulations in Spectra of Galactic Gamma-ray sources as a result of photon-ALPs mixing," *ArXiv e-prints*, Oct. 2017.

[83] J. Majumdar, F. Calore, and D. Horns, "Spectral modulation of non-Galactic plane Gamma-ray pulsars due to photon-ALPs mixing in Galactic magnetic field.," p. 168, Oct. 2017.

[84] P. Weltevrede and A. A. e. a. Abdo, "Gamma-ray and Radio Properties of Six Pulsars Detected by the Fermi Large Area Telescope," *Astrophys.J.708*, vol. 708, pp. 1426–1441.

[85] M. S. E. Roberts, R. W. Romani, and S. Johnston, "Multiwavelength Studies of PSR J1420-6048, a Young Pulsar in the Kookaburra," *Astrophysical J.*, vol. 561, pp. L187–L190, Nov. 2001.

[86] R. Terrier, M. Roberts, and A. Djannati-Ataï, "Multiwavelength observations of HESS J1420-607," vol. 37, p. 3170, 2008.

[87] M. Kramer, J. F. Bell, R. N. Manchester, A. G. Lyne, F. Camilo, I. H. Stairs, N. D'Amico, V. M. Kaspi, G. Hobbs, D. J. Morris, F. Crawford, A. Possenti, B. C. Joshi, M. A. McLaughlin, D. R. Lorimer, and A. J. Faulkner, "The Parkes Multibeam Pulsar Survey - III. Young pulsars and the discovery and timing of 200 pulsars," *Monthly Notices of the Royal Astronomical Society*, vol. 342, pp. 1299–1324, July 2003.

[88] J. M. Cordes and T. J. W. Lazio, "NE2001.I. A New Model for the Galactic Distribution of Free Electrons and its Fluctuations," *ArXiv Astrophysics e-prints*, July 2002.

[89] A. Abramowski, F. Acero, F. Aharonian, A. G. Akhperjanian, and G. e. a. Anton, "Discovery of extended VHE γ-ray emission from the vicinity of the young massive stellar cluster Westerlund 1," *Astronomy & Astrophysics*, vol. 537, p. A114, Jan. 2012.

[90] M. Sakai, H. Matsumoto, Y. Haba, Y. Kanou, and Y. Miyamoto, "Discovery of Diffuse Hard X-Ray Emission from the Vicinity of PSR J1648-4611 with Suzaku," *Publications of the Astronomical Society of Japan*, vol. 65, p. 64, June 2013.

[91] F. Aharonian, A. G. Akhperjanian, A. R. Bazer-Bachi, M. Beilicke, W. Benbow, D. Berge, and K. e. a. Bernlöhr, "The H.E.S.S. Survey of the Inner Galaxy in Very High Energy Gamma Rays," *The Astrophysical Journal*, vol. 636, pp. 777–797, Jan. 2006.

[92] F. Aharonian, A. G. Akhperjanian, A. R. Bazer-Bachi, B. Behera, M. Beilicke, W. Benbow, D. Berge, K. Bernlöhr, C. Boisson, O. Bolz, and V. e. a. Borrel, "Discovery of two candidate pulsar wind nebulae in very-high-energy gamma rays," *Astronomy and Astrophysics*, vol. 472, pp. 489–495, Sept. 2007.

[93] F. Aharonian, A. G. Akhperjanian, U. Barres de Almeida, A. R. Bazer-Bachi, B. Behera, M. Beilicke, W. Benbow, K. Bernlöhr, C. Boisson, and O. e. a. Bolz, "HESS very-high-energy gamma-ray sources without identified counterparts," *Astronomy and Astrophysics*, vol. 477, pp. 353–363, Jan. 2008.

[94] R. N. Manchester, A. G. Lyne, F. Camilo, J. F. Bell, V. M. Kaspi, N. D'Amico, N. P. F. McKay, F. Crawford, I. H. Stairs, A. Possenti, M. Kramer, and D. C. Sheppard, "The Parkes multi-beam pulsar survey - I. Observing and data analysis systems, discovery and timing of 100 pulsars," *Monthly Notices of the Royal Astronomical Society*, vol. 328, pp. 17–35, Nov. 2001.

[95] J. W. T. Hessels, M. S. E. Roberts, S. M. Ransom, V. M. Kaspi, R. W. Romani, C.-Y. Ng, P. C. C. Freire, and B. M. Gaensler, "Observations of PSR J2021+3651 and its X-Ray Pulsar Wind Nebula G75.2+0.1," *The Astrophysical Journal*, vol. 612, pp. 389–397, Sept. 2004.

[96] E. Aliu, T. Aune, B. Behera, M. Beilicke, W. Benbow, K. Berger, R. Bird, A. Bouvier, and J. H. e. a. Buckley, "Spatially Resolving the Very High Energy Emission from MGRO J2019+37 with VERITAS," *The Astrophysical Journal*, vol. 788, p. 78, June 2014.

[97] A. Kirichenko, A. Danilenko, P. Shternin, Y. Shibanov, E. Ryspaeva, D. Zyuzin, M. Durant, O. Kargaltsev, G. Pavlov, and A. Cabrera-Lavers, "Optical Observations of Psr J2021+3651 in the Dragonfly Nebula With the GTC," *The Astrophysical Journal*, vol. 802, p. 17, Mar. 2015.

[98] A. A. Abdo, M. Ackermann, M. Ajello, W. B. Atwood, L. Baldini, J. Ballet, G. Barbiellini, and D. e. a. Bastieri, "Pulsed Gamma-rays from PSR J2021+3651 with the Fermi Large Area Telescope," *The Astrophysical Journal*, vol. 700, pp. 1059–1066, Aug. 2009.

[99] G. Theureau, D. Parent, I. Cognard, G. Desvignes, D. A. Smith, J. M. Casandjian, C. C. Cheung, H. A. Craig, D. Donato, R. Foster, L. Guillemot, A. K. Harding, J.-F. Lestrade, P. S. Ray, R. W. Romani, D. J. Thompson, W. W. Tian, and K. Watters, "PSRs J0248+6021 and J2240+5832: young pulsars in the northern Galactic plane. Discovery, timing, and gamma-ray observations," *Astronomy and Astrophysics*, vol. 525, p. A94, Jan. 2011.

[100] P. A. Caraveo, A. D. Luca, R. P. Mignani, and G. F. Bignami, "The distance to the vela pulsar gauged with hubble space telescope parallax observations," *The Astrophysical Journal*, vol. 561, no. 2, p. 930, 2001.

[101] D. A. Sanchez and C. Deil, "Enrico : a Python package to simplify Fermi-LAT analysis," *ArXiv e-prints*, July 2013.

[102] M. Ajello, A. Albert, B. Anderson, L. Baldini, and F. et al., "Search for Spectral Irregularities due to Photon-Axionlike-Particle Oscillations with the Fermi Large Area Telescope," *Physical Review Letters*, vol. 116, p. 161101, Apr. 2016.

[103] M. Meyer, D. Horns, and M. Raue, "First lower limits on the photon-axion-like particle coupling from very high energy gamma-ray observations," *Physical Review D*, vol. 87, p. 035027, Feb. 2013.

[104] M. Ackermann and M. e. a. Ajello, "Detection of the Characteristic Pion-Decay Signature in Supernova Remnants," *Science*, vol. 339, pp. 807–811, Feb. 2013.

[105] T. Jogler and S. Funk, "Revealing w51c as a cosmic ray source using fermi-lat data," *The Astrophysical Journal*, vol. 816, no. 2, p. 100, 2016.

[106] A. Djannati-Ataï, G. Giavitto, M. Holler, B. Rudak, C. Venter, and H.E.S.S. Collaboration, "Probing Vela pulsar down to 20 GeV with H.E.S.S. II observations," vol. 1792, p. 040028, Jan. 2017.

[107] T. Güver, F. Özel, and D. Psaltis, "Systematic Uncertainties in the Spectroscopic Measurements of Neutron-star Masses and Radii from Thermonuclear X-Ray Bursts. II. Eddington Limit," *The Astrophysical Journal*, vol. 747, p. 77, Mar. 2012.

[108] M. Tsujimoto, M. Guainazzi, P. P. Plucinsky, A. P. Beardmore, M. Ishida, L. Natalucci, J. L. L. Posson-Brown, A. M. Read, R. D. Saxton, and N. V. Shaposhnikov, "Cross-calibration of the X-ray instruments onboard the Chandra, INTEGRAL, RXTE, Suzaku, Swift, and XMM-Newton observatories using G21.5-0.9," *Astronomy and Astrophysics*, vol. 525, p. A25, Jan. 2011.

[109] V. Anastassopoulos, S. Aune, K. Barth, A. Belov, H. Bräuninger, G. Cantatore, J. M. Carmona, J. F. Castel, S. A. Cetin, F. Christensen, and J. I. e. a. Collar, "New CAST limit on the axion-photon interaction," *Nature Physics*, vol. 13, pp. 584–590, June 2017.

[110] M. S. Pshirkov, P. G. Tinyakov, P. P. Kronberg, and K. J. Newton-McGee, "Deriving the Global Structure of the Galactic Magnetic Field from Faraday Rotation

Measures of Extragalactic Sources," *The Astrophysical Journal*, vol. 738, p. 192, Sept. 2011.

[111] J. Majumdar, F. Calore, and D. Horns, "Search for gamma-ray spectral modulations in galactic pulsars," *Journal of Cosmology and Astroparticle Physics*, vol. 2018, no. 04, p. 048, 2018.

[112] K. Kohri and H. Kodama, "Axion-like particles and recent observations of the cosmic infrared background radiation," *Physical Review D*, vol. 96, p. 051701, Sept. 2017.

[113] A. Abramowski, F. Acero, F. Aharonian, F. Ait Benkhali, A. G. Akhperjanian, E. Angüner, G. Anton, S. Balenderan, A. Balzer, A. Barnacka, and et al., "Constraints on axionlike particles with H.E.S.S. from the irregularity of the PKS 2155-304 energy spectrum," *Physical Review D*, vol. 88, p. 102003, Nov. 2013.

[114] A. Payez, C. Evoli, T. Fischer, M. Giannotti, A. Mirizzi, and A. Ringwald, "Revisiting the SN1987A gamma-ray limit on ultralight axion-like particles," *Journal of Cosmology and Astroparticle physics*, vol. 2, p. 006, Feb. 2015.

[115] R. Bähre, B. Döbrich, J. Dreyling-Eschweiler, S. Ghazaryan, R. Hodajerdi, D. Horns, F. Januschek, E.-A. Knabbe, A. Lindner, D. Notz, A. Ringwald, J. E. von Seggern, R. Stromhagen, D. Trines, and B. Willke, "Any light particle search II – Technical Design Report," *Journal of Instrumentation*, vol. 8, p. T09001, Sept. 2013.

[116] J. K. Vogel, F. T. Avignone, G. Cantatore, J. M. Carmona, S. Caspi, S. A. Cetin, F. E. Christensen, and A. e. a. Dael, "IAXO - The International Axion Observatory," *ArXiv e-prints*, Feb. 2013.

[117] Z.-Q. Xia, C. Zhang, Y.-F. Liang, L. Feng, Q. Yuan, Y.-Z. Fan, and J. Wu, "Searching for spectral oscillations due to photon-ALP conversion using the Fermi-LAT observations of bright supernova remnants," *ArXiv e-prints*, Jan. 2018.

[118] A. A. Abdo, M. Ajello, A. Allafort, L. Baldini, J. Ballet, G. Barbiellini, M. G. Baring, D. Bastieri, A. Belfiore, R. Bellazzini, and et al., "The Second Fermi Large Area Telescope Catalog of Gamma-Ray Pulsars," *APJ*, vol. 208, p. 17, Oct. 2013.

[119] P. S. Ray, M. Kerr, and D. e. a. Parent, "Precise γ-ray Timing and Radio Observations of 17 Fermi γ-ray Pulsars," *The Astrophysical Journal Supplement*, vol. 194, p. 17, June 2011.

[120] A. Danilenko, P. Shternin, A. Karpova, D. Zyuzin, and Y. Shibanov, "The γ-ray Pulsar J0633+0632 in X-rays," *Publications of the Astronomical Society of Australia*, vol. 32, p. e038, Oct. 2015.

[121] A. V. Karpova, D. A. Zyuzin, A. A. Danilenko, and Y. A. Shibanov, "Xmm-newton observations of the -ray pulsar j0633+0632," *Journal of Physics: Conference Series*, vol. 932, no. 1, p. 012010, 2017.

[122] C. E. Fichtel, R. C. Hartman, D. A. Kniffen, D. J. Thompson, H. Ogelman, M. E. Ozel, T. Tumer, and G. F. Bignami, "High-energy gamma-ray results from the second small astronomy satellite," *Astrophysical Journal*, vol. 198, pp. 163–182, May 1975.

[123] G. F. Bignami, P. A. Caraveo, and R. C. Lamb, "An identification for 'Geminga' (2CG 195+04) 1E 0630+178 - A unique object in the error box of the high-energy gamma-ray source," *Astrophysical Journal*, vol. 272, pp. L9–L13, Sept. 1983.

[124] G. F. Bignami, P. A. Caraveo, J. A. Paul, L. Salotti, and L. Vigroux, "A deep optical study of the field of IE 0630 + 178," *Astrophysical Journal*, vol. 319, pp. 358–361, Aug. 1987.

[125] C. Y. Hui, J. Lee, A. K. H. Kong, P. H. T. Tam, J. Takata, K. S. Cheng, and D. Ryu, "Rapid x-ray variations of the geminga pulsar wind nebula," *The Astrophysical Journal*, vol. 846, no. 2, p. 116, 2017.

[126] E. V. Sokolova and G. I. Rubtsov, "Search for differences between radio-loud and radio-quiet gamma-ray pulsar populations with fermi-lat data," *The Astrophysical Journal*, vol. 833, no. 2, p. 271, 2016.

[127] P. M. Saz Parkinson and M. e. a. Dormody, "Eight γ-ray Pulsars Discovered in Blind Frequency Searches of Fermi LAT Data," *The Astrophysical Journal*, vol. 725, pp. 571–584, Dec. 2010.

[128] A. Rappoldi, F. Lucarelli, C. Pittori, and F. e. a. Longo, "Search of MeV-GeV counterparts of TeV sources with AGILE in pointing mode," *Astronomy & Astrophysics*, vol. 587, p. A93, Mar. 2016.

[129] M. Ajello, A. Albert, W. B. Atwood, and G. e. a. Barbiellini, "Fermi-LAT Observations of High-Energy Gamma-Ray Emission toward the Galactic Center," *The Astrophysical Journal*, vol. 819, p. 44, Mar. 2016.

[130] T. M. Braje, R. W. Romani, M. S. E. Roberts, and N. Kawai, "Chandra Imaging of the Gamma-Ray Source GeV J1809-2327," *The Astrophysical Journal*, vol. 565, pp. L91–L95, Feb. 2002.

[131] L. C.-C. Lin and H.-K. Chang, "Periodicity search for possible x-ray counterparts to radio-quiet gamma-ray pulsar candidates," *Monthly Notices of the Royal Astronomical Society*, vol. 387, no. 2, pp. 729–734, 2008.

[132] L. C.-C. Lin, "Radio-quiet Gamma-ray Pulsars," *Journal of Astronomy and Space Sciences*, vol. 33, pp. 147–166, Sept. 2016.

[133] A. M. W. Mitchell, C. Mariaud, P. Eger, S. Funk, J. Hahn, J. Hinton, R. D. Parsons, and V. Marandon, "Detailed VHE studies of the pulsar wind nebula HESS J1825-137," vol. 1792, p. 040035, Jan. 2017.

[134] S. Carrigan, F. Brun, R. C. G. Chaves, C. Deil, A. Donath, H. Gast, V. Marandon, M. Renaud, and for the H. E. S. S. collaboration, "The H.E.S.S. Galactic Plane Survey - maps, source catalog and source population," *ArXiv e-prints*, July 2013.

[135] B. Bartoli and P. B. et al., "Observation of the tev gamma-ray source mgro j1908+06 with argo-ybj," *The Astrophysical Journal*, vol. 760, no. 2, p. 110, 2012.

[136] A. A. Abdo, M. Ackermann, and Ajelloet al., "PSR J1907+0602: A Radio-Faint Gamma-Ray Pulsar Powering a Bright TeV Pulsar Wind Nebula," *The Astrophysical Journal*, vol. 711, pp. 64–74, Mar. 2010.

[137] L. Trepl, C. Y. Hui, K. S. Cheng, J. Takata, Y. Wang, Z. Y. Liu, and N. Wang, "Multiwavelength properties of a new Geminga-like pulsar: PSRJ2021+4026," *Monthly Notices of the Royal Astronomical Society*, vol. 405, pp. 1339–1348, June 2010.

[138] A. Allafort, L. Baldini, J. Ballet, and G. e. a. Barbiellini, "PSR J2021+4026 in the Gamma Cygni Region: The First Variable γ-Ray Pulsar Seen by the Fermi LAT," *The Astrophysical Journal Letters*, vol. 777, p. L2, Nov. 2013.

[139] Y. Ladouceur and S. Pineault, "New perspectives on the supernova remnant G78.2+2.1," *Astronomy and Astrophysics*, vol. 490, pp. 197–211, Oct. 2008.

[140] J. Takata, P. H. T. Tam, C. W. Ng, K. L. Li, A. K. H. Kong, C. Y. Hui, and K. S. Cheng, "High-energy Emissions from the Pulsar/Be Binary System PSR J2032+4127/MT91 213," *The Astrophysical Journal*, vol. 836, p. 241, Feb. 2017.

[141] J. P. Halpern, F. Camilo, E. V. Gotthelf, D. J. Helfand, M. Kramer, A. G. Lyne, K. M. Leighly, and M. Eracleous, "Psr j2229+6114: Discovery of an energetic young pulsar in the error box of the egret source 3eg j2227+6122," *The Astrophysical Journal Letters*, vol. 552, no. 2, p. L125, 2001.

[142] G. Joncas and L. A. Higgs, "The DRAO galactic-plane survey. II - Field at L = 105 deg," *Astronomy and Astrophysics Supplement Series*, vol. 82, pp. 113–144, Jan. 1990.

[143] M. Ajello, W. B. Atwood, L. Baldini, and J. e. a. Ballet, "3FHL: The Third Catalog of Hard Fermi-LAT Sources," *The Astrophysical Journal Supplement Series*, vol. 232, p. 18, Oct. 2017.

[144] M. L. Lister, M. F. Aller, H. D. Aller, T. Hovatta, W. Max-Moerbeck, A. C. S. Readhead, J. L. Richards, and E. Ros, "Why Have Many of the Brightest Radio-loud Blazars Not Been Detected in Gamma-Rays by Fermi?," *The Astrophysical Journal Letters*, vol. 810, p. L9, Sept. 2015.

[145] D. A. Prokhorov and A. Moraghan, "A search for cyclical sources of γ-ray emission on the period range from days to years in the Fermi-LAT sky," *Monthly Notices of the Royal Astronomical Society*, vol. 471, pp. 3036–3042, Nov. 2017.

[146] J. H. Fan, J. H. Yang, Y. Liu, G. Y. Luo, C. Lin, Y. H. Yuan, H. B. Xiao, A. Y. Zhou, T. X. Hua, and Z. Y. Pei, "The Spectral Energy Distributions of Fermi Blazars," *The Astrophysical Journal Supplement Series*, vol. 226, p. 20, Oct. 2016.

[147] M. Ackermann and M. e. a. Ajello, "The Third Catalog of Active Galactic Nuclei Detected by the Fermi Large Area Telescope," *The Astrophysical Journal*, vol. 810, p. 14, Sept. 2015.

[148] M. Ackermann and M. e. a. Ajello, "The First Fermi-LAT Catalog of Sources above 10 GeV," *The Astrophysical Journal Supplement*, vol. 209, p. 34, Dec. 2013.

[149] T. Joubert, D. Castro, P. Slane, and J. Gelfand, "Fermi-LAT Observations of Supernova Remnant G5.7-0.1, Believed to be Interacting with Molecular Clouds," *The Astrophysical Journal*, vol. 816, p. 63, Jan. 2016.

[150] F. Aharonian and A. G. e. a. Akhperjanian, "Discovery of very high energy gamma-ray emission coincident with molecular clouds in the W 28 (G6.4-0.1) field," *Astronomy and Astrophysics*, vol. 481, pp. 401–410, Apr. 2008.

[151] G. Ghirlanda, G. Ghisellini, F. Tavecchio, and L. Foschini, "Correlation of Fermi Large Area Telescope sources with the 20-GHz Australia Telescope Compact Array radio survey," *Monthly Notices of the Royal Astronomical Society*, vol. 407, pp. 791–803, Sept. 2010.

[152] M. Ackermann and M. e. a. Ajello, "Detection of the Characteristic Pion-Decay Signature in Supernova Remnants," *Science*, vol. 339, pp. 807–811, Feb. 2013.

[153] T. Jogler and S. Funk, "Revealing w51c as a cosmic ray source using fermi-lat data," *The Astrophysical Journal*, vol. 816, no. 2, p. 100, 2016.

[154] A. Ginsburg, "A review of the W51 Cloud," *ArXiv e-prints*, Feb. 2017.

[155] K. Berger and G. e. a. Giavitto, "Exploring the very high energy gamma-ray emission (E $\geq$ 100 GeV) of the hard spectrum Fermi sources 1FGL J2001.1+4351 and B3-2247+381 with MAGIC," *ArXiv e-prints*, Oct. 2011.

[156] J. Aleksić and S. e. a. Ansoldi, "First broadband characterization and redshift determination of the VHE blazar MAGIC J2001+439," *Astronomy & Astrophysics*, vol. 572, p. A121, Dec. 2014.

[157] P. Munar-Adrover, S. Sabatini, G. Piano, M. Tavani, L. H. Nguyen, F. Lucarelli, F. Verrecchia, and C. Pittori, "The Gamma-Ray Source AGL J2241+4454 as the Possible Counterpart of MWC 656," *The Astrophysical Journal*, vol. 829, p. 101, Oct. 2016.

[158] L. Bassani, R. Landi, N. Masetti, P. Parisi, A. Bazzano, and P. Ubertini, "On the identification of the Fermi/LAT source 0FGL J2001.0+4352 with a BL Lac," *Monthly Notices of the Royal Astronomical Society*, vol. 397, pp. L55–L59, July 2009.

[159] R. P. Mignani, A. de Luca, N. Rea, A. Shearer, S. Collins, D. F. Torres, D. Hadasch, and A. Caliandro, "Deep optical observations of the γ-ray pulsar PSR J0007+7303 in the CTA 1 supernova remnant," *Monthly Notices of the Royal Astronomical Society*, vol. 430, pp. 1354–1358, Apr. 2013.

[160] "Pulsar Astronomy - 2000 and Beyond," vol. 202, 2000.

[161] A. A. Abdo, M. Ackermann, W. B. Atwood, and M. e. a. Axelsson, "Pulsed Gamma Rays from the Millisecond Pulsar J0030+0451 with the Fermi Large Area Telescope," *The Astrophysical Journal*, vol. 699, pp. 1171–1177, July 2009.

[162] A. De Luca, M. Marelli, R. P. Mignani, P. A. Caraveo, W. Hummel, S. Collins, A. Shearer, P. M. Saz Parkinson, A. Belfiore, and G. F. Bignami, "Discovery of a Faint X-Ray Counterpart and a Parsec-long X-Ray Tail for the Middle-aged, γ-Ray-only Pulsar PSR J0357+3205," *The Astrophysical Journal*, vol. 733, p. 104, June 2011.

[163] C. G. Bassa, J. Antoniadis, F. Camilo, I. Cognard, D. Koester, M. Kramer, S. R. Ransom, and B. W. Stappers, "Cool white dwarf companions to four millisecond pulsars," *Monthly Notices of the Royal Astronomical Society*, vol. 455, pp. 3806–3813, Feb. 2016.

[164] P. S. Ray, Z. Arzoumanian, K. C. Gendreau, S. Bogdanov, P. Bult, D. Chakrabarty, D. Chakrabarty, S. Guillot, A. Harding, W. C. G. Ho, F. Lamb, S. Mahmoodifar, C. Miller, T. Strohmayer, C. Wilson-Hodge, M. T. Wolff, and NICER Science Team Working Group on Pulsation Searches and Multiwavelength Coordination, "Searching for X-ray Pulsations from Neutron Stars Using NICER," vol. 231, p. 243.17, Jan. 2018.

[165] R. W. Romani, A. V. Filippenko, J. M. Silverman, S. B. Cenko, J. Greiner, A. Rau, J. Elliott, and H. J. Pletsch, "Psr j13113430: A heavyweight neutron star with a flyweight helium companion," *The Astrophysical Journal Letters*, vol. 760, no. 2, p. L36, 2012.

[166] H. J. Pletsch, L. Guillemot, and H. e. a. Fehrmann, "Binary Millisecond Pulsar Discovery via Gamma-Ray Pulsations," *Science*, vol. 338, p. 1314, Dec. 2012.

[167] A. A. Abdo, M. Ackermann, M. Ajello, W. B. Atwood, L. Baldini, and J. B. et al., "Fermi large area telescope observations of psr j1836+5925," *The Astrophysical Journal*, vol. 712, no. 2, p. 1209, 2010.

[168] R. P. Mignani, V. Testa, N. Rea, M. Marelli, D. Salvetti, D. Torres, and E. de Ona Wilhelmi, "Observations of one young and three middle-aged γ-ray pulsars with the Gran Telescopio Canarias," 2018.

[169] P. M. Saz Parkinson, M. Dormody, M. Ziegler, P. S. Ray, A. A. Abdo, J. Ballet, M. G. Baring, A. Belfiore, T. H. Burnett, G. A. Caliandro, F. Camilo, P. A. Caraveo, A. de Luca, E. C. Ferrara, P. C. C. Freire, J. E. Grove, C. Gwon, A. K. Harding, R. P. Johnson, T. J. Johnson, S. Johnston, M. Keith, M. Kerr, J. Knödlseder, A. Makeev, M. Marelli, P. F. Michelson, D. Parent, S. M. Ransom, O. Reimer, R. W. Romani, D. A. Smith, D. J. Thompson, K. Watters, P. Weltevrede, M. T. Wolff, and K. S. Wood, "Eight γ-ray Pulsars Discovered in Blind Frequency Searches of Fermi LAT Data," *The Astrophysical Journal*, vol. 725, pp. 571–584, Dec. 2010.

[170] M. Marelli, D. Pizzocaro, A. De Luca, F. Gastaldello, P. Caraveo, and P. Saz Parkinson, "The Tale of the Two Tails of the Oldish PSR J2055+2539," *The Astrophysical Journal*, vol. 819, p. 40, Mar. 2016.

[171] R. W. Romani, P. Slane, and A. Green, "The Asymmetric Bowshock/PWN of PSR J2124−3358," *ArXiv e-prints*, Nov. 2017.

[172] J. Schroeder and J. Halpern, "Observations and Modeling of the Companions of Short Period Binary Millisecond Pulsars: Evidence for High-mass Neutron Stars," *The Astrophysical Journal*, vol. 793, p. 78, Oct. 2014.

[173] I. Cognard, L. Guillemot, T. J. Johnson, D. A. Smith, C. Venter, A. K. Harding, M. T. Wolff, C. C. Cheung, and D. e. a. Donato, "Discovery of Two Millisecond Pulsars in Fermi Sources with the Nançay Radio Telescope," *The Astrophysical Journal*, vol. 732, p. 47, May 2011.

[174] G. Stratta, M. Capalbi, P. Giommi, R. Primavera, S. Cutini, D. Gasparrini, and on behalf of the ASDC team, "The ASDC SED Builder Tool description and Tutorial," *ArXiv e-prints*, Mar. 2011.

[175] E. L. Wright, X. Chen, N. Odegard, C. L. Bennett, R. S. Hill, G. Hinshaw, N. Jarosik, E. Komatsu, M. R. Nolta, L. Page, D. N. Spergel, J. L. Weiland, E. Wollack, J. Dunkley, B. Gold, M. Halpern, A. Kogut, D. Larson, M. Limon, S. S. Meyer, and G. S. Tucker, "Five-Year Wilkinson Microwave Anisotropy Probe Observations: Source Catalog," *The Astrophysical Journal Supplement*, vol. 180, pp. 283–295, Feb. 2009.

[176] J. H. Fan, J. H. Yang, H. B. Xiao, C. Lin, D. Constantin, G. Y. Luo, Z. Y. Pei, J. M. Hao, and Y. W. Mao, "Intrinsic Correlations for Flaring Blazars Detected by Fermi," *The Astrophysical Journal Letters*, vol. 835, p. L38, Feb. 2017.

[177] M. Giroletti and F. e. a. Massaro, "High-energy sources at low radio frequency: the Murchison Widefield Array view of Fermi blazars," *Astronomy & Astrophysics*, vol. 588, p. A141, Apr. 2016.

[178] S. Chandra, K. S. Baliyan, S. Ganesh, and U. C. Joshi, "Optical polarimetry of the blazar cgrabs j0211+1051 from mount abu infrared observatory," *The Astrophysical Journal*, vol. 746, no. 1, p. 92, 2012.

[179] A. D. Haschick, P. C. Crane, and J. M. van der Hulst, "Time variations of the neutral hydrogen absorption spectrum of NGC 1275 /3C 84/," *Astrophysical Journal*, vol. 262, pp. 81–86, Nov. 1982.

[180] R. C. Walker, V. Dhawan, J. D. Romney, K. I. Kellermann, and R. C. Vermeulen, "VLBA Absorption Imaging of Ionized Gas Associated with the Accretion Disk in NGC 1275," *The Astrophysical Journal*, vol. 530, pp. 233–244, Feb. 2000.

[181] Y. Fujita and H. Nagai, "Discovery of a new subparsec counterjet in NGC 1275: the inclination angle and the environment," *Monthly Notices of the Royal Astronomical Society*, vol. 465, pp. L94–L98, Feb. 2017.

[182] J. A. Hodgson, B. Rani, and J. Oh, "Gamma-rays in the radio galaxy 3C 84: A complex situation," *ArXiv e-prints*, Feb. 2018.

[183] R. Falomo, J. Kotilainen, and A. Treves, "Near-Infrared Imaging of the Host Galaxies of Three Radio-loud Quasars at z˜1.5," *The Astrophysical Journal*, vol. 547, pp. 124–128, Jan. 2001.

[184] M. F. Aller, P. A. Hughes, H. D. Aller, and T. Hovatta, "Probing Jet Conditions with Multi-frequency, Centimeter-band Linear Polarization: PKS 0420-01," *ArXiv e-prints*, Feb. 2013.

[185] P.-f. Zhang, D.-h. Yan, N.-h. Liao, W. Zeng, J.-c. Wang, and L.-J. Cao, "Possible Quasi-periodic Modulation in the z = 1.1 Gamma-Ray Blazar PKS 0426-380," *The Astrophysical Journal*, vol. 842, p. 10, June 2017.

[186] V. Cayatte and H. Sol, "The active galaxy PKS 0521-36 and its optical jet," *Astronomy & Astrophysics*, vol. 171, pp. 25–32, Jan. 1987.

[187] A. A. Abdo, M. Ackermann, and M. e. a. Ajello, "Observations of the Large Magellanic Cloud with Fermi," *Astronomy and Astrophysics*, vol. 512, p. A7, Mar. 2010.

[188] M. L. Lister, M. Aller, and H. e. a. Aller, "γ-Ray and Parsec-scale Jet Properties of a Complete Sample of Blazars From the MOJAVE Program," *The Astrophysical Journal*, vol. 742, p. 27, Nov. 2011.

[189] W. Max-Moerbeck, T. Hovatta, J. L. Richards, O. G. King, T. J. Pearson, A. C. S. Readhead, R. Reeves, M. C. Shepherd, M. A. Stevenson, E. Angelakis, L. Fuhrmann, K. J. B. Grainge, V. Pavlidou, R. W. Romani, and J. A. Zensus, "Time correlation between the radio and gamma-ray activity in blazars and the production site of the gamma-ray emission," *Monthly Notices of the Royal Astronomical Society*, vol. 445, pp. 428–436, Nov. 2014.

[190] M. Valtonen and S. Ciprini, "OJ287 binary black hole system.," *Memorie della Societa Astronomica Italiana*, vol. 83, p. 219, 2012.

[191] P. Kushwaha, A. C. Gupta, and P. J. e. a. Wiita, "Multiwavelength temporal and spectral variability of the blazar OJ 287 during and after the 2015 December flare: a major accretion disc contribution," *Monthly Notices of the Royal Astronomical Society*, vol. 473, pp. 1145–1156, Jan. 2018.

[192] X. Liu, L.-G. Mi, J. Liu, L. Cui, H.-G. Song, T. P. Krichbaum, A. Kraus, L. Fuhrmann, N. Marchili, and J. A. Zensus, "Intra-day variability observations and the VLBI structure analysis of quasar S4 0917+624," *Astronomy & Astrophysics*, vol. 578, p. A34, June 2015.

[193] D. P. Schneider, G. T. Richards, and P. B. e. a. Hall, "The Sloan Digital Sky Survey Quasar Catalog. V. Seventh Data Release," *The Astronomical Journal*, vol. 139, p. 2360, June 2010.

[194] E. V. Kravchenko, Y. Y. Kovalev, T. Hovatta, and V. Ramakrishnan, "Multiwavelength observations of the γ-ray flaring quasar S4 1030+61 in 2009-2014," *Monthly Notices of the Royal Astronomical Society*, vol. 462, pp. 2747–2761, Nov. 2016.

[195] T. Hovatta *et al.*, "Optical polarization of high-energy BL Lacertae objects," *Astron. Astrophys.*, vol. 596, p. A78, 2016.

[196] M. S. Shaw, R. W. Romani, G. Cotter, S. E. Healey, P. F. Michelson, A. C. S. Readhead, J. L. Richards, W. Max-Moerbeck, O. G. King, and W. J. Potter, "Spectroscopy of Broad-line Blazars from 1LAC," *The Astrophysical Journal*, vol. 748, p. 49, Mar. 2012.

[197] W. A. Barkhouse and P. B. Hall, "Erratum: "quasars in the 2mass second incremental data release" [astron. j. 121, 2843 (2001)]," *The Astronomical Journal*, vol. 122, no. 1, p. 496, 2001.

[198] A. Neronov, D. Semikoz, A. M. Taylor, and I. Vovk, "Very high-energy γ-ray emission from high-redshift blazars," *Astronomy & Astrophysics*, vol. 575, p. A21, Mar. 2015.

[199] R. Mirzoyan, "Detection of very-high-energy gamma-ray emission from the FSRQ Ton 0599 with the MAGIC telescopes," *The Astronomer's Telegram*, vol. 11061, Dec. 2017.

[200] Y. T. Tanaka, Ł. Stawarz, and D. J. e. a. Thompson, "Fermi Large Area Telescope Detection of Bright γ-Ray Outbursts from the Peculiar Quasar 4C +21.35," *The Astrophysical Journal*, vol. 733, p. 19, May 2011.

[201] M. Ackermann *et al.*, "Multifrequency Studies of the Peculiar Quasar 4C +21.35 during the 2010 Flaring Activity," *Astrophys. J.*, vol. 786, p. 157, 2014.

[202] L. Stawarz, "On the jet activity in 3C 273," *Astrophys. J.*, vol. 613, pp. 119–128, 2004.

[203] C. Chidiac, B. Rani, T. P. Krichbaum, E. Angelakis, L. Fuhrmann, I. Nestoras, J. A. Zensus, A. Sievers, H. Ungerechts, R. Itoh, Y. Fukazawa, M. Uemura, M. Sasada, M. Gurwell, and E. Fedorova, "Exploring the nature of the broadband variability in the flat spectrum radio quasar 3C 273," *Astronomy & Astrophysics*, vol. 590, p. A61, May 2016.

[204] J.-M. Casandjian and I. A. Grenier, "A revised catalogue of EGRET γ-ray sources," *Astronomy & Astrophysics*, vol. 489, pp. 849–883, Oct. 2008.

[205] P. L. Nolan, A. A. Abdo, M. Ackermann, M. Ajello, A. Allafort, E. Antolini, W. B. Atwood, M. Axelsson, L. Baldini, J. Ballet, and et al., "Fermi Large Area Telescope Second Source Catalog," *The Astrophysical Journal Supplement*, vol. 199, p. 31, Apr. 2012.

[206] L. Pacciani, I. Donnarumma, and K. D. e. a. Denney, "The characterization of the distant blazar GB6 J1239+0443 from flaring and low activity periods," *Monthly Notices of the Royal Astronomical Society*, vol. 425, pp. 2015–2026, Sept. 2012.

[207] S. Tsujimoto, J. Kushida, K. Nishijima, and K. Kodani, "Very-high-energy gamma-ray emission from high-redshift blazars with Fermi-LAT data in the southern hemisphere," in *Proceedings, 33rd International Cosmic Ray Conference (ICRC2013): Rio de Janeiro, Brazil, July 2-9, 2013*, p. 0354.

[208] M. Ackermann, R. Anantua, and K. A. et al., "Minute-timescale >100 mev -ray variability during the giant outburst of quasar 3c 279 observed by fermi-lat in 2015 june," *The Astrophysical Journal Letters*, vol. 824, no. 2, p. L20, 2016.

[209] K. V. Sokolovsky, F. K. Schinzel, and Y. T. e. a. Tanaka, "Two active states of the narrow-line gamma-ray-loud AGN GB 1310+487," *Astronomy & Astrophysics*, vol. 565, p. A26, May 2014.

[210] J. Yang and B. Zhou, "Radiation mechanisms and physical properties of gev -ray source gb 1310+487," *Publications of the Astronomical Society of the Pacific*, vol. 128, no. 962, p. 044101, 2016.

[211] X.-L. Fan, J.-M. Bai, and J. Mao, "What determines the observational differences of blazars?," *Res. Astron. Astrophys.*, vol. 16, no. 11, p. 173, 2016.

[212] V. A. Acciari, E. Aliu, T. Arlen, and T. A. et al., "Discovery of very high energy gamma rays from pks 1424+240 and multiwavelength constraints on its redshift," *The Astrophysical Journal Letters*, vol. 708, no. 2, p. L100, 2010.

[213] M. Cerruti, W. Benbow, X. Chen, J. P. Dumm, L. F. Fortson, and K. Shahinyan, "Luminous and high-frequency peaked blazars: the origin of the γ-ray emission from PKS 1424+240," *Astronomy & Astrophysics*, vol. 606, p. A68, Oct. 2017.

[214] J. Aleksi *et al.*, "MAGIC long-term study of the distant TeV blazar PKS 1424+240 in a multiwavelength context," *Astron. Astrophys.*, vol. 567, p. A135, 2014.

[215] S. Saito, Ł. Stawarz, Y. T. Tanaka, T. Takahashi, G. Madejski, and F. D'Ammando, "Very Rapid High-amplitude Gamma-Ray Variability in Luminous Blazar PKS 1510-089 Studied with Fermi-LAT," *The Astrophysical Journal Letters*, vol. 766, p. L11, Mar. 2013.

[216] M. L. Ahnen *et al.*, "Multiwavelength observations of a VHE gamma-ray flare from PKS 1510089 in 2015," *Astron. Astrophys.*, vol. 603, p. A29, 2017.

[217] S. Adrian-Martinez *et al.*, "Search for muon-neutrino emission from GeV and TeV gamma-ray flaring blazars using five years of data of the ANTARES telescope," *JCAP*, vol. 1512, no. 12, p. 014, 2015.

[218] G. Ghisellini, F. Tavecchio, and G. Ghirlanda, "Jet and accretion power in the most powerful Fermi blazars," *Monthly Notices of the Royal Astronomical Society*, vol. 399, pp. 2041–2054, Nov. 2009.

[219] N. Pekeur, R. Taylor, and R. Kraan-Korteweg, "The Optical Polarization Variability of PKS 2155-304: Correlations at Low and High Energies," *PoS*, vol. HEASA2016, p. 023, 2017.

[220] H.E.S.S. Collaboration, A. Abramowski, F. Acero, and F. e. a. Aharonian, "VHE γ-ray emission of PKS 2155-304: spectral and temporal variability," *Astronomy and Astrophysics*, vol. 520, p. A83, Sept. 2010.

[221] A. U. Abeysekara, "VERITAS long term monitoring of Gamma-Ray emission from the BL Lacertae object," *PoS*, vol. ICRC2017, p. 610, 2017.

[222] L. Maraschi, G. Ghisellini, E. G. Tanzi, and A. Treves, "Spectral Properties of Blazars. II. an X-Ray Observed Sample," *Astrophysical Journal*, vol. 310, p. 325, Nov. 1986.

[223] M. Ackermann and M. e. a. Ajello, "2FHL: The Second Catalog of Hard Fermi-LAT Sources," *The Astrophysical Journal Supplement Series*, vol. 222, p. 5, Jan. 2016.

[224] M. Whiting, A. Oshlack, and R. L. Webster, "Near-infrared micro-variability of radio-loud quasars," *Publ. Astron. Soc. Austral.*, vol. 19, p. 222, 2002.

[225] Z. Wang, R. Xue, L. Du, Z. Xie, D. Xiong, T. Yi, Y. Xu, and W. Liu, "On estimators of the jet bolometric luminosity of Fermi 2LAC blazars," *Astrophysics and Space Science*, vol. 362, p. 191, Oct. 2017.

[226] M. Tornikoski, S. J. Tingay, A. Mcke, A. Chen, V. Connaughton, D. L. Jauncey, M. Johnston-Hollitt, J. Kemp, E. A. King, P. McGee, F. Rantakyr, D. Rayner,

O. Reimer, and A. K. Tzioumis, "Multiwavelength observations of pks 2255-282," *The Astronomical Journal*, vol. 118, no. 3, p. 1161, 1999.

[227] D. J. Macomb, N. Gehrels, and C. R. Shrader, "A gamma-ray flare from pks 2255-282," *The Astrophysical Journal*, vol. 513, no. 2, p. 652, 1999.

[228] W. K. Scott, E. B. Fomalont, S. Horiuchi, J. E. J. Lovell, G. A. Moellenbrock, R. G. Dodson, P. G. Edwards, G. V. Coldwell, S. Fodor, S. Frey, L. I. Gurvits, H. Hirabayashi, M. L. Lister, L. Mosoni, Y. Murata, Z. Paragi, B. G. Piner, Z.-Q. Shen, A. R. Taylor, and S. J. Tingay, "The VSOP 5 GHz Active Galactic Nucleus Survey. III. Imaging Results for the First 102 Sources," *The Astrophysical Journal Supplement Series*, vol. 155, pp. 33–72, Nov. 2004.

[229] H.E.S.S. Collaboration, A. Abramowski, F. Acero, F. Aharonian, F. Ait Benkhali, A. G. Akhperjanian, E. Angüner, G. Anton, S. Balenderan, A. Balzer, and et al., "Discovery of very high energy γ-ray emission from the BL Lacertae object PKS 0301-243 with H.E.S.S.," *Astronomy & Astrophysics*, vol. 559, p. A136, Nov. 2013.

[230] P.-F. Zhang, D.-H. Yan, J.-N. Zhou, Y.-Z. Fan, J.-C. Wang, and L. Zhang, "A -ray quasi-periodic modulation in the blazar pks 0301243?," *The Astrophysical Journal*, vol. 845, no. 1, p. 82, 2017.

[231] H. Landt and H. E. Bignall, "On the relationship between BL Lacertae objects and radio galaxies," *Monthly Notices of the Royal Astronomical Society*, vol. 391, pp. 967–985, Dec. 2008.

[232] H.E.S.S. Collaboration, A. Abramowski, F. Acero, and A. G. e. a. Akhperjanian, "Discovery of TeV γ-ray emission from PKS 0447-439 and derivation of an upper limit on its redshift," *Astronomy & Astrophysics*, vol. 552, p. A118, Apr. 2013.

[233] S. Tsujimoto, J. Kushida, K. Nishijima, and K. Kodani, "Very-high-energy gamma-ray emission from high-redshift blazars with Fermi-LAT data in the southern hemisphere," p. 0354.

[234] S. Ciprini, L. O. Takalo, G. Tosti, C. M. Raiteri, M. Fiorucci, M. Villata, G. Nucciarelli, L. Lanteri, K. Nilsson, and J. A. Ros, "Ten-year optical monitoring of PKS 0735+178: historical comparison, multiband behavior, and variability timescales," *Astronomy and Astrophysics*, vol. 467, pp. 465–483, May 2007.

[235] M. Tornikoski, I. Jussila, P. Johansson, M. Lainela, and E. Valtaoja, "Radio Spectra and Variability of Gigahertz-Peaked Spectrum Radio Sources and Candidates," *The Astronomical Journal*, vol. 121, pp. 1306–1318, Mar. 2001.

[236] L. Costamante and G. Ghisellini, "TeV candidate BL Lac objects," *Astronomy and Astrophysics*, vol. 384, pp. 56–71, Mar. 2002.

[237] M. Cerruti and VERITAS Collaboration, "VERITAS long-term (2006-2014) observations of the BL Lac object 1ES 0806+524," vol. 34, p. 805, July 2015.

[238] V. Acciari, E. Aliu, and T. e. a. Arlen, "Discovery of Very High Energy Gamma-ray Radiation from the BL Lac 1ES 0806+524," *The Astrophysical Journal Letters*, vol. 690, pp. L126–L129, Jan. 2009.

[239] F. Aharonian, A. G. Akhperjanian, and K.-M. e. a. Aye, "Observations of Mkn 421 in 2004 with HESS at large zenith angles," *Astronomy and Astrophysics*, vol. 437, pp. 95–99, July 2005.

[240] M. Akiyama, Y. Ueda, K. Ohta, T. Takahashi, and T. Yamada, "VizieR Online Data Catalog: ASCA AGN optical identifications (Akiyama+, 2003)," *VizieR Online Data Catalog*, vol. 214, Oct. 2003.

[241] A. U. Abeysekara, S. Archambault, and A. e. a. Archer, "A Luminous and Isolated Gamma-ray Flare from the Blazar B2 1215+30," *The Astrophysical Journal*, vol. 836, p. 205, Feb. 2017.

[242] T. Armstrong, A. M. Brown, and P. M. Chadwick, "Fermi-LAT high-z active galactic nuclei and the extragalactic background light," *Monthly Notices of the Royal Astronomical Society*, vol. 470, pp. 4089–4098, Oct. 2017.

[243] Y. G. Zheng and L. Zhang, "Rapid TeV Flaring in Markarian 501," *The Astrophysical Journal*, vol. 728, p. 105, Feb. 2011.

[244] A. A. Abdo, M. Ackermann, M. Ajello, A. Allafort, L. Baldini, J. Ballet, G. Barbiellini, M. G. Baring, D. Bastieri, K. Bechtol, and et al., "Insights into the High-energy γ-ray Emission of Markarian 501 from Extensive Multifrequency Observations in the Fermi Era," *The Astrophysical Journal*, vol. 727, p. 129, Feb. 2011.

[245] J. Jaeckel, E. Massó, J. Redondo, A. Ringwald, and F. Takahashi, "Need for purely laboratory-based axionlike particle searches," *Physical Review D*, vol. 75, p. 013004, Jan. 2007.

[246] A. A. Abdo, M. Ackermann, M. Ajello, A. Allafort, E. Antolini, W. B. Atwood, M. Axelsson, L. Baldini, J. Ballet, G. Barbiellini, and et al., "Fermi Large Area Telescope First Source Catalog," *The Astrophysical Journal Supplement*, vol. 188, pp. 405–436, June 2010.

[247] X.-H. Sun and W. Reich, "The Galactic halo magnetic field revisited," *Research in Astronomy and Astrophysics*, vol. 10, pp. 1287–1297, Dec. 2010.

Acknowledgements

Many people have been involved with the past three years of my PhD life whom I would like to thank from the bottom of my heart for their constant love and support.

Firstly, I would like to express my sincere gratitude to my advisor Prof. Dr. Dieter Horns for giving me an opportunity to pursue scientific work in such an exciting topic. I am really grateful to him for his continuous support and confidence in me and how he gave me freedom to develop my project during my Ph.D study. His guidance motivated me in all the time of research and writing of this thesis. The joy and never ending enthusiasm he has for his research was contagious and inspirational for me, even during tough times in the Ph.D. pursuit. I could not have imagined having a better advisor and mentor for my Ph.D study.

Besides my advisor, I would like to thank Prof. Dr. Alessandro Mirizzi for co-refereeing my thesis and my defense. My earnest thanks goes to the rest of my thesis committee: Prof. Caren Hagner , Prof. Guenter Sigl, and Dr. Christian Sander, for their kind acceptance to be the part of the defense committee . I am very much grateful to Prof. Dieter Horns and Dr. Martin Tluczykont for their help regarding physics as well as computational problems. A heartful big thanks goes to my collaborator Dr. Francesca Calore for her constant help in my project, whenever I needed.

I am grateful to my parents, who have provided me through moral and emotional support in my life. I am also grateful to my other family members and friends who have supported me along the way.

A very special gratitude goes out to all down at Research Fund SFB 676 for helping and providing the funding for the work and the work related travel. I would like to thank PIER graduate school for giving me the opportunities to pursue the extra curricular activities besides research.

I thank my fellow officemates in for the stimulating discussions, for the late nights when we were working together before deadlines, and for all the fun we have had in the last three years. First of all, I want to thank my officemates, two cheerful ladies

Noemie Bastidon and Ludmilla Dirson for making the nice working atmosphere. A heartful thanks goes to Le Hoang Nguyen for all the academic, non-academic discussions (specially related to cooking) and the enjoyable conferences where we went together. Also I thank my dear group mates: Andrei Lobanov, Chao Zhang, Rayk Nachtigall, Maike Kunnas, Padam Ghimire, Gu Yikun, Kin Hang Yeung, Junghoon, Ali, Henric and the other members of the group. Especially, I would like to thank Le Hoang Nguyen, Ludmilla Dirson and Dr. Martin Tluczykont for proof-reading and their kind suggestion for phrasing. A warm thanks goes to Rainer Peter Feller and the whole IT team of the University of Hamburg for their constant support regarding IT issues.

And finally, last but by no means least, I cannot thank enough my Indian friends: Anand Kamlapure, Aritra Mukhopadhaya, Swathi Sashikumar and others in DESY campus for making a sweet home here away from home. I could not finish my PhD without their constant support when I needed.

Eidesstattliche Versicherung

Declaration on oath

Hiermit erklare ich an Eides statt, dass ich die vorliegende Dissertationsschrift selbst verfasst und keine anderen als die angegebenen Quellen und Hilfsmittel benutzt habe.

I hereby declare, on oath, that I have written the present dissertation by my own and have not used other than the acknowledged resources and aids.

Hamburg
17th May, 2018
Unterschrift